Hi-line Mapping of Large-Scale Structures in the Zone of Avoidance

Mpati Ramatsoku

26 November 2012

A project submitted in partial fulfilment of the requirements for the degree M.Sc. in the Department of Astronomy, as part of the National Astrophysics and Space Science Programme
UNIVERSITY OF CAPE TOWN

Supervisors: Prof. R.C. Kraan-Korteweg, Dr A.C. Schröder and Dr. W. van Driel

Abstract

This dissertation presents a survey made in the 21 cm wavelength line of the neutral hydrogen (HI) to determine redshifts of 928 galaxy candidates in the Zone of Avoidance (ZoA). The 2MASS Redshift Survey (2MRS) is currently the most uniform "whole-sky" redshift survey for mapping large-scale structures, and studying the dynamics in the nearby Universe and the Cosmic Microwave Background (CMB) dipole. While this survey is supposed to cover the whole sky, it excludes the inner ZoA ($|b| \lesssim 5^\circ$) because of difficulties in detecting galaxies due to the heavy obscuration caused by dust and stellar crowding. The lack of redshift data in the ZoA remains the main source of uncertainties in studies of the nearby Universe.

To improve on this, the 100m-class Nançay Radio Telescope was used to measure the 21 cm line emission of 928 near-infrared bright galaxy candidates without redshift information in the ZoA which are accessible from the NRT (Dec $> -39^\circ$), hence focuses predominantly on the mostly unexplored northern ZoA. The selected galaxy candidates were extracted from the near-infrared 2MASS Extended Source Catalog (2MASX) and have extinction-corrected magnitudes of $K_s^o \leq 11\overset{\mathrm{m}}{.}25$. This survey complements the existing 2MRS as well as the ongoing 2MASS Tully-Fisher survey which also leaves out the inner ZoA. Of the 1000 2MASX galaxy candidates in the NRT sample, 928 were observed by 31 March 2012, the cut-off date for analysis of this thesis. Of the 928 observed galaxies, 249 (27%) were detected to an rms sensitivity limit of 3.3 mJy and a radial velocity limit of 10500 km s^{-1}.

The resulting redshift distribution reveals various new large-scale structures crossing the ZoA that were hitherto uncharted. The most obvious filamentary structures cross the Galactic Plane at $\ell \approx 90^\circ$, $\ell \approx 160^\circ$ as well as $\ell \approx 180^\circ$. They are all closely linked to the larger Perseus-Pisces Supercluster ($v \approx 6500\,\mathrm{km\,s^{-1}}$). A previously suspected structure crossing the ZoA at $\ell \approx 90^\circ$ is confirmed for the first time, i.e., an extension of the second Perseus-Pisces arm. Another conspicuous structure crosses the Galactic Plane at $\ell \approx 160^\circ$. Within that wall-like structure an X-ray cluster seems embedded which also hosts two identified strong radio galaxies (3C 129 and 3C 129.1). This ridge extends from the Perseus-Pisces Complex across the ZoA towards the northern Galactic hemisphere and links the Perseus cluster (A 426; $\ell, b, v \simeq 150^\circ, -13^\circ, 5000\,\mathrm{km\,s^{-1}}$) to Abell 569 ($\ell, b, v \simeq 168^\circ, 23^\circ, 5800\,\mathrm{km\,s^{-1}}$). These new structures imply that the PPScl is potentially more extended and massive than indicated in previous studies. Through the success of this

survey the power of revealing previously unknown large-scale structures in the ZoA through HI observations of intrinsically bright (extinction-corrected) NIR galaxies is demonstrated.

Some of the main results of chapter 4 were presented and will appear in the peer reviewed proceedings of the South African Institute of Physics (SAIP2012): Ramatsoku, M., Kraan-Korteweg, R.C., Schröder A.C., & van Driel, W., Extragalactic large-scale structures in the northern Zone of Avoidance.

Acknowledgements

I would like to express my sincere and deep gratitude to my supervisors Prof. R.C. Kraan-Korteweg, Dr A.C. Schröder and Dr. W. van Driel for their supervision, enthusiasm and admirable patience. I have greatly benefited from ideas generously given and time spent on this thesis. Many thanks to Observatoire de Paris-Meudon for the hospitality I received.

I would also like to thank my colleagues and friends at the UCT Astronomy Department and those who have left for their support and feedback. I especially like to thank Kosma, Tom, Wendy, Zolile and Deanne for sharing their knowledge of Python with me. You were never too busy to help and for that I am deeply grateful.

To my family, thank you all for the encouragements and unwavering support throughout my studies, Ke a leboha!!. An extra special thanks to my father for making it possible for me to make it this far. I take this opportunity to express my gratitude to Mpho for the comfort, encouragement and support when things got tough. I am grateful to all my amazing friends who have always been there to ensure my well being.

Finally, I am thankful for the financial support of the South African SKA project and that of the UCT Astronomy multi-wavelength grant.

This publication makes use of data products from the Two Micron All Sky Survey, which is a joint project of the University of Massachusetts and the Infrared Processing and Analysis Center/California Institute of Technology, funded by the National Aeronautics and Space Administration and the National Science Foundation

This research has made use of the NASA/IPAC Extragalactic Database (NED) which is operated by the Jet Propulsion Laboratory, California Institute of Technology, under contract with the National Aeronautics and Space Administration.

The Digitized Sky Surveys were produced at the Space Telescope Science Institute under U.S. Government grant NAG W-2166. The images of these surveys are based on photographic data obtained using the Oschin Schmidt Telescope on Palomar Mountain and the UK Schmidt Telescope. The plates were processed into the present compressed digital form with the permission of these institutions.

Plagiarism Declaration

I, Mpati Ramatsoku, know the meaning of plagiarism and declare that all of the work in the document, save for that which is properly acknowledged, is my own.

Contents

List of Figures

List of Tables

Chapter 1

Introduction

The Universe has a complex topology, a "cosmic web" of galaxy filaments, clusters, sheets and voids (Davis et al. 1982, de Lapparent et al. 1986). These structures define its present state (Bond et al. 1996, Holtzman 1989, Springel et al. 2006). The distribution of mass within the Universe constitutes of the visible and the not so easily measurable dark matter and dark energy. The former is traced by light while the true mass distribution (i.e, visible and dark) can be determined by velocity flow fields which occur because of the influence of gravity.

These flow fields are observed through the motions of large-scale structures, which are defined for instance by Fairall (1998) as "condensations of galaxies with a galaxy-galaxy separation less than 200 km s^{-1} in redshift space". These structures resulted from the gravitational instability of a relatively smooth medium in the Early Universe. Their non-linear patterns observed today evolved from minute density fluctuations on a homogeneous isotropic background (Guth & Pi 1982, Hawking 1982, Bond et al. 1996).

The global motion of these extragalactic large-scale structures, which arises due to the cosmological principle of the expanding Universe (Sandage et al. 1972), is described by the Hubble law (Hubble 1929) and the resulting motion pattern is referred to as the Hubble flow.

In general the Hubble flow holds on large scales but not locally due to the non-uniform matter distribution. Galaxies in the nearby Universe are distributed in irregular tangles of large-scale structure hierarchies (Davis & Peebles 1983, Navarro et al. 1997). Fluctuations of the gravitational field deflects them from the "pure" Hubble flow. These slight differences are referred to as "peculiar motions" (Strauss & Willick 1995).

These peculiar motions play a fundamental role in the measurement of the matter responsible for their origin. This is because there is a direct correlation between the size of the motion and their mass density field (Bird 1994). In other words, the larger the observed peculiar motion, the higher the value of the cosmological density parameter and consequently, the matter content in that volume of the Universe (Bertschinger & Dekel 1989, Dekel et al. 1990).

There are two ways of measuring these motions, directly and indirectly. The direct method measures distances to galaxies using various extragalactic distance indicators and then subtracts the Hubble flow parameter to obtain the peculiar velocities (Strauss & Willick 1995). The indirect technique measures the redshift space through dedicated redshift surveys of a large number of galaxies. This enables the redshift distribution of the sample, hence the velocity of galaxies to be measured assuming the Hubble law is preserved.

If there are peculiar motions in the sample, they will distort the redshift space map. Since peculiar velocities are not directly proportional to the distance but have a dependence on the matter density (Strauss et al. 1992, Bird 1994), this manifests itself in a strong gravitational field force in dense regions of these maps and thus the observation of random peculiar motions.

There are disadvantages associated with both methods. The direct method experiences problems due to difficulties caused by implicit errors in extragalactic distance scales calibrations (Mould et al. 2000). The indirect technique requires very large and uniform galaxy redshift samples.

Obtaining uniform whole-sky redshift samples, moreover, is impeded by the small number of galaxies found behind the Galactic Plane in the so called Zone of Avoidance (ZoA). This is where foreground dust extinction and the high star densities in the Galactic Plane prevents the detection of galaxies across 20% of the sky (e.g., within $|b| \lesssim 10^{\circ}$) in the optical wavelength (Kraan-Korteweg 2005).

To bypass this problem, density interpolation methods across the ZoA are often used (Dekel et al. 1990, Yahil et al. 1991, Lahav 1994). These try to "fill in" the ZoA gap with the average density of galaxies by replicating galaxies from adjacent regions at higher latitudes on both sides of the Galactic Plane (GP) into the ZoA (Lynden-Bell et al. 1989). More elaborate methods of interpolating galaxy density fields expand the angular distribution of IRAS galaxies in spherical harmonics and extrapolate these into the ZoA (Hoffman et al. 1991, Scharf et al. 1992, Lahav 1994).

While these methods try to circumvent the ZoA gap they still suffer from systematic errors due to the lack of data in this region, as will be described in more detail in sections to follow. As a result, a great deal of work over the last two decades has gone into unveiling the galaxy distribution behind the Galactic Plane (e.g., for a review see Kraan-Korteweg 2005). The two motivations for this being dynamical studies of large structures and to obtain a complete whole-sky map of their distribution in the local Universe. This has resulted in progress in the reduction of the ZoA using various dedicated surveys at almost all electromagnetic wavelengths, however, they are not without problems (see Kraan-Korteweg & Lahav 2000). For instance, optical surveys suffer from dust extinction which dims the brightness of galaxies, while near-infrared (NIR) wavelengths, where dust extinction is greatly diminished, suffer from stellar crowding, particularly near the Galactic bulge. The most effective method of probing the ZoA for redshift determinations has proved to be at radio wavelengths, where effects of dust extinction are insignificant, by using the 21 cm line emission of galaxies (Kerr & Henning 1987). It should however, be kept in mind that HI is only detected in gas-rich

galaxies.

This dissertation presents an HI survey of NIR bright galaxies without previous redshift information in hitherto hardly explored regions (∼6000 square degrees) of the ZoA with in $270° \lesssim \ell \gtrsim -20°$. The data set is used to reveal new structures behind the Galactic Plane and complement the near-infrared 2MASS Redshift Survey (Huchra et al. 2005, Huchra et al. 2012) which is currently the deepest and uniform systematic "all-sky" redshift survey. These data can also be used to gauge the mass distribution in the Local Universe, which will in turn contribute to ongoing cosmological studies of the Cosmic Microwave Background dipole anisotropy.

In the following sections more background to the problem setting, results achieved so far and the approach pursued of selecting NIR bright in the ZoA in HI is given. Section 1.1 of this chapter gives a historic overview of the ZoA and discusses the role played by dust extinction and stellar densities in creating this gap. In Sect. 1.2 a description of peculiar velocities and the origin of the CMB dipole in relation to problems posed by the ZoA is given. This is followed in Sect. 1.3 by a discussion of multi-wavelength techniques employed for the reduction of this gap. The main focus of this project and the motivation behind filling the gap in the galaxy distribution of the northern part of the ZoA is described in Sect. 1.4. This will be followed by an outline of the thesis in Sect. 1.5.

1.1 The Zone of Avoidance

In 1878, Proctor (Proctor 1878) noticed that the General Catalogue of Nebulae (Herschel 1864) had no nebulae near the Galactic Plane. This was at a time when it was not yet known that most of these "nebulae" were actually extragalactic objects. It was only after Cepheids were observed in spiral nebulae (Hubble 1925) that their distances were determined to be extragalactic and because of this these nebulae were afterwards known as galaxies. In addition, Galactic extinction was poorly understood at the time and no explanation regarding the "avoidance" of galaxies in that region of the sky was offered. It was only in 1930 that Trumpler showed that the obscuration caused by interstellar dust within the Milky Way made extragalactic objects in the Galactic Plane appear fainter and smaller, resulting in the apparent sparse population of galaxies in that region (Trumpler 1930). Due to the great difficulty in detecting objects in this region and this apparent avoidance of galaxies, it became known as the "Zone of Avoidance" (ZoA). Shapley's (1961) first formal definition of the ZoA was that of a region bounded by "the isopleth of galaxies of five galaxies per square degree from the Lick and Harvard Surveys" (Shapley 1961). For comparison, the typical density of galaxies far from the Galactic Plane is 54 galaxies per square degree (Shane & Wirtanen (1967).

Since extinction is a function of wavelength, the ZoA extent is dependent on the wavelength of observation. For instance, at optical wavelengths about 20% of the sky is heavily obscured (absorption of about $A_B = 1\overset{\text{m}}{.}0$) (Kraan-Korteweg 2005) whereas only about 10% of the sky is obscured in the near infrared (NIR) (Jarrett et al. 2000). The main cause of the

obscuration is optical dust extinction, which increases towards the Galactic Plane (Schlegel et al. 1998). In the NIR, the diminishing effect is caused by high stellar densities around the Galactic Bulge and Plane resulting in confusion in the identification of diffuse galaxy images.

1.1.1 Galactic Dust Extinction

Dust particles decrease the intensity of starlight by absorbing and scattering it in the NIR and optical wavelength (Cardelli et al. 1989). The amount of absorption and scattering decreases towards longer wavelengths. In other words, blue wavelengths (e.g., 450-495 nm) suffer more extinction than red (e.g., 635-700 nm).

Extinction A(λ) is defined as the difference between the observed magnitude of an object and its intrinsic magnitude at a given wavelength:

$$A(\lambda) \equiv -2.5(log_{10}I(\lambda) - log_{10}I_o(\lambda)), \tag{1.1}$$

where $I(\lambda)$ and $I_o(\lambda)$ are the observed and intrinsic intensities, respectively.

In general, interstellar dust particles have various sizes, chemical composition as well as shapes and so the amount of absorption and scattering is also dependent on those factors (Gordon et al. 2003). In addition the distribution of particles in the interstellar medium (ISM) is not homogeneous and this results in the variation of the amount of extinction depending on the line of sight.

The extinction curve is given by:

$$k(\lambda) = \frac{A(\lambda)}{A_V}, \tag{1.2}$$

where A_V is the extinction in the V band.

The extinction curve $k(\lambda)$ is dependent on the column density as function of wavelength, which is a function of the particle size as well as the distribution along the line of sight. Typical extinction curves are given in Fig. 10 of Gordon et al. (2003).

Dust extinction is represented by (Cardelli et al. 1989):

$$A_V \equiv R_V E(B-V), \tag{1.3}$$

where the factor R_V varies with the line of sight and $E(B-V)$ is the colour excess representing the degree of reddening caused by scattering.

To determine dust extinction within a certain bandpass (A_{bp}) the extinction law is integrated over the filter response curve,

$$A_{bp} = -2.5log_{10}\left(\frac{\int W_{bp}(\lambda)S(\lambda)10^{-0.4k(\lambda)R_V E(B-V)}d\lambda}{\int W_{bp}(\lambda)S(\lambda)d\lambda}\right), \tag{1.4}$$

where $W_{bp}(\lambda)$ and $S(\lambda)$ represent the filter function of the bandpass and the spectral energy

distribution (SED) of the object respectively. Typical extinction values, A_{bp}, as determined by Schlegel et al. (1998) are

$$\begin{aligned} A_B &= 4.315E(B-V), \\ A_J &= 0.902E(B-V), \\ A_H &= 0.576E(B-V), \\ A_K &= 0.367E(B-V). \end{aligned} \tag{1.5}$$

Extinction Maps

The Galactic extinction in the optical and near-infrared is estimated from the Schlegel et al. (1998) (SFD) all-sky maps of Galactic reddening, which are based on the far-infrared (FIR) emission of dust. These dust maps were made using a combination of FIR maps by the Infrared Astronomical Satellite IRAS (Neugebauer et al. 1984), the IRAS Sky Satellite Survey, ISSA (Wheelock et al. 1994) and the Cosmic Background Explorer Diffuse Infrared Background Experiment (COBE/DIRBE; Hauser 1988). The SFD maps were calibrated using DIRBE data and the angular resolution controlled and improved using IRAS data.

In the first instance a dust temperature map from the 100μm and 240μm was used to create a dust column density map. This map was then converted to an $E(B-V)$ colour excess map using elliptical galaxies as standard colour indicators. An all-sky map of $E(B-V)$ in Galactic coordinates from Schlegel et al. (1998) is shown in Fig. 1.1.

It should be kept in mind however, that the DIRBE extinction maps are not calibrated at the lowest latitudes ($|b| < 5°$), i.e, the region of interest for this dissertation, because of bright source contamination caused by high source densities. It has been found that a direct extrapolation of DIRBE, $E(B-V)$ values at low Galactic latitudes ($|b| < 10°$) gives an overestimate of $\sim$ 13 - 33% (Schröder et al. 2007). This correction is not applied in the analysis of the data presented in this thesis.

1.1.2 Star Densities

The surface density of stars increases exponentially towards the Galactic disk, resulting in an increase in the average sky background noise (Jarrett et al. 2000) and a decrease in the number of galaxies seen. This stellar density effect restrains the level of completeness and reliability achievable by catalogues such as the near-infrared 2MASS Extended Source Catalog (Skrutskie et al. 2006) (detailed discussion in section 1.3.4). The stellar density causes confusion in galaxy identification which occurs when one or more stars appear close to the extended target. The variation of stellar number density with Galactic latitude and longitude is shown in Fig. 1.2, which shows the number of stars per square degree brighter than $K_s < 14\overset{\text{m}}{.}00$ in the 2MASS Point Source Catalog (Cutri et al. 2003). The number density in the Galactic Plane ranges from $\log N_{K_s<14} < 3.2$ (light grey region) to $\log N_{K_s<14} > 4.5$ in the Galactic bulge (white region).

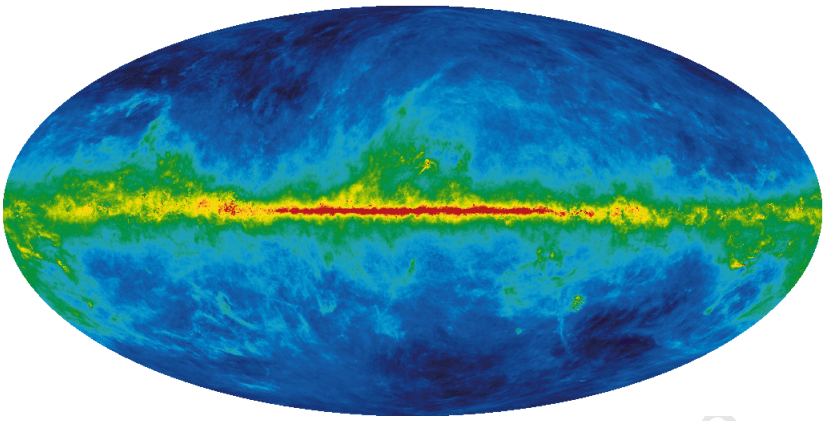

Figure 1.1: An all-sky $E(B-V)$ extinction map in Galactic coordinates from Schlegel et al. (1998). It is from the Legacy Archive for Microwave Background Data Analysis (LAMBDA). The map shows $E(B-V)$ values on a logarithmic scale, ranging from $0\overset{\text{m}}{.}004$ (dark blue) to $6\overset{\text{m}}{.}300$ (red). The Galactic Centre is located in the middle.

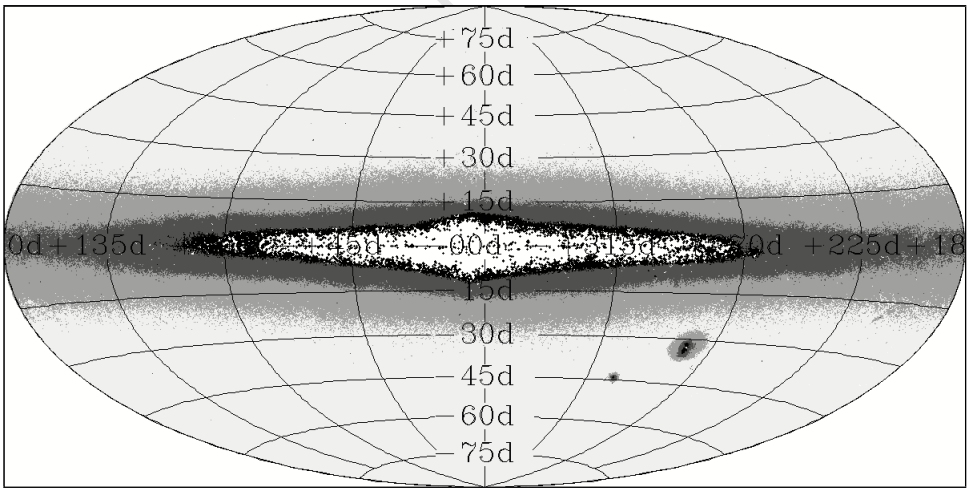

Figure 1.2: The number N of stars per square degree brighter than $K_s < 14\overset{\text{m}}{.}00$ in the 2MASS Point Source Catalog (Cutri et al. 2003). The light grey region indicate areas where stellar density is low, $\log N_{K_s<14} < 3.2$, and the white region are those with high stellar densities of $\log N_{K_s<14} > 4.5$ (Jarrett et al. 2000). It coincides with the area in which the 2MASS Extended Catalog becomes highly incomplete.

1.2 The ZoA and Velocity Flow Fields

Redshift surveys give a wealth of data that assist in discovering and describing large-scale structures. The more fundamental cosmological issue being addressed by them is the distribution of mass in the Universe, which is traced by peculiar velocity flow fields. In this section a relation between peculiar velocities and the mass density distribution is described in detail.

1.2.1 Peculiar Velocity Fields

Studies have shown that galaxies are receding from one another, caused by the expansion of the Universe as expressed by the Hubble law (Hubble 1929),

$$v = cz = H_0 r, \tag{1.6}$$

Where H_0 is the Hubble constant (taken to be 70 km s^{-1} Mpc^{-1} for this thesis), v is the radial velocity of a galaxy and r its distance.

Eq. (1.6) shows that recession velocity of a galaxy is proportional to its distance r. This law determines Hubble flow velocities in the nearby Universe accurately because the influence of relativistic effects are negligible. However, galaxies have a peculiar component associated with their space motion with respect to the local rest frame, which can be substantial compared to their Hubble flow velocities.

These *peculiar motions* result in peculiar velocities in addition to the Hubble velocities of galaxies, whose radial velocities therefore deviate from the uniform Hubble expansion and as a result Eq. (1.6) becomes (Strauss & Willick 1995),

$$v = cz = H_0 r + \hat{r}[\tilde{v}(r) - \tilde{v}(0)], \tag{1.7}$$

In this equation $\hat{r}$ is the unit vector in the direction of a galaxy, $\tilde{v}$(r) is its peculiar velocity at position r and $\tilde{v}(0)$ its peculiar velocity. Peculiar motions are related to the non-uniform mass distribution of large-scale structures in the Local Universe.

In cosmic dynamical studies linear perturbation theory states that peculiar motions are proportional to the gravitational acceleration,

$$v(r) = \frac{H_0 f}{4\pi} \int \delta(r') \frac{r' - r}{|r' - r|^3} d^3 r, \tag{1.8}$$

In this equation r is measured in units of km s^{-1} and therefore $H_0 \equiv 1$. The implication of this is that by comparing the velocity and density fields, $v(r)$ and $\delta(r)$ respectively, the rate of growth of the perturbations, f, can be measured (Lahav et al. 1991) accordingly,

$$f = \Omega_0^{0.6} + \frac{\Omega_\Lambda}{70}(1 + 0.5\Omega_0), \tag{1.9}$$

This will lead to constraints on $\Omega_0^{0.6}$ (the density parameter)* and Ω_Λ, the cosmological con-

*The superscript 0.6 is the redshift (z) at which different cosmologies of the same Ω_0 can be tested with

stant in the standard cold dark matter model (ΛCDM). This cosmological model attempts to explain the formation of large-scale structures and the existence of the Cosmic Microwave Background.

The radial component of the peculiar velocity of a galaxy, $v(r)$ is obtained by separating the velocity contribution of the expanding universe and the peculiar motion of a galaxy,

$$v(r) = cz - H_0 r, \tag{1.10}$$

However this requires the distance, r, to be measured independent of the redshift. The radial component is the only component of peculiar velocities that can be measured.

This means that to extract all the other components available in the velocity field, methods such as POTENT (Dekel et al. 1990) have to be used. The POTENT reconstruction method assumes that the observed radial velocity field is proportional to the gradient of the potential field,

$$v(r) = - \bigtriangledown \Phi(r), \tag{1.11}$$

where $\Phi(r)$ is the potential field and $v(r)$ the velocity field. The validity of this equation stems from the assumption that large-scale structures evolved from gravitational instabilities (Strauss & Willick 1995). The implication of this is curl free velocities on large-scales, which in turn results in negligible vorticity due to the decay of vorticity modes in the linear regime of the expanding universe (Dekel 1994). This linear assumption breaks down near the high-density cores of superclusters.

The integration of (1.11) along radial rays gives the potential, while the transverse component of the velocity field is recovered by differentiating (1.11) in the transverse direction. The mass density $\delta(r)$ can then be derived from linear theory, using

$$\delta(r) = -\Omega_0^{0.6} \bigtriangledown .v(r), \tag{1.12}$$

The POTENT method is applicable because observed velocities allow for the density field to be mapped independent of the distribution of galaxies.

Although reconstruction methods such as POTENT, Wiener Filter (Wiener 1949) and spherical harmonics (Fisher et al. 1994) try to overcome the problem of the ZoA. They also suffer from incompleteness sampling due to the heavy smoothing required. The result is that only large-scale structures such as superclusters can be mapped. This results in errors because of the inhomogeneous coverage of individual measurements.

Large-Scale Structure Dynamics

The key to complete studies of large-scale dynamics are redshift-independent distance measurements of large data sets. This can be done using distance indicator relations which essentially relate two intrinsic properties of a galaxy, a distance independent property such as

the Hubble diagram of type 1a supernovae

surface brightness and a distance dependent such as diameter. Many empirical correlations between distance dependent and distance independent properties have been used in dynamical studies. However, the two that remain the most useful in determining peculiar velocities are the Tully-Fisher relation (Tully & Fisher 1977) for spirals and the Fundamental-Plane (Djorgovski & Davis 1987) for elliptical galaxies.

1.2.2 The CMB Dipole

The Cosmic Microwave Background (CMB) is the uniform thermal radiation that fills the universe. It is a useful probe of the early universe due to its dominant brightness at millimetre wavelengths. The CMB has a monopole component with a mean temperature of $T = 2.725 \pm 0.001$ K (Mather et al. 1999) but also has a dipole anisotropy of $\delta T/T \approx 10^{-3}$. This anisotropy is a result of the Doppler shift effect caused by the motion of the Earth relative to the cosmic rest frame. Transformed to the centre of mass of the Local Group (LG), the velocity of this motion is $627 \pm 22\,\mathrm{km\,s^{-1}}$ toward $(l,\ b) \sim (276^\circ \pm 3^\circ,\ 30^\circ \pm 3^\circ)$ (Kogut et al. 1993).

One of the many goals of redshift surveys is to be able to apply Eq. (1.8) to the Local Group (Strauss & Willick 1995). The motion of this group would then be compared with the dipole moment of the galaxy distribution to directly measure the angular dipole moment of the CMB. Since gravity and the received light both follow the inverse square law, the peculiar velocity is then directly proportional to the ratio of the dipole moments of the light distribution. This implies that assuming a full-sky redshift survey and constant mass-to-light to ratio Eq. (1.8) can be applied using angular data only (Strauss & Willick 1995). The precise measurements of this vector in the CMB from the matter distribution of the LG motion will lead to constraints on the cosmological density parameter.

1.2.3 The ZoA Problem

A whole-sky survey is required for peculiar velocity and direction determinations as discussed in section 1.2.2. However, due to the obscuration close to the Galactic Plane the ZoA still remains sparsely sampled. Because of this our understanding of the distribution of structures behind the GP remains uncertain. This ZoA barrier is particularly problematic in explorations of the motion of the LG with respect to the CMB, which shows discrepancies because of the possible unknown structures behind the GP (Loeb & Narayan 2008). The lack of data in this region is also responsible for large systematic errors in dynamical models.

Several methods have been used to "fill" this gap statistically so as to determine the velocity fields and the dipole, these include:

- Cloning methods which duplicate galaxies from the adjacent high latitude regions into the ZoA (c.f., Yahil et al. 1991).
- Expanding the angular distribution of galaxies using spherical harmonics analysis

methods and extrapolating them into the ZoA. This is done by mask inversion using Wiener filtering (Hoffman et al. 1991, Scharf et al. 1992, Lahav 1994, Fisher et al. 1995)

- Correcting for the ZoA by assuming a homogeneous sample across this region by statistical interpolation methods of the mass density distribution (e.g., Lynden-Bell et al. 1989).

Although these procedures have tried to go around the ZoA barrier, due to the non-uniform data sampling and incorrect assumptions of the ZoA galaxy distribution, they remain unsatisfactory.

For example a derivation of the Local Group (LG) acceleration within $b \pm 20^\circ$ was done using interpolation methods (Kolatt et al. 1995). This showed that based on the mass distribution at $\sim 6000\,\mathrm{km\,s^{-1}}$ the LG vector (see section 1.2.2) changes direction by $\sim 31^\circ$, to about $4^\circ \pm 19^\circ$ of the CMB (Kolatt et al. 1995). This clearly indicate that cosmological parameters are likely to be strongly affected by the mass distribution in the ZoA. A reliable census of this region is paramount in order to minimise these uncertainties (Kraan-Korteweg & Lahav 2000).

1.3 Surveys in the ZoA

The extent of the ZoA in the distribution of galaxies, even clusters of galaxies depends on the wavelength at which it is being observed. It is therefore important to employ a multi-wavelength approach when observing this region to get as complete a census as possible. In this section a brief overview of surveys in the ZoA at different wavelengths is discussed.

1.3.1 Optical

Over the years great efforts have gone into revealing galaxies behind the GP in the band apparently void of galaxies that takes up 20% of the sky at optical wavelengths (see e.g., Kraan-Korteweg 2005 for a review of optical surveys in the ZoA up to that date). An Aitoff projection of galaxies detected in the optical is shown in Fig. 1.3. These are galaxies with an extinction-corrected isophotal diameter $D \geq 1\farcm3$. The ZoA is the band void of galaxies within $|b| \lesssim 10^\circ$. The advantage of the optical wavelength is the lack of bias toward any morphological type. Deep optical surveys have been able to reduce the ZoA by a factor of $2-3$, compared to the status before these surveys, resulting in a ZoA that is now $|b| \lesssim 5^\circ$. The disadvantage of optical surveys is that they are affected most by dust extinction which increases towards the Galactic Plane. This causes incompleteness in optical catalogues because of the reduced brightness of galaxies and the extension of their visibility.

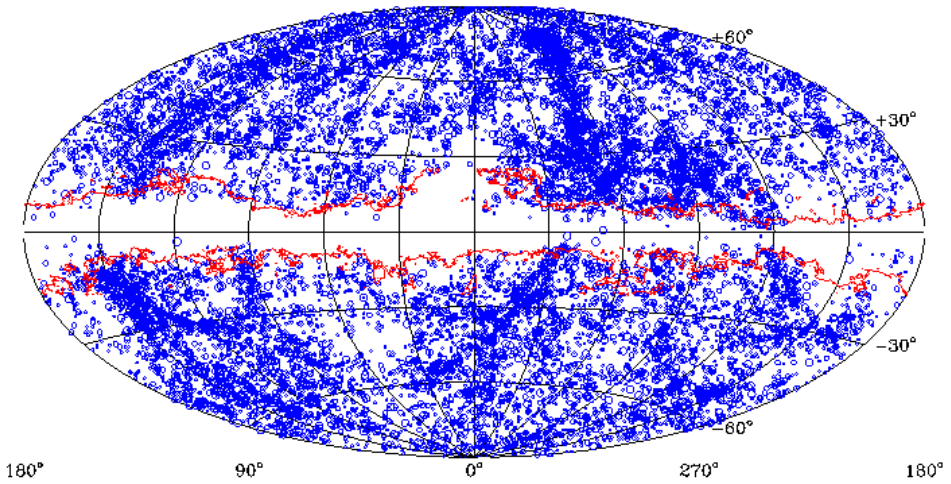

Figure 1.3: The distribution of optically detected galaxies with $D \geq 1'.3$. The red contours mark the $A_B = 1^{\rm m}.0$ extinction (Schlegel et al. 1998) which closely traces the ZoA band between $|b| \approx \pm\ 10°$. Figure from Kraan-Korteweg (2005).

1.3.2 X-rays

The X-ray band is an interesting option for exploring structures behind the ZoA. This is because rich clusters with more than 10^{14}M$\odot$ of diffuse hot (10^{7-8}K) gas emit at this wavelength (Ebeling et al. 1998), which makes this wavelength an ideal tracer of galaxy clusters. The ROSAT-ESO X-ray sample (REFLEX; Böhringer et al. 2001) and the Brightest Clusters Sample (BCS; Ebeling et al. 1998) have surveyed the whole sky at $|b| > 20°$ in the soft X-ray (0.1 – 2.4) keV band with about a 3×10^{-12} erg.cm^{-2} flux limit. The extent of the ZoA at $|b| > 30°$ in X-rays is shown in Fig. 1.4, which is an equal-area projection of the distribution of Galactic hydrogen column density. The red band at $|b| \lesssim 30°$ is the region of high n_H which is responsible for the "X-ray ZoA". At $|b| < 20°$ the ongoing Clusters in the Zone of Avoidance survey (CIZA; Ebeling et al. 2005) is systematically searching for clusters behind the Galaxy in the (0.1 – 2.4) keV band. Although X-ray surveys overcome dust extinction and stellar confusion that plague optical and near-infrared (see section 1.1.1 and 1.1.2) wavelengths, they, in their turn, are limited by the hydrogen column density (n_H) which gradually increases towards the Galactic Plane causing photoelectric absorption of the target emission. This is the most problematic in the 0.1 - 2.4 keV band and less adverse at hard X-rays (> 2.5 keV) but so far no systematic hard X-ray surveys exist for the ZoA. CIZA has been able to penetrate the most obscured regions of the Galactic Plane and detect many new clusters but, areas with $n_H \gtrsim 10^{22}$ cm^{-2} are still problematic to probe at X-ray wavelengths (Ebeling et al. 2005).

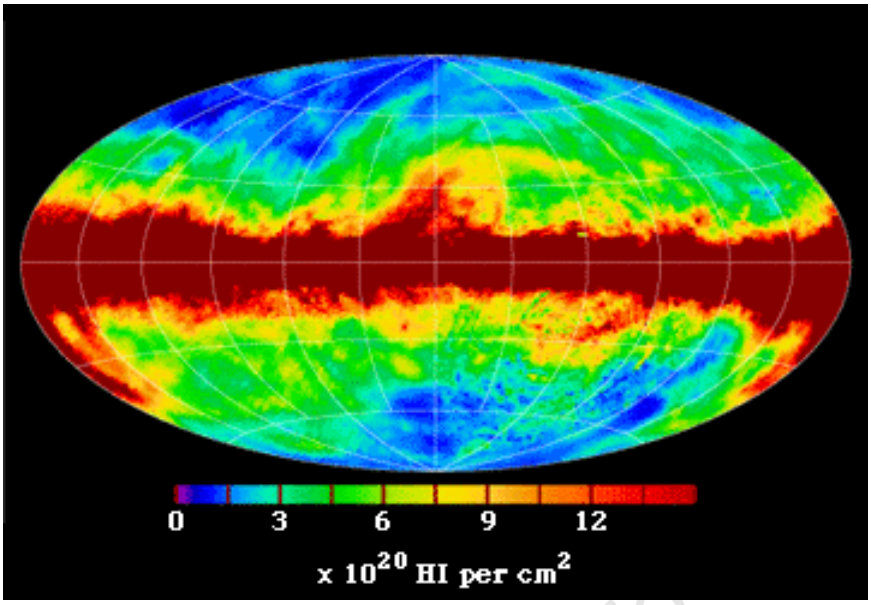

Figure 1.4: An equal-area projection in galactic coordinates centred on $\ell \simeq 0°$ of the distribution of the Galactic n_H. The red band at $|b| \lesssim 30°$ marks regions of $n_H \gtrsim 10^{22}$ cm^{-2} responsible for the "X-ray ZoA". The image is from the NASA Goddard Space Flight Centre*.

1.3.3 21 cm H I line emission

The neutral hydrogen atom consists of an electron that exists in the neighbourhood of a proton in one of a number discrete atomic orbitals. The ground state of the hydrogen atom is not a single definite energy state, but four very closely spaced states – this phenomenon is known as hyperfine splitting. Transitions between these hyperfine states give rise to the so called 21 cm spectral line emission which occurs when photons are emitted due to a spontaneous "spin flip" (parallel to anti-parallel) of the proton and electron. The change in energy, ΔE, between the parallel and the anti-parallel spins is 5.88×10^{-6} eV (Griffiths 1982). The laboratory frequency of the photon emitted in this transition is $\nu = \Delta E \,/\, 2\pi\hbar = 1420.40$ MHz, which corresponds to a wavelength of $\sim \lambda = c/\nu \simeq 21.12$ cm $\simeq 21$ cm.

On average, it takes a hydrogen atom 11 million years to undergo the spin flip responsible for the 21 cm line emission (Hey 1971). Although it may appear that the probability of detecting this radiation is very low, there is such an immense number of hydrogen atoms in the interstellar medium of a galaxy ($\sim 90\%$ of atoms) that at any one time a sizeable proportion of hydrogen atoms are in their excited state.

Detecting the neutral atomic hydrogen (HI) emitting at this wavelength is a very effective method of probing the most obscured regions in the ZoA since dust is transparent at this long (21 cm) radio wavelength. This spectral line was first observed by Ewen & Purcell (1951) within the Galaxy and later independently confirmed by Muller & Oort (1951) and Christiansen & Hindman (1951). The first extragalactic HI emission was detected by Kerr & Hindman (1953).

The Galaxy is completely transparent at the 21 cm wavelength of the HI radiation. This is evident from the projection plot (Fig. 1.5) in which galaxies detected at 21 cm wavelength by the HI Parkes All Sky Survey (HIPASS; Meyer et al. 2004) are plotted. In this plot no ZoA is visible. This has made it possible to detect gas-rich galaxies right behind the GP and extract information such as redshifts and their rotational properties.

Radio surveys behind the Galactic Plane were initiated by Kerr & Henning (1987) who conducted a blind HI survey in the northern ZoA using the 91-m Green Bank radio telescope. The first systematic survey in the most obscured regions of the northern ZoA was the Dwingeloo Obscured Galaxy Survey (DOGS; Kraan-Korteweg et al. 1994). It surveyed regions within $30^\circ \leq l \leq 220^\circ$, at $b = \pm\ 5^\circ$ with an rms limit of 40 mJy, out to 4000 km s^{-1} at a resolution of 40 km s^{-1} (Henning et al. 1998).

In 1997 the Multi-Beam (MB) receiver on the Parkes 64-m radio telescope was introduced. The receiver consists of 13 horns in a focal plane array which makes it faster for systematic surveys (Staveley-Smith et al. 1996). A few thousands of galaxies have been uncovered by the MB surveys such as HIPASS (Meyer et al. 2004). It surveyed the southern regions from declinations (δ) of -90° to +25° at an rms level of 13 mJy.

A deeper survey has been the Parkes Multi-Beam HI Zone of Avoidance survey (HIZOA) with an rms noise limit of 6 mJy $beam^{-1}$ covering the -1200 to 12700 km s^{-1} velocity range with a resolution of 27 km s^{-1} (Henning et al. 2010). It covers the Galactic longitude range of $52^\circ \leq l \leq 196^\circ$, extending to the northern ZoA at $36^\circ \leq l \leq 52^\circ$ and $196^\circ \leq l \leq 212^\circ$ (Donley et al. 2005).

Currently a blind HI survey for the whole northern sky (north of $\delta <$ -5°) with the same sensitivity as HIPASS is being conducted by the Effelsberg-Bonn HI survey (EBHIS; Kerp et al. 2011). It is surveying more than 8000 square degrees using the 100-m Effelsberg telescope at a velocity resolution of 1.3 km s^{-1} with most of the surveyed area being at lower Galactic latitudes out to a redshift of $cz \approx 16000$ km s^{-1}.

Another deeper survey, the ALFA ZoA survey (Henning et al. 2010) is being conducted using the Arecibo L-Band Feed Array (ALFA) searching the northern, inner Galaxy ZoA at $30^\circ \leq l \leq 75^\circ$, $b = \pm\ 10^\circ$ with an rms noise level of 5 mJy. In addition, there are the recently launched deep ALFA ZoA surveys (Henning et al. 2008) for both the inner and outer Galaxy ($|b| < 5^\circ$), with an rms $\sim$ 1 mJy. Although these ALFA ZoA surveys have begun, it will take several years for the data to be available.

An even longer timeline holds for the forthcoming interferometric HI whole-sky imaging surveys, Wallaby with SKA Pathfinder ASKAP (Australia), which is expected to start in 2016, and its proposed complement in the north, WNSHS (with APERTIF at Westerbork), expected to start in 2015 only. Together will not be biased to the ZoA, hence provide ZoA unprecedented depth in volume and angular resolution, as well as sensitivity.

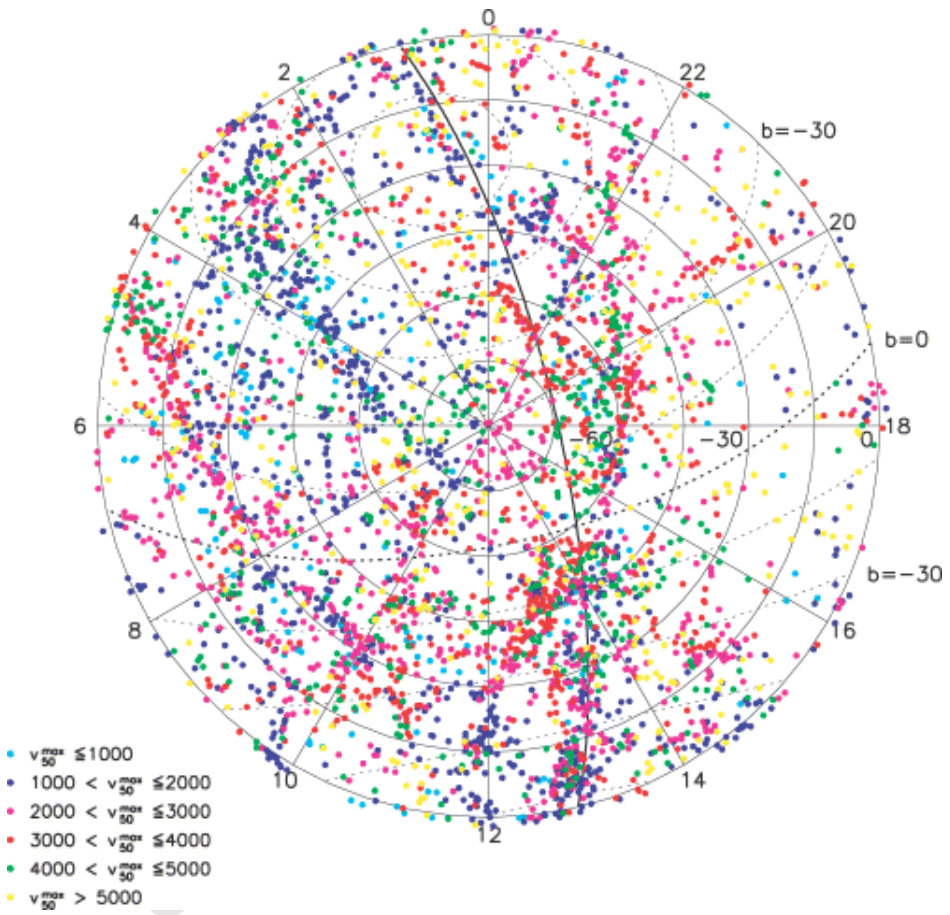

Figure 1.5: A projection of galaxies detected in HI by HIPASS. The plot is in polar coordinates with Galactic coordinates indicated by the dotted lines. Objects are colour coded by radial velocity. Image from Meyer et al. (2004)

1.3.4 Near-Infrared

Surveys in the near infrared (NIR; 0.75 - 5 μm) have provided complementary data to optical surveys. This is due to the decreasing extinction as a function of wavelength with I (0.8 μm), J (1.25 μm), H_s (1.63 μm) and K_s (2.15 μm) bands being only 45%, 21%, 14% and 9% extinct relative to the optical $B-$band (Schröder et al. 1997). To show how dust extinction affects galaxy searches in the ZoA in the optical compared to the NIR an illustration is given in Fig. 1.3.4. The top panel shows examples of composite 2MASS JHK_s-band colour images of ZoA galaxies detected in this HI line survey (see chapter 3). The image sizes vary from 0.′8 to 3.′2. The bottom panel shows examples of the same galaxies in the $B-$band. Compared to the near-infrared images in the bottom panel illustrates the detrimental effect of the higher dust extinction in the optical on galaxy searches in the ZoA.

The major completed NIR surveys are the DEep Near Infrared Southern Sky Survey (DENIS; Epchtein et al. 1997) and the 2 Micron All Sky Survey (2MASS; Skrutskie et al. 2006). The currently ongoing two deeper surveys are the UKIRT Infrared Deep Sky Survey (UKIDSS; Lawrence et al. 2007) and the Visible and Infrared Telescope for Astronomy (VISTA; Emerson 2001).

DENIS observed the Southern sky covering -88° $< \delta <$ +2° in the I_c (0.8 μm), J (1.25 μm) and K_s (2.15 μm) bands (Epchtein et al. 1997). The UKIDSS Galactic Plane Survey is searching $\approx$ 1800 square degree of the northern ZoA ($|b| \lesssim 5°$) within $-15° < \delta < +60°$ in the *JHK* bands (Hewett et al. 2006). VISTA is looking at the southern sky in the *J, H* and K_s (Emerson 2001).

2MASS delivered homogeneous and precise photometry as well as astrometry of the entire sky in the J, H and K_s NIR photometric bands (Jarrett et al. 2003). It has produced two catalogues, the point source catalogue (2MASS PSC; Cutri et al. 2003) which contains 1.65 million stars and the extended source catalogue (2MASS XSC; Jarrett et al. 2000) with 0.5 million extended objects. These are predominantly galaxies but closer to the GP it also contains Galactic sources such as Galactic Nebulae, HII regions and "blended" star systems. The 2MASS XSC has extended source sensitivity limits of $14.^{\rm m}7$ (2.1 mJy), $13.^{\rm m}9$ (3.0 mJy) and $13.^{\rm m}1$ (4.1 mJy) in the J, H, and K bands respectively, at the 10σ integrated flux level. The only current systematic whole-sky redshift survey based on 2MASS is the 2MASS Redshift Survey (2MRS; Huchra et al. 2005), with about 20000 redshifts for galaxies brighter than $K_s^o = 11.^{\rm m}25$ in the first data release and $\sim$ 40000 redshift in the second data release which is complete to $K_s^o = 11.^{\rm m}75$ (Huchra et al. 2012). While this dedicated redshift survey is supposed to cover the whole sky, it excludes the inner ZoA at $|b| < 5°$ due to the obscuration caused by stellar crowding. The effect of stellar crowding and its contribution to the redshift ZoA gap is shown in Fig. 1.7, which shows the distribution of all 2MRS galaxies in the first data release.

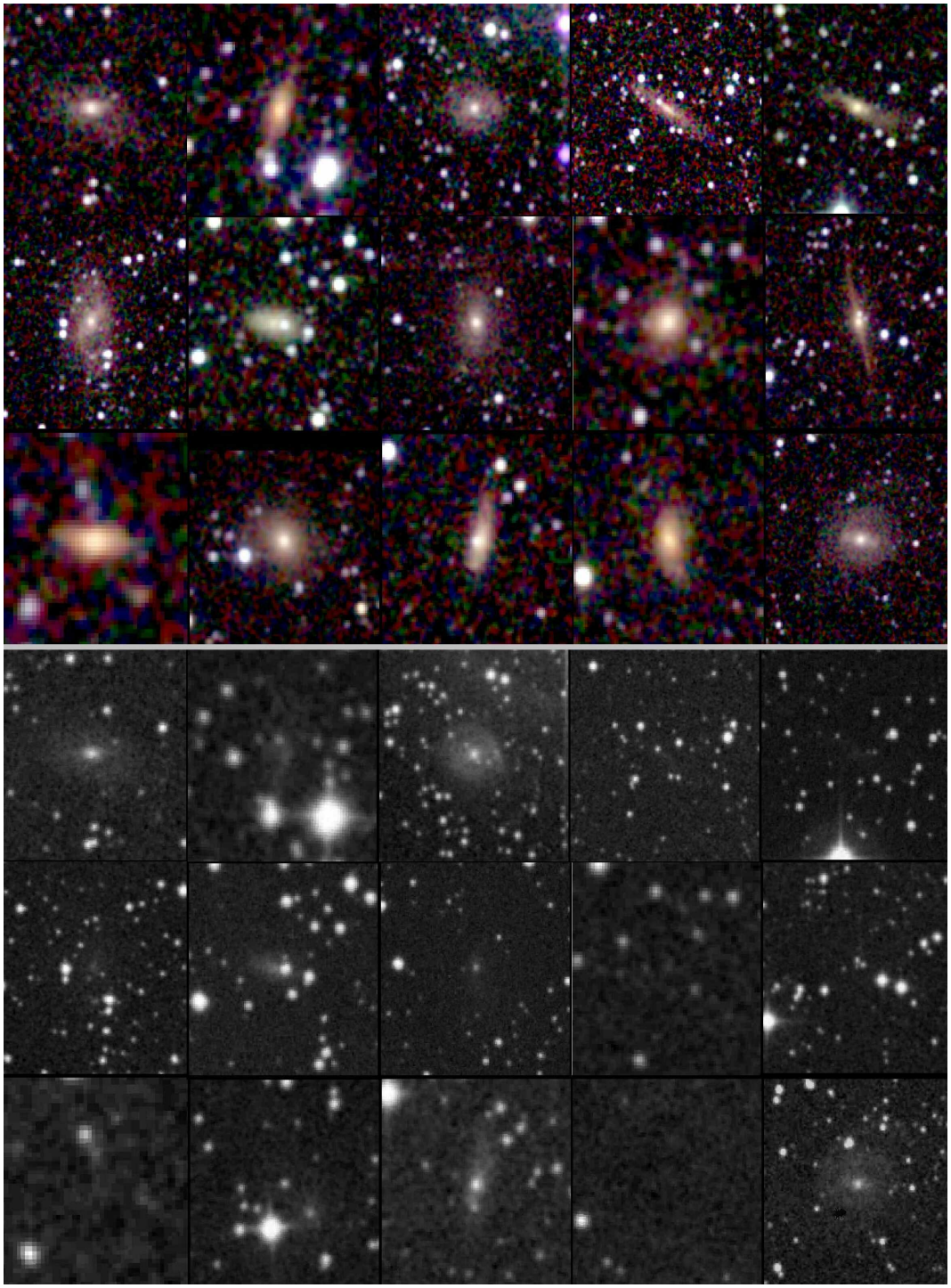

Figure 1.6: The *top* panel shows examples of composite 2MASS JHK_s-band colour images of ZoA galaxies detected in this HI line survey. Shown are the first 15 targets listed in Table 3.1. The image sizes vary from 0.′8 to 3.′2. In the *bottom* panel $B-$band DSS2 images of the same galaxies are given.

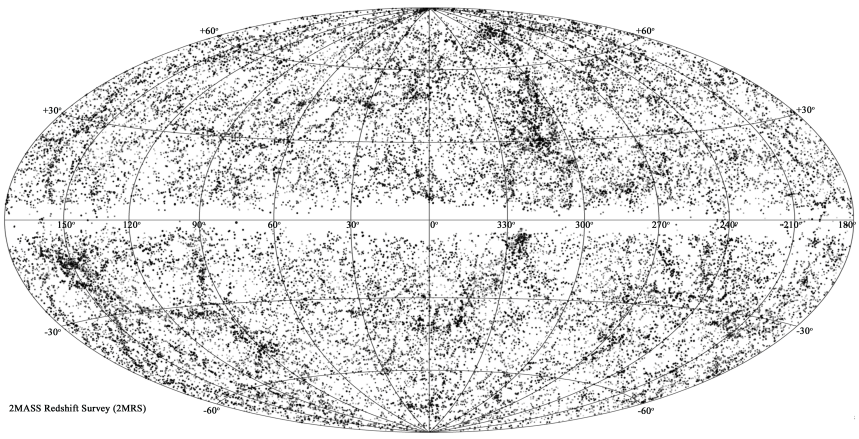

Figure 1.7: An Aitoff projection plot of 2MASS Redshift Survey (2MRS) galaxies from the first data release, containing galaxies brighter than $K_s^o = 11\overset{\text{m}}{.}25$.

1.4 Motivation for a northern ZOA H I survey

Direct approaches have resulted in a clear reduced ZoA. However, most methods described in the previous sections remain with a ZoA of $|b| \lesssim 5°$. While the NIR does not suffer from dust extinction much it remains with a redshift ZoA due to the inherent difficulties in obtaining good quality spectra. The method that has proved to be most effective at probing the ZoA is HI observations. Through this method the lack of galaxy redshifts in the ZoA has improved. However, HI surveys such as HIPASS with their rms of 13 mJy are very shallow (with a redshift distribution limit around 1800 $\mathrm{km\,s^{-1}}$) and was sparsely sampled with about 1 galaxy per 10 square degrees only.

Most of the current HI surveys have focused on the southern regions with only small extensions in the north. No systematic HI survey exists for the remaining regions of the northern ZoA.

Deeper ongoing and future surveys, i.e., Arecibo HI ALFA ZoA (5 mJy rms), deep ALFA ZoA (1 mJy rms) surveys, the planned interferometric Westerbork Northern Sky HI Survey (WNSHS) and the SKA Pathfinder shallow HI whole-sky survey (Wallaby), will be long before their data is available. In the mean time it is very important to start addressing some of the uncertainties caused by the largest remaining gap in the ZoA as described in Sec. 1.2.

To improve on this, a method of observing bright NIR ZoA galaxies in HI has been adopted for this project. This combines the power of the less adverse effect of dust on the NIR and HI observations. Pointed HI observations of NIR sources in the remaining ZoA can prove particularly important for complementary redshift purposes to all-sky redshift surveys such as the optical 2MRS which does not, and cannot, go deeper into the ZoA at Galactic latitudes of $|b| < 5°$. The complete sample of the survey presented here can be used for improved and more accurate studies of the large scale dynamics in the Local Universe. HI characteristics of detected sources will be used for Tully-Fisher analysis and mapping of

flow fields in the ZoA. This will complement the existing "whole-sky" 2MASS Tully Fisher Relation survey (2MTF; Masters et al. 2008) which also excludes the inner ZoA ($|b| < 5°$).

1.5 Thesis Outline

The thesis has the following structure. Chapter 2 presents details of the sample selection, the observations and data reduction. In Chapter 3 the catalogue of the HI detections is presented as well as a detailed discussion of their characteristics as a function of stellar densities and foreground dust extinction. The spectra of these detections are also presented in this chapter. The non-detections are briefly described and their catalogue presented in Appendix A. Large-scale structures uncovered by the new detection are discussed in detail in Chapter 4. Chapter 5 gives a summary and future perspectives. The full 2MASX catalogue of the extinction-corrected bright ZoA galaxies is given in Appendix B.

Chapter 2

Observations and Data Reduction

The sample selection criteria are discussed in Sect. 2.1. This is followed by a description of the observations with the Nançay Radio Telescope in Sect .2.2. In Section 2.3 the data reduction techniques are discussed. Finally, a description of the data quality and uncertainties associated with the derived parameters is also given.

2.1 Sample Selection

The galaxy candidates selected for this project were extracted from the 2MASS XSC (Jarrett et al. 2000) in the ZoA accessible from the NRT, namely $-39° < \mathrm{dec} < +70°$. This covers the ZoA for the longitude range of $-20° \lesssim \ell \lesssim 270°$. Since the 2MASX catalogue does not only contain galaxies but other extended objects as well it is important to find selection criteria that discriminate galaxies from other extended sources in the Galaxy.

A total of 122850 sources within $|b| \lesssim 10°$ and $\mathrm{dec} \geq -39°$ were extracted from the 2MASS XSC. Their K_s-band magnitudes at 20 mag.arcsec^{-2} surface brightness were corrected for foreground dust extinction based on DIRBE/IRAS dust Maps (see Sect. 1.1.1). An extinction-corrected magnitude consistent with the first data release of the 2MRS, $K_s^o < 11\overset{\mathrm{m}}{.}25$ was then imposed. This led to a sample of 4743 extended sources with extinction-corrected magnitudes $K_s^o < 11\overset{\mathrm{m}}{.}25$. To discriminate galaxies from other extended sources a visual inspection of images was done through the 2MASS NIR images as well as Digitized Sky Survey (DSS)* in the optical by one of the collaborators within the group (Schröder). This classification was based on the colour, spatial extension shape and appearance of the source in DSS and NIR bands. A total of 2546 sources were thus identified as candidate galaxies, with an additional 42 sources being classified as "uncertain" or possible candidates.

*http://stdatu.stsci.edu/dss/

2.1.1 Characteristics of the 2MASX Sample

To assess the reliability of the galaxy identification procedure Fig. 2.1 is plotted. The blue dashed line represents all 4743 extended sources from the 2MASX catalogue within the survey's magnitude and declination limits. The solid black line is the distribution of all sources which were classified as galaxies (henceforth referred to as "CG").

To determine the mean number of galaxies expected, independent of large-scale structure distribution, the 2MRS data ($K_s^o \leq 11\overset{\text{m}}{.}25$) for $|b| > 10°$ (82.5% of the sky) was used. The mean is 0.61 galaxies per square degree. In Fig. 2.1 this mean is indicated by the red solid line, scaled to the actual area regarded in the plot ($-20°$ to $270°$). The plot shows a high number of 2MASX extended sources for $|b| < 5°$, this can be attributed to confusion with extended Galactic objects such as HII regions, Galactic nebulae and "merged" stars. The elimination process removed these Galactic objects, reducing the blue dashed line to the solid black curve. The curve is fairly flat but lies slightly below the expected number density of galaxies. Moreover it shows a slight dip around $|b| < 5°$, which is taken to be an indication of incompleteness.

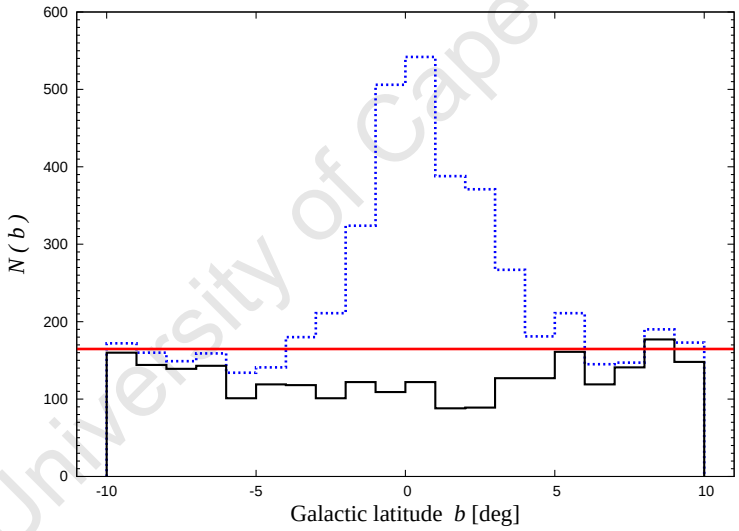

Figure 2.1: The distribution of 2MASX extended objects classified as galaxies (solid black line) as a function of Galactic latitude. The blue dashed histogram represents all 2MASX extended objects meeting the selection criteria. The solid red line indicates the expected mean per square degree in the longitude range of the survey.

To investigate the cause of the incompleteness and this dip, Fig. 2.2 is plotted. It shows ZoA 2MASX objects classified as galaxies together with contours of constant stellar density for log $N(SD_{Ks<14.0})$. This is the number of stars per square degree brighter than $K_s \leq 14\overset{\text{m}}{.}0$. The contour values 3.6, 4.0, 4.4, 4.8 are represented by green, yellow, orange and brown respectively. There is a pronounced lack of classified galaxies for log $N(SD_{Ks<14.0}) > 4.00$ suggesting, not surprisingly, that the dip in Fig. 2.1 is most likely

due to stellar crowding particularly in the Galactic Bulge (GB) region ($\ell < 90°$). To verify this, both samples have been separated into two longitude ranges, one away from the GB where log $N(SD_{Ks<14.0}) < 4.00$ ($\ell > 90°$), hence no incompleteness is expected and around the GB ($\ell < 90°$). These are shown as a function of Galactic latitude in Figs. 2.3 and 2.4 respectively. Figure 2.4 shows an obvious drop-off within $|b| < 5°$ which is not seen in Fig. 2.3. The distribution in Fig. 2.3 agrees with the average number of galaxies expected in those regions (red solid line). This implies that the ZoA CG sample is complete and reliable away from the bulge, with the completeness decreasing close to the GB due to the star crowding (red contour). A point to note is that both figures also have an asymmetric distribution probably cause by the Galactic warp.

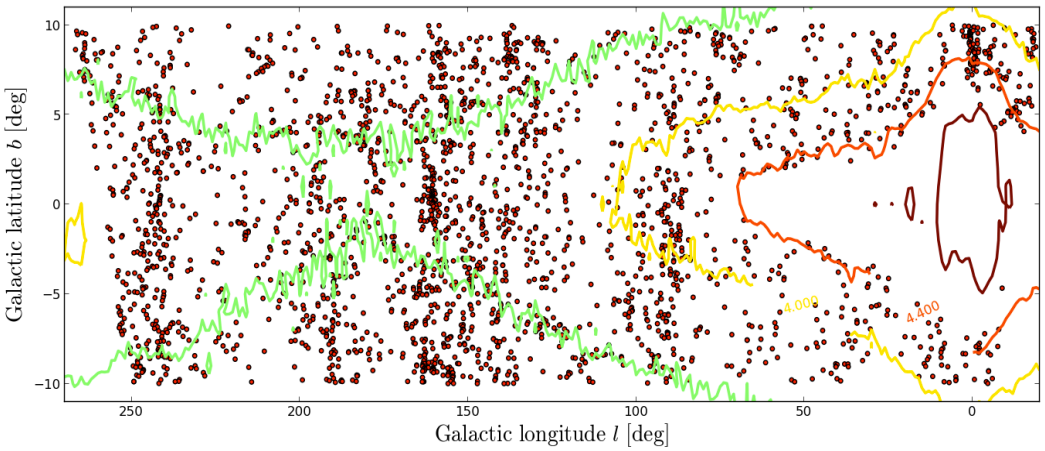

Figure 2.2: The spatial distribution of 2MASX ZoA extended sources classified as galaxies (red filled circles). The stellar density contours of log $N(SD_{Ks<14.0}) = 3.6$, 4.0, 4.4 and 4.8 in green, yellow, orange and brown respectively are superimposed.

As a final step in the sample selection procedure, catalogue cross-correlations were done with the aim of excluding as many galaxies with velocities as could be identified through the NASA/IPAC Extragalactic Database (NED; Helou et al. 1991) and private communications with other collaborators within this survey's group.

The distribution of the final NRT observing sample as a function of Galactic latitude is plotted in Fig. 2.5. The histogram shows the distribution of all the ZoA CG sample in black. Galaxies with prior redshift information from the 2MRS ($K_s^o \leq 11\overset{\text{m}}{.}25$) are indicated by the red dashed line. The inner ZoA excluded by the 2MRS is very clearly visible at $|b| < 5°$, galaxies with redshift information in that distribution are from the Huchra et al. (2005) ZCAT compilation. The final NRT observing sample contain all galaxy candidates without redshift information from 2MRS. Their distribution with Galactic latitude is indicated by the grey dashed line (see Fig. 2.5). Their spatial distribution is shown in Fig. 2.6 with 2MRS ($K_s^o \leq 11\overset{\text{m}}{.}25$) indicated by red dots and NRT galaxy candidates by black triangles .

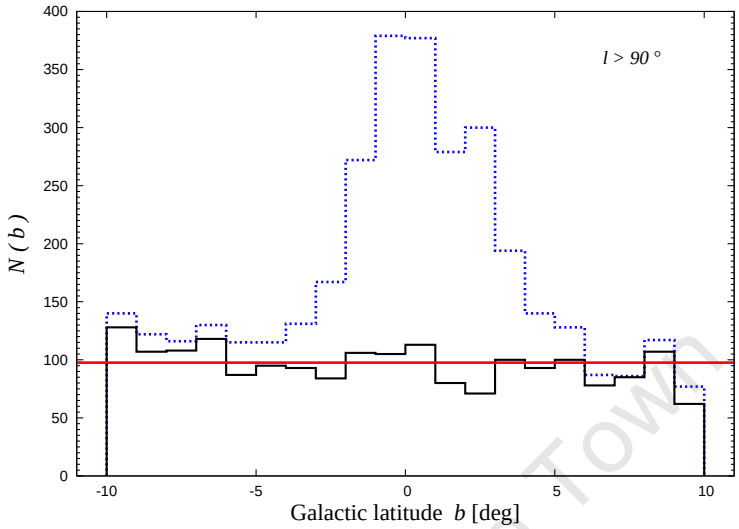

Figure 2.3: The distribution of 2MASX extended sources (blue dashed line) and sources classified as candidate galaxies in the candidates sample (black solid line) for $\ell > 90°$. The solid red line marks the expected mean per square degree within the longitude of 90° to 250°.

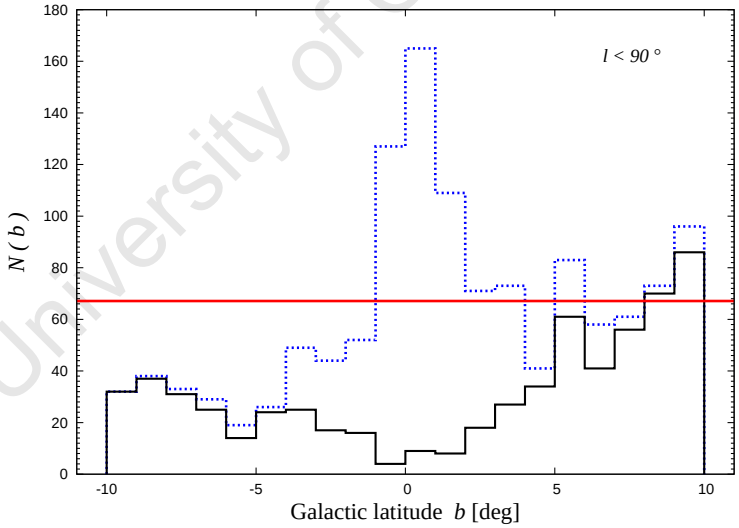

Figure 2.4: The distribution of 2MASX extended sources (blue dashed line) and sources classified as candidate galaxies (black solid line) around the Galactic bulge ($\ell < 90°$). The solid red line marks the expected mean per square degree within the longitude of $-20°$ to 90°.

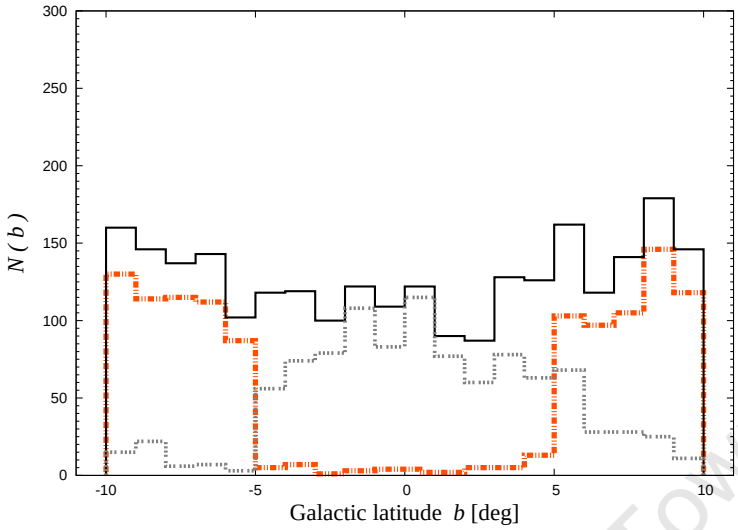

Figure 2.5: The distribution of the final NRT sample as a function of Galactic latitude. Sources classified as galaxies are represented by the solid black line. Galaxies from the 2MRS ($K_s^o \leq 11\overset{\mathrm{m}}{.}25$) sample are indicated by the red dashed line. The final NRT sample is indicated by the grey dashed line.

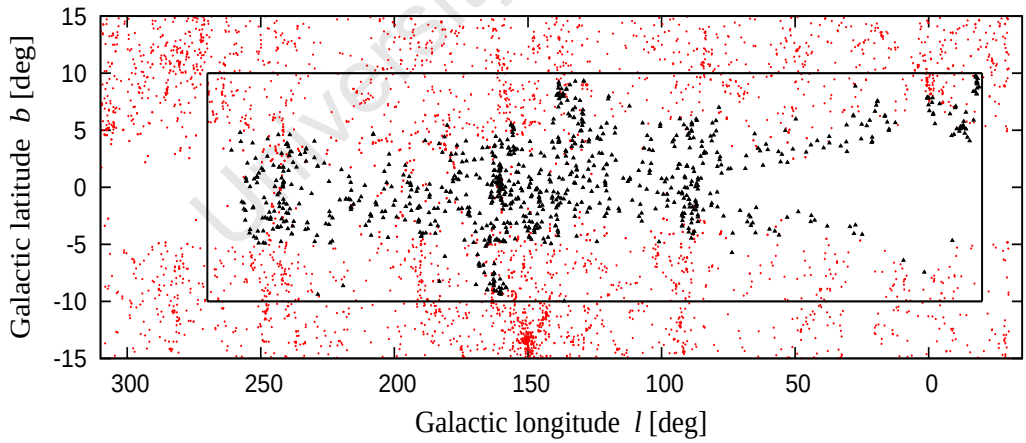

Figure 2.6: The distribution on the sky of the final NRT sample of about 1000 galaxy candidates(black triangles). The rectangle demarcates the region observed by this survey. The 2MRS galaxies in the first data release are represented by red dots.

2.2 Data Acquisition

2.2.1 The Nançay Radio Telescope (NRT)

Observations of the target 2MASX bright galaxies were made with the Nançay Radio Telescope (NRT)*. It is located near the town of Nançay, France, 200 km due South of Paris. Its design is of the Kraus/Ohio (see Fig. 2.7) type. The telescope is a meridian transit-type instrument (Monnier Ragaigne et al. 2003) capable of detecting radiation emitted in the frequency range of $1 - 3$ GHz with an effective collecting area of about $7000\,\mathrm{m}^2$, equivalent to that of a 94-m circular parabolic dish. It consists of a flat reflector (200 m wide and 40 m high) which can be tilted to point at any desired declination (δ), and a fixed spherical reflector (300 m wide and 35 m high). Receivers are placed in a focal carriage between the two reflectors such that sources can be tracked by moving the carriage along a curved 100 m rail track. The purpose of the flat reflector is to direct the radiation beam to the spherical mirror. The beam is then focused onto the two mirrors (main reflector and sub-reflector, Fig. 2.8) in the Gregorian feed system and enters the receiver horn.

Figure 2.7: Arial view of the 100-m class Nançay Radio Telescope. The fixed spherical mirror (300 m × 35 m in size) is on the left, the focal carriage in the centre and the tiltable flat mirror (200 m × 40 m) on the right.

*http://www.nrt.obspm.fr/

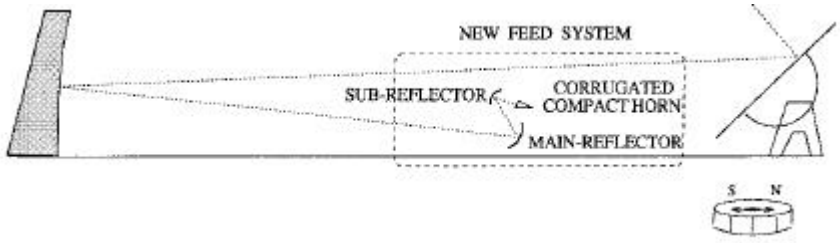

Figure 2.8: A schematic cross section of the NRT (Granet et al. 1997).

Any source at $\delta > -39°$ can be observed and the maximum continuous tracking time for sources at $\delta = 0°$ is about 60 min per day. However, the maximum tracking time increases with declination as $1/\cos(\delta)$. At a wavelength of 21 cm, the telescope's half-power beam width (HPBW) is $\sim 4'$ in right ascension, independent of the declination. However, the beam diameter is more extended in the N−S direction, due to the E-W elongated shape of the telescope, N-S HPBW = $22'.0$ for $\delta < 20°$. Due to the geometrical effect of the flat mirror being pointed towards higher declinations, the N-S HPBW increases (θ_{N-S}) with the declination of the source, above 20°, as shown in Fig. 2.9. The HPBW increases to $25'$ at $\delta \sim 40°$ and to $33'$ at $\delta \sim 71°$, which is the maximum declination observed for this survey (van Driel et al. 2009).

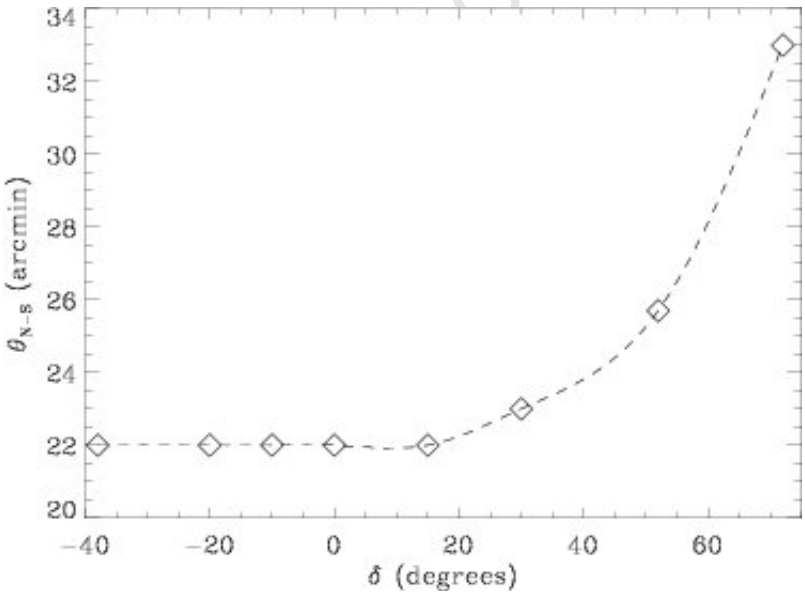

Figure 2.9: The (N−S) HPBW (in arcminutes) of the NRT as a function of declination (in degrees) (Matthews & van Driel 2000).

The effective collecting area and thus the gain of the telescope also vary as a function of declination. The variation follows the shape illustrated in Fig. 2.10 as approximated by Theureau et al. (2005).

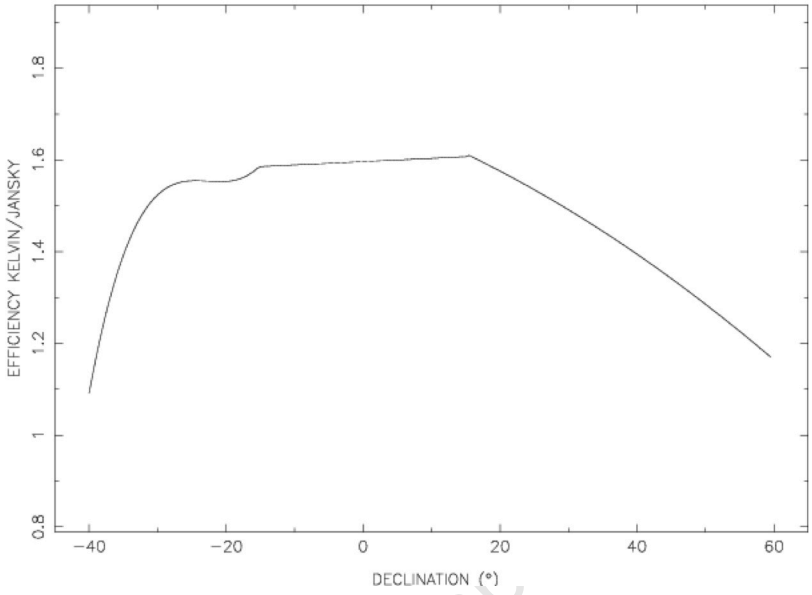

Figure 2.10: NRT gain, in Jy/K, as a function of declination (Theureau et al. 2005).

At the lowest declinations, atmospheric absorption and ground scatter is responsible for the decrease in the gain. At high declinations the vertical size of the tiltable mirror decreases, as seen from the fixed spherical mirror, thereby decreasing the effective collecting area of the telescope, and its gain.

The galaxy candidates were observed in position-switching mode also known as total power mode. This was done using pairs of equal-duration ON/OFF-source integrations. The sky background signal contribution was determined with the OFF-source position $20'$ east of the target and then subtracted from the spectrum as described in section 2.2.2. Candidates were typically observed for 40-minute long periods till an rms noise level of 3.3 mJy was reached, unless a clear detection was obtained after the first 20 min integration.

Because the target galaxies had no prior redshift information, a standard NRT auto-correlator set-up for galaxy searches was used, which represents a trade-off between total velocity coverage, velocity resolution and sensitivity. The radial velocity range covered was limited to -500 to 10500 km s^{-1}, as at higher velocities the 100-m class NRT can only detect very rare, extremely massive HI-rich galaxies, and unwanted Radio Frequency Interference blankets most of the band. Observations were made simultaneously in two orthogonal linear polarizations instead of one in order to get a $2^{0.5}$ times lower rms noise level. They are referred to as EE and WW respectively, leading to 2×2048 channels over the same velocity range. The original velocity resolution of 2.6 km s^{-1} was later smoothed to 18 km s^{-1} for further analysis.

A summary of the observational parameters is given in Table.2.1.

Table 2.1: NRT ZoA survey observational parameters.

Parameter	Value
Area coverage	$-20^\circ \lesssim l \lesssim 270^\circ$, most $\lvert b\rvert < 5^\circ$, some $\lvert b\rvert \lesssim 10^\circ$
Velocity coverage	-500 km s$^{-1} < v < 10500$ km s^{-1}
Velocity resolution	18 km s^{-1}
Target rms noise level	~ 3.3 mJy beam^{-1}

2.2.2 Flux density calibration

The raw output of a radio telescope is measured by the system noise temperature given by:

$$T_{sys} = T_{cmb} + T_{sky} + T_{spillover} + T_{rx} + T_b, \tag{2.1}$$

In this equation, T_{cmb} is the noise contribution from the Cosmic Microwave Background, T_{sky} is due to atmospheric emission, the spillover radiation picked up by the feed in directions beyond the edges of the reflector is $T_{spillover}$, the noise generated by the receiver itself is T_{rx} (which includes noise due to losses in the feed as well as the injected noise) and T_b is from the observed astronomical source and is typically much smaller than the total system noise, $T_{sys} \gg T_b$.

Certain contributions to the noise temperature (T_{cmb}, T_{sky}, T_{rx} and $T_{spillover}$) were eliminated before converting the signal output of the source (T_b) from antenna temperature (K) to flux density (Jy). The noise contribution from the cosmic microwave background is known to be $T_{cmb} \approx 2.73$ K (Lineweaver 1997). Noise due to the sky background was eliminated by OFF-source pointings of the telescope. This was done by observing a patch of the sky without the source in position switching mode of the telescope for the same duration as the ON-scan.

T_{rx} was kept at a minimum by cooling the receiver to cryogenic temperatures, i.e., by placing the terminal resistor of the receiver in liquid helium[‡]. This precisely determined the resistor's noise temperature and allowed for T_{rx} to be determined by regular, short-duration insertions of a noise diode tube of known temperature in the receiver.

Lastly, the tertiary and quaternary mirrors in the focal cabin of the NRT are specially shaped to minimize the spillover radiation ($T_{spillover}$).

The brightness temperature (T_b in K) is the contribution from the source object. It is related to its flux density and determined by subtracting all of the aforementioned noise temperature contributions. The relation between this temperature and the flux density is given by (Westpfahl 1999):

[‡]Liquid helium boils at 4.2 K (-268.98 centigrade)

$$T_b = F_c S_\nu, \tag{2.2}$$

Where S_ν is the flux density (Jy) and F_c (K Jy^{-1}) the conversion factor given by:

$$F_c = \frac{c^2}{2k_B \nu^2 \omega}, \tag{2.3}$$

Where k_B is Boltzmann's constant and ν the observed frequency (Hz). ω (steradians) is the solid angle formed by the beam on the sky, represented by,

$$\omega = \frac{\pi \theta_0^2}{4ln2}, \tag{2.4}$$

Where θ_0 is the Gaussian HPBW (arcseconds). This is the angular separation within which the magnitude of the radiation pattern decreases by 50%. For the NRT, equation 2.4 is an approximation as it does not take into account the elongated beam shape of the telescope. The NRT's F_c was 1.4 K/Jy and the system temperature 35 K at the 21 cm wavelength.

For observations of the project presented in this thesis the NRT staff measured the cold load calibrators and monitored strong continuum sources on a regular basis. These calibration data were used in the reduction procedure to determine the flux density scale (K mJy^{-1}) as a function of declination. This procedure yields a calibration accuracy of $\sim$15%. This scale was further checked through regular HI observations of galaxies with well known HI line fluxes from the O'Neil (2004) catalogue throughout the observation runs. These gave average integrated flux values 0.89 ± 0.08 times the literature values. Line fluxes of the survey presented here were not multiplied by a factor 1/0.89 as this deviation of -11% compared to the values measured with other radio telescopes is within their respective estimated absolute flux calibration uncertainties.

2.3 Data Reduction

Owing to their high sensitivities, radio telescopes are susceptible to radio frequency interference (RFI) with signal strengths that can be much higher than those of the sources being observed. There are different methods employed to mitigate this, but there is currently no one generic method to mitigate all classes of interference. This is because each method depends on its ability to detect interference. Fig 2.11 shows an example of three classes of RFI based on their strength and their impact on radio astronomical observations.

Data reduction and RFI mitigations for the project presented were done using the Nançay Processing Software (NAPS) and the Systéme Interactif de Réduction (SIR), both developed by the NRT staff.

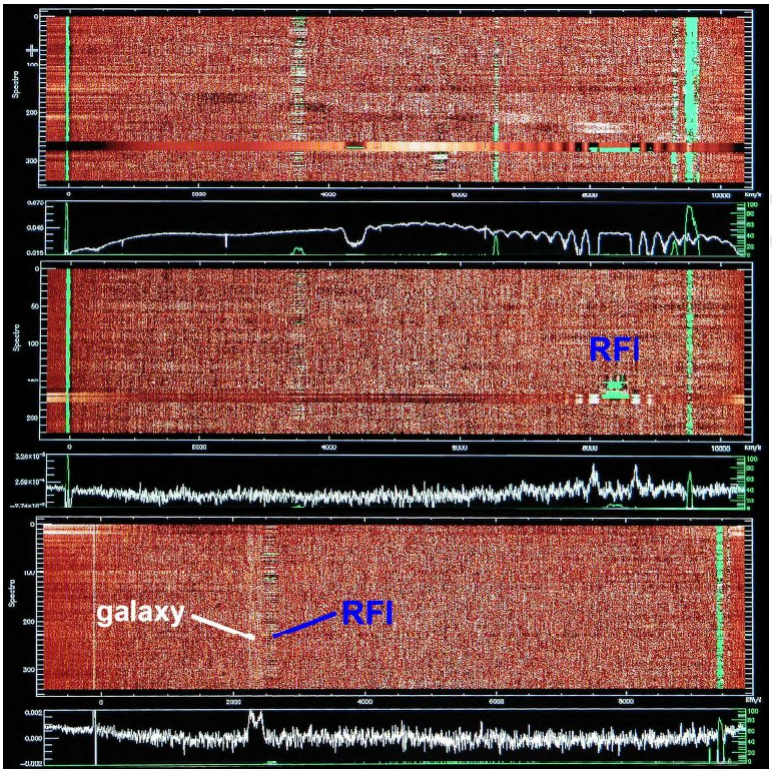

Figure 2.11: An illustration (van Driel 2008) showing three classes of radio frequency interference (RFI), based on their strength (data flagged in green) in radio data from a single-dish telescope (the NRT). The red-hued colour scale indicates the signal strength. Shown are ON-OFF subtracted spectra. The *top* panel shows RFI that is so strong that it renders data unusable. The *middle* panel is RFI that imitates HI line profiles, potentially leading to "fake detections", and the *bottom* RFI is faint enough that is can be removed without affecting the target line signal.

2.3.1 NAPS

The NAPS package processes the system temperature data of the ON - OFF/OFF spectra. It also performs RFI mitigation and displays data in a 2D waterfall display showing the strongest RFI flagged in green (cf. Fig 2.12).

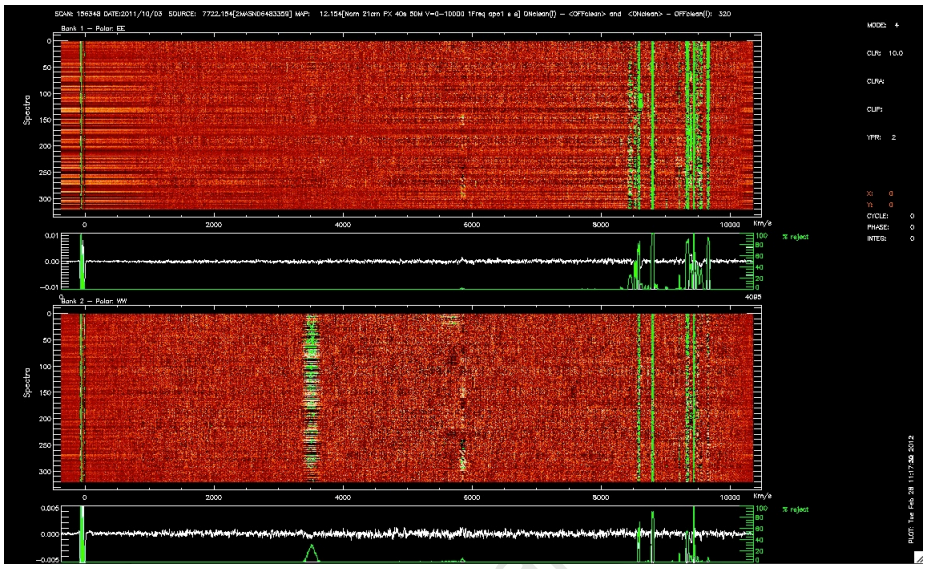

Figure 2.12: A 2D display of strong RFI flagged in green from NAPS (data from this survey). The red-hued colour scale indicates the signal strength. Shown are ON-OFF subtracted spectra. The two panels shows the two linear polarizations used, EE (upper) and WW (lower). The *bottom* panel figure shows internal RFI at 3500 km s^{-1} (in the WW polarisation), inconsistent narrow radar RFI at $v \approx 6000$ km s^{-1} and numerous strong, narrow RFI signals (due to radar) at 8500 km s^{-1}, 8750 km s^{-1} and 9500 km s^{-1} in both polarisations.

RFI in the observations was minimised/removed using the program's algorithm, which basically checks for time variable signals throughout the spectra, as outlined by Monnier Ragaigne et al. (2003):

1. All OFF-source spectra in the cycle were averaged and subtracted from each individual ON-spectrum of the observation.
2. For each individual ON - <OFF> spectrum, the average rms and signal strength were calculated after 25% rejection level of the highest and the lowest peaks.
3. Channels with signal strengths differing by 10σ in each 40/40 s ON/OFF were removed and replaced by a linear interpolation between unaffected channels, this was done for each individual spectrum.
4. The "clean" ON-spectra was then averaged and subtracted from each OFF-spectrum.
5. As in step 1, each resulting individual channels with a mean signal greater than $\pm N\sigma$ replaced by linear interpolation, resulting in clean individual OFF-spectra.
6. Ultimately, step 1 was repeated on individual ON-spectra using the cleaned OFF-spectrum from step 2.
7. Adding all the final cleaned ON-spectra produced the spectrum of the data from each receiver bank.

A very important result of this method is that it flags the RFI, cautioning the observer which data are tainted or unusable. No RFI mitigation process is capable of completely removing all interference, however, certainly not without the risk of removing some of the target source line emission. This is illustrated in Fig. 2.12 where the strongest and most persistent RFIs are pointed out. This implies that the radial velocity ranges at which these RFIs occurred could not be used for HI line searches.

It should be noted that according to international regulations, the radio astronomy 21cm line band is only protected from detrimental interference down to a frequency of 1400 MHz, or about 5500 km s^{-1}. At higher velocities, regulatory protection depends on national and regional measures. Hence the strict national legislation implemented in South Africa to protect the SKA precursor MeerKAT and the planned future SKA instruments to be built in the North Cape inside a Radio Quiet Zone.

2.3.2 SIR

The SIR program takes the NAPS results as input. It was used to convert the system temperature (K) to flux density (Jy). The program also does an interactive baseline fitting and produces the final reduced spectrum from which the HI line parameters (recessional velocity, line widths and integrated flux density) and the rms noise level are extracted. The data reduction procedure using the SIR package is as follows:

- Spectra from NAPS for each linear polarisation (EE and WW) are selected and averaged. The individual EE and WW polarisation spectra are displayed and inspected for an HI signal. Flawed spectra such as those with strong RFI were discarded. An example of a clean spectrum as displayed in SIR is shown in Fig. 2.13, after smoothing to a velocity resolution of 18 km s^{-1}. It shows the flux density in mJy as a function of radial velocity ($km\,s^{-1}$) in the radio convention. The strong signal at 0 $km\,s^{-1}$ is due to HI emission from the Galaxy. The increase in flux density at $v \approx 3900\,km\,s^{-1}$ is the HI signal from the target object. There is also strong RFI seen at $v > 8500\,km\,s^{-1}$, which could not be removed during the NAPS procedure because it was below the 10σ trigger level.

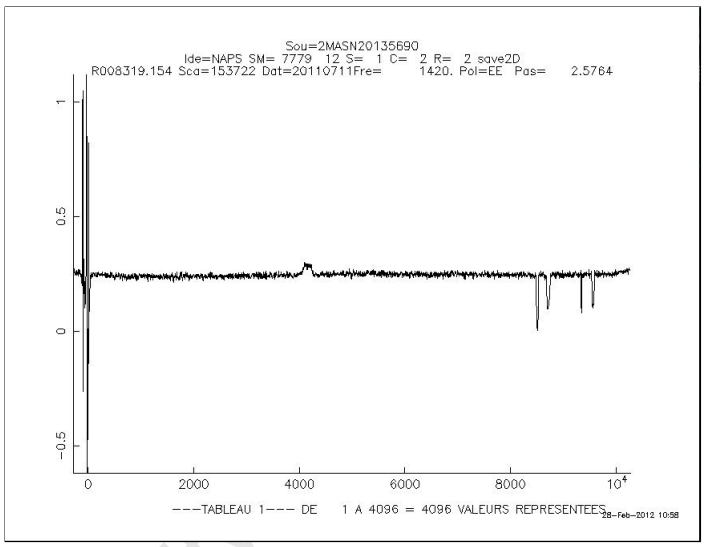

Figure 2.13: The full HI spectrum of our target 2MASX J20135690+2902036 as displayed by SIR. It shows the flux density in mJy as a function of radial velocity ($km\,s^{-1}$). The increase in flux density at $v \approx 3900\,km\,s^{-1}$ is the HI signal from the target object. Galactic emission can also be seen at 0 $km\,s^{-1}$ and strong RFI that could not be removed is apparent at $v > 8500\,km\,s^{-1}$.

- As a second step a $5000\,km\,s^{-1}$ wide section centred on the HI line signal was selected for further analysis, provided no strong RFI was present. However, if any RFI was present, the velocity ranges spanned by it were not used in the baseline fitting and rms noise calculations. An example of a zoomed-in spectrum centred on the HI spectral line is shown in Fig 2.14. This is a typical double-horned profile of an inclined spiral galaxy, 2MASX J20135690+2902036, with a peak signal to noise ratio (SNR) of 18.21.

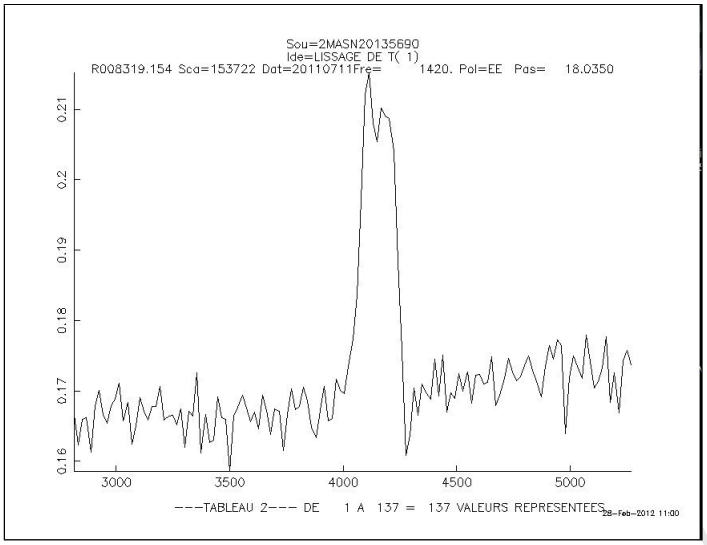

Figure 2.14: This figure shows the 5000 km s^{-1} wide region centred on the HI line detection of a target galaxy, before baseline subtraction.

- A 5th order polynomial was then fitted to the data so as to subtract any residual baseline variations (see Fig. 2.15). This order was chosen because residual baselines at the NRT tend to have various low-level ripples and those are best fitted by higher order polynomials. Sections marked as target signal and RFI were not used during this baseline fitting procedure.

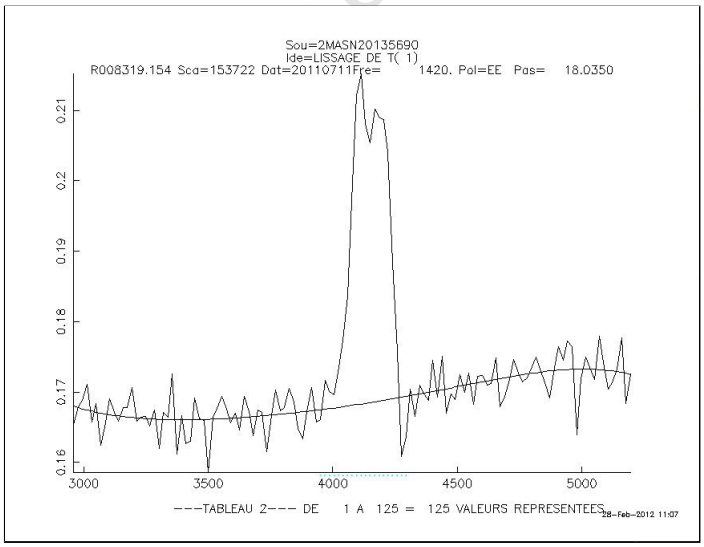

Figure 2.15: A 5th order polynomial fitted to the baseline (cf. Fig. 2.9).

- The last step was to select the maximum intensity of the signal. This then allowed the determination of the HI line parameters, i.e., velocity widths at 50% and 20% levels of

line peak flux density (w_{50} and w_{20}), the average radial velocity at the 50% and 20% levels (v_{50} and v_{20}) and the integrated line flux, as well as the rms noise level. Shown in Fig 2.16 is the final residual baseline subtracted and smoothed spectrum.

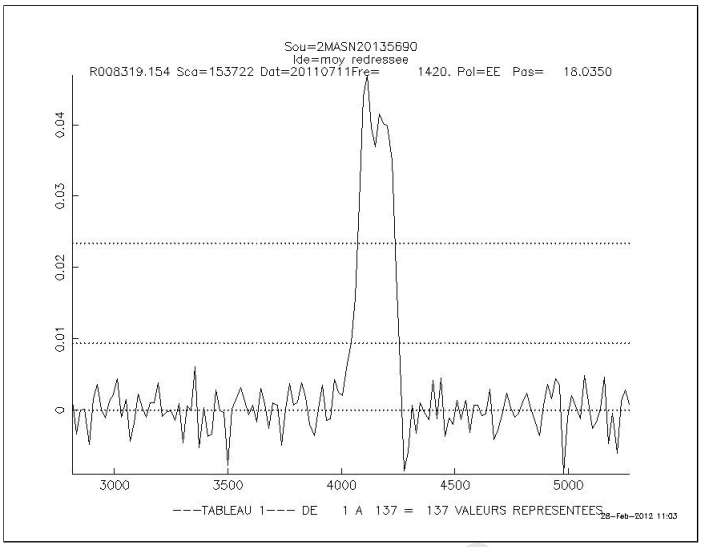

Figure 2.16: The final baseline-subtracted, velocity-smoothed spectrum. From the final spectrum HI parameters such as the w_{50} and w_{20} velocity widths, the mean radial velocity and integrated flux were extracted.

All data were box-car smoothed to a velocity resolution of 18 km s^{-1}. This was applied to improve the signal to noise ratio. This resolution is a compromise between the accuracy in the measured HI parameters and improving the detection rate. The reason being that if all spectra were strong detections, a higher velocity resolution would be preferable, but this would limit the number of faint detections.

Measurements were all made in the heliocentric reference frame, using the radio convention, which measures velocities through $\delta(\nu)$. These were converted to the optical convention, in which velocities are measured through $\delta(\lambda)$ by:

$$v_{optical} = \frac{1}{\frac{1}{v_{radio}} - \frac{1}{c}}, \tag{2.5}$$

where c is the speed of light taken to be $c = 299792.5\,\mathrm{km\,s^{-1}}$.

Non-Detections

In cases were a spectrum did not show an HI signal of the target source (non-detection) only the rms noise level was determined. Three velocity regions were considered for this. They were 500 – 3500 km s^{-1}, 4000 – 7000 km s^{-1} and 7000 – 9000 km s^{-1}. The 3500-4000 km s^{-1} region was avoided because of internal RFI.

The rms over a 3000 km s^{-1} range in each radial velocity regions mentioned was then measured and compared. Fig. 2.17 shows the rms noise level as a function of integration

cycles (Ncyc). From this plot it can be seen that the 7000 – 9000 km s^{-1} region gives higher rms noise level values than the 500 – 3500 km s^{-1} and 4000 – 7000 km s^{-1}. This is due to the prevalent, broad GPS at 8300 km s^{-1} and narrow radar RFIs at 8000 – 9800 km s^{-1} that is present at the NRT. The noise rms remained fairly constant over the 500 – 3500 km s^{-1} and 4000 – 7000 km s^{-1} regions, as can be seen in Fig. 2.17. As a result the 4000 - 7000 km s^{-1} range was used preferentially for the rms noise level determination. However, in some cases there was intermittent RFI at 6000 km s^{-1} (cf. Fig. 2.12), and as a result the rms noise had to be determined between $500 < v < 3500$ km s^{-1}.

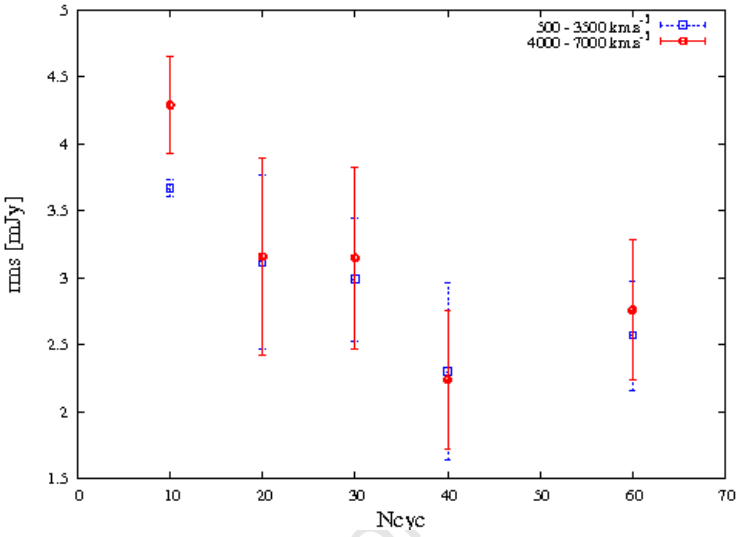

Figure 2.17: The rms noise level (in mJy) for non-detections as a function of the integration time (Ncyc, the number of 40/40 sec ON/OFF cycles) measured between 500 – 3500 km s^{-1} (blue points) and 4000 – 7000 km s^{-1} (red points) only. Note that the rms does not decrease with one over the square root of the number of cycles as each bin contains sources with a different mix of declinations, and the high-declination sources will have higher noise levels due to the decreased telescope gain (see Sect. 2.2).

Data quality

Some data showed baseline ripples caused by standing waves between the surfaces of the radio telescope due to the presence of strong continuum sources. At the NRT this standing wave has a 110 km s^{-1} wavelength (e.g., Allen 1969). Since it always occurs at the same wavelength it can be easily identified in the Fast Fourier Transform deconvolution of the spectrum and removed. This will be done later using an algorithm developed recently for another NRT project.

SNALFA

In order to check the reliability of the target detections, the line width- and flux-dependent signal to noise ratio adopted by the Arecibo Legacy Fast ALFA Survey (ALFALFA) was used (Saintongé 2007).

$$S/N_{ALFA} = \frac{1000 \times F_{HI}}{w_{50} \times \frac{\sqrt{\omega}}{rms}}, \tag{2.6}$$

where $\omega = w_{50}/2 \triangle v$ and $\triangle v$ is the velocity resolution (18 km s^{-1}).

This signal to noise ratio accounts for the fact that a broader line will have substantially more signal that a narrow line with the same peak SNR. It was found that for $S/N_{ALFA} > 5.5$ a detection becomes more reliable (Saintongé 2007). The survey presented in this dissertation opted for $S/N_{ALFA} > 6.00$ as a first detection reliability threshold. This accommodates even the narrow line galaxies.

Uncertainties

The resulting HI integrated line flux ($F_{\rm HI}$), HI centre velocities ($v_{\rm HI}$), and velocity line widths at 50% and 20% of peak levels are direct measurements. They were not corrected for effects of velocity resolution or cosmological stretching. Uncertainties in the $F_{\rm HI}$ and $v_{\rm HI}$ parameters were calculated following Schneider et al. (1990).

The statistical uncertainty in $F_{\rm HI}$ is:

$$\sigma_{F_{\rm HI}} = 2\sigma_{rms}\sqrt{1.2 w_{20} \triangle v}, \tag{2.7}$$

where σ_{rms} is the rms noise level, w_{20} is the line width at the 20% level and δv the velocity resolution of the spectrum.

The uncertainty in the central line velocity $v_{\rm HI}$ (km s^{-1}) is given by

$$\sigma_{v_{\rm HI}} = \frac{1.5 \Delta w}{SNR}, \tag{2.8}$$

where Δw is $(w_{20} - w_{50})$ in km s^{-1} and SNR is the peak signal to noise ratio. Following Schneider et al. 1990, the uncertainty in the w_{50} and w_{20} line widths is expected to be 2 and 3.1 times $\sigma_{v_{\rm HI}}$.

Chapter 3

HI Data Results

In this chapter a catalogue of HI-detected galaxies and their spectra are presented in Sect. 3.1.1. This is followed by a brief discussion of the characteristics of the HI profiles in Section 3.1.2. In Sect. 3.1.3 the acccuracy of the detected galaxies is discussed. A very brief overview of the non-detections is presented in Sect. 3.1.4. This is followed by assessment of the characteristics of detections in relation to Galactic latitude, stellar densities and dust extinction in Sect. 3.1.5. In Sect. 3.2 the HI mass distribution of detected galaxies is presented. Finally, a summary of this chapter is given in Sect. 3.3.

3.1 HI data for observed galaxies

The target candidate galaxies presented in this thesis were observed with the NRT from July 2009 to March 2012. Of the 1000 galaxy candidates in the NRT sample, 928 were observed in that period, using close to 1200 hours of observing time. At the start of this dissertation, data from July 2009 to June 2011 had already been reduced. From that date onwards data was reduced by the author of this thesis.

A total of 249 are detected out of the 928 observed targets, i.e., the detection rate is 27%. These detections are out to a radial velocity of $\sim 8500\,\mathrm{km\,s^{-1}}$, beyond this RFI and telescope sensitivity limits the number of galaxies seen. It is an improved detection rate to that of the NRT pilot study of (22/132) 17% (van Driel et al. 2009). This improvement can be attributed to the visual inspection method used in this survey. It is a respectable detection rate given that no pre-selection was made according to morphological type (which is not straightforward in the NIR, nor in the ZoA).

Of the total 249 detected galaxies, 84% (210) are clear detections (listed in Table 3.1 and displayed in Fig. 3.1) and 16% (39) are classified as marginal detections (Table 3.2 and Fig. 3.2). The total number of detections include spectra which revealed two independent signals. This was found for five NRT pointings listed in Table 3.3 and comprise 2% of the overall detections.

To determine whether a galaxy is detected or not, spectra were first visually inspected

by the author of the thesis during the different steps of the data reduction procedure (see Sect. 2.3) for the signature of any HI emission, where if detected, the HI parameters were determined. Besides using statistical criteria, such as different signal-to-noise estimates (Sect. 2.3.2), the reliability of all potentially detected HI lines was then assessed independently by three collaborators (A.C. Schröder, W van Driel and P.A. Henning), followed by an adjudication by another collaborator (R.C. Kraan-Korteweg). Both clear detections as well as non-detections which had reached the target rms noise level of 3.3 mJy were catalogued as such, whereas marginal or possible detections were filed for re-observations and their results continuously updated as new data came in. In this thesis the status of the data as taken up to 31 March 2012 is presented; the observations and reductions are still continuing and will be rounded off by the end of the current observing semester, i.e., December 2012.

The 249 HI detections have a peak signal-to-noise ratio $S/N_{peak} \gtrsim 5.0$. The linewidth- and flux-dependent S/N_{ALFA} of reliable detections is larger than $S/N_{ALFA} > 6.0$, while marginals typically have $5.0 \lesssim SNR_{ALFA} \lesssim 6.0$.

3.1.1 The HI-data Catalogue

In Tables 3.1 and 3.2 the HI parameters of the 210 reliable detections and 39 marginal detections, respectively, are listed. A table of non-detections with their rms noise level is presented in Appendix A.

Parameters listed in the catalogue are:

Column 1: The 2MASXJhhmmssss±ddmmsss identifier of the galaxy. The first 8 numbers represent the right ascension in hh:mm:ss.ss and the last 7 characters the declination of the source in dd:mm:ss.s (J2000.0).

Column 2: Galactic longitude l in degrees.

Column 3: Galactic latitude b in degrees.

Column 4: The number of 40 second ON/40 second OFF observation cycles (Ncyc).

Column 5: The rms level in mJy.

Column 6: The peak signal to noise ratio S/N_{peak}.

Column 7: The linewidth- and flux-dependent signal to noise ratio as described in Sect. 2.3.2 (S/N_{ALFA})

Column 8: The heliocentric velocity ($v_{\rm HI}$) measured at the mid-point of the profile peak at the 50% level of the profile peak value in km s^{-1}, with its uncertainty, estimated as described in Sect. 2.3.2.

Column 9: The velocity line width at the 50% level of the profile peak value in km s^{-1} (w_{50}). Its uncertainty is expected to be twice that of $v_{\rm HI}$).

Column 10: The velocity line width at the 20% level of the profile peak value in km s^{-1} (w_{20}). Its uncertainty is expected to be 3.1 times that of $v_{\rm HI}$).

Column 11: The integrated line flux ($F_{\rm HI}$) in Jy, with its uncertainty, estimated as described in Sect. 2.3.2.

Column 12: The logarithm of the HI mass ($M_{\rm HI}$) in $M\odot$ is derived as follows,

$$M_{\rm HI} = 2.356 \times 10^5 D^2 F_{HI}, \tag{3.1}$$

where $F_{\rm HI}$ is the integrated line flux in Jy km s^{-1}. The distance, D, is determined Mpc^{-1} directly from the heliocentric velocity (v_{hel}), using a Hubble constant of $H_o = 70$ km s^{-1} Mpc^{-1},

$$D = \frac{v_{hel}}{H_o}, \tag{3.2}$$

This distance computation ignores the bulk-flow term.

The baseline-subtracted HI profiles of the reliable and marginal detections are plotted in Figs. 3.1 and 3.2 respectively. Galaxies with an asterisk (*) next to their indentifier are those with two galaxy detections in their spectrum (see Sect. 3.1.2).

Table 3.1: A catalogue of reliable detections.

Name 2MASXJ *Col(1)*	gal l [deg] *Col(2)*	gal b [deg] *Col(3)*	Ncyc no. *Col(4)*	rms [mJy] *Col(5)*	S/N$_{peak}$ *Col(6)*	S/N$_{ALFA}$ *Col(7)*	$v_{\rm HI}$ [km s^{-1}] *Col(8)*	w_{50} [km s^{-1}] *Col(9)*	w_{20} [km s^{-1}] *Col(10)*	$F_{\rm HI}$ [Jy] *Col(11)*	log(M_{HI}) [M$_\odot$] *Col(12)*
00141253+7036448	119.82	7.97	13	6.2	5.8	12.4	6958±9	398	431	9.3±1.2	10.3
00360888+6319171	121.22	0.50	69	2.7	4.4	8.9	7316±46	370	503	2.7±0.6	9.8
00384223+6017130	121.35	-2.55	16	4.5	6.0	9.4	4354±5	222	241	3.8±0.7	9.5
00475430+6807433	122.60	5.26	14	5.9	8.3	14.6	3764±5	339	364	9.6±1.1	9.8
01191829+6219297	126.16	-0.37	16	4.5	5.0	10.2	4041±18	294	354	4.7±0.8	9.6
01203021+6525055	125.95	2.72	16	4.5	10.2	19.5	4148±4	413	440	10.6±0.9	9.9
01230734+6049177	126.79	-1.81	54	2.9	4.1	9.4	5821±28	400	475	3.2±0.6	9.7
01261932+6046064	127.18	-1.81	49	2.7	6.2	14.5	5958±3	477	490	5.1±0.6	9.9
01273787+6308155	127.01	0.55	35	3.5	7.5	17.8	6223±40	95	294	3.6±0.6	9.8
01281012+6313517	127.05	0.65	55	3.2	4.6	8.4	6040±53	158	320	2.0±0.5	9.5
01330236+6404589	127.46	1.58	38	3.0	4.9	9.8	4002±38	250	374	2.8±0.5	9.3
01475111+6305278	129.26	0.91	46	2.6	5.7	9.2	4242±21	195	275	2.0±0.4	9.2
01485859+6045514	129.90	-1.33	15	4.7	6.0	12.5	4391±11	266	311	5.7±0.8	9.7
01572719+6601408	129.58	4.01	29	3.7	5.5	10.2	3909±21	224	299	3.4±0.6	9.4
02013241+6824219	129.34	6.41	27	5.9	5.5	6.8	3771±8	78	108	2.1±0.6	9.2
02023124+6008000	131.68	-1.53	42	2.8	4.9	8.9	4579±9	277	305	2.5±0.5	9.4
02085980+7114029	129.15	9.30	20	4.8	7.6	11.2	3305±7	168	204	4.2±0.6	9.3
02101852+6300516	131.74	1.50	31	3.3	5.0	10.1	4306±18	187	248	2.7±0.5	9.4
02235399+6337032	132.99	2.57	17	4.0	4.9	9.7	3636±30	170	268	3.1±0.6	9.3
02243924+5926126	134.54	-1.32	34	3.0	4.5	9.0	6746±5	437	452	3.4±0.6	9.9
02294695+6523350	132.94	4.45	36	2.9	5.8	12.5	6430±8	361	392	4.2±0.5	9.9
02322165+6454104	133.38	4.10	28	3.6	6.0	9.8	5351±11	289	331	3.6±0.6	9.7
02332153+6009100	135.29	-0.25	13	4.5	5.1	8.1	4558±9	249	279	3.5±0.7	9.5
02440181+7005273	132.30	9.29	12	5.5	6.1	10.6	4132±5	199	221	5.0±0.8	9.6
02442271+5507524	138.67	-4.25	90	2.0	4.4	6.2	4293±21	125	188	0.8±0.3	8.9
02455702+5522336	138.77	-3.94	31	3.1	4.3	7.1	7258±19	247	302	2.0±0.5	9.7
02472414+6239425	135.81	2.73	29	3.9	7.7	13.4	5917±4	496	519	7.0±0.8	10.1
02483731+6300467	135.78	3.10	35	3.0	5.6	6.4	6132±0	290	290	2.0±0.5	9.6
02531969+5529140	139.66	-3.38	24	3.2	8.6	21.7	4462±52	121	421	4.5±0.6	9.6
02531969+5529140	139.66	-3.38	24	3.2	22.8	32.0	3824±2	61	94	4.8±0.3	9.5
02545129+5625144	139.43	-2.45	29	3.1	8.7	13.6	4188±4	233	256	3.8±0.5	9.5
02545198+5812134	138.61	-0.86	51	2.5	7.3	14.3	4166±19	113	205	2.3±0.3	9.3
02550583+6624065	134.88	6.44	18	4.3	6.4	12.9	3482±6	363	389	6.3±0.8	9.6

Table 3.1 – Continued

Name 2MASXJ *Col(1)*	gal l [deg] *Col(2)*	gal b [deg] *Col(3)*	Ncyc no. *Col(4)*	rms [mJy] *Col(5)*	S/N_{peak} *Col(6)*	S/N_{ALFA} *Col(7)*	$v_{\rm HI}$ [km s^{-1}] *Col(8)*	w_{50} [km s^{-1}] *Col(9)*	w_{20} [km s^{-1}] *Col(10)*	$F_{\rm HI}$ [Jy] *Col(11)*	$\log(M_{HI})$ [M$_\odot$] *Col(12)*
02570346+5658488	139.44	-1.81	17	3.5	20.4	45.0	3565±2	297	325	16.2±0.6	10.0
02590152+5318199	141.41	-4.93	39	2.0	4.7	6.2	7175±9	286	313	1.2±0.3	9.5
02592153+5736175	139.42	-1.11	17	4.0	9.3	15.9	2177±4	286	312	6.5±0.7	9.2
03082803+5745174	140.41	-0.39	15	4.4	7.8	15.1	2252±19	218	317	5.8±0.7	9.2
03104409+6106477	138.96	2.65	50	2.8	4.5	7.3	2488±21	211	273	1.8±0.4	8.7
03111176+6105047	139.03	2.66	24	3.8	6.4	11.8	2773±10	156	197	3.4±0.5	9.1
03124721+6231391	138.45	3.99	21	3.9	4.7	9.6	6321±13	219	260	3.3±0.6	9.8
03135317+6232589	138.54	4.08	43	3.1	6.0	12.1	2052±13	618	669	5.5±0.7	9.1
03202205+6645055	136.89	8.01	41	3.3	10.2	18.1	2994±4	178	203	4.8±0.4	9.3
03264399+5419084	144.39	-1.95	66	1.8	4.9	7.9	4861±34	169	279	1.1±0.3	9.1
03290640+6458319	138.63	7.03	16	4.6	10.6	19.3	2464±4	417	446	10.8±0.9	9.5
03292877+5429573	144.62	-1.58	59	2.2	4.5	7.7	5061±19	324	382	1.8±0.4	9.4
03331908+6609092	138.31	8.24	14	4.7	9.2	20.4	5598±5	377	407	11.1±0.9	10.2
03362290+5048356	147.61	-3.98	17	3.6	9.9	19.3	5052±7	338	381	7.6±0.6	10.0
03385418+6617499	138.68	8.69	17	4.7	4.7	10.2	6049±32	197	296	4.1±0.8	9.9
03393937+6527116	139.25	8.06	18	4.8	6.4	15.0	5174±13	343	400	8.0±0.9	10.0
03394709+6528486	139.25	8.09	9	6.2	7.3	14.2	5197±30	274	421	8.8±1.2	10.1
03403139+6649043	138.49	9.20	18	5.4	35.4	59.4	1591±3	73	145	16.4±0.6	9.3
03514420+5105033	149.36	-2.29	27	2.6	5.2	9.5	4817±6	217	237	2.2±0.4	9.4
03543651+4910571	150.93	-3.47	17	3.3	7.8	10.3	4163±4	282	301	3.4±0.5	9.5
04062549+5321492	149.59	0.90	14	4.9	11.6	24.7	5780±10	213	290	10.7±0.8	10.2
04075531+4549400	154.84	-4.52	13	3.8	16.0	31.6	4470±3	276	310	11.9±0.6	10.1
04114143+3841285	160.26	-9.26	16	3.2	5.7	10.5	5723±14	154	207	2.5±0.4	9.6
04115755+3838463	160.33	-9.25	8	4.0	5.3	10.1	5761±8	569	596	5.8±0.9	10.0
04115864+3842213	160.29	-9.21	32	2.2	8.3	16.9	5757±14	522	599	5.2±0.5	9.9
04120068+3846073	160.25	-9.16	23	2.8	8.4	18.0	5771±15	491	578	6.7±0.6	10.0
04121283+3842023	160.33	-9.18	37	2.2	7.2	18.8	5780±26	498	624	5.6±0.5	10.0
04124119+3843433	160.38	-9.10	26	2.7	7.2	22.8	6343±100	46	526	2.5±0.6	9.7
04131853+3819491	160.74	-9.30	29	2.3	17.9	40.3	6441±3	249	283	8.7±0.4	10.2
04151246+3840071	160.78	-8.80	16	2.9	5.8	11.8	5955±46	359	539	3.8±0.6	9.8
04191179+5552439	149.22	4.00	14	4.2	8.3	12.8	5255±5	372	402	6.2±0.8	9.9
04202281+4535327	156.58	-3.19	17	2.7	4.4	8.1	7237±40	239	357	2.1±0.5	9.7
04204654+5237183	151.67	1.84	49	2.5	4.3	11.7	5638±23	203	270	2.5±0.4	9.6

Table 3.1 – Continued

Name 2MASXJ *Col(1)*	gal l [deg] *Col(2)*	gal b [deg] *Col(3)*	Ncyc no. *Col(4)*	rms [mJy] *Col(5)*	S/N_{peak} *Col(6)*	S/N_{ALFA} *Col(7)*	$v_{\rm HI}$ [km s^{-1}] *Col(8)*	w_{50} [km s^{-1}] *Col(9)*	w_{20} [km s^{-1}] *Col(10)*	$F_{\rm HI}$ [Jy] *Col(11)*	$\log(M_{HI})$ [M$_\odot$] *Col(12)*
04230274+3722007	162.81	-8.62	16	3.0	6.0	13.6	5832±6	411	436	5.0±0.6	9.9
04244617+4244494	159.16	-4.63	14	2.6	5.3	9.5	6007±4	505	518	3.3±0.6	9.8
04250287+4726453	155.83	-1.31	15	2.6	23.2	43.1	5661±3	140	191	8.0±0.3	10.1
04254161+4222276	159.54	-4.77	37	1.8	6.1	8.1	5872±7	136	165	1.0±0.2	9.2
04263959+4700055	156.34	-1.43	34	2.6	4.3	6.4	5630±17	346	395	1.8±0.5	9.4
04264449+3810182	162.73	-7.54	66	1.8	4.1	6.8	6546±32	129	216	0.8±0.2	9.2
04271586+5049248	153.66	1.30	17	3.4	13.2	29.0	4429±5	242	284	9.2±0.5	9.9
04283316+3625579	164.26	-8.47	14	2.9	9.6	22.2	6812±9	409	464	7.7±0.6	10.2
04302392+5020090	154.35	1.32	28	2.8	5.6	7.3	2330±8	83	114	1.1±0.3	8.5
04313523+4714048	156.75	-0.66	22	3.5	5.5	11.7	5812±21	372	448	4.7±0.7	9.9
04333811+4530061	158.25	-1.58	12	3.8	7.2	17.1	3852±15	306	377	6.8±0.7	9.7
04340516+4101321	161.61	-4.55	36	2.0	7.9	13.1	6230±12	246	307	2.5±0.3	9.7
04382270+4746546	157.12	0.55	18	3.1	5.9	11.2	6163±6	322	345	3.7±0.5	9.8
04390278+3532568	166.36	-7.49	14	3.0	4.4	8.0	6416±30	177	265	1.9±0.4	9.6
04431899+4032175	163.14	-3.58	45	1.7	4.8	8.2	6351±40	143	272	1.0±0.3	9.3
04433407+4536452	159.33	-0.21	31	2.4	4.5	7.1	5885±40	140	259	1.2±0.4	9.3
04464159+4943063	156.56	2.86	34	2.4	6.3	8.6	6587±5	340	363	2.3±0.4	9.7
04481997+3436502	168.32	-6.65	17	2.6	8.2	16.0	6125±38	79	290	2.2±0.4	9.6
04494005+4511185	160.35	0.33	62	1.4	7.0	17.7	4300±23	728	835	4.0±0.4	9.6
04514426+3856227	165.41	-3.37	26	2.3	12.3	24.5	3919±3	350	372	6.4±0.4	9.7
04534877+4218445	163.04	-0.93	34	2.0	9.2	21.5	6860±13	331	410	4.6±0.4	10.0
04562691+4555425	160.53	1.71	28	2.4	5.5	10.7	7106±40	430	577	3.2±0.5	9.9
04563494+3723521	167.21	-3.60	25	2.5	5.3	9.2	6498±14	387	436	2.7±0.5	9.7
04574731+4607167	160.52	2.02	24	3.1	4.7	7.9	7201±10	369	402	2.8±0.6	9.8
05014040+4338109	162.90	1.02	12	3.5	4.9	9.8	7167±10	556	589	4.8±0.8	10.1
05043136+3731335	168.08	-2.28	38	2.3	5.5	11.2	6095±12	390	433	3.0±0.4	9.7
05095533+4436308	163.02	2.79	16	3.1	10.1	20.1	6099±11	410	482	7.5±0.6	10.1
05115386+4537142	162.41	3.67	14	3.5	5.7	10.6	6241±27	238	342	3.5±0.6	9.8
05200866+4314313	165.21	3.49	27	2.6	29.6	59.0	3785±2	132	172	10.4±0.3	9.9
05221454+3826469	169.38	1.09	61	1.4	5.1	9.6	6229±43	407	553	1.6±0.3	9.5
05295184+3835341	170.09	2.41	60	1.4	5.1	8.3	6957±37	167	293	0.9±0.2	9.3
05382465+3241509	175.99	0.67	54	1.9	5.2	8.0	8525±5	323	340	1.6±0.3	9.8
05515780+1807051	190.03	-4.32	42	1.4	3.9	7.7	5846±17	177	222	0.9±0.2	9.2

Table 3.1 – Continued

Name 2MASXJ *Col(1)*	gal l [deg] *Col(2)*	gal b [deg] *Col(3)*	Ncyc no. *Col(4)*	rms [mJy] *Col(5)*	S/N$_{peak}$ *Col(6)*	S/N$_{ALFA}$ *Col(7)*	$v_{\rm HI}$ [km s^{-1}] *Col(8)*	w_{50} [km s^{-1}] *Col(9)*	w_{20} [km s^{-1}] *Col(10)*	$F_{\rm HI}$ [Jy] *Col(11)*	log(M_{HI}) [M$_\odot$] *Col(12)*
05540495+3127485	178.77	2.87	16	3.4	29.0	49.2	4413±7	124	254	11.1±0.5	10.0
05540715+1759352	190.40	-3.94	15	2.8	40.0	51.3	5725±1	45	73	5.8±0.2	10.0
05583483+1754200	191.01	-3.06	59	2.2	7.6	14.4	6092±16	123	204	2.1±0.3	9.6
05585447+1759445	190.97	-2.95	17	2.4	5.9	12.5	5973±50	121	317	2.0±0.4	9.5
05590035+1806455	190.88	-2.87	16	2.5	6.1	13.9	6050±20	269	351	3.4±0.4	9.8
05590393+1804285	190.92	-2.88	18	2.3	7.9	15.9	6038±18	248	343	3.5±0.4	9.8
06023546+2201525	187.89	-0.20	16	2.5	7.3	15.7	2609±33	108	271	2.4±0.4	8.9
06074379+1608036	193.63	-2.03	18	2.2	14.3	27.6	5554±7	164	226	4.8±0.3	9.9
06110644+1551489	194.26	-1.45	10	3.5	7.2	12.8	5423±11	395	446	5.4±0.7	9.9
06200969+1650483	194.43	0.93	37	1.9	9.0	14.2	5202±4	188	210	2.3±0.3	9.5
06225815+1108312	199.78	-1.15	12	2.6	23.6	47.6	5490±2	359	395	13.9±0.5	10.3
06284616+0149197	208.72	-4.21	16	2.5	5.9	8.0	2882±10	159	199	1.5±0.3	8.8
06352675+0230578	208.87	-2.41	48	1.8	8.6	18.1	6352±21	99	220	1.9±0.2	9.6
06353794+0022498	210.79	-3.34	32	1.6	6.7	14.9	6146±10	391	435	2.9±0.3	9.7
06354230+0226468	208.96	-2.38	71	1.4	6.1	11.3	6425±23	179	272	1.3±0.2	9.4
06455492-1812493	228.68	-9.38	15	3.2	107.0	223.3	839±0	183	208	58.0±0.4	9.3
06474744-0048518	213.24	-1.18	27	1.9	8.0	14.9	4216±14	169	243	2.3±0.3	9.3
06503679-0352597	216.29	-1.95	48	1.4	5.7	10.2	6521±5	401	421	1.8±0.3	9.6
06535387-0337410	216.44	-1.11	45	1.5	5.4	11.3	6557±8	489	519	2.2±0.3	9.7
06541984-1208232	224.09	-4.87	20	2.1	8.9	14.9	9844±5	461	489	4.0±0.4	10.3
06552670-0411095	217.11	-1.02	29	1.8	6.2	9.8	5459±7	265	292	1.7±0.3	9.4
06572149-0508597	218.19	-1.03	30	2.0	35.9	81.7	2568±1	267	301	15.8±0.3	9.7
06590153+0634579	207.92	4.68	29	1.6	9.1	16.1	6360±4	363	390	3.0±0.3	9.8
07005613-1147344	224.51	-3.27	17	2.4	21.1	48.3	2737±2	424	451	14.4±0.5	9.7
07021533-0313467	217.04	0.93	28	2.2	10.9	16.2	6682±3	385	409	4.2±0.4	10.0
07093459-0525404	219.83	1.54	16	2.6	21.9	49.2	1715±2	265	294	12.5±0.4	9.2
07165094-1852251	232.57	-3.11	18	2.6	8.9	17.9	2807±9	266	319	4.5±0.4	9.2
07165193-1852341	232.58	-3.11	29	2.0	10.6	19.3	2802±3	264	286	3.8±0.3	9.2
07245535-2430057	238.44	-4.08	65	1.3	8.1	11.5	4636±7	288	325	1.5±0.2	9.2
07245535-2430057	238.44	-4.08	65	1.2	57.7	113.3	907±2	130	197	9.4±0.2	8.6
07304535-2823585	242.50	-4.77	35	2.1	20.1	29.9	8080±1	299	319	6.5±0.3	10.3
07344923-2404306	239.14	-1.90	29	1.7	8.3	16.4	4471±19	333	439	3.0±0.3	9.5
07360443-2748552	242.55	-3.46	48	1.6	5.4	12.0	7760±5	377	396	2.3±0.3	9.8

Table 3.1 – Continued

Name 2MASXJ *Col(1)*	gal l [deg] *Col(2)*	gal b [deg] *Col(3)*	Ncyc no. *Col(4)*	rms [mJy] *Col(5)*	S/N_{peak} *Col(6)*	S/N_{ALFA} *Col(7)*	$v_{\rm HI}$ [km s^{-1}] *Col(8)*	w_{50} [km s^{-1}] *Col(9)*	w_{20} [km s^{-1}] *Col(10)*	$F_{\rm HI}$ [Jy] *Col(11)*	$\log(M_{HI})$ [M$_\odot$] *Col(12)*
07385822-2855357	243.84	-3.45	35	2.0	6.9	13.3	5003±7	345	377	3.0±0.4	9.6
07403156-2618279	241.72	-1.86	48	1.6	7.1	11.2	3578±4	299	320	1.8±0.3	9.1
07413554-2544190	241.34	-1.37	29	2.1	11.9	24.2	7808±3	299	322	5.2±0.3	10.2
07414115-2231134	238.56	0.24	14	2.9	27.2	61.3	3074±2	449	487	22.4±0.6	10.0
07414792-3028212	245.49	-3.67	13	3.1	8.5	18.7	7482±5	391	419	6.9±0.6	10.3
07431472-2545501	241.55	-1.06	16	2.6	23.4	35.2	7074±2	312	348	9.7±0.5	10.4
07440237-2721456	243.03	-1.71	36	1.8	6.7	10.2	7934±3	416	430	2.3±0.4	9.8
07475295-3041265	246.33	-2.65	44	2.0	5.6	7.3	4732±14	330	383	1.6±0.4	9.2
07483070-2532370	241.95	0.07	12	3.4	6.2	13.9	4389±8	413	445	5.7±0.7	9.7
07483252-2516431	241.73	0.21	16	2.8	10.3	15.7	6811±5	354	387	4.9±0.5	10.0
07492337-3542214	250.83	-4.89	23	3.2	76.5	92.5	2861±0	47	69	12.2±0.2	9.7
07530159-2158341	239.41	2.78	31	1.9	5.6	12.5	7090±53	207	407	2.1±0.4	9.7
07533288-2129485	239.06	3.13	12	2.9	5.5	11.6	7064±18	419	484	4.1±0.6	10.0
07545229-2756453	244.75	0.07	28	2.2	7.0	8.7	1572±9	40	84	0.7±0.2	7.9
07545280-3318173	249.34	-2.70	12	3.9	13.1	20.8	2719±3	260	283	7.9±0.6	9.5
07561560-3656270	252.60	-4.33	28	3.9	4.9	9.4	5402±27	294	381	3.8±0.7	9.7
08015503-3810213	254.25	-4.01	25	3.9	6.7	12.4	8902±17	273	349	4.8±0.7	10.3
08111394-3854530	255.85	-2.88	60	2.7	4.7	7.7	5348±7	378	401	2.4±0.5	9.5
08191136-3833104	256.41	-1.38	41	3.9	7.1	14.1	2959±34	58	222	2.5±0.5	9.0
08213966-3903268	257.10	-1.27	50	3.3	4.4	7.4	5143±21	190	252	2.0±0.5	9.4
08243293-3637484	255.44	0.58	26	3.1	5.2	7.9	5549±33	103	218	1.5±0.4	9.4
08255863-3639240	255.62	0.80	31	4.1	9.0	19.3	5357±18	327	436	8.7±0.8	10.1
1618262-373604	341.99	9.11	16	5.1	7.7	14.9	4589±10	152	203	5.6±0.7	9.8
16182851-3739379	341.95	9.06	17	3.8	7.5	10.8	4589±7	156	192	3.1±0.5	9.5
16254669-3707583	343.36	8.39	32	3.2	6.6	9.7	4353±4	324	341	3.4±0.6	9.5
16434955-3705384	345.82	5.75	16	4.5	3.5	6.5	1261±44	288	391	3.0±0.8	8.4
16463421-3903086	344.68	4.07	64	3.0	5.4	8.2	6453±11	229	269	2.2±0.4	9.6
16490239-3642570	346.79	5.20	53	2.0	6.5	11.9	6385±7	474	504	3.2±0.4	9.8
16490503-3619500	347.09	5.43	43	2.5	7.2	13.5	3845±4	244	261	3.1±0.4	9.3
16500224-3712073	346.54	4.73	27	3.8	8.9	15.1	7911±7	227	269	5.2±0.6	10.2
16520999-3550026	347.87	5.27	28	3.2	9.3	12.3	6394±7	242	285	3.6±0.5	9.9
16532065-3532311	348.25	5.27	17	4.0	8.3	13.9	6159±4	344	367	6.2±0.7	10.1
16540803-3534375	348.32	5.12	12	4.2	9.2	16.5	6334±17	125	228	4.7±0.6	10.0

Table 3.1 – Continued

Name 2MASXJ *Col(1)*	gal l [deg] *Col(2)*	gal b [deg] *Col(3)*	Ncyc no. *Col(4)*	rms [mJy] *Col(5)*	S/N_{peak} *Col(6)*	S/N_{ALFA} *Col(7)*	$v_{\rm HI}$ [km s^{-1}] *Col(8)*	w_{50} [km s^{-1}] *Col(9)*	w_{20} [km s^{-1}] *Col(10)*	$F_{\rm HI}$ [Jy] *Col(11)*	$\log(M_{HI})$ [M$_\odot$] *Col(12)*
17054244-3329451	351.44	4.52	62	1.8	8.8	20.2	6183±32	64	248	1.8±0.3	9.5
17172214-2650068	358.35	6.38	49	1.8	9.2	19.8	6198±24	215	364	3.2±0.3	9.8
19194212+0721408	42.71	-2.88	8	3.7	4.3	7.3	8209±15	268	310	2.6±0.6	9.9
19505731+1822281	56.06	-4.20	9	3.9	12.5	24.5	3973±4	296	328	9.8±0.7	9.9
19521116+3229039	68.34	2.76	17	3.1	6.7	15.2	8228±17	393	469	5.5±0.6	10.3
20084824+4339589	79.61	5.83	11	3.6	4.2	7.7	5020±11	281	311	2.8±0.6	9.5
20135690+2902036	67.91	-3.03	18	2.7	18.2	34.9	4211±4	165	214	7.4±0.4	9.8
20170253+3150065	70.61	-2.03	18	3.2	14.0	36.4	1235±4	278	312	11.7±0.5	8.9
20183871+4041003	78.11	2.67	12	5.4	7.0	14.5	4324±10	262	307	7.6±0.9	9.8
20201209+4039396	78.26	2.41	38	4.3	4.8	10.9	4225±16	172	225	3.7±0.6	9.5
20214907+4400399	81.20	4.07	18	3.1	9.6	14.8	5085±3	168	186	3.5±0.4	9.6
20321211+3255568	73.35	-4.02	15	3.2	24.0	46.5	4157±6	307	406	15.8±0.6	10.1
20363702+4647294	84.98	3.58	37	3.2	5.3	7.4	4584±5	259	277	2.3±0.5	9.4
20363825+4546254	84.17	2.96	39	2.6	4.8	8.6	5196±8	333	357	2.4±0.5	9.5
20435702+5032583	88.71	4.91	13	3.8	12.2	24.4	3342±2	335	352	10.2±0.7	9.7
20440241+5043362	88.86	5.00	16	3.7	11.5	25.0	3341±25	337	529	10.1±0.8	9.7
20441259+4940566	88.05	4.34	27	2.6	6.0	9.9	7716±11	379	422	3.0±0.5	9.9
20470471+4046165	81.39	-1.61	29	2.4	10.8	17.5	9177±11	254	331	3.9±0.4	10.2
20501144+4516514	85.25	0.79	13	4.0	16.9	29.3	4601±2	131	156	8.1±0.5	9.9
20571736+4738373	87.84	1.38	12	3.8	6.8	10.8	3357±5	186	207	3.3±0.5	9.3
20572285+4808542	88.24	1.69	17	3.2	6.9	11.8	5690±9	387	427	4.5±0.6	9.8
20581676+4615252	86.90	0.34	10	3.7	4.6	9.5	5230±13	303	342	3.7±0.6	9.7
21012083+4624515	87.37	0.05	13	3.8	14.7	29.1	3510±6	205	262	9.6±0.6	9.8
21060821+4500472	86.88	-1.51	17	3.1	8.0	15.6	5421±20	473	582	6.2±0.7	9.9
21061631+4503203	86.93	-1.50	16	3.1	10.5	28.9	5402±27	433	621	11.2±0.7	10.2
21064188+4525375	87.25	-1.30	15	2.9	9.0	14.3	5177±5	287	315	4.2±0.5	9.7
21071353+4456529	86.96	-1.70	15	4.4	3.3	7.7	4793±46	469	570	3.9±1.0	9.6
21095816+5437431	94.39	4.53	75	2.7	5.3	12.4	6166±4	408	423	4.1±0.5	9.9
21104814+4341173	86.47	-3.02	12	4.1	8.0	12.4	4310±5	120	149	3.3±0.5	9.5
21123923+4556037	88.33	-1.72	12	4.2	7.9	11.5	3491±5	292	319	5.0±0.7	9.5
21132159+4945237	91.19	0.82	18	3.7	6.9	16.2	5814±58	361	627	6.8±0.9	10.0
21132528+4956168	91.33	0.94	28	2.9	6.2	13.9	5955±6	613	636	6.0±0.7	10.0
21155335+4726430	89.81	-1.08	27	2.5	3.8	7.4	7858±17	393	435	2.3±0.5	9.8

Table 3.1 – Continued

Name 2MASXJ *Col(1)*	gal l [deg] *Col(2)*	gal b [deg] *Col(3)*	Ncyc no. *Col(4)*	rms [mJy] *Col(5)*	S/N_{peak} *Col(6)*	S/N_{ALFA} *Col(7)*	$v_{\rm HI}$ [km s^{-1}] *Col(8)*	w_{50} [km s^{-1}] *Col(9)*	w_{20} [km s^{-1}] *Col(10)*	$F_{\rm HI}$ [Jy] *Col(11)*	$\log(M_{HI})$ [M$_\odot$] *Col(12)*
21183139+5431287	95.17	3.56	13	4.1	5.3	12.6	6086±16	463	518	6.6±0.9	10.1
21185980+4401180	87.73	-3.86	12	3.5	10.1	15.4	4100±5	134	166	3.7±0.4	9.5
21273041+4525157	89.80	-3.93	12	4.1	5.6	8.7	5308±5	159	179	2.7±0.5	9.6
21305323+4813559	92.15	-2.29	17	2.9	17.6	28.3	3780±3	229	260	7.4±0.4	9.7
21310014+4814279	92.17	-2.29	10	4.6	13.1	23.9	3782±3	234	259	10.1±0.7	9.8
21375000+5929172	100.52	5.33	19	3.7	5.2	8.8	2199±33	20	133	0.9±0.4	8.3
21512814+5316383	97.92	-0.62	46	2.0	4.5	10.9	4681±9	462	489	2.9±0.4	9.5
21554534+5228186	97.92	-1.66	15	3.9	7.1	16.3	6132±30	99	240	3.8±0.6	9.8
21584706+5408535	99.31	-0.61	14	5.1	8.6	13.0	1028±12	85	153	3.7±0.6	8.3
22352646+6048150	107.09	2.19	27	3.5	6.0	10.4	3571±6	272	297	3.6±0.6	9.3
22555131+5622305	107.39	-2.97	49	2.1	6.1	7.4	6683±18	147	220	1.1±0.3	9.4
23553308+6014324	116.05	-1.88	18	4.1	10.8	25.4	4657±14	294	397	10.6±0.8	10.0

Table 3.2: A catalogue of marginal detections.

Name 2MASXJ *Col(1)*	gal l [deg] *Col(2)*	gal b [deg] *Col(3)*	Ncyc no. *Col(4)*	rms [mJy] *Col(5)*	S/N_{peak} *Col(6)*	S/N_{ALFA} *Col(7)*	$v_{\rm HI}$ [km s^{-1}] *Col(8)*	w_{50} km s^{-1}] *Col(9)*	w_{20} [km s^{-1}] *Col(10)*	$F_{\rm HI}$ [Jy] *Col(11)*	$\log(M_{HI})$ [M$_\odot$] *Col(12)*
00265906+6049388	119.95	-1.90	84	1.9	3.8	5.4	7101±10	366	390	1.1±0.3	9.4
00553400+6551452	123.36	2.99	56	2.8	3.6	3.2	2035±8	339	357	1.0±0.5	8.3
02072277+5931285	132.43	-1.94	41	2.8	4.0	5.7	4520±21	174	230	1.3±0.4	9.1
02085980+7114029	129.15	9.30	20	4.8	4.1	3.9	2950±7	233	253	1.7±0.7	8.9
02153787+6139179	132.75	0.40	50	2.8	5.2	4.9	6527±4	406	419	1.6±0.5	9.5
02324853+6418145	133.65	3.56	60	2.8	4.3	5.5	4518±16	174	221	1.2±0.4	9.1
02421337+6723309	133.30	6.78	30	3.6	3.4	5.3	5974±23	371	423	2.2±0.7	9.6
04055619+5023102	151.53	-1.36	29	2.2	4.3	4.5	5739±38	150	261	0.7±0.3	9.1
04112872+5518091	148.82	2.83	28	2.8	3.7	2.3	4789±24	92	151	0.4±0.3	8.6
04363002+4426469	159.38	-1.92	13	4.5	4.8	3.9	4557±6	145	163	1.3±0.5	9.1
04412856+4622171	158.52	0.01	22	2.7	3.1	4.6	7279±21	198	242	1.0±0.4	9.4
04413675+4203562	161.77	-2.81	70	1.4	4.2	4.3	3799±4	442	454	0.8±0.3	8.7
04501168+4506057	160.48	0.34	39	2.0	3.8	4.9	4542±25	289	352	1.0±0.3	9.0
04524568+4501058	160.83	0.64	11	4.2	3.3	5.4	7482±5	459	470	2.9±0.8	9.9
04564373+4424037	161.75	0.80	13	3.3	3.5	2.8	4816±7	29	46	0.3±0.2	8.5
05004115+4238061	163.58	0.27	34	2.2	3.4	5.6	7085±34	357	435	1.4±0.4	9.5
05115105+3131317	173.80	-4.64	52	1.6	3.4	4.3	5753±21	106	155	0.4±0.2	8.8
05192943+3408562	172.59	-1.81	45	1.5	4.5	5.5	2087±8	249	272	0.8±0.2	8.2
05295184+3835341	170.09	2.41	60	1.4	3.6	4.9	7310±10	154	178	0.5±0.2	9.1
05332905+3110137	176.71	-1.03	39	1.6	4.0	5.2	7219±9	258	281	0.8±0.2	9.3
05395434+2656147	181.04	-2.12	65	1.5	3.7	5.3	2978±32	144	221	0.6±0.2	8.4
06133075+1604359	194.35	-0.84	31	1.6	3.3	4.8	5798±31	148	217	0.6±0.2	8.9
0658452+063640	207.87	4.63	49	1.6	3.2	4.3	6079±13	267	295	0.7±0.3	9.1
07573774-2540197	243.12	1.77	33	1.9	4.7	5.4	6991±14	69	113	0.5±0.2	9.1
07573774-2540197	243.12	1.77	33	1.9	4.4	5.4	6495±8	124	148	0.7±0.2	9.1
08142154-3819354	255.69	-2.04	38	3.7	5.6	5.7	2205±16	43	101	0.8±0.3	8.3
17184154-2750144	357.69	5.56	19	2.2	3.7	6.0	6230±25	326	388	1.4±0.4	9.4
18513759-0859297	24.94	-4.13	16	3.5	4.7	6.0	5502±8	67	92	1.0±0.3	9.2
19255928+2100385	55.47	2.22	14	3.9	4.8	5.7	7656±11	71	107	1.1±0.4	9.5
20194861+4046363	78.32	2.54	44	3.5	4.8	4.2	4305±5	360	377	1.7±0.6	9.2
20540993+4608346	86.35	0.81	30	2.9	4.8	5.4	4989±6	146	164	1.1±0.3	9.1
21055135+4957389	90.52	1.85	17	3.1	3.5	4.4	6139±6	178	192	1.1±0.4	9.3
21064324+4741525	88.94	0.22	20	2.9	4.2	4.9	3575±15	49	91	0.6±0.3	8.6

Table 3.2 – Continued

Name 2MASXJ *Col(1)*	gal l [deg] *Col(2)*	gal b [deg] *Col(3)*	Ncyc no. *Col(4)*	rms [mJy] *Col(5)*	S/N_{peak} *Col(6)*	S/N_{ALFA} *Col(7)*	$v_{\rm HI}$ [km s^{-1}] *Col(8)*	w_{50} km s^{-1}] *Col(9)*	w_{20} [km s^{-1}] *Col(10)*	$F_{\rm HI}$ [Jy] *Col(11)*	$\log(M_{HI})$ [M$_\odot$] *Col(12)*
21154360+4725180	89.77	-1.08	50	2.5	4.2	5.4	7799±8	269	291	1.4±0.4	9.6
21172770+4646547	89.52	-1.73	26	2.8	3.4	5.8	5436±25	185	240	1.3±0.4	9.3
21173015+4915194	91.29	-0.01	48	2.4	3.2	4.1	1874±23	405	454	1.2±0.5	8.3
22134060+6026059	104.63	3.29	43	2.7	5.1	8.0	7657±38	433	563	2.7±0.6	9.9
22143934+5902441	103.95	2.08	62	2.0	4.1	3.1	4370±6	245	262	0.6±0.3	8.7
22202196+5447486	102.25	-1.89	74	1.8	4.0	4.9	6664±7	397	415	1.0±0.3	9.3

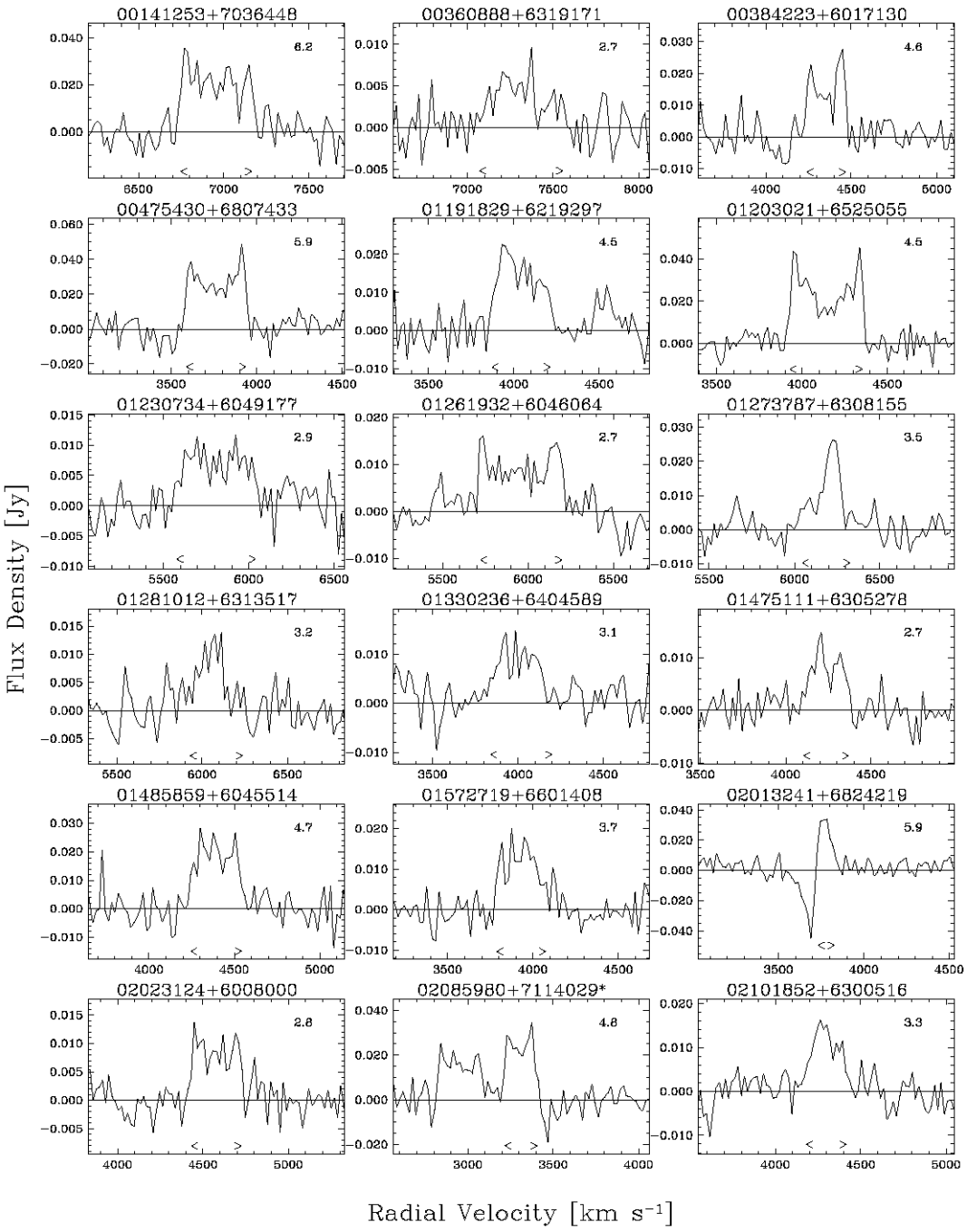

Figure 3.1: The baseline-subtracted HI line spectra of reliable detections in order of Right Ascension. Plotted is the HI flux density in Jy as function of heliocentric radial velocity (in the optical convention) in $\mathrm{km\,s^{-1}}$. The velocity resolution of the spectra is 18 $\mathrm{km\,s^{-1}}$. The two markers just above the velocity axis show the line width at 20% of the profile peak level. The labels at the top of each spectrum are the 2MASXJ galaxy equatorial coordinate identifiers in hhmmssss±ddmmssss. Spectra with more than one galaxy detection are marked by (*). The value in the top right corner of each plot gives the rms noise level (mJy).

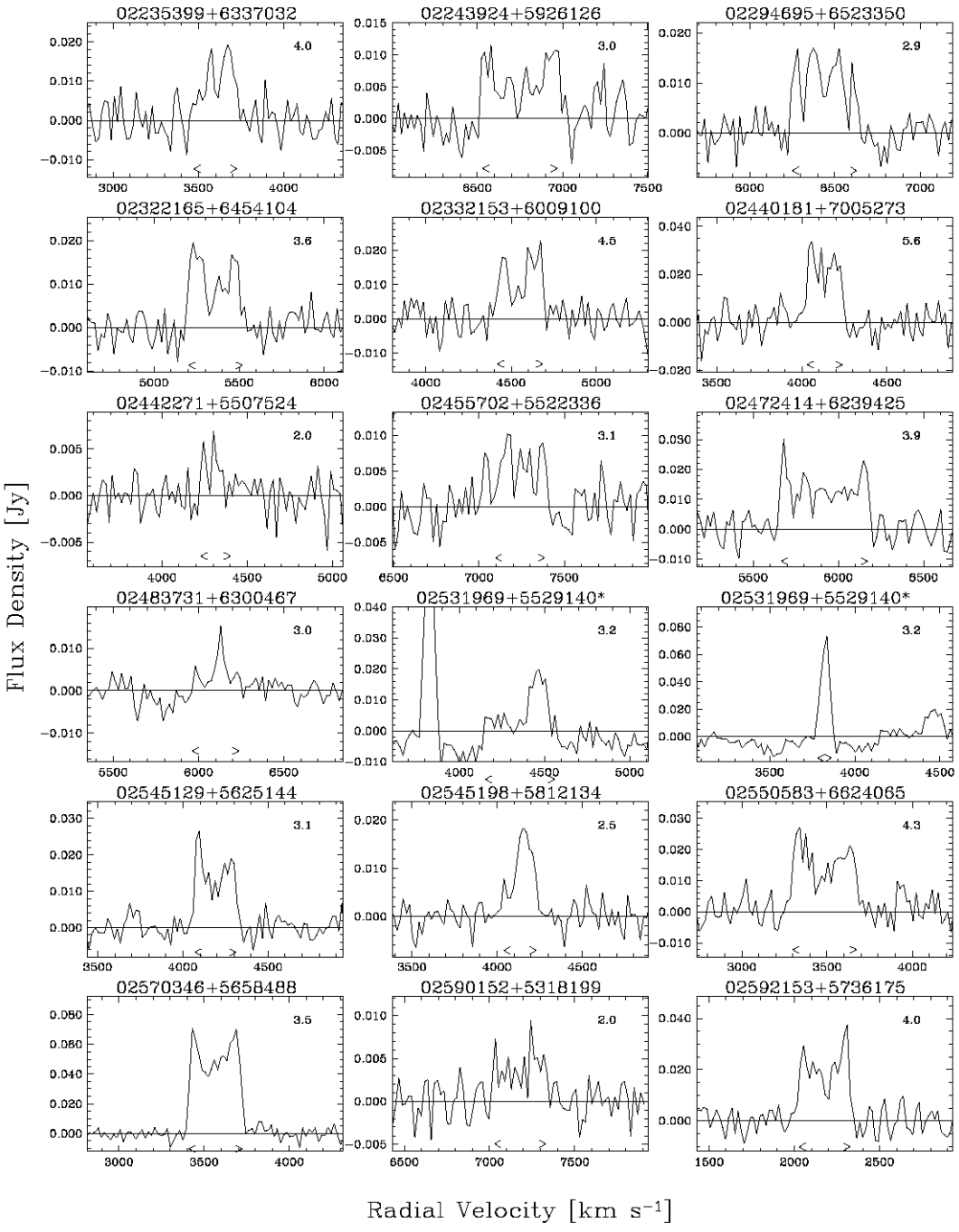

Figure 3.1: Continued

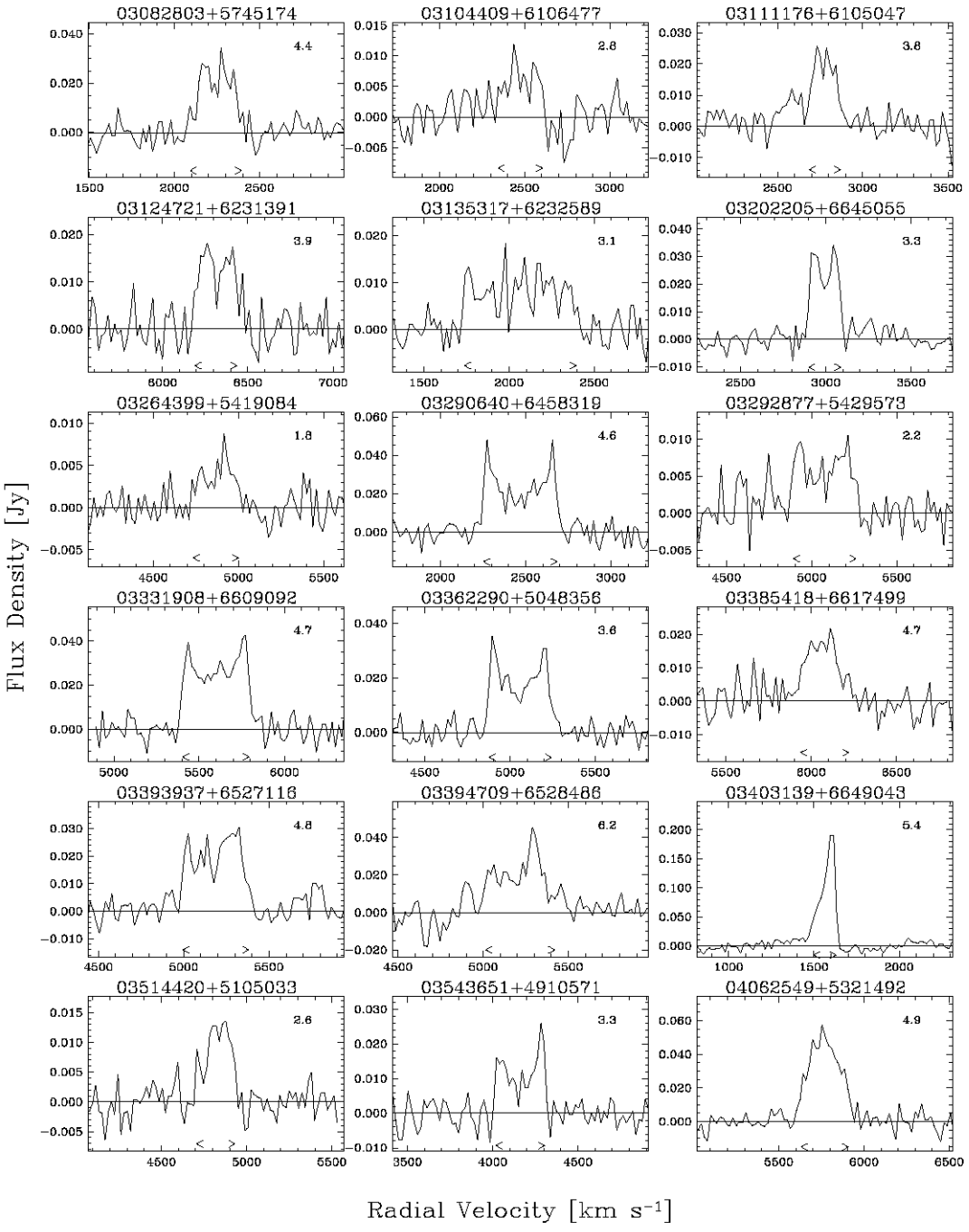

Figure 3.1: Continued

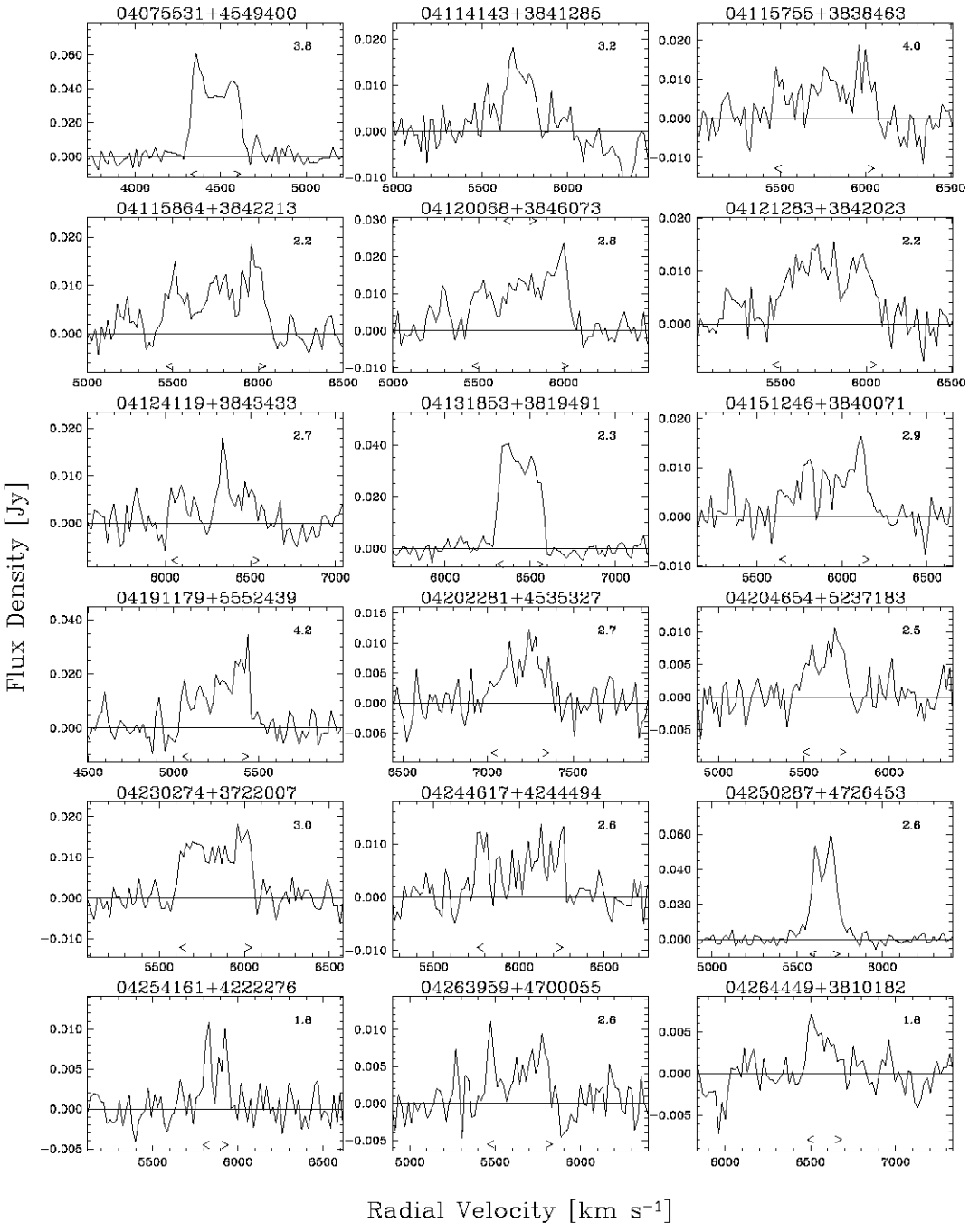

Figure 3.1: Continued

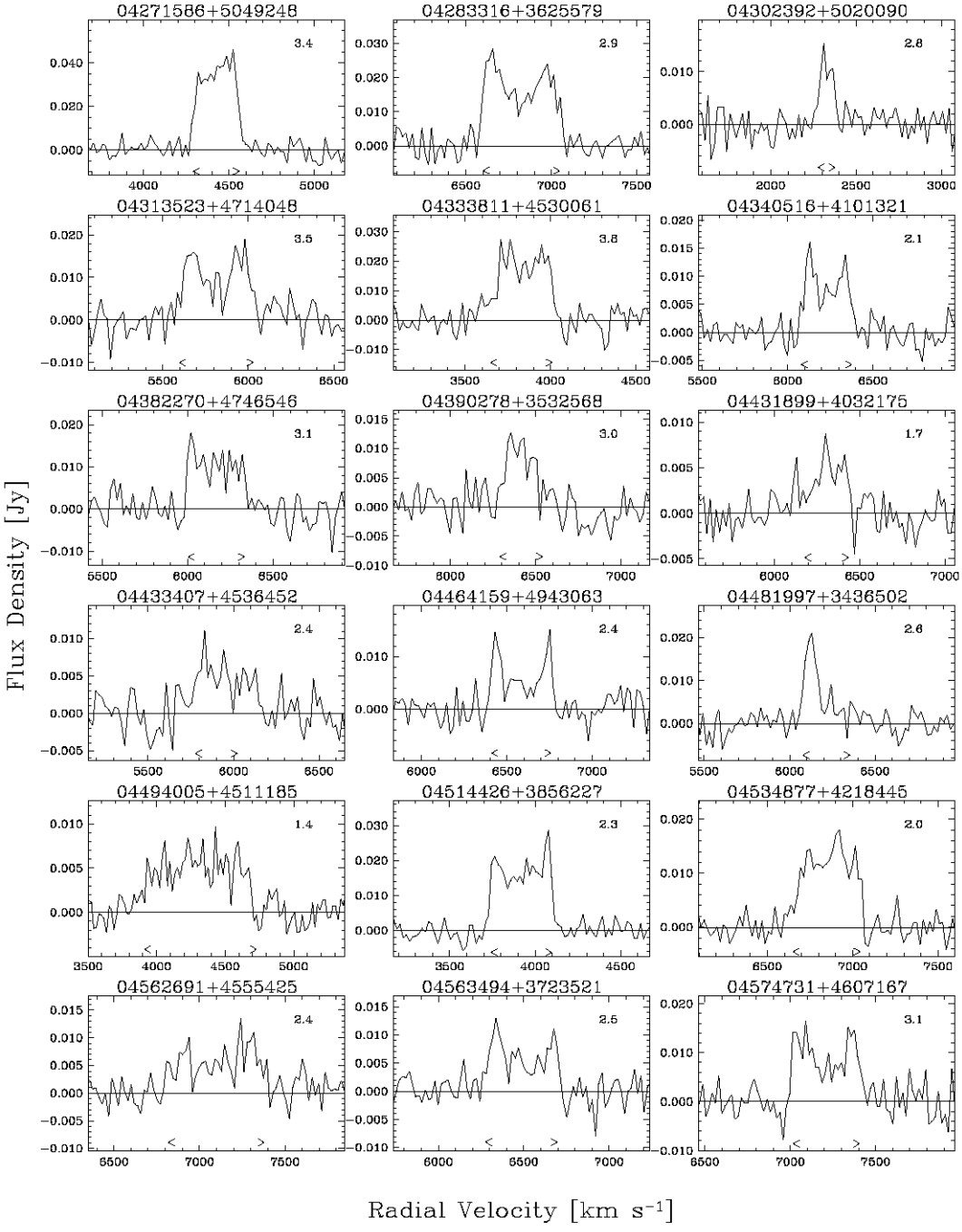

Figure 3.1: Continued

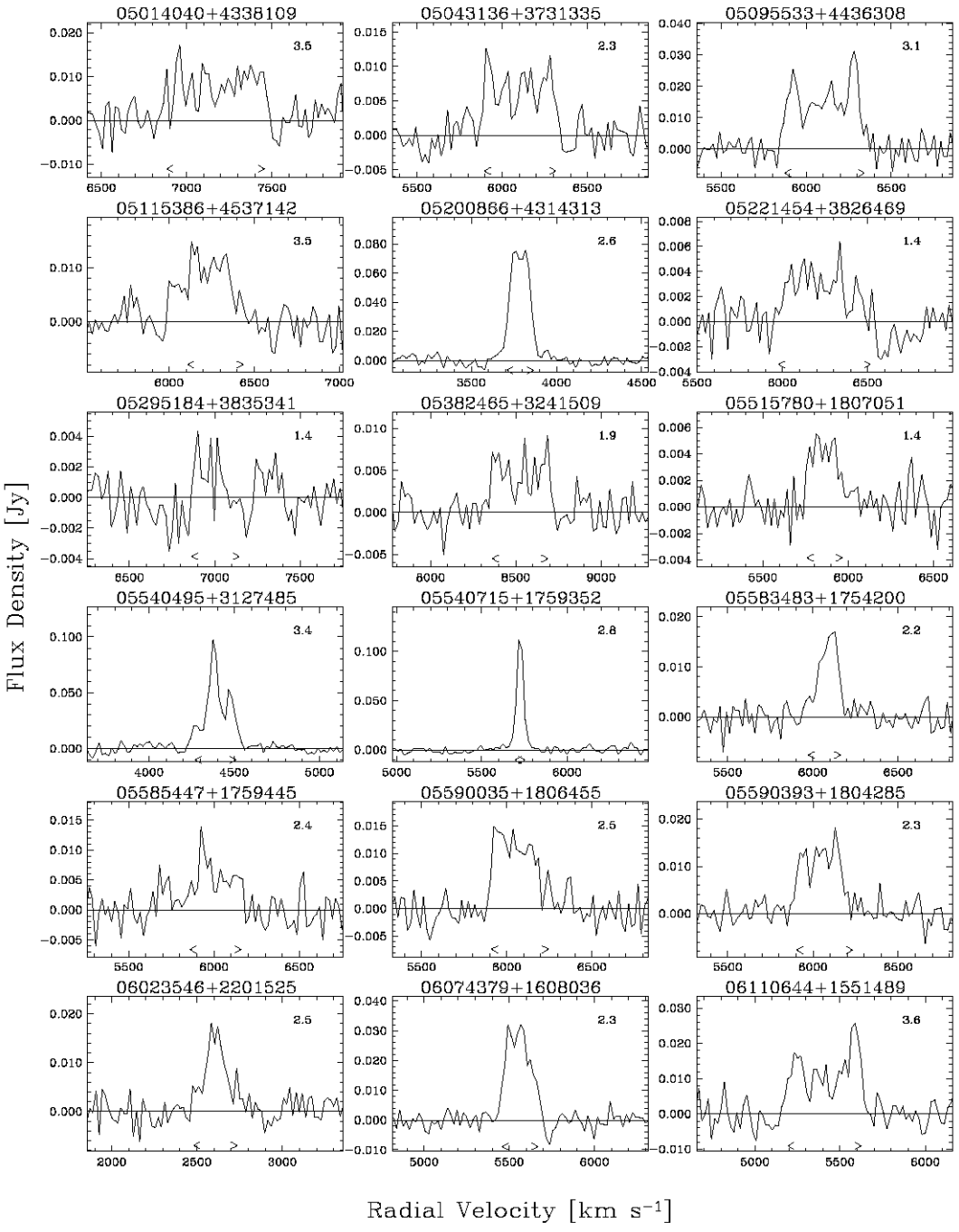

Figure 3.1: Continued

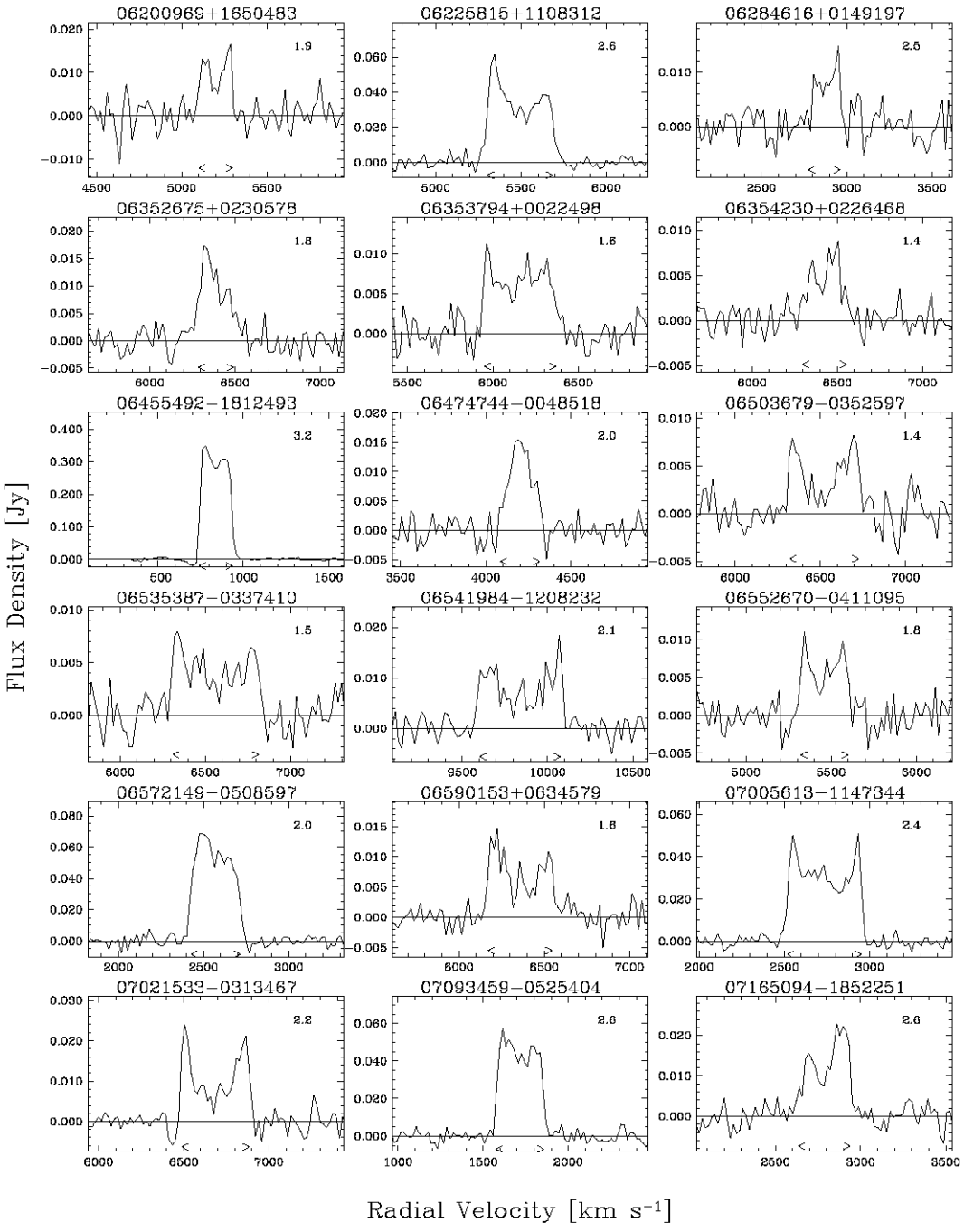

Figure 3.1: Continued

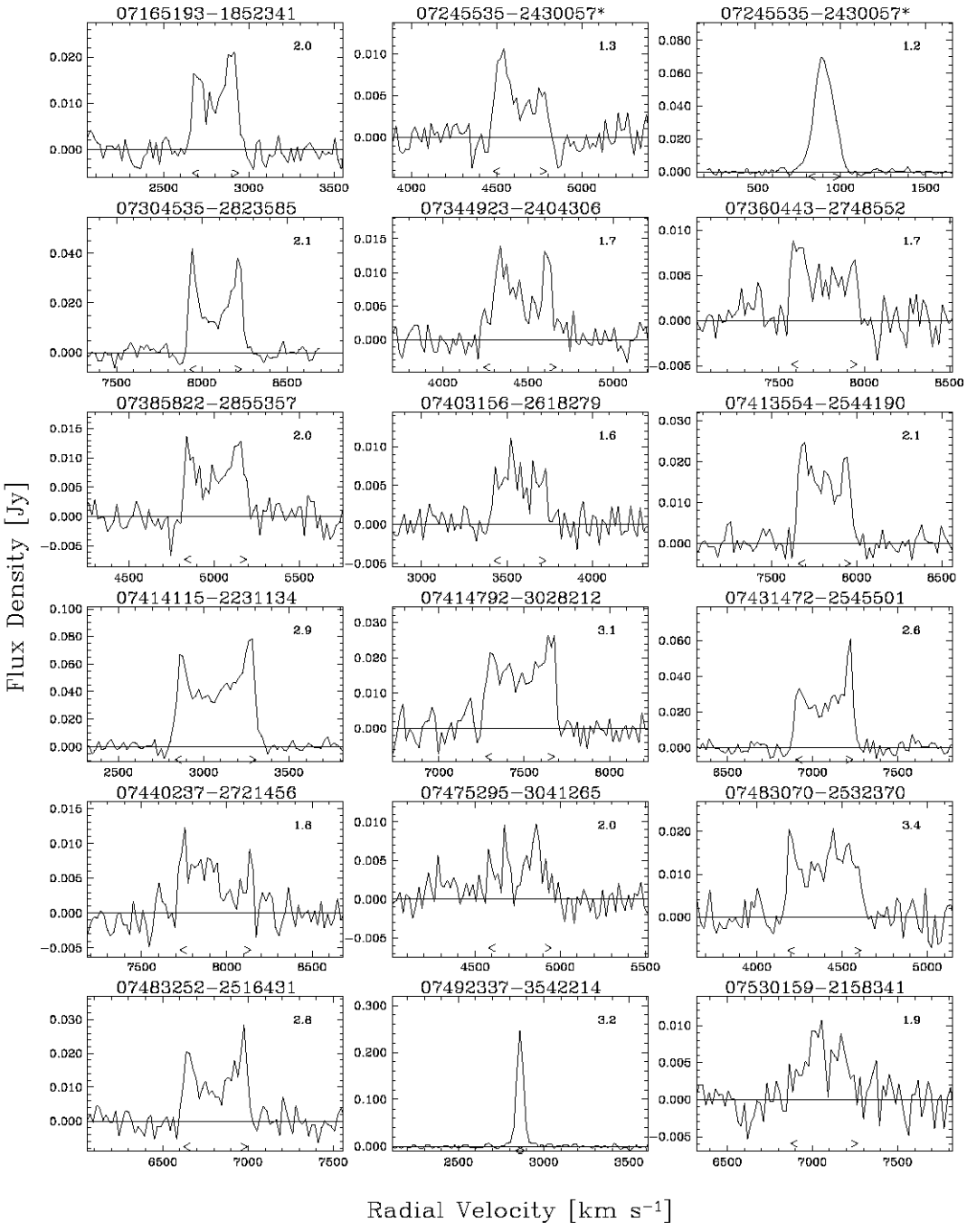

Figure 3.1: Continued

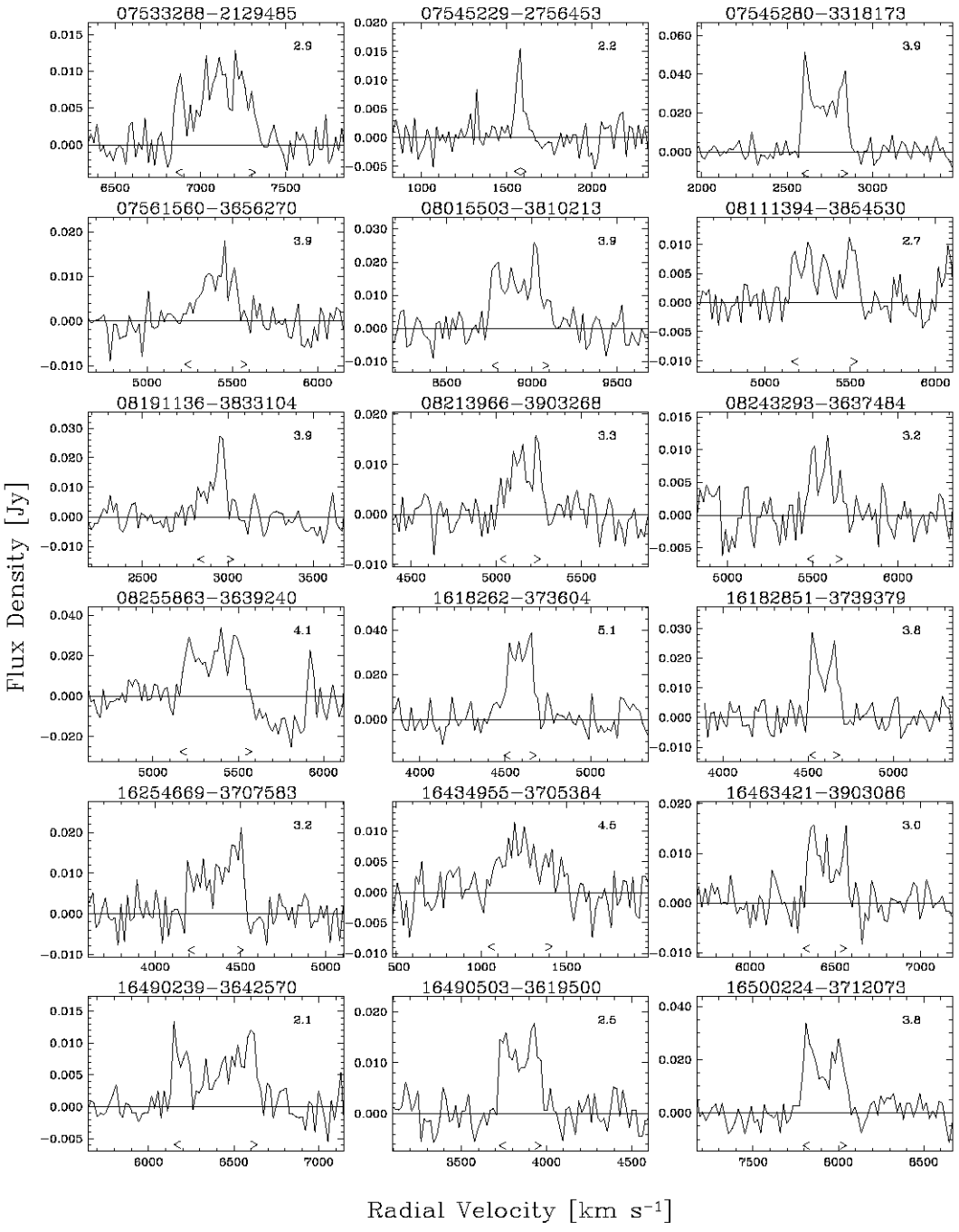

Figure 3.1: Continued

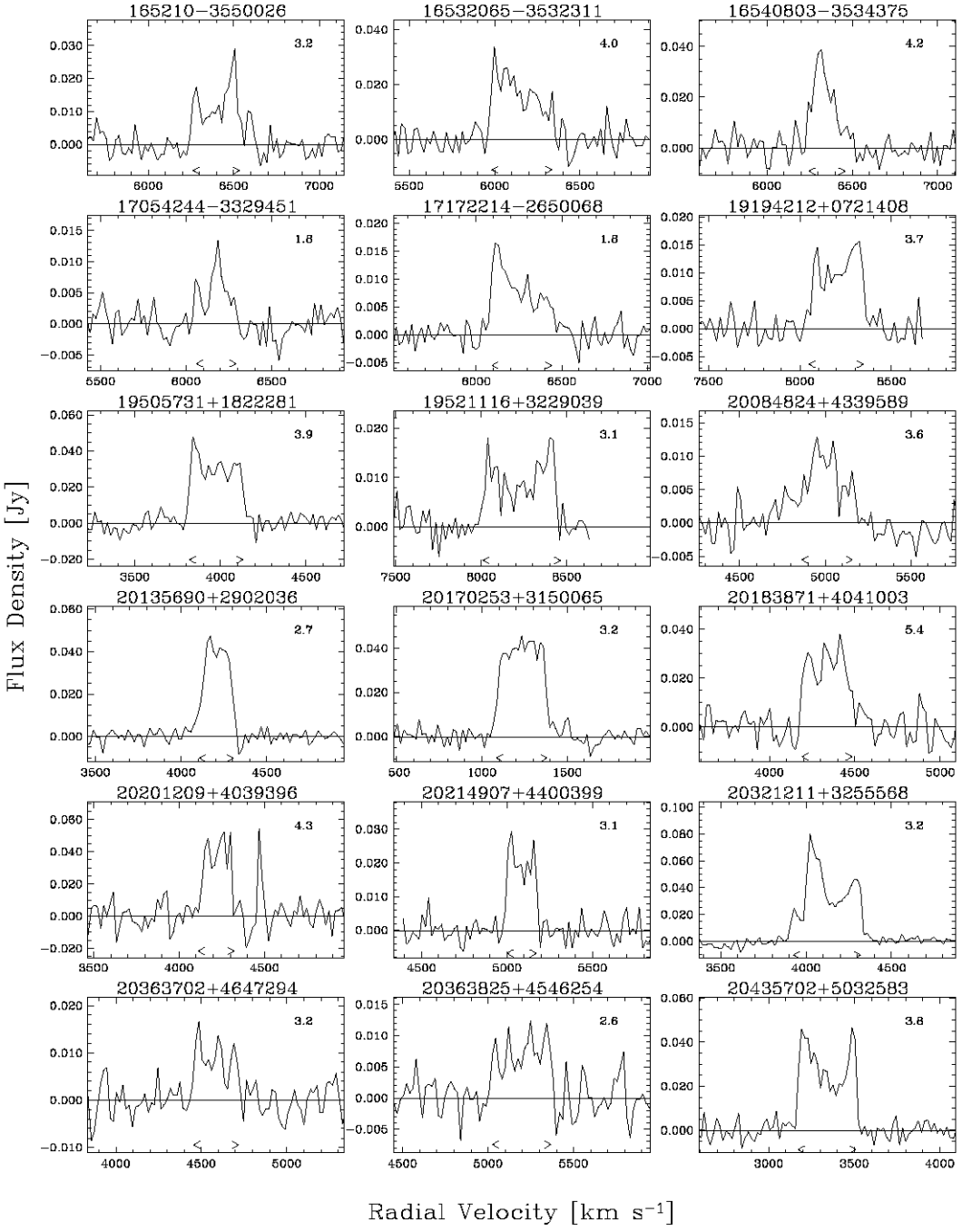

Figure 3.1: Continued

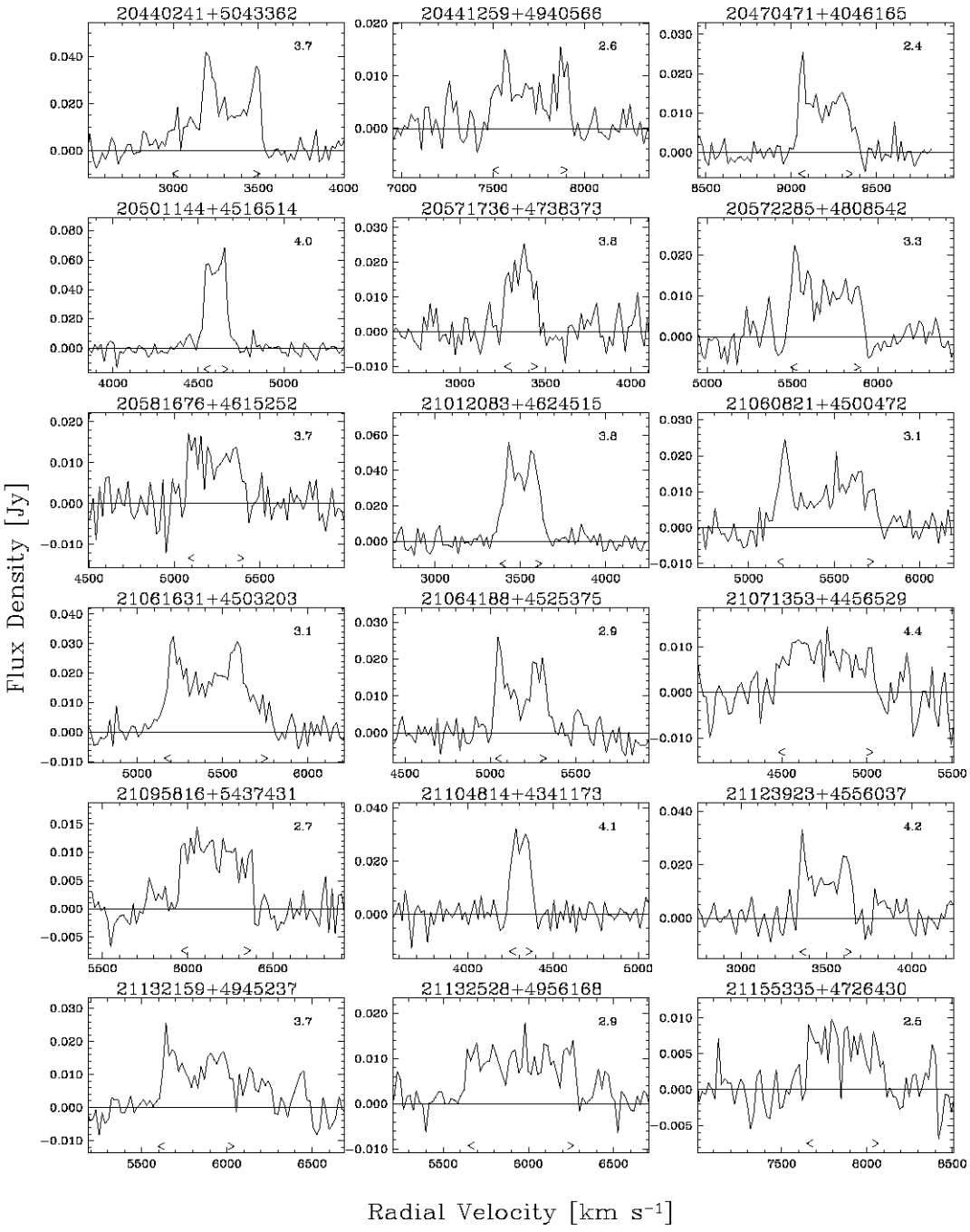

Figure 3.1: Continued

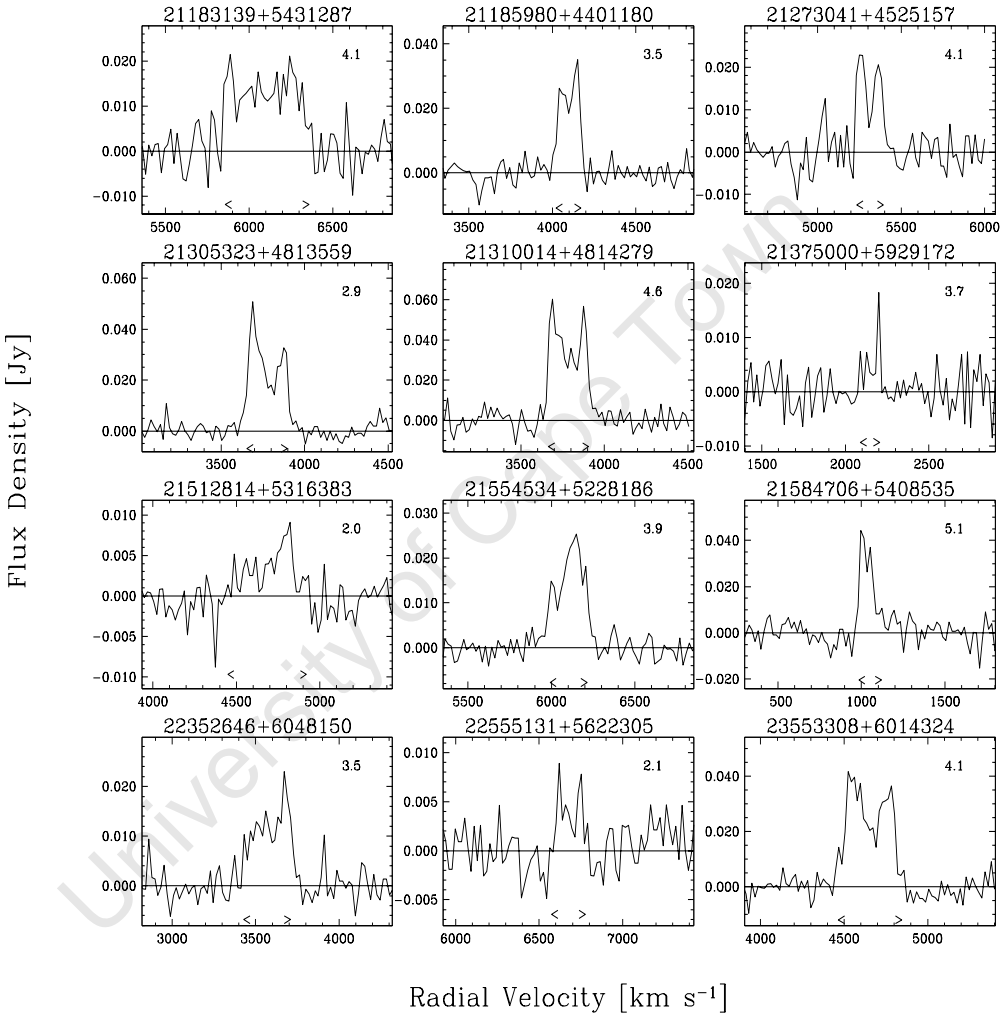

Figure 3.1: Continued

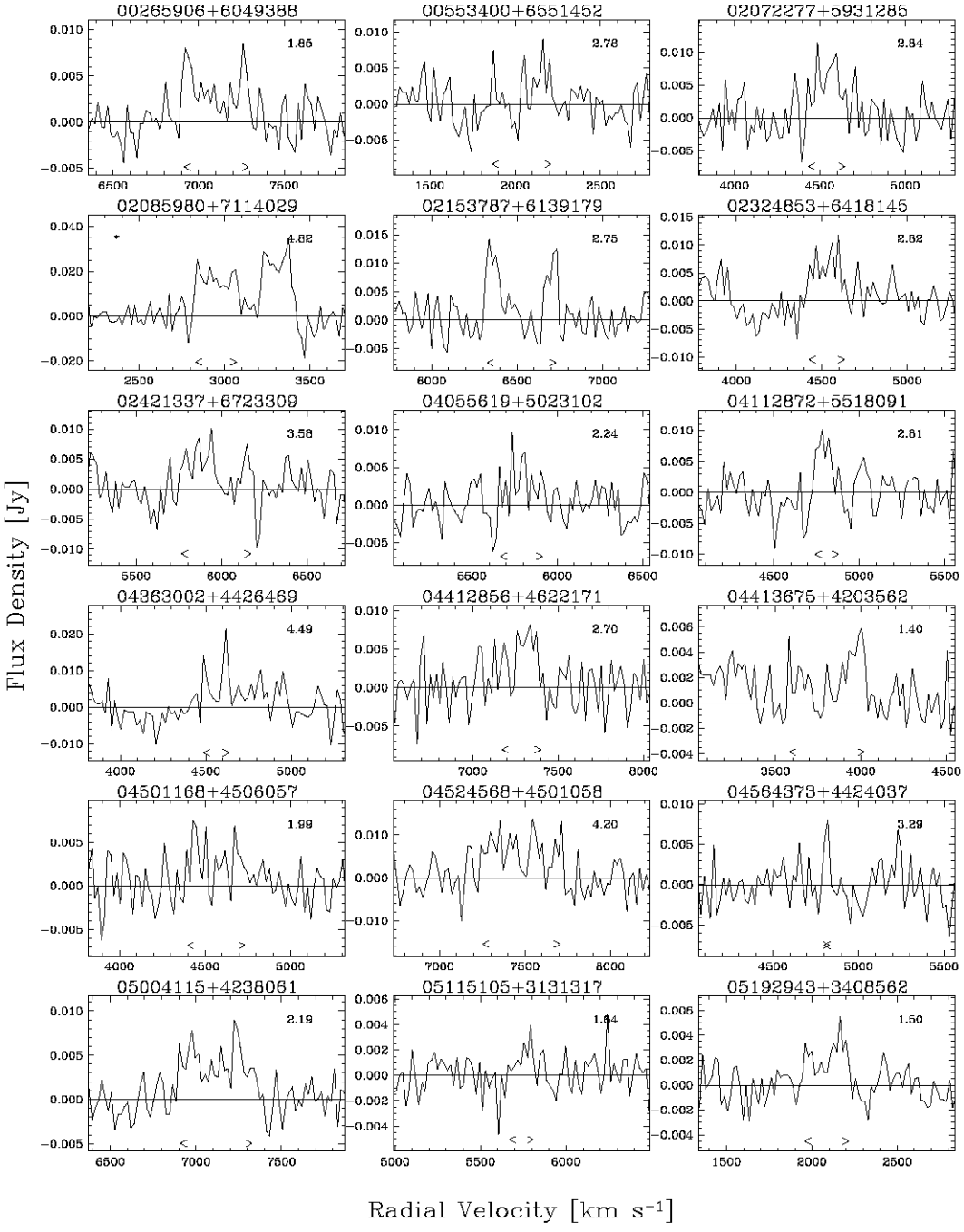

Figure 3.2: The HI profile spectra of marginal detections.

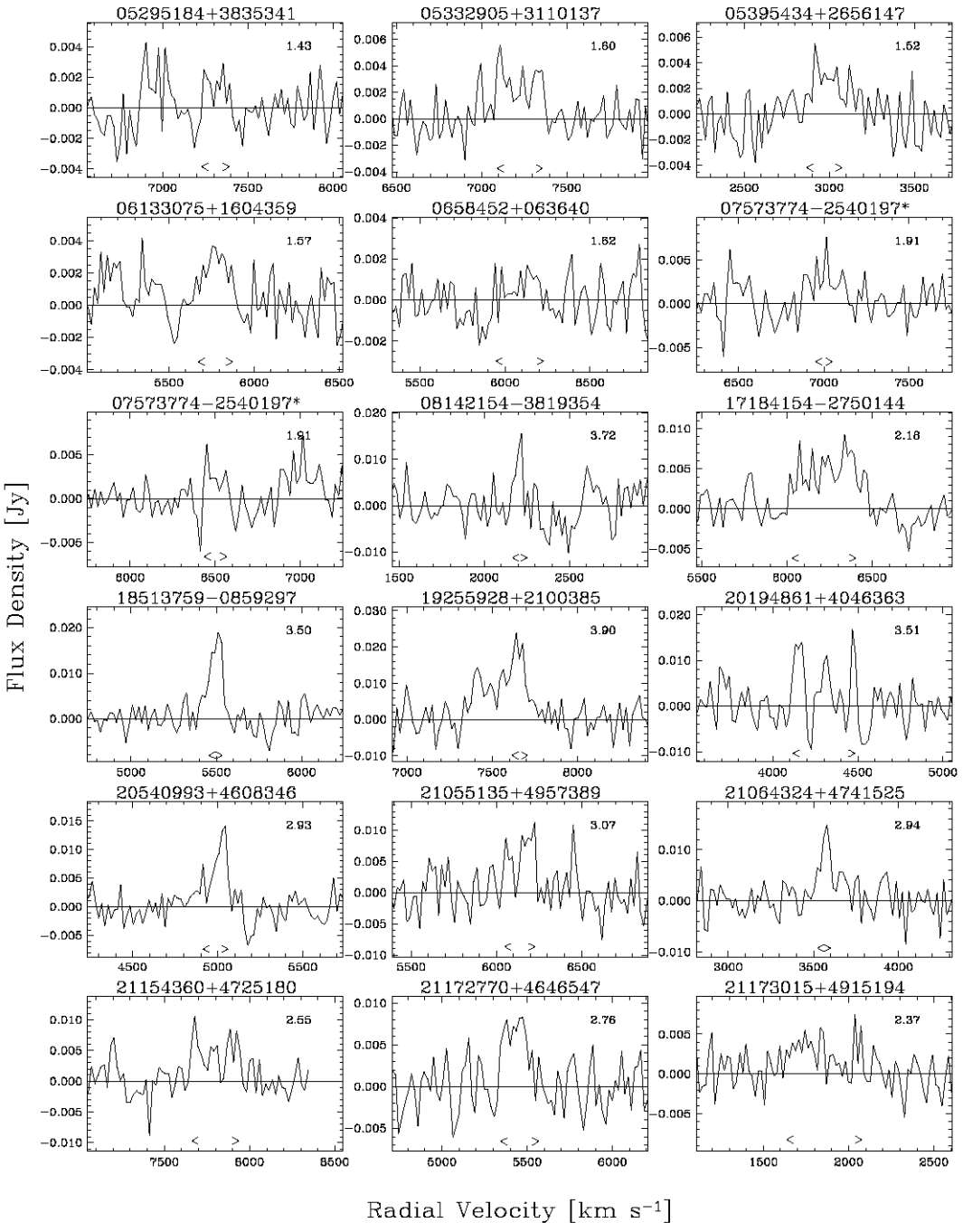

Figure 3.2: Continued

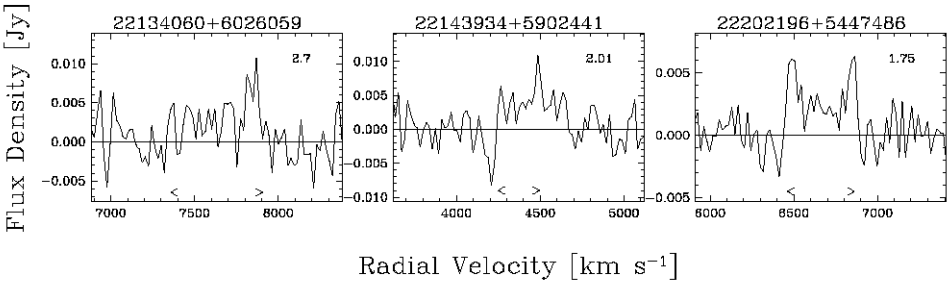

Figure 3.2: Continued

3.1.2 Additional Detections in the Telescope Beam

Some spectra revealed two HI galaxy line profiles in a single pointing. These multiple detections in a single pointing are not unexpected given the relatively large beam size of the NRT ($4' \times 22'$), which enhances the probability of detecting an additional galaxy within the beam, besides the target source. These spectra are marked by (*) in Figs. 3.1 and 3.2. Of the total target list, only five spectra (2%) had such "multiple" detections. Four of these are separated by less than 1000 $\mathrm{km\,s^{-1}}$ in radial velocity and one by more than 1000 $\mathrm{km\,s^{-1}}$. In all cases, the two profiles could be clearly distinguished in velocity and analysed separately in the data reduction procedure.

In Table 3.3 a list of these galaxies is presented. The first column gives the 2MASX names, the second and third columns their Galactic coordinates in degrees, the fourth column are their respective radial velocities in $\mathrm{km\,s^{-1}}$ and the last is $K-$band dust extinction.

Table 3.3: Target sources with two detections.

Name	gal l [deg]	gal b [deg]	v_{HI} [km s^{-1}]	A_{K_s} [mag]
1. 2MASXJ02085980+7114029	129.15	9.30	2921±3 3269±11	0.27
2. 2MASXJ02531969+5529140	139.66	-3.37	3776±29 4397±25	0.50
3. 2MASXJ05295184+3835341	170.09	2.41	6799±8 7136±4	0.50
4. 2MASXJ07245535-2430057	238.44	-4.08	903±102 4550±13	0.60
5. 2MASXJ07573774-2540197	243.12	1.77	6357±5 6832±5	0.10

To try and find the galaxies belonging to these "additional" signals, IR DSS2 images were examined (see Figs. 3.3). The NRT HPBW $\sim(4' \times 22')$ is marked by the green ellipse. In only one (3 in Table 3.3) of the five cases no other galaxy was found in the image, it could be because its background showed too much structure. The four galaxies with "additionals" are shown in Fig. 3.3 marked by a cyan cirle. The first case is identified as 2MASXJ02084091+7102087 (*top* panel of Fig. 3.3) at an optical velocity of 3380 ±11 $\mathrm{km\,s^{-1}}$ (Lavaux & Hudson 2011) with a K_s-band magnitude of $10\overset{\mathrm{m}}{.}94$. The second case is 2MASX J02531475+5528143 with a K_s-band magnitude of $10\overset{\mathrm{m}}{.}68$, and no previously known redshift. In the top panel of Fig. 3.3 (page over leaf) the other galaxy is identified as LDC 502 J072520.97-2428114 at $v = 800$ $\mathrm{km\,s^{-1}}$ (Crook et al. 2007). The last galaxy in the bottom panel was visually identified, however no further information on it was found.

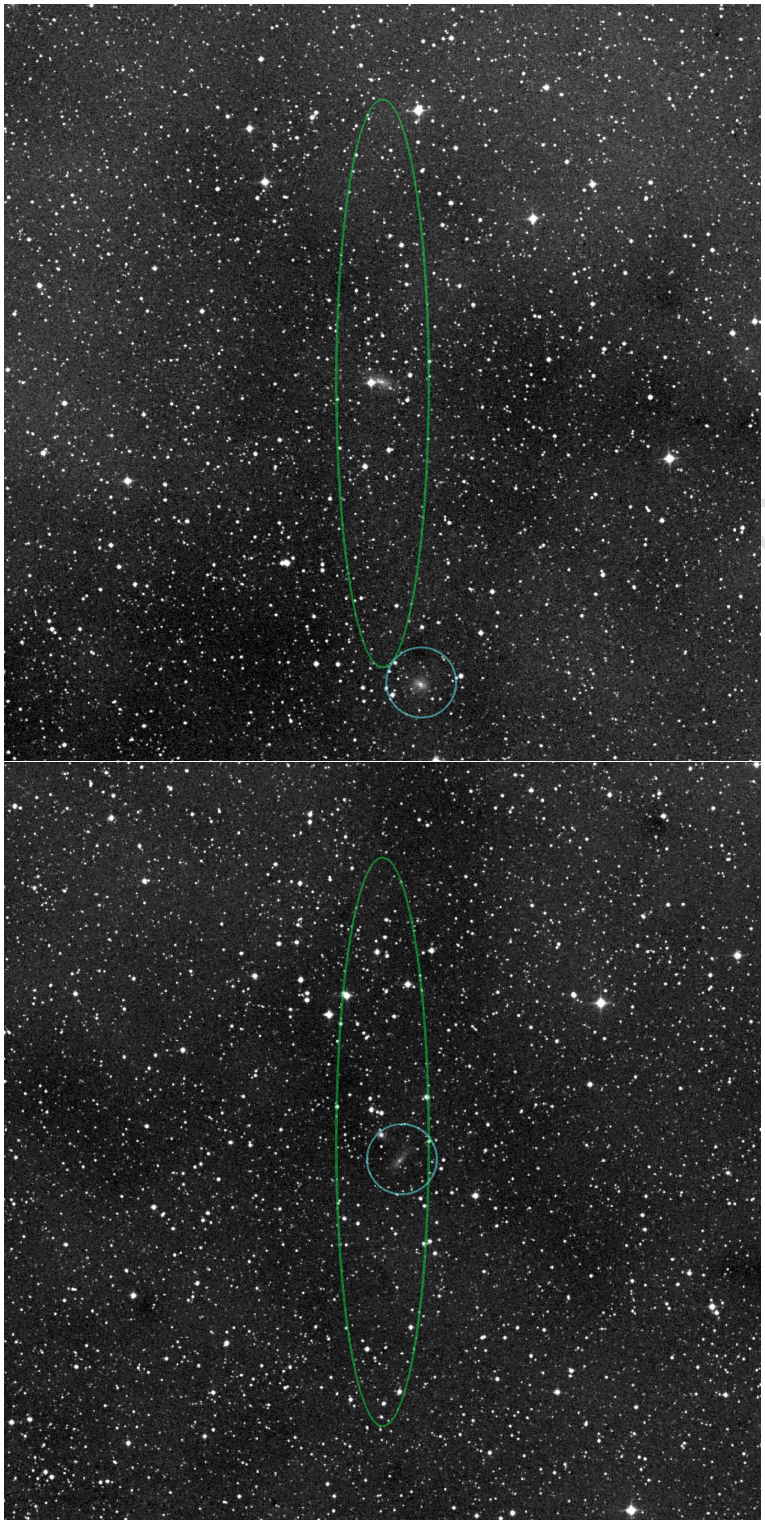

Figure 3.3: DSS images in the $IR-$band showing the 4 cases where two galaxies were identified in a single pointing. The green ellipse marks the NRT HPBW ($4' \times 22'$). Any extra galaxy found in the image is marked a cyan circle. Top image is centred on 2MASXJ02085980+7114029 and bottom on 2MASXJ02531969+5529140.

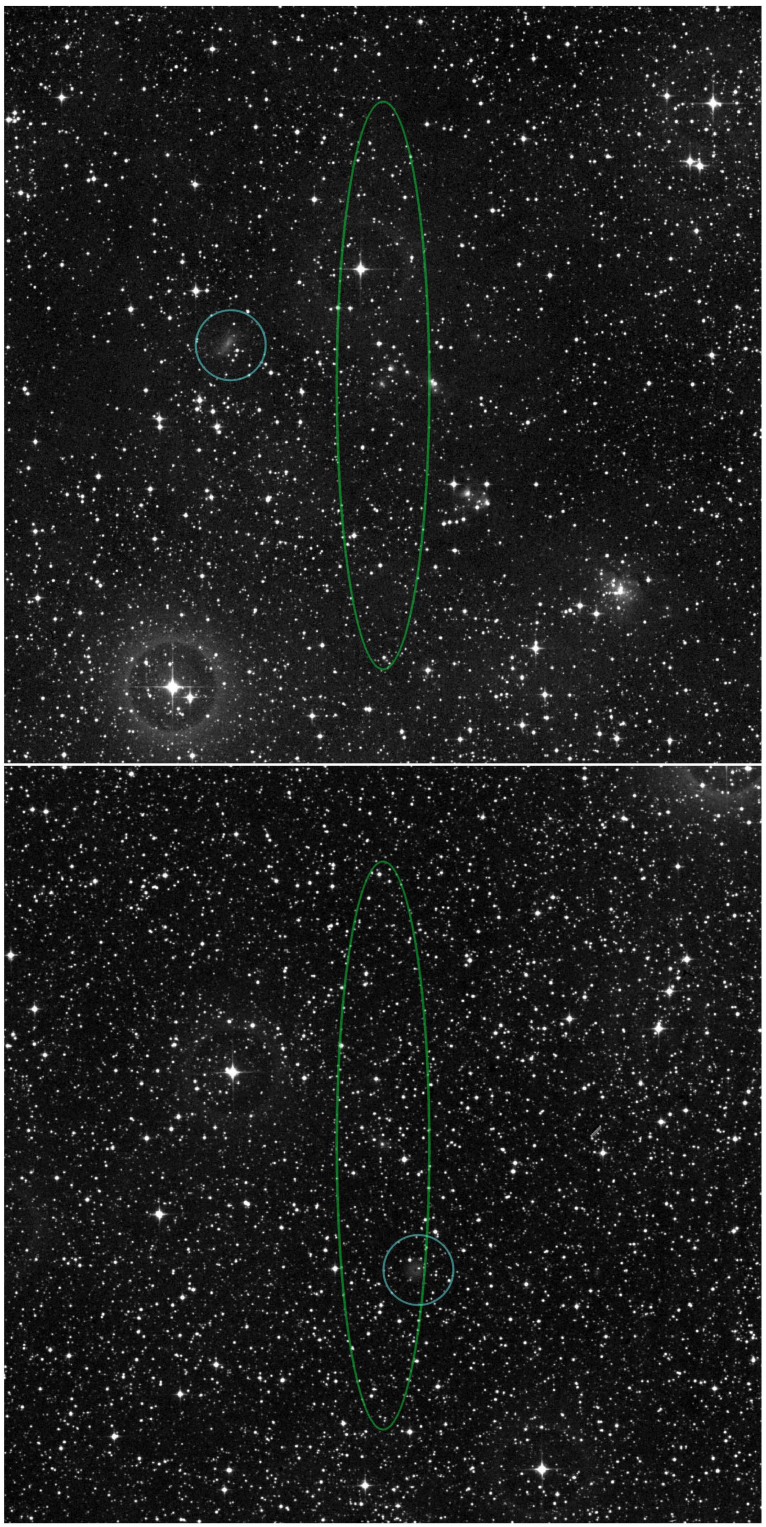

Fig. 3.3. continued. Top image is centred on 2MASXJ07245535-2430057 and the bottom one on 2MASXJ07573774-2540197.

3.1.3 Comparison of HI Parameters

A total of 10 galaxies among the NRT detections have been found to have published HI profiles in the literature. They were used for a comparison of HI line parameters. The galaxies are six from Paturel et al. (2003), three by Meyer et al. (2004) and one extracted from Springob et al. (2005). Galaxies from Paturel et al. (2003) were observed with the NRT. The three sources from Meyer et al. (2004) were observed with the Multi-Beam receiver on the Parkes 64 m radio telescope. The one galaxy from Springob et al. (2005) is a re-measurements of the Green Bank 300ft telescope.

Table. 3.4 lists the radial velocity $v_{\rm HI}$, the velocity linewidth (w_{50}) and the integrated flux ($F_{\rm HI}$) for the NRT data set (*top* row), and the literature data (*bottom* row). The parameters are compared in Fig. 3.4.

The compared v_{HI} and w_{50} are generally in good agreement with values in the literature. The deviations do not significantly exceed errors quoted in the literature and the scatter in both v_{HI} and w_{50} can be accounted for by internal errors of the different datasets. The single outlier in w_{50}, v_{HI} and F_{int} is 2MASX J05115386+4537142. It shows a large difference due to the complex nature of its spectrum. The low-velocity left component of the spectrum was included in linewidths and velocity determinations by Paturel et al. (2003) but excluded in this survey as likely noise (see Fig. 3.1). It is not known whether it is part of the galaxy or a satellite galaxy. Only improving the signal to noise ratio for this observation would clear up this confusion.

The regular observations of HI flux calibrator galaxies (see Sect.2.2.2) show that the NRT flux scale is correct, to within 10% or so, as are those of other telescopes.

The integrated fluxes indicate that the NRT measurements slightly underestimate the flux. This most likely is caused by the narrow beam of the telescope in the E-W direction ($4'$) which results in incomplete measurements of the flux in right ascension for very nearby extended galaxies. An example of this is 2MASX J07414115-2231134 which has an NIR diameter of $104\farcm8$. Allowing for the fact that HI diameters (of unobscured galaxies) are typically 2 – 3 times larger than NIR (e.g., Broeils & Rhee 1997), the difference of 16.3 mJy in F_{int} clearly indicates that the flux measurements of the NRT are slightly underestimated.

Table 3.4: Comparison of HI parameters

2MASS name	$v_{\rm HI}$	w_{50}	F_{int}	
	[km s^{-1}]	[km s^{-1}]	[Jy]	
Lit name	$v_{\rm HI}$	w_{50}	F_{int}	Ref
2MASX J21310014+4814279	3782±3	234±6	10.01±0.69	
IRAS21292+4801	3791±6	241±12	9.15±1.05	1
2MASX J04514426+3856227	3918±3	350±6	6.43±0.42	
IRAS04483+3851	3913±6	356±13	7.15±0.96	1
2MASX J05115386+4537142	6239±46	232	3.37 ±0.45	
IRAS05082+4533	6195±14	357±27	2.94±0.84	1
2MASX J07093459-0525404	1705±2	265±4	12.50±0.42	
SAIT 575- 1	1716±4	278±8	18.03±1.18	1
2MASX J01191829+6219297	4041±5	294±10	4.73±0.79	
IRAS01159+6203	4050±7	306±14	7.10±1.55	1
2MASX J04075531+4549400	4470±3	276±6	11.90±0.62	1
IRAS04043+4541	4470±6	278±12	11.52±1.39	
2MASX J07005613-1147344	2736±2	424±4	14.40±0.48	
J0701-11	2744	419	22.50	2
2MASX J07414115-2231134	3074±2	449±4	22.40±0.59	
J0741-22b	3074	460	38.70	2
2MASX J19505731+1822281	3973±4	296±8	9.82±0.66	
J1950+18b	3979	311	17.60	2
2MASX J05014040+4338109	7167±10	556±20	4.84±0.79	
Wein 91	7160	530	3.47	3

References: [1] Paturel et al. 2003, [2] Meyer et al. 2004, [3] Springob et al. 2005

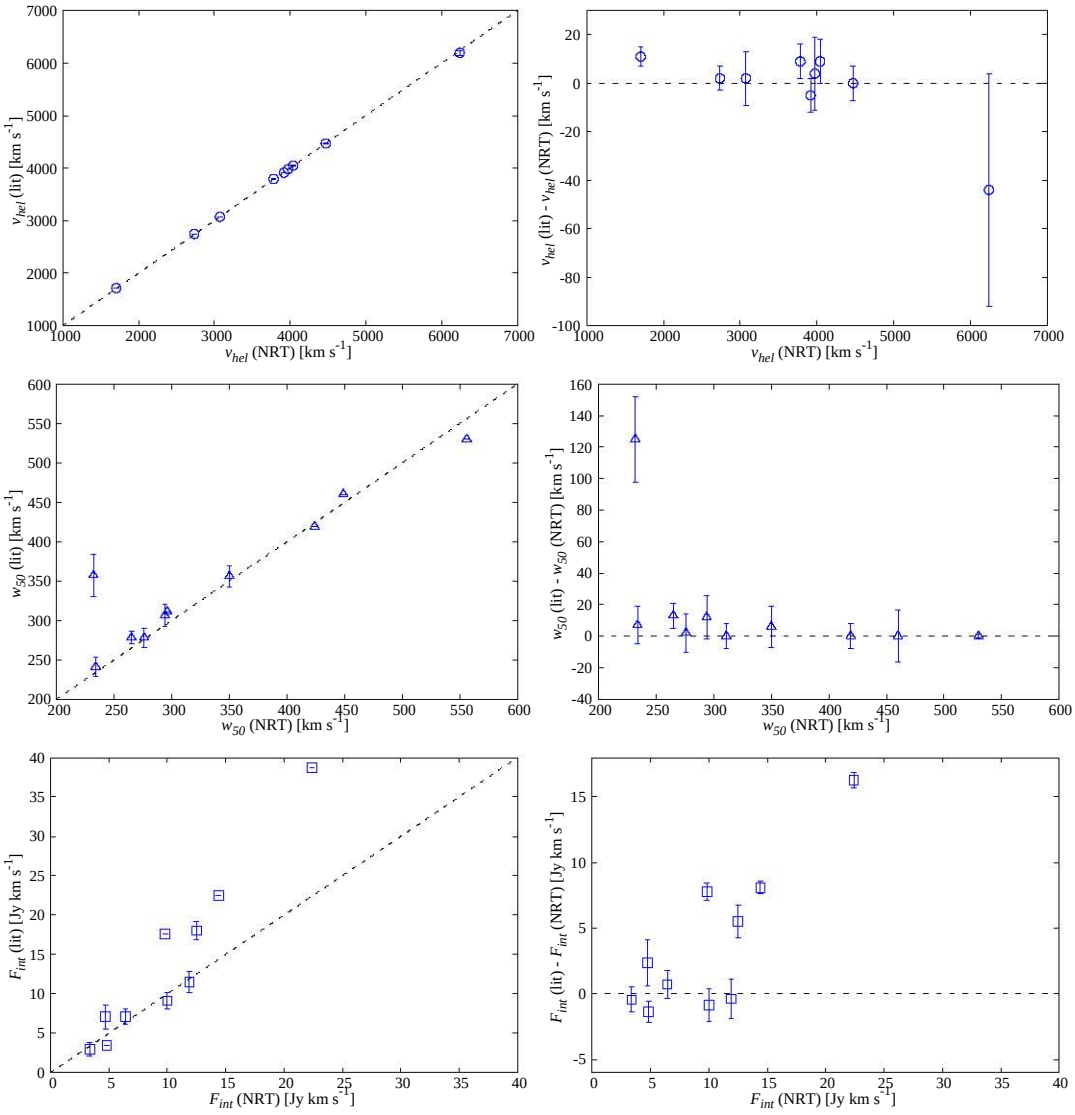

(a) (b)

Figure 3.4: Comparison of radial velocities $v_{\rm HI}$ in $\mathrm{km\,s^{-1}}$ (*top* panel), w_{50} in $\mathrm{km\,s^{-1}}$ (*middle* panel) and integrated flux, F_{int} in Jy (*bottom* panel). Left panel, literature values versus NRT values. The dashed line indicates equality. Right panel, difference between literature values and NRT values as a function NRT velocity.

3.1.4 Characteristics of Non-detections

A total of 679 observed galaxy candidates did not have a recognisable galactic HI signal in their spectrum. These are classified as non-detections and listed in Appendix A. Their rms noise distribution is shown in Fig. 3.5. In this plot the mean rms (2.86 ± 0.83 mJy) is marked by a vertical dashed line. Of all the non-detections, 83% (565) were observed until the target rms of 3.3 mJy was reached, or surpassed, but 17% (113) still had rms > 3.3 mJy. The latter galaxies were scheduled for further re-observations, which is currently ongoing.

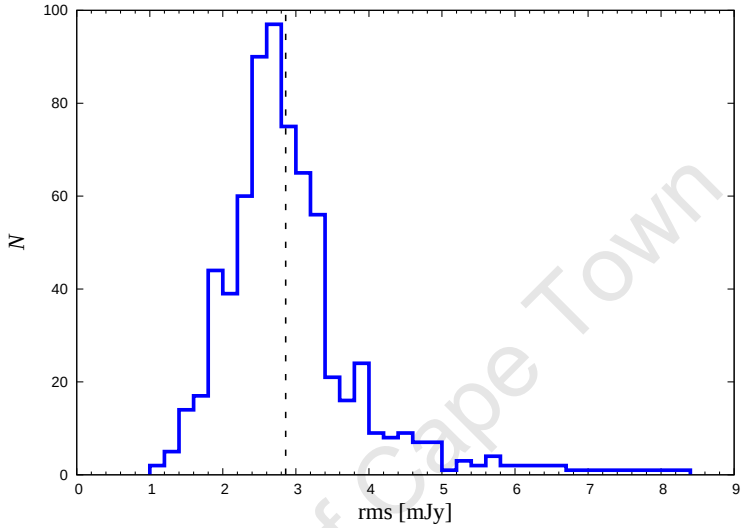

Figure 3.5: The rms noise level distribution of non-detection. The vertical dashed line marks the average value of 2.86 mJy.

3.1.5 Detection Rates

In this section a discussion of the detection rate is presented. When analysing the detection rates, it should be noted that the galaxy sample is NIR selected, hence will not be sensitive to the blue star forming dwarf galaxies, in particular LSBs. A distribution of the detected galaxies as well as detection rates as a function of Galactic latitude, stellar densities and dust extinction is displayed in Fig. 3.6. (In the *left* panel, the blue dashed histograms represents all galaxies that were observed and red are the detections. The variation of the detection rate with b is shown in the *top right* panel. The plot confirm a detection rate that is independent of b, i.e., observations at the 21 cm wavelength penetrate the ZoA without any dependence on the Galactic latitude.

A distribution of detections and non-detections as a function of stellar densities is shown in Fig. 3.7 where observed galaxies are represented by grey open circles and detected galaxies by blue filled circles. Contours overlaid are of stellar densities of log $N(SD_{Ks<14.0}) = 3.60$, 4.00, 4.40 and 4.80 shown in green, yellow, orange and brown respectively. As expected there seems to be no dependence of detection rates on stellar crowding because it does not

affect the HI emission. The few detections seen at high stellar densities are not an effect of the detection efficiency but rather of stellar crowding the NIR source selection. This is confirmed with the *middle* panel in Fig. 3.6 which shows a histograms of the number of observed and detected galaxies and the detection rates as a function of stellar densities. The distribution of the detection rates is flat around 27% hence confirming what is seen in Fig. 3.7. The mean stellar density around detected galaxies is $\log N = \langle 3.82 \rangle$ with a scatter of $\sigma = 0.27$.

To confirm that HI detection rates are not affected by the foreground extinction as expected the *bottom* panel of Fig. 3.6 is plotted. It shows the distribution of observed and detected galaxies as well as the detection rate as a function of K_s-band foreground extinction (A_{ks}) respectively. The plot also shows a flat distribution around this survey's detection rate of 27%, also proving that detections are not affected by foreground extinction. Most ($> 98.9\%$) detected galaxies have $A_{ks} < 0\overset{\text{m}}{.}7$ (black dashed line).

.

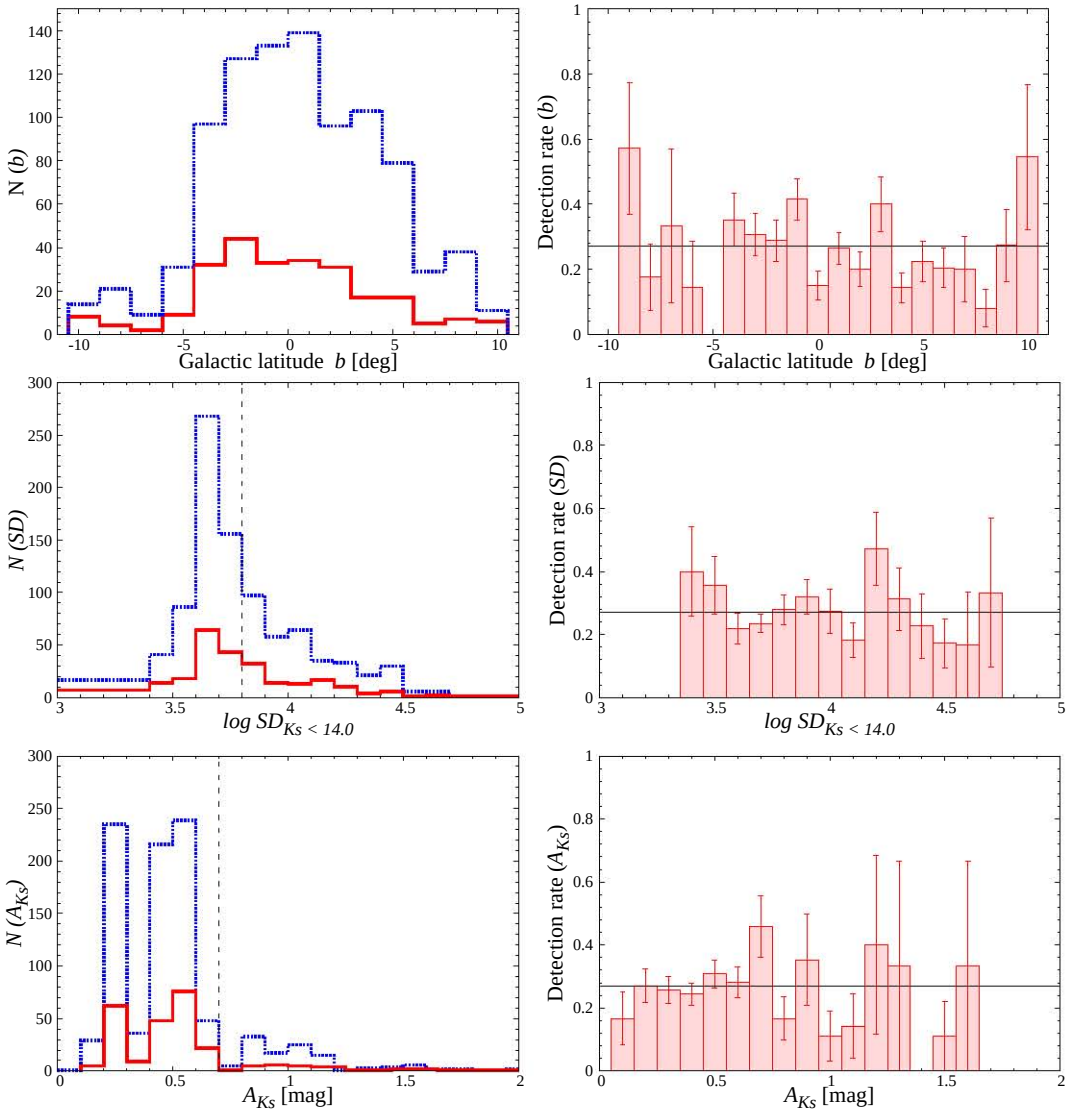

Figure 3.6: The distribution of galaxies detected (left panel) and detection rate (right panel) as a function of the Galactic latitude,b (*top* panel), stellar density, SD (*middle* panel) and foreground extinction, A_{Ks}, (*bottom* panel). The black dashed line (*middle left* panel) marks the average stellar density. In the *bottom left* panel the dashed line marks detected galaxies ($> 98.9\%$) with $A_{ks} < 0\overset{\text{m}}{.}7$. The solid horizontal line (right panel) marks the 27% total detection rate.

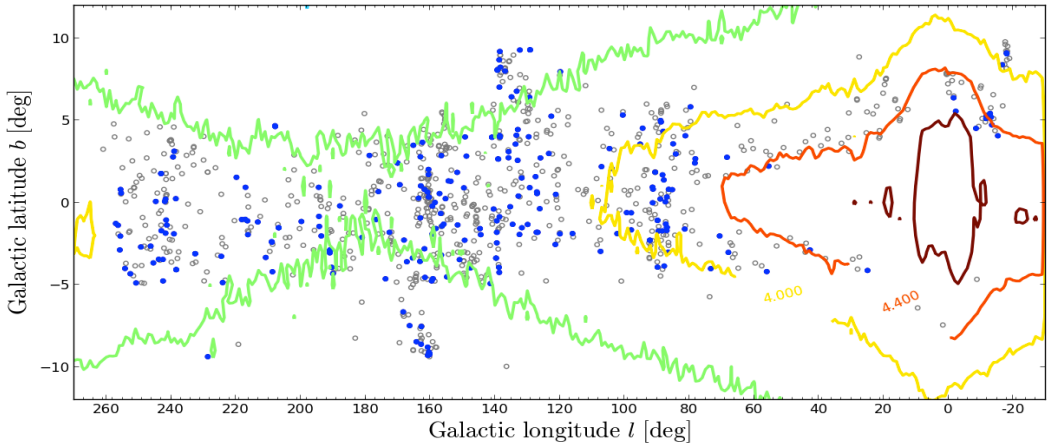

Figure 3.7: The spatial distribution of detected and observed galaxies, with Galactic stellar density contours superimposed. The grey open circles show the observed galaxies and detected galaxies are indicated by blue filled circles. The 2MASX stellar density contours of log $N(SD_{Ks<14.0}) = 3.60$, 4.00, 4.40 and 4.80 (green, yellow, orange and brown lines) are overlaid.

3.2 HI Mass Distribution

In this section the HI mass distribution of the detected galaxies is discussed. Figure 3.8 shows the HI mass of the detected galaxies as a function of recessional velocity. The HI masses were calculated using Equation 3.1. The dotted lines superimposed indicate the 3σ HI mass detection limits of the NRT survey (1.2 and 3.8) $\times 10^8$ $M_\odot$, for the target rms level of 3.3 mJy and assuming two typical linewidths, i.e., a w_{50} of 100 $\mathrm{km\,s^{-1}}$ and 250 $\mathrm{km\,s^{-1}}$, respectively. As a comparison, the characteristic HI mass, $M^*_{HI} = 6.5 \times 10^9$ $M_\odot$, as derived by Zwaan et al. (2005) from fitting a Schecter function to the HIPASS data is indicated by a black horizontal line.

Most of the detected galaxies are found at the Perseus-Pisces Supercluster velocity of $cz \approx 6000$ km s^{-1}. At this distance the typical HI mass ranges between log $M_{\mathrm{HI}} = 9$ to 10.5 $M_\odot$. For velocities greater than 8000 $\mathrm{km\,s^{-1}}$ the survey is only sensitive to the most massive galaxies (see *bottom* panel of Fig. 3.8). The increased RFI and the fact that HI observations are not sensitive to all galaxy types limits detections for galaxies at $v > 8500\,\mathrm{km\,s^{-1}}$.

The lowest HI mass detected is 7.0 $\times$ $10^7 M_\odot$ and the highest 2.30 $\times$ 10^{10} $M_\odot$ (see Fig. 3.9). The low mass galaxy is 2MASXJ07545229-2756453. It is a dwarf galaxy located deep within the Galactic Plane at $(\ell, b) \approx (244.7°, 0.06°)$ with a radial velocity of $1572\,\mathrm{km\,s^{-1}}$, making it a possible new member of the Puppis filament. The most massive galaxy in the sample is 2MASXJ00141253+7036448. It is an inclined spiral which lies at $(\ell, b) \approx (119.8°, 7.9°)$ at a velocity of $6958\,\mathrm{km\,s^{-1}}$.

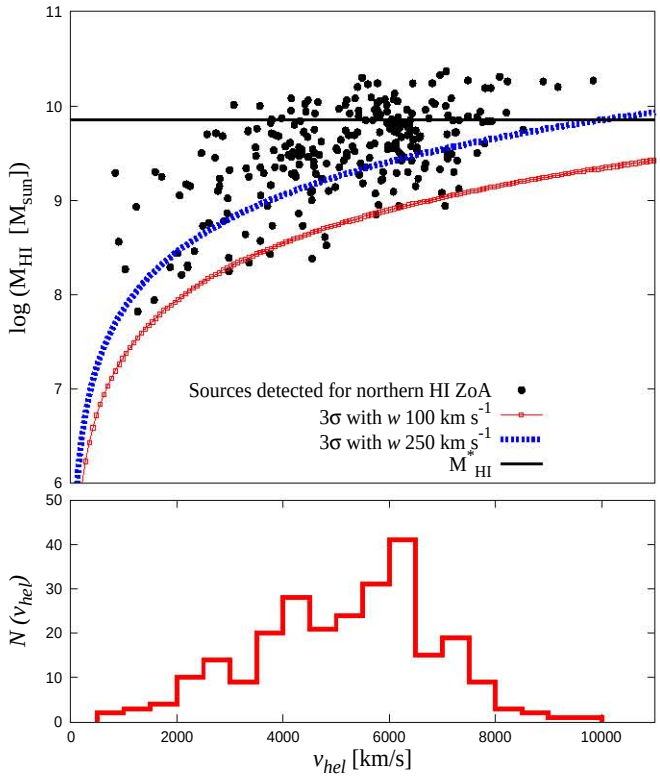

Figure 3.8: The top panel: Total HI masses of the NRT detections as function of radial velocity. The red and the blue line indicate 3σ upper limits of our survey to the HI mass as a function of recessional velocity, for line widths of 100 km s^{-1} and 250 km s^{-1}, respectively. The solid horizontal line is $M^*_{HI} = 6.5 \times 10^9$ M$_\odot$ (Zwaan et al. 2005). The bottom panel, a histogram of the number of detected galaxies as function of radial velocity.

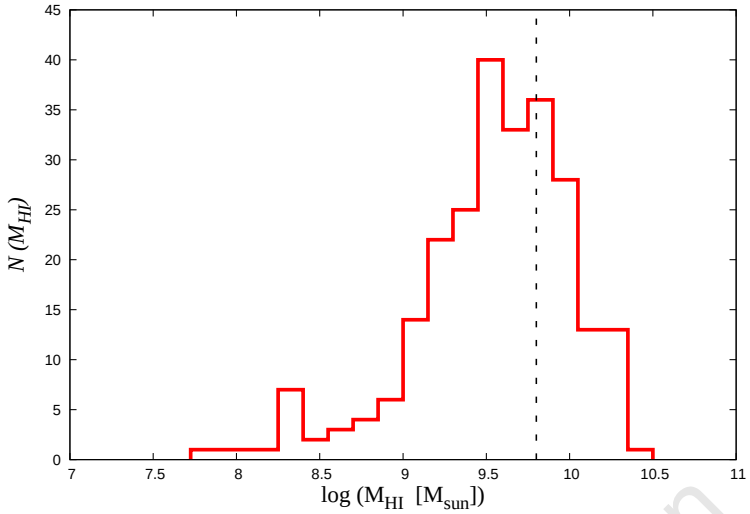

Figure 3.9: Histogram of the distribution of HI masses of the detected galaxies for this survey. The mean HI mass of 3.2×10^9 $M_\odot$ is marked by the black dashed line.

3.3 Summary

An overview of this chapter is as follows:

From a total of 2546 (plus 42) identified galaxies from 2MASX, about 1000 without redshift information were selected for observations. Of these, 928 were observed from July 2009 and 31 March 2012.

A catalogue and spectra of 210 reliable and 39 marginal NRT HI detections is presented. The detection rate is 27%. This is good considering that galaxies were not pre-selected by their morphology. The detection rate is independent of Galactic latitude hence showing that detections are not affected by dust extinction and stellar crowding.

The velocity detection distribution shows a good coverage for $v < 8000$ km s^{-1} in redshift space. This limit is due to the telescope sensitivity and strong RFI above 8000 km s^{-1}.

Chapter 4

Large-Scale Structures

In this chapter results of the survey are used to describe and characterise the three-dimensional distribution of the large-scale structures (LSS) revealed by the NRT HI data. The first section of this chapter describes the velocity distribution of the detected galaxies. This is followed by a presentation of LSS in Sections 4.2 and 4.3. In Sect. 4.4 a detailed discussion of interesting structures is given.

4.1 The Velocity Distribution of Detections

Galaxies were found over most of the observed redshift range (see Fig. 4.1). However, the majority lie within $2000 - 8000\,\mathrm{km\,s^{-1}}$. At $v > 8500\,\mathrm{km\,s^{-1}}$ recurring radar RFI makes detection of galaxies difficult. Moreover persistent RFI at $3500\ \mathrm{km\,s^{-1}}$ also affects the number of detections in the velocity distribution. The velocity histogram shows a clear peak at $6000\,\mathrm{km\,s^{-1}}$, probably due to the prevalence of galaxies connected to the Perseus-Pisces Supercluster (PPScl). This structure is the most prominent in the northern sky with distinct clusters and filaments. Its galaxy members have radial velocities within 4000 to $6000\,\mathrm{km\,s^{-1}}$ (Haynes & Giovanelli 1986). The most prominent clusters embedded in this wall-like structure are the Perseus cluster Abell 426 $(\ell, b, v) \approx (150°, -13°, 5006\,\mathrm{km\,s^{-1}})$, Abell 347 $(\ell, b, v) \approx (141°, -18°, 5156\,\mathrm{km\,s^{-1}})$ and Abell 262 $(\ell, b, v) \approx (136°, -25°, 4527\,\mathrm{km\,s^{-1}})$. The Perseus-Pisces chain possibly extends across the ZoA and connects to Abell cluster 569 at $\ell, b \approx 168°, 23°$. It is approximately $5000\,\mathrm{km\,s^{-1}}$ long, $500\,\mathrm{km\,s^{-1}}$ thick and $2000\,\mathrm{km\,s^{-1}}$ deep (Fairall 1998). This was the size of the PPScl as of that date, however, with the new detections presented in this thesis the size might be far larger.

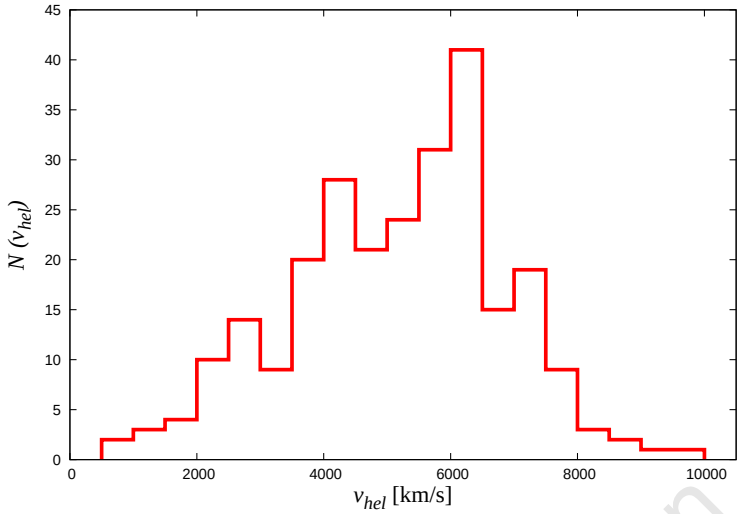

Figure 4.1: The velocity distribution of all the detected NRT galaxies.

4.2 Links to Known Structures

To study the distribution of the detections as a function of Galactic longitude, Fig. 4.2 is plotted. It is a longitude histogram of all HI-detected NRT galaxies. The large variation in the number count of galaxies as a function of longitude is explained by the various large-scale structure intersecting the ZoA. The drop off at $\ell \approx 120°$ is due to a void in that region. The second Perseus-Pisces arm at $\ell \approx 90°$ is apparent. The two high density regions also associated with the PPScl are clearly visible at $\ell \approx 135°$ and $160°$. Galaxy clustering corresponding to the Puppis filament occurs at $\ell \approx 240°$.

To investigate the large-scale structures revealed by the NRT HI detections, their spatial distribution in Galactic coordinates centred on the northern Milky Way is plotted in Fig. 4.3. It includes 2MRS data to test for continuity of the newly identified features with previously known structures (filaments, walls, voids) at higher Galactic latitudes. The outlined rectangular region demarcates the approximate NRT survey area.

The top panel shows the 2MRS galaxies with $K_s^o \leq 11\overset{\text{m}}{.}25$, as well as data in the $|b| \lesssim 5°$ strip from the ZCAT ($K_s^o \leq 11\overset{\text{m}}{.}25$) compilation by Huchra (priv comm). The middle panel displays the distribution of the 249 NIR-bright 2MASX galaxies detected with the NRT. In the bottom panel the new detections have been merged with the previously known data of objects to the $K_s^o \leq 11\overset{\text{m}}{.}25$ completeness limit. In all three panels the galaxies are colour-coded by velocity: the $v \leq 2500\,\mathrm{km\,s^{-1}}$ velocity range is shown in cyan, $2500 < v \leq 4500\,\mathrm{km\,s^{-1}}$ in blue, $4500 < v \leq 6500\,\mathrm{km\,s^{-1}}$ in black, $6500 < v \leq 8500\,\mathrm{km\,s^{-1}}$ range in red and $8500 < v \leq 10500\,\mathrm{km\,s^{-1}}$ in green. The blue and black colours coincide with the approximate velocity range of the PPScl.

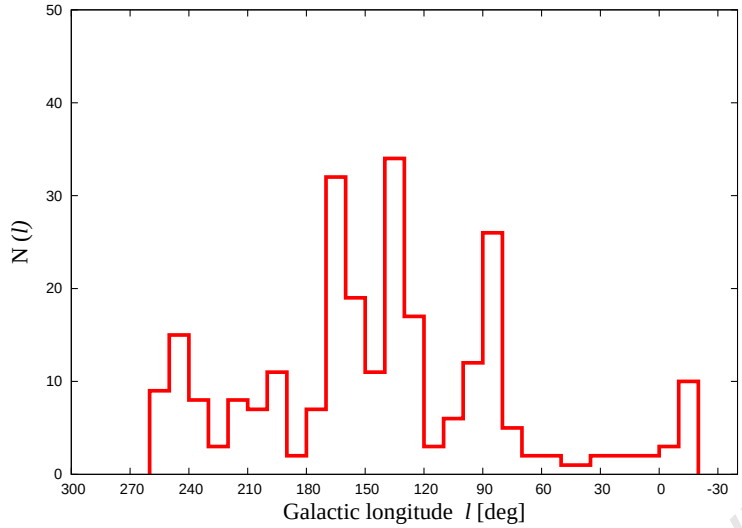

Figure 4.2: The distribution in Galactic longitude of all NRT HI-detected galaxies.

A comparison of the bottom and top panels (i.e., the status before and after the NRT observations) shows the obvious power of revealing previously unknown large-scale structures in the ZoA through HI observations of intrinsically bright (i.e., extinction-corrected) NIR galaxies. Several prominent filaments and walls are now seen to cross the ZoA which were previously not – or at most marginally – visible. The most obvious filamentary structures cross the Galactic Plane at $\ell \approx 90°$ (Cygnus), $\ell \approx 135°$ (Cassiopeia), $\ell \approx 160°$ (Perseus), $\ell \approx 180°$, as well as at the Puppis filament, $\ell \approx 240°$ (Kraan-Korteweg & Huchtmeier 1992). An underdense region of galaxies is apparent at $\ell \approx 120°$ and $-2° \lesssim b \lesssim 5°$, stretching from $cz \approx 4000$ to $7000\,\mathrm{km\,s^{-1}}$.

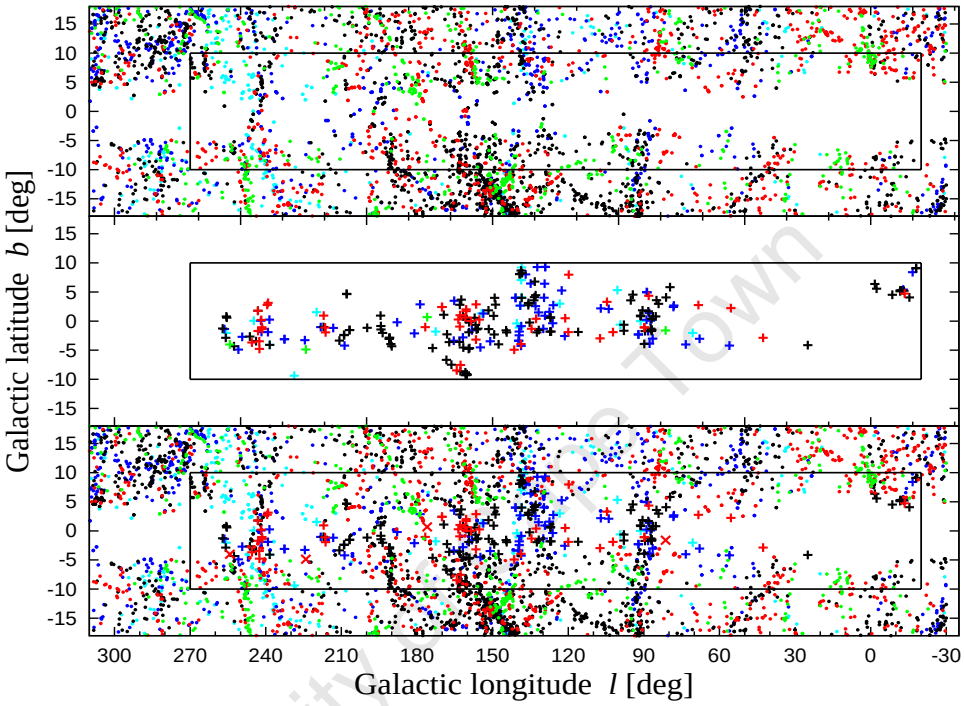

Figure 4.3: The spatial distribution of galaxies in Galactic coordinates in the ZoA. The survey area explored with the NRT is marked by the black rectangle. Galaxies are colour-coded by their velocity range: the $v \leq 2500\,\mathrm{km\,s^{-1}}$ velocity range is shown in cyan, $2500 < v \leq 4500\,\mathrm{km\,s^{-1}}$ in blue, $4500 < v \leq 6500\,\mathrm{km\,s^{-1}}$ in black, $6500 < v \leq 8500\,\mathrm{km\,s^{-1}}$ range in red and $8500 < v \leq 10500\,\mathrm{km\,s^{-1}}$ in green. The top panel shows the 2MRS galaxies ($K_s^o \leq 11\overset{\mathrm{m}}{.}25$) together with low-latitude 2MASX galaxies with known redshifts from ZCAT (Huchra, priv comm). The middle panel displays the HI-detections obtained with the NRT. The bottom panel shows the combined data and emphasizes the links with previously known structures.

Positions of these newly uncovered (by this survey) ZoA crossing ridges are pointed out by blue arrows in Fig. 4.4, which is an all-sky projection of ∼22000 galaxies in the 2MRS first data release which is complete to $K_s^o \leq 11\overset{\text{m}}{.}25$ (Huchra et al. 2005) (For a representation of the entire local universe derived from 2MASS XSC and 2MASS PSC see Fig. 1 of Jarrett (2004)). The markings R1, R2 and R3 in Fig. 4.4 refer to the most prominent ZoA ridges located in the constellations of Cygnus, Cassiopeia and Perseus respectively. The V1 marking points to an under-dense region centred at $\ell \approx 120^\circ$. Well known structures, i.e., the Perseus cluster (Abell 426) in the Perseus-Pisces chain and Abell cluster 569 and Puppis are pointed out by black arrows.

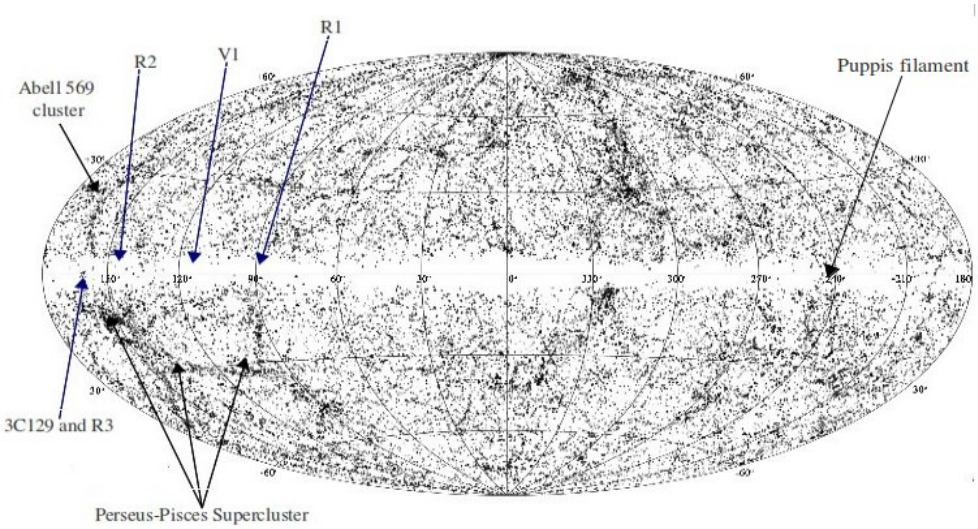

Figure 4.4: An all-sky redshift distribution of galaxies in the 2MRS first data release ($K_s^o \leq 11\overset{\text{m}}{.}25$). The black arrows point to the location of the Perseus-Pisces Supercluster (PPScl) and the cluster Abell 569. The blue arrows point to the locations of the ZoA crossing ridges (R1, R2 and R3) and the void V1 outlined by the new NRT HI detections.

4.3 Redshifts of the detections

To look at the distribution in more detail, the bottom panel of Fig. 4.3 has been subdivided into redshift slices of width 2500 $\mathrm{km\,s^{-1}}$. See Fig. 4.5, with its 5 panels showing the velocity ranges of (top to bottom) $v \leq 2500\,\mathrm{km\,s^{-1}}$ in cyan, $2500 < v \leq 4500\,\mathrm{km\,s^{-1}}$ in blue, $4500 < v \leq 6500\,\mathrm{km\,s^{-1}}$ in black, $6500 < v \leq 8500\,\mathrm{km\,s^{-1}}$ in red and $8500 < v \leq 10500\,\mathrm{km\,s^{-1}}$ in green.

The *top* panel of Fig. 4.5 plotted in cyan shows galaxies with $v \leq 2500\,\mathrm{km\,s^{-1}}$. The Supergalactic plane is seen crossing the ZoA at $\ell \approx 135°$ and the Puppis filament (Kraan-Korteweg & Huchtmeier 1992) is visible at $\ell \approx 240°$.

The *second* panel shown in blue represent structures in the $2500 < v \leq 4500\,\mathrm{km\,s^{-1}}$ range. In this panel a hint of an overdensity associated with the Perseus-Pisces supercluster starts being visible at $\ell \approx 90°$ with the Supergalactic plane still visible and peaking at $\ell \approx 135°$.

In the *middle* panel galaxies with $4500 < v \leq 6500\,\mathrm{km\,s^{-1}}$ are shown in black. These are linked with various arms of the PPScl across the Galactic Plane. The second arm of the PPScl which previously stopped where the Galactic extinction became high, is now found to extend all the way across the ZoA at $\ell \approx 90°$. It seems to blend with the structure at $\ell, b \approx 90°, -10°$ to about $\ell, b \approx 70°, 10°$. Right next to this overdensity there appears an area void of galaxies centred at $\ell \approx 120°$ within the $-2° \lesssim b \lesssim 5°$ Galactic latitude strip. There is also a very high density region at $\ell \approx 135°$ in this velocity range. This is the extension of the Perseus cluster (A 426; $\ell \approx 150°, b \approx -13°$) connecting the high ($|b| > 10°$) and low latitude ($|b| < 10°$) PPScl across the Galactic Plane. Another region of very high galaxy clustering, at $\ell \approx 160°$, is the other arm of the PPScl which runs across the Galactic Plane, connecting to the Abell cluster 569 at $\ell, b \approx 168°, 23°$. This *middle* panel also shows a hint of density enhancement at $\ell \approx 180°$, a low density Gemini-Monoceros filament (Focardi et al. 1984), which is a clustering of galaxies mainly composed of spirals.

The *fourth* panel ($6500 < v \leq 8500\,\mathrm{km\,s^{-1}}$; red) shows a clear overdensity at $\ell \approx 160°$ which is probably related to the structure in the *middle* panel. A filament in Puppis is also visible at $\ell \approx 240°$ (Chamaraux & Masnou 2004).

In the *bottom* panel galaxies within the velocity range of $8500 < v \leq 10500\,\mathrm{km\,s^{-1}}$ are shown in green. At these velocities the survey is only sensitive to extreme HI-massive galaxies and the level and density of recurring RFI has an adverse effect on the number of detections at $> 8500\,\mathrm{km\,s^{-1}}$. The results of both effects are shown in the top and bottom panel of in Fig. 3.8 respectively.

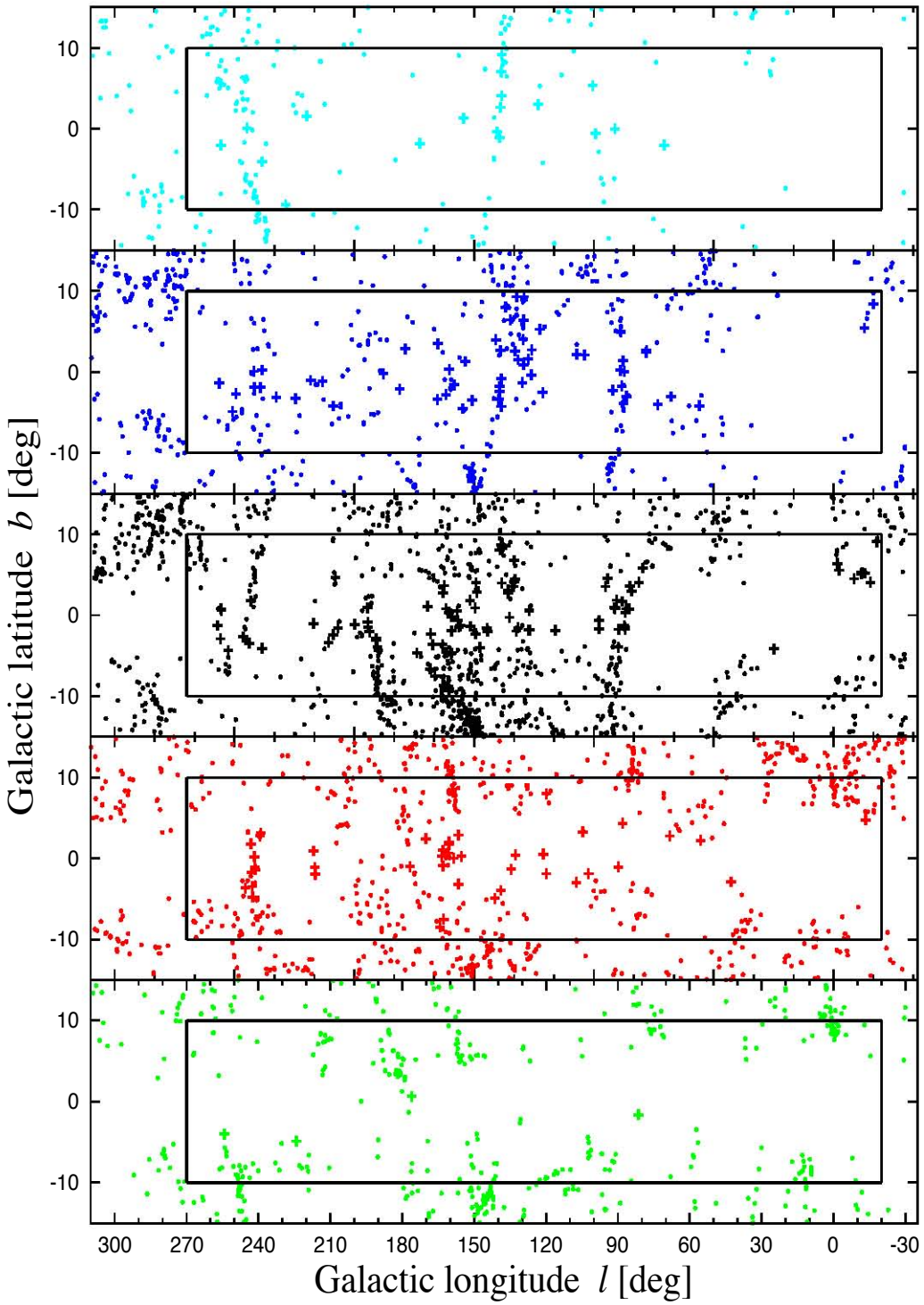

Figure 4.5: The spatial distribution of galaxies in the ZoA in five velocity bins. Solid lines demarcates regions explored by this survey. Panels show the combined 2MRS ($K_s^o \leq 11\overset{\text{m}}{.}25$; dots) and HI detected NRT galaxies (crosses). The velocity bins from top to bottom are: $v \leq 2500\,\mathrm{km\,s^{-1}}$ shown in cyan, $2500 < v \leq 4500\,\mathrm{km\,s^{-1}}$ in blue, $4500 < v \leq 6500\,\mathrm{km\,s^{-1}}$ in black, $6500 < v \leq 8500\,\mathrm{km\,s^{-1}}$ in red and $8500 < v \leq 10500\,\mathrm{km\,s^{-1}}$ in green.

4.4 Details of Uncovered Structures

In the next sections three of the most striking newly revealed features are discussed in more detail. These are the ones at $\ell \approx 90°$, $\ell \approx 160°$ and $\ell \approx 180°$.

4.4.1 The extension of the second PP arm towards Cygnus ($\ell \approx 90°$)

In the constellation of Cygnus (around $\ell \approx 90°$) the ZoA detections outline a very prominent filament that can be traced from below the Plane at $\ell, b \approx 80°, -10°$ extending up to the other side of the ZoA at a slight angle to $\ell, b \approx 100°, -10°$. This is also visible in Fig. 4.6 which is a wedge diagram of the ZoA $|b| < 10°$ for velocities out to 10500 km s^{-1}. The 2MRS galaxies are indicated by red dots and the HI-detected NRT galaxies by blue dots. The filament seems to form part of the second (eastern) Perseus-Pisces arm that emanates southwards from the Perseus A 426 cluster (ℓ,b) $\approx$ (150°, -13°), then bends backwards towards the Galactic Plane (at about $\ell, b \approx 110°, -30°$; see Fig. 4.4) and re-enters (Fig. 4.3) the plot at about $\ell, b \approx 80°, -15°$. Most previous studies of the PPScl were uncertain of its extension into the ZoA, as it appeared to stop around $\ell, b \approx 90°, -10°$. No signature was found in any of the earlier optical galaxy searches (Seeberger et al. 1994) nor was any indication of a continuation apparent on the other side of the dust-obscured Milky Way band. The new NRT data clearly confirms such a continuation. It implies the eastern Perseus-Pisces chain to be considerably more extended than evidenced in any previous survey of the PPScl complex.

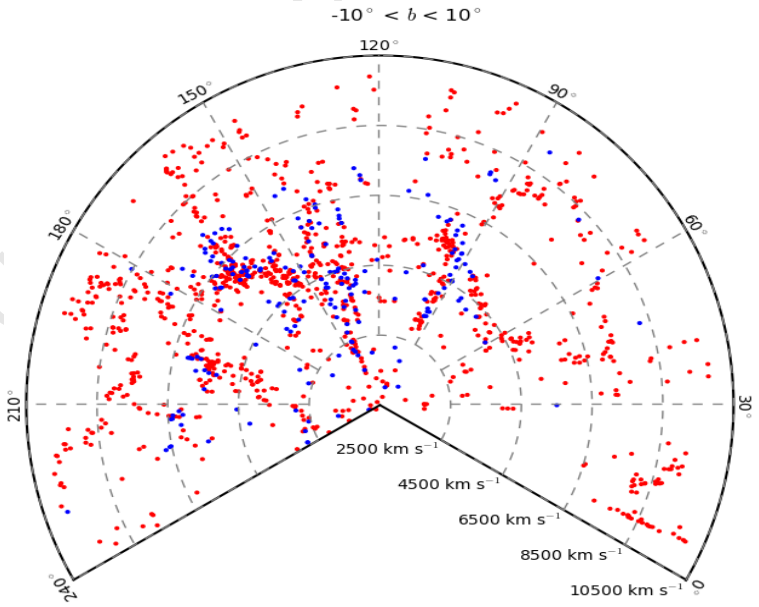

Figure 4.6: A wedge diagram of galaxies within $|b| < 10°$ strip. The red dots with $K_s^o \leq 11\overset{m}{.}25$ are 2MRS galaxies and the blue dots are new NRT HI-detections.

4.4.2 A Perseus-Pisces Supercluster and Abell 569 connection?

The second prominent feature is a concentration of HI-detections at $\ell \approx 160^\circ$ right in the middle of the ZoA ($b = 0\overset{\circ}{.}5$). It lies within a nearly vertical (in Fig. 4.5) wall-like structure (at $v \approx 6000 \pm 1000\,\mathrm{km\,s^{-1}}$ in velocity space) and can be traced across the full width of the ZoA.

There has been much debate since the 1980's about a possible extension of the Perseus-Pisces Complex below the Galactic Plane across the ZoA towards the northern Galactic hemisphere linking the Perseus cluster (A 426; $\ell, b, v \simeq 150^\circ, -13^\circ, 5000\,\mathrm{km\,s^{-1}}$) to Abell 569 ($\ell, b, v \simeq 168^\circ, 23^\circ, 5800\,\mathrm{km\,s^{-1}}$), see Fig. 4.4. It would traverse the Galactic Plane at the region which coincides with the location of an excess of galaxies at $\ell \approx 160^\circ$. The debate continued over the years (e.g., Hauschildt 1987, Chamaraux et al. 1990, Lu & Freudling 1995, Pantoja et al. 1997), however despite all of these arguments put forward no conclusive results were found due to the lack of (redshift) data in this dust-enshrouded region.

The NRT data finds a clear connection between structures mentioned above and puts the controversy to rest. To show this, 2MRS ($K_s^o \leq 11\overset{\mathrm{m}}{.}25$) galaxies within the Galactic latitude strip $|b| < 30^\circ$ have been plotted in Fig. 4.7. together with the NRT HI detections, to emphasize this extension. The *top* panel shows galaxies at $2500 < v \leq 4500\,\mathrm{km\,s^{-1}}$ and the *bottom* panel galaxies at $4500 < v \leq 6500\,\mathrm{km\,s^{-1}}$. In the top panel only hints of the ZoA crossings discussed in Sect. 4.3 can be seen. Radial velocities plotted in the bottom panel coincide with those of the Perseus-Pisces chain. The Perseus cluster (A 426; $\ell, b, v \simeq 150^\circ, -13^\circ, 5000\,\mathrm{km\,s^{-1}}$) enters the ZoA at a slight angle at $\ell, b \simeq 160^\circ, -10^\circ$ and connects with the NRT detections over the full width of the ZoA at $\ell \simeq 160^\circ$, $|b| < 10^\circ$. This continues outside the ZoA at $b > 10^\circ$ and extends to the galaxy cluster Abell 569 at $\ell, b \simeq 168^\circ, 23^\circ$.

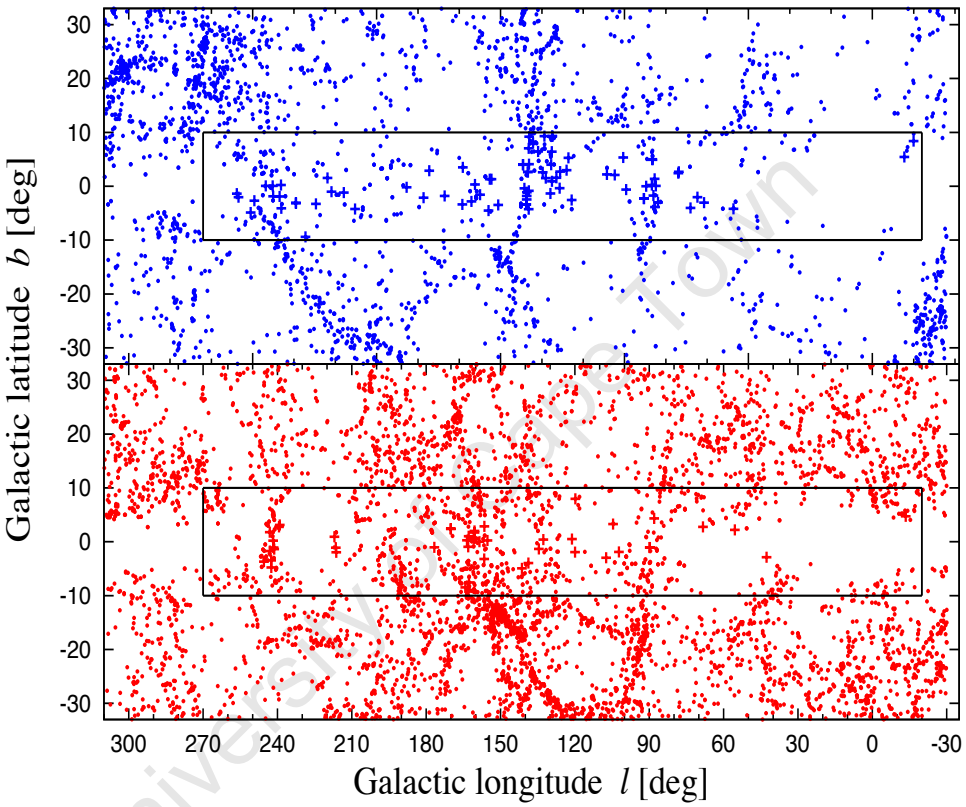

Figure 4.7: The distribution of galaxies within $|b| < 30°$ in the velocity ranges $2500 < v \leq 4500\,\mathrm{km\,s^{-1}}$ (*top* panel) and $4500 < v \leq 6500\,\mathrm{km\,s^{-1}}$ (*bottom* panel). Plotted are the 2MRS ($K_s^o \leq 11\overset{\mathrm{m}}{.}25$; dots) and the NRT HI-detected galaxies (crosses) The rectangular region demarcates the region of this survey.

4.4.3 A Potentially Massive Hidden Cluster

It is interesting to note that within this wall, at the core of the galaxy concentration, two very strong (1-8 Jy), nearby radio galaxies are located. Their position and redshifts (6236 and 6655 km s^{-1}, respectively; Spinrad 1975) confirm that they reside inside the galaxy concentration outlined by the NRT detections. The two sources are a head-tail source (3C 129) and a double-lobed giant elliptical radio galaxy (3C 129.1) (Spinrad 1975). Their positions are shown in Fig. 4.8, which is a close-up of the galaxies detected around $\ell \approx 160°, |b| < 3°$.

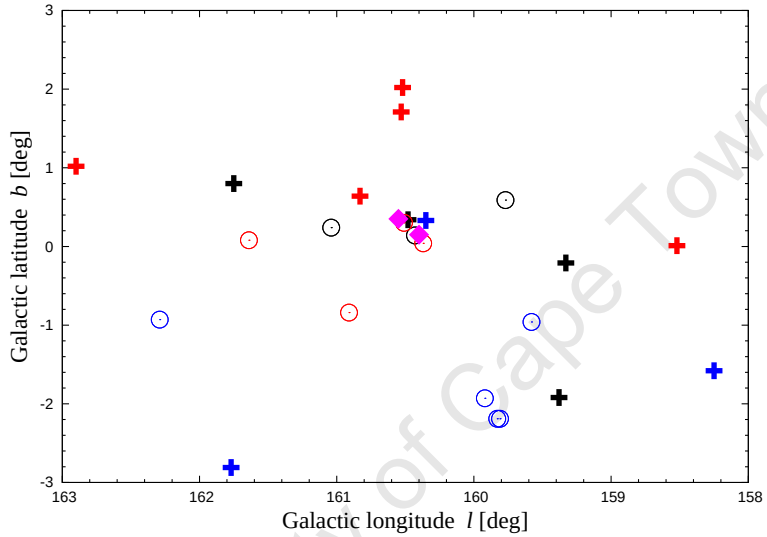

Figure 4.8: Close up of the velocity distribution around $\ell \approx 160°$. The 2MRS galaxies ($K_s^o \leq 11\overset{m}{.}25$) are indicated by open circles and NRT detections by crosses. The pink diamonds represent the positions of the two strong radio sources, 3C 129 and 3C 129.1.

The presence of such radio sources with bent-lobe morphologies usually indicates a rich cluster environment. The suspicion that 3C 129 and 3C 129.1 form part of a massive hidden cluster was substantiated through the identification of the X-ray cluster CIZA J0450.0+4501 at $\ell, b \approx 160.52°, 0.28°$ (Ebeling et al. 1998). The radio sources lie within the X-ray emission of this CIZA cluster and are at the same distance. With an X-ray luminosity of $L_{\rm X} = 1.89 \times 10^{44}$ h_{50}^{-2}erg s^{-1}, it is not among the most luminous ROSAT X-ray clusters. Its luminosity is about 20% that of the Norma cluster A 3627, the central cluster of the Great Attractor (Kraan-Korteweg et al. 1996) – which, as an aside, also hosts 2 radio sources of the same morphology as 3C 129 and 3C 129.1. It should be noted, that the intervening high gas column density ($N_H \gtrsim 10^{21}$ cm^{-2}) in the Galaxy have reduced the flux of the low energy X-ray photons in the ROSAT $0.1 - 2.4$ keV band, resulting in an underestimation of its luminosity. The cluster might therefore be more massive than its X-ray luminosity suggests.

4.4.4 The ZoA Gemini-Monoceros and PPScl

Another structure of interest lies at $\ell \approx 180^\circ$ (see the distribution of galaxies at $cz \leq 5000\,\mathrm{km\,s^{-1}}$ Fig. 4.3). This is the extension of the so-called Gemini-Monoceros filament (Takata et al. 1994). It crosses the ZoA within $|b| < 5^\circ$ and peaks in the $cz \approx 4500\,\mathrm{km\,s^{-1}}$ range. It is also apparent in the *top* panel of Fig. 4.4.2. This filament might be connected to the N1600 supercluster at $(\ell, b, v) = (194^\circ, 24^\circ, 4400\,\mathrm{km\,s^{-1}})$ (Saunders et al. 1991). The Gemini-Monoceros filament does not have a rich cluster of galaxies along its filamentary structure. It is connected to a detached collection of groups of galaxies in the Cancer cluster $(\ell, b, v) = (203^\circ, 29^\circ, 4704\,\mathrm{km\,s^{-1}})$ (Focardi et al. 1986). The filament is defined by 48 galaxies. It has a high spiral content with only 4 early-type galaxies in the Uppsala Catalogue (Nilson 1973). These early-type galaxies only occupy a very narrow strip surrounding spirals in that region of the Perseus-Pisces complex (Giovanelli et al. 1985). This characteristic is attributed to the relatively low galaxy density in this region and is important for morphological segregation studies of the nearby large-scale structures (Giovanelli et al. 1985).

The PPScl Extension

Prior to the survey presented here and the new ZoA crossings unveiled by it, the PPScl chain could be traced over 90° across the sky. The new ZoA ridges seem to indicate that the western arm of the filament extends from A 426 $(\ell, b, v \simeq 150^\circ, -13^\circ)$ to Abell 569 at $\ell, b \simeq 168^\circ, 23^\circ$ and eastern arm from A 426 to $\ell, b \approx 80^\circ, -15^\circ$. These extensions increases the area over which it can be traced across the sky by 35°. This means that PPScl chain can now be traced over about 125° across the sky. This chain lies at a mean redshift of $6000\,\mathrm{km\,s^{-1}}$ and with these new extensions it now extends over an estimated length of about 187 Mpc from the northern to the southern hemisphere. This is about twice its previous length.

Chapter 5

Summary and Future work

5.1 Summary

The near-infrared 2MASS Redshift Survey (2MRS) is currently the most complete and uniform systematic "whole-sky" survey for mapping large-scale structures and cosmic flows in the nearby Universe. Although it is intended to be an all-sky survey it excludes the inner ZoA, at $|b| < 5°$, due to difficulties in obtaining good signal to noise optical spectra. To fill in this "2MRS ZoA" a project was started to systematically observe all likely 2MASX candidate galaxies in this region in HI as the 21 cm wavelength is not affected by dust extinction. Although HI is not affected by dust, it is biased to gas-rich galaxies, and thus a tracer of field galaxies, filaments and some groups.

A total of 4743 extended near-infrared sources with $K_s^o \leq 11\overset{\text{m}}{.}25$ were extracted from 2MASX, of which 2546 were visually classified as galaxy candidates (plus 42 possibles). The identification process resulted in completeness successfully achieved for the ZoA away from the Galactic Bulge $|\ell| \gtrsim 90°$. The final sample consists of 1000 NIR bright galaxy candidates without redshifts in the ZoA ($-20° \lesssim \ell \lesssim 270°$; $|b| \leq 10°$), with the great majority ($\gtrsim 83\%$) of them located in the $|b| < 5°$ strip. The Nançay Radio Telescope was used for pointed observations of these ZoA galaxy candidates. From July 2009 to March 2012, 928 of the 1000 galaxy candidates were observed out to $v = 10500\,\mathrm{km\,s^{-1}}$, to a target rms noise level of 3.3 mJy. A total of 249 candidates were detected, leading to a respectable detection rate of 27%. The HI detection rate was shown to be independent of the Galactic latitude b, extinction and star density. The measured HI line parameters were generally found to be in good agreement with the few sources in common with the literature.

While galaxies were found over the entire observed redshift range, the majority lie within $2000 - 8000\,\mathrm{km\,s^{-1}}$ peaking at $6000\,\mathrm{km\,s^{-1}}$, because of the prevalence of galaxies connected to the Perseus Pisces Super Cluster. For $v > 8500$ $\mathrm{km\,s^{-1}}$, strong radar RFI and telescope sensitivity severely limited the number of detected galaxies.

Several prominent filaments and walls which were previously not or marginally visible are now seen crossing the ZoA. The most striking are filamentary structures at $\ell \approx 90°$,

$\ell \approx 135°$, $\ell \approx 160°$ and $\ell \approx 180°$.

The interesting filament that was revealed is an extension of the (eastern) Perseus-Pisces arm across the ZoA at $\ell \approx 90°$. This structure had been assumed to end around $(\ell, b) \approx (90°, -10°)$ because no further signature of its continuation was found on either side of the ZoA band in optical galaxy surveys. The presented data clearly confirms such a continuation, implying the eastern Perseus-Pisces chain to be considerably larger than outlined in previous surveys.

Another structure of most interest is a concentration of HI detections at $\ell \approx 160°, b = 0\overset{\circ}{.}5$. Based on the NRT observations, this ridge possibly connects Perseus cluster (A 426; $\ell, b, v \simeq 150°, -13°, 5000\,\mathrm{km\,s^{-1}}$) in the south and Abell 569 in the northern Galactic hemisphere at $(\ell, b, v \simeq 168°, 23°, 5800\,\mathrm{km\,s^{-1}})$. This is an issue that had been debated quite extensively in the past. The wall-like connection in the ZoA was found to be associated with the CIZA X-ray cluster ($L_\mathrm{X} = 1.89 \times 10^{44}$ $\mathrm{h_{50}^{-2}erg\ s^{-1}}$) which also hosts two strong radio galaxies. Both clues are indicative of a rich cluster environment. Moreover the cluster might be more massive than its soft X-ray luminosity suggests, because the intervening high Galactic gas column density may well have reduced its X-ray flux. Despite its possible connection to the wider PPScl complex, it previously had not received much attention.

In summary, the 249 new HI detections in this previously unexplored region of the ZoA have revealed new and interesting structures that are clearly part of the Pisces-Perseus Supercluster (PPScl). These new structures seem to imply that the PPScl is more extended than previously thought and potentially much more massive, in particular with the identified cluster in the $\ell \approx 160°$ filament. This may well have implications for our understanding of the dynamics and flow-fields observed in this region.

5.2 Future Perspectives

This study has shown the potential of HI observations in revealing previously unknown structures in the ZoA. While the first aim was to map large-scale structures, another was to use this data set as a basis to complement the 2MASS Tully Fisher (2MTF) catalogue (Masters et al. 2008) and so the next steps within this project will be to conduct a Tully-Fisher analysis. This will be done selecting sufficiently inclined, HI-detected spiral galaxies. The analysis will be used to determine the peculiar velocities of the galaxies, in the ZoA rather than being restricted to intepolation across or statistical reconstruction of the matter distribution.

Only the intrinsically brightest ($K_s^o \leq 11\overset{\mathrm{m}}{.}25$) NIR galaxy candidates were used in this survey. Therefore the structures uncovered here are just the tip of the iceberg. Probing regions surrounding the unveiled ZoA filaments (particularly the one at $\ell \approx 90°$) with more sensitive HI instruments will find less massive and fainter galaxies. The HIdetection rate could also be improved by searching the Wide-field Infrared Survey Explorer (WISE) data (Wright et al. 2010) of the NIR selected galaxies which are star forming galaxies. This will increase the ZoA redshift samples in those regions. With an increased and more uniform

sample, more precise studies of peculiar velocity fields can be done.

One of the most striking new features uncovered by this survey shows a hint of a potentially massive cluster at $\ell \approx 160^\circ$ hosting two radio sources. This cluster has already been allocated over 200 hours of observing time on the Westerbork Synthesis Radio Telescope (WSRT). The project will conduct HI imaging over a $2.^\circ4 \times 2.^\circ4$ mosaicked area around the cluster. This deep and detailed study of the cluster will give an insight into its properties and its role in as well its relation to the observed local flow fields.

Since this study has proved itself to be powerful at unveiling structures in the ZoA from the Northern hemisphere, it would be valuable to extend it to the Southern hemisphere. This will be done by conducting HI observations of the brightest NIR-selected galaxy candidates using the Parkes 64 m radio Telescope, on which 55 hours have been allocated for a pilot study.

The survey presented in this dissertation has shown the feasibility of detecting galaxies within the heavily obscured ZoA. It therefore serves as a preparation for the next generation of surveys which will be conducted using the SKA pathfinders MeerKAT and ASKAP in South Africa and Australia, plus the similar WSRT APERTIF system in the Netherlands, which are all planned to be operational in 2016, and ultimately with the giant Square Kilometre Array itself.

Appendix A

The Catalogue of non-detections

In this appendix all the non-detections are listed in Table. A.1. They are sorted by right ascension as follows:

Column 1: 2MASX identifier [2MASXJhhmmss.sss ± ddmmss.ss].

Column 2: Galactic longitude [deg].

Column 3: Galactic latitude [deg].

Column 4: The number of observation cycles, Ncyc. [no.]

Column 5: The noise rms [mJy].

Table A.1: A list of non-detections

2MASX identifier [hhmmssss ± ddmmssss] Col (1)	gal l [deg] Col (2)	gal b [deg] Col (3)	Ncyc no. Col (4)	rms [m Jy] Col (5)
00102576+6520598	118.67	2.82	21	2.80
00161976+7025219	119.97	7.75	24	4.44
00223972+6139447	119.52	-1.02	48	2.84
00253292+6821442	120.54	5.61	23	3.96
00265869+6054037	119.96	-1.83	29	3.32
00281959+6447011	120.47	2.02	16	4.10
00295328+6350552	120.56	1.08	33	4.33
00303425+6444585	120.71	1.97	25	3.86
00314802+6227440	120.66	-0.32	40	3.07
00321813+6029565	120.58	-2.29	45	2.53
00343086+6257451	121.01	0.15	68	2.11
00343656+6310260	121.04	0.36	35	2.93
00402126+6732350	121.87	4.69	47	2.96
00402382+6428443	121.74	1.63	28	3.57
00450852+6549280	122.29	2.96	32	3.87
00501956+6702517	122.82	4.18	51	3.24
00532380+6128104	123.17	-1.40	55	2.48
01010569+5804266	124.21	-4.77	30	2.92

Table A.1 – Continued

2MASX identifier [hhmmssss ± ddmmssss] *Col (1)*	gal l [deg] *Col (2)*	gal b [deg] *Col (3)*	Ncyc no. *Col (4)*	rms [m Jy] *Col (5)*
01010771+6254430	124.04	0.06	60	2.31
01013460+6715038	123.92	4.40	34	2.92
01021854+6708091	123.99	4.29	48	3.33
01135448+6440014	125.33	1.90	37	2.95
01311294+6735115	126.72	5.01	21	3.86
01312331+6019128	127.86	-2.17	50	3.31
01312488+6450068	127.17	2.29	31	2.96
01343229+6641235	127.19	4.18	43	2.98
01345732+6628216	127.26	3.97	32	3.15
01472075+6207593	129.41	-0.03	24	3.26
01575636+5726026	131.82	-4.29	45	2.55
01582742+6744421	129.23	5.70	29	4.44
02002296+6531178	130.00	3.60	35	2.67
02021798+6721240	129.69	5.42	31	3.92
02034595+6650152	129.97	4.96	42	2.94
02034762+6843532	129.45	6.78	36	3.67
02035883+6737172	129.77	5.72	34	4.07
02055021+6749477	129.88	5.97	24	3.62
02061555+6823324	129.76	6.52	48	2.81
02063421+5855125	132.51	-2.55	44	2.85
02082184+6640353	130.45	4.94	36	3.80
02084861+6228485	131.74	0.94	26	3.14
02103987+6304565	131.76	1.58	36	3.05
02121002+6144326	132.33	0.35	51	2.49
02132797+6316450	132.00	1.86	35	3.26
02163334+5039016	136.44	-9.98	52	1.90
02173999+6701444	131.22	5.56	17	5.81
02174785+6911364	130.51	7.60	11	5.99
02220408+6500169	132.32	3.80	62	2.50
02240808+6458272	132.54	3.85	34	3.37
02245812+6214020	133.59	1.31	85	5.46
02293092+6148180	134.24	1.11	38	4.07
02341102+6700106	132.74	6.11	22	3.97
02343179+6755266	132.41	6.97	17	4.62
02353356+6656497	132.88	6.11	33	3.37
02361585+6845014	132.23	7.79	12	5.63
02370546+5936210	135.94	-0.57	37	3.62
02403604+5854138	136.63	-1.03	34	3.33
02422242+6213323	135.47	2.08	34	3.01
02471213+5528163	138.89	-3.77	32	2.88
02473993+5804489	137.82	-1.39	33	2.81
02475005+5832219	137.64	-0.97	32	3.30
02484584+6020478	136.96	0.71	25	3.98
02491146+6628401	134.31	6.24	31	3.45
02495036+6304092	135.88	3.21	32	3.29
02504965+5616424	138.99	-2.83	32	2.93
02531484+5732583	138.72	-1.54	81	1.89
02545182+5720004	139.01	-1.63	26	3.03
02573053+5825188	138.82	-0.51	30	2.85
02585431+5950161	138.32	0.83	29	2.80
03022154+6855070	134.29	8.99	34	3.40
03040456+6716077	135.24	7.62	25	4.16
03070158+5315165	142.48	-4.39	32	2.35
03071054+5517545	141.48	-2.61	34	2.37
03073914+5645235	140.81	-1.31	32	2.75

Table A.1 – Continued

2MASX identifier [hhmmssss ± ddmmssss] *Col (1)*	gal l [deg] *Col (2)*	gal b [deg] *Col (3)*	Ncyc no. *Col (4)*	rms [m Jy] *Col (5)*
03095915+5707553	140.90	-0.83	17	4.01
03101644+5656203	141.03	-0.97	30	3.04
03113572+6241207	138.25	4.06	57	2.43
03121951+6758295	135.57	8.63	18	4.82
03124522+5213583	143.75	-4.84	22	3.15
03130062+6752475	135.67	8.58	35	3.36
03132009+6224130	138.56	3.92	36	2.94
03161119+6242593	138.68	4.36	64	2.90
03162208+5215460	144.21	-4.52	12	3.86
03181353+6649422	136.67	7.96	18	4.63
03185163+5754376	141.51	0.46	69	1.99
03210915+6655186	136.86	8.19	39	3.25
03212339+6654460	136.88	8.20	23	4.08
03214230+6649371	136.96	8.14	31	3.25
03221550+5752157	141.92	0.67	33	3.15
03231132+6548189	137.65	7.37	14	4.51
03235035+6102426	140.35	3.44	35	2.65
03244319+5811161	142.01	1.11	14	4.33
03245871+5310146	144.82	-3.05	24	3.05
03251590+5624122	143.06	-0.33	26	3.23
03273938+5221060	145.61	-3.50	33	2.45
03285780+6656000	137.49	8.63	18	4.32
03292042+6601389	138.05	7.91	14	5.67
03302327+6110135	140.93	3.98	42	2.55
03302327+6110135	140.93	3.98	42	2.55
03312960+6541405	138.42	7.76	46	2.72
03313677+5148312	146.42	-3.61	8	3.75
03334905+5201071	146.58	-3.24	33	2.24
03345483+5349073	145.67	-1.68	58	2.06
03360608+5416062	145.54	-1.21	24	3.12
03362571+5132236	147.19	-3.39	13	3.05
03363315+6240256	140.65	5.63	14	5.46
03363871+6306096	140.40	5.98	17	4.71
03364414+5248386	146.48	-2.34	27	2.79
03373489+5412366	145.75	-1.13	45	2.08
03373616+5052062	147.73	-3.82	35	4.87
03373823+5106002	147.60	-3.63	28	2.56
03374463+5502466	145.28	-0.44	31	3.08
03374624+5357452	145.92	-1.31	10	4.41
03374715+6542199	138.95	8.15	17	4.73
03380124+6642455	138.36	8.97	34	3.46
03381210+6642567	138.37	8.98	16	4.95
03384742+5421089	145.81	-0.91	13	3.99
03393055+5421369	145.89	-0.84	16	3.39
03393065+5449231	145.62	-0.47	26	2.76
03395792+4940197	148.75	-4.56	34	2.32
03433015+5825154	143.89	2.73	26	2.96
03441609+4919572	149.51	-4.41	30	2.45
03441729+5102202	148.47	-3.06	16	3.33
03450943+4921435	149.61	-4.30	15	3.62
03454256+5638563	145.21	1.51	25	2.80
03460488+5432382	146.54	-0.12	46	2.81
03462398+5430563	146.59	-0.11	28	3.25
03475375+5601049	145.83	1.20	37	2.75
03480684+4955450	149.64	-3.56	30	2.92

Table A.1 – Continued

2MASX identifier [hhmmssss ± ddmmssss] *Col (1)*	gal l [deg] *Col (2)*	gal b [deg] *Col (3)*	Ncyc no. *Col (4)*	rms [m Jy] *Col (5)*
03480963+4955140	149.65	-3.56	58	1.90
03481049+5409119	147.02	-0.24	62	1.83
03481767+5413029	147.00	-0.18	29	2.69
03482002+4955207	149.67	-3.54	24	2.78
03492038+5029171	149.44	-3.00	30	3.01
03492373+4924181	150.13	-3.84	12	4.73
03522801+5748301	145.20	2.99	15	3.72
03541837+5249110	148.57	-0.70	22	2.80
03551424+5231391	148.86	-0.84	30	2.82
03573082+4956387	150.80	-2.58	12	3.88
03585689+4911167	151.47	-3.01	33	2.17
04012641+5343171	148.80	0.68	28	2.99
04014132+5315002	149.14	0.35	47	2.30
04015541+4924171	151.69	-2.53	33	2.58
04020732+5241528	149.55	-0.03	32	3.05
04024870+5244088	149.60	0.07	30	2.43
04050668+4028583	158.08	-8.81	15	2.69
04060596+4020487	158.32	-8.79	32	2.19
04093213+4922208	152.64	-1.73	28	2.58
04104442+3957368	159.24	-8.47	14	2.73
04110830+3837269	160.23	-9.38	16	3.64
04111032+4710144	154.34	-3.16	43	2.19
04113162+3914215	159.85	-8.88	13	3.02
04122913+3838553	160.40	-9.18	15	3.51
04124692+3835153	160.49	-9.19	23	2.35
04133389+5041476	152.21	-0.32	42	2.19
04161779+5034094	152.61	-0.11	28	2.64
04164549+3925359	160.46	-8.05	18	2.32
04170636+4910038	153.68	-1.03	33	2.61
04173955+3745411	161.77	-9.10	17	3.23
04175296+4911337	153.75	-0.92	30	2.44
04210584+4830168	154.61	-1.04	11	3.82
04211472+3710123	162.70	-9.02	15	2.87
04220023+4302560	158.59	-4.78	36	2.16
04225185+4402328	157.99	-3.97	32	3.01
04230985+4410103	157.94	-3.85	28	2.43
04233241+3748200	162.56	-8.25	27	2.23
04233266+5010274	153.71	0.42	17	2.85
04241490+3725180	162.94	-8.41	33	3.35
04242347+3724490	162.96	-8.40	15	2.80
04251272+4453366	157.67	-3.08	16	3.09
04253229+3739096	162.95	-8.07	14	2.85
04254171+4631366	156.56	-1.88	16	3.16
04254723+4408199	158.29	-3.53	16	3.11
04263635+3813072	162.68	-7.52	17	2.73
04264042+3810182	162.73	-7.55	15	3.39
04273027+3750036	163.09	-7.66	11	3.17
04273554+4647302	156.60	-1.46	34	2.25
04292626+4855120	155.27	0.24	27	2.38
04292839+3849211	162.63	-6.70	34	2.45
04293884+5125188	153.48	1.98	18	3.17
04295264+3521545	165.24	-9.00	24	2.29
04295532+4353088	158.99	-3.17	19	3.37
04300586+3522252	165.26	-8.96	16	3.10
04301103+4729248	156.40	-0.66	27	3.86

Table A.1 – Continued

2MASX identifier [hhmmssss ± ddmmssss] *Col (1)*	gal l [deg] *Col (2)*	gal b [deg] *Col (3)*	Ncyc no. *Col (4)*	rms [m Jy] *Col (5)*
04303090+5312130	152.28	3.30	14	3.87
04304765+4131316	160.82	-4.67	52	1.94
04312427+4748209	156.31	-0.29	44	1.99
04312715+4752279	156.26	-0.24	20	3.73
04360363+4030314	162.24	-4.63	13	3.06
04361434+4500084	158.93	-1.58	29	2.34
04383916+5154076	154.08	3.34	29	2.58
04390214+4608079	158.42	-0.46	23	2.91
04393567+4436440	159.62	-1.40	14	3.15
04400189+4540140	158.88	-0.64	22	2.79
04414382+4433342	159.91	-1.15	26	2.36
04415187+5045599	155.26	2.96	37	2.32
04421071+5120222	154.86	3.37	32	2.59
04422924+5108582	155.04	3.29	29	2.50
04424005+3541451	166.74	-6.84	17	2.48
04424586+3848466	164.38	-4.79	16	2.68
04424681+4052046	162.82	-3.44	14	3.33
04425181+5101358	155.17	3.25	43	2.10
04425353+5114549	155.00	3.40	31	2.62
04430935+4425043	160.19	-1.05	13	3.32
04431593+3850025	164.42	-4.70	23	2.70
04440032+3900361	164.38	-4.47	27	2.56
04440562+3853161	164.49	-4.54	37	2.04
04441374+3911350	164.27	-4.32	25	2.53
04442990+4429146	160.29	-0.83	26	2.65
04445716+3231058	169.49	-8.53	18	2.43
04445949+4533441	159.53	-0.06	13	3.28
04450255+3758177	165.31	-4.99	11	3.06
04453613+5059042	155.48	3.55	27	3.16
04461266+3725188	165.88	-5.17	18	2.55
04463939+4540516	159.63	0.24	21	2.65
04464394+3435108	168.13	-6.92	35	1.86
04465712+4729304	158.29	1.45	35	2.28
04471937+4417021	160.77	-0.58	54	1.87
04472295+4013271	163.88	-3.19	17	2.78
04472421+4459281	160.24	-0.11	22	2.53
04473473+4529122	159.89	0.24	11	3.92
04475352+4432511	160.64	-0.33	9	4.22
04475541+3428204	168.38	-6.80	16	2.69
04482813+4952069	156.63	3.18	34	2.67
04484325+4452164	160.49	-0.01	32	3.41
04484660+4334294	161.48	-0.83	29	2.42
04491793+4453124	160.54	0.08	10	4.48
04492256+3730389	166.22	-4.64	27	2.00
04493984+4409215	161.14	-0.34	15	3.16
04494400+4911411	157.28	2.90	16	3.61
04501843+4541517	160.03	0.74	17	3.20
04502798+4434077	160.92	0.04	33	2.21
04503277+4454116	160.67	0.26	14	3.65
04504074+4503124	160.57	0.38	31	3.00
04504592+4506595	160.53	0.43	28	2.41
04504934+4457425	160.66	0.34	30	2.37
04505300+4508055	160.53	0.46	18	2.54
04510938+5128076	155.67	4.53	34	2.22
04511770+4512083	160.52	0.56	17	2.88

Table A.1 – Continued

2MASX identifier [hhmmssss ± ddmmssss] *Col (1)*	gal l [deg] *Col (2)*	gal b [deg] *Col (3)*	Ncyc no. *Col (4)*	rms [m Jy] *Col (5)*
04512165+4517254	160.46	0.62	20	3.27
04512932+4518524	160.46	0.65	30	2.50
04515659+4458144	160.77	0.50	16	3.39
04521994+4515456	160.59	0.73	16	3.27
04522577+4934396	157.26	3.48	28	2.67
04523133+4927346	157.37	3.42	27	2.52
04523985+5203046	155.37	5.08	33	3.07
04524698+5135515	155.73	4.80	18	2.98
04525192+4441218	161.10	0.44	41	2.37
04525281+5204476	155.36	5.12	49	5.77
04525545+5156396	155.47	5.04	17	5.23
04525591+3438448	168.90	-5.90	18	2.40
04532441+4511276	160.77	0.84	14	3.39
04532674+4419006	161.45	0.29	28	2.48
04532922+4152201	163.35	-1.25	20	2.77
04533259+4532326	160.51	1.08	13	3.98
04534624+4507475	160.86	0.85	42	2.39
04541186+4127583	163.75	-1.41	25	2.56
04541490+4503149	160.97	0.86	16	3.11
04542558+5203496	155.53	5.29	16	3.19
04544599+4620599	160.02	1.75	18	2.76
04550178+5159483	155.64	5.32	28	3.23
04550702+4559478	160.33	1.58	29	2.39
04552286+4546214	160.53	1.47	28	2.52
04554245+4402134	161.92	0.43	30	2.31
04554990+4533540	160.75	1.40	30	2.41
04563241+4534186	160.82	1.50	17	2.93
04565773+4426507	161.74	0.86	15	3.22
04570846+4942147	157.65	4.16	33	3.08
04571144+4420115	161.85	0.82	16	3.13
04574655+4126307	164.19	-0.90	23	2.10
04574727+4146237	163.93	-0.69	20	2.69
04580654+4552108	160.76	1.90	38	2.46
04580915+4208498	163.68	-0.41	16	2.71
04580946+5134192	156.27	5.44	31	3.15
04584955+5133076	156.35	5.51	26	2.77
04595512+4312240	163.05	0.51	18	2.81
05003753+4231251	163.66	0.19	17	3.37
05012183+3409111	170.37	-4.84	16	2.61
05015592+4419410	162.39	1.48	32	1.96
05021216+4734599	159.84	3.51	16	2.93
05024020+3520357	169.59	-3.90	23	2.44
05031826+4357546	162.82	1.46	24	2.68
05032503+4749366	159.77	3.82	29	2.45
05055384+4121469	165.18	0.26	25	2.39
05062450+3535105	169.85	-3.14	58	1.77
05063010+4512499	162.17	2.67	15	3.29
05063335+4417469	162.91	2.12	14	3.08
05072947+4723396	160.53	4.11	26	2.16
05122582+4519525	162.70	3.57	35	2.33
05123258+4426135	163.44	3.07	40	2.49
05141860+4622066	162.05	4.45	46	2.13
05142584+3423225	171.80	-2.53	16	2.68
05154589+3413462	172.08	-2.40	19	2.24
05165475+3421093	172.12	-2.13	17	2.82

Table A.1 – Continued

2MASX identifier [hhmmssss ± ddmmssss] *Col (1)*	gal l [deg] *Col (2)*	gal b [deg] *Col (3)*	Ncyc no. *Col (4)*	rms [m Jy] *Col (5)*
05165843+3403392	172.37	-2.29	35	2.07
05170274+3352532	172.52	-2.38	23	2.24
05171201+3921481	168.07	0.81	20	2.85
05174322+3442322	171.93	-1.79	11	3.26
05215822+4058480	167.26	2.49	25	2.41
05221961+2150424	183.15	-8.25	12	2.59
05250816+3221028	174.75	-1.86	59	1.42
05252560+2443418	181.13	-6.06	17	2.57
05253779+3419073	173.17	-0.67	33	2.13
05254062+4141530	167.06	3.46	67	1.58
05281320+3116566	176.00	-1.91	13	3.06
05313269+3529135	172.87	0.98	16	2.76
05372363+3604312	173.02	2.30	31	1.87
05385507+3337492	175.26	1.26	36	1.85
05393522+2841388	179.51	-1.25	21	2.43
05402435+3311311	175.79	1.29	42	2.15
05402818+3313361	175.77	1.32	31	1.95
05405882+3159438	176.87	0.76	49	1.80
05411745+3440059	174.64	2.23	25	2.03
05411834+2249028	184.71	-4.03	16	2.40
05413586+2357039	183.78	-3.38	16	2.33
05413712+2930454	179.05	-0.44	15	2.59
05414547+2937244	178.97	-0.36	44	1.53
05425805+3049039	178.10	0.50	30	1.92
05431777+3138489	177.43	0.99	26	1.90
05434263+3516031	174.39	2.96	29	2.32
05434892+3056391	178.08	0.72	14	2.67
05452013+3649316	173.23	4.05	36	1.75
05452124+2321174	184.74	-2.96	28	1.83
05454087+2813165	180.62	-0.36	31	1.89
05471940+2444422	183.78	-1.85	13	2.83
05480756+2141579	186.49	-3.27	33	1.87
05491821+1947083	188.28	-4.01	22	2.15
05501167+3258153	177.05	2.92	17	2.59
05502254+2334244	185.14	-1.86	29	1.65
05504707+2701149	182.23	-0.01	48	1.84
05511944+1855027	189.27	-4.04	16	2.50
05515128+1818051	189.86	-4.25	15	2.34
05521278+3344455	176.60	3.68	48	1.60
05524113+3056577	179.06	2.35	49	1.98
05531219+2144149	187.06	-2.23	16	2.56
05575173+2233406	186.89	-0.88	8	3.51
05583187+2244210	186.81	-0.66	13	2.78
06020437+2311047	186.83	0.27	16	3.93
06021688+1901026	190.48	-1.75	11	2.96
06022068+2844085	182.03	3.06	15	2.87
06031802+1847563	190.79	-1.65	15	2.86
06034588+1812362	191.35	-1.84	18	2.27
06060282+3003307	181.27	4.41	15	2.90
06080358+3122592	180.31	5.42	33	1.70
06080417+2802003	183.26	3.82	33	1.80
06092756+1338133	196.02	-2.87	32	1.66
06095101+1839501	191.66	-0.36	17	2.23
06095948+1910113	191.23	-0.08	32	1.87
06130977+1427300	195.73	-1.69	32	1.76

Table A.1 – Continued

2MASX identifier [hhmmssss ± ddmmssss] *Col (1)*	gal l [deg] *Col (2)*	gal b [deg] *Col (3)*	Ncyc no. *Col (4)*	rms [m Jy] *Col (5)*
06141832+1658308	193.65	-0.24	27	2.19
06160639+1659496	193.84	0.15	16	2.55
06162063+0717492	202.41	-4.40	46	1.97
06162583+1654326	193.95	0.18	11	2.86
06163615+1058407	199.19	-2.61	11	3.48
06171616+1655575	194.03	0.36	11	3.44
06193159+1601422	195.08	0.41	12	2.85
06201192+2332563	188.51	4.09	24	2.34
06222944+1027158	200.34	-1.58	13	2.76
06245794+1458369	196.62	1.08	32	1.74
06255436+0632286	204.19	-2.66	15	2.75
06262702+0727287	203.45	-2.11	30	2.07
06263895+1601067	195.89	1.92	17	2.42
06283437+0623064	204.64	-2.14	16	2.74
06294669+1032181	201.10	0.05	16	2.63
06315346-0930076	219.24	-8.63	26	1.92
06341652+0758280	203.88	-0.15	16	2.50
06343138+0904375	202.93	0.41	51	1.44
06343673+0238144	208.66	-2.54	16	2.75
06344020+0139344	209.54	-2.97	33	1.84
06344281+0445594	206.78	-1.53	96	1.18
06344281+0445594	206.78	-1.53	96	1.22
06355362+0438272	207.03	-1.33	24	2.04
06383251+1035536	202.04	1.99	18	2.38
06393966+0846004	203.79	1.39	32	1.63
06414770+1102252	202.01	2.90	44	1.55
06473930-0000098	212.50	-0.84	79	1.09
06483359+0145387	211.04	0.16	33	1.47
06503049-0248387	215.33	-1.49	46	1.48
06504824-0336287	216.07	-1.79	7	3.45
06513438-0350052	216.36	-1.72	51	1.36
06532549-1122118	223.30	-4.72	31	1.68
06562541-0300515	216.18	-0.27	31	1.98
06570322-0501137	218.04	-1.04	58	1.24
06590970-0249301	216.33	0.43	32	1.51
07003437-1020151	223.17	-2.69	16	2.31
07011704-0711332	220.45	-1.10	41	1.49
07030812-1109581	224.20	-2.51	55	1.63
07031926-1246259	225.65	-3.20	57	1.85
07044419-1106510	224.33	-2.14	32	1.86
07052068-1711008	229.81	-4.77	33	1.77
07054925-1611251	228.98	-4.22	17	2.22
07143657-1857385	232.41	-3.62	32	1.86
07143807-1003285	224.52	0.51	41	1.49
07160927-1950273	233.36	-3.71	28	1.91
07231967-1618397	231.03	-0.55	49	1.54
07235168-1053287	226.32	2.13	35	1.59
07264631-2351096	238.06	-3.41	52	1.47
07273064-1308046	228.72	1.85	16	2.55
07273273-2319396	237.68	-3.00	31	2.32
07273400-1308106	228.72	1.86	31	1.88
07291623-2048113	235.65	-1.45	31	2.07
07294973-2534569	239.92	-3.62	43	1.73
07323290-1923246	234.78	-0.09	48	1.83
07324220-1354035	229.99	2.59	45	1.38

Table A.1 – Continued

2MASX identifier [hhmmssss ± ddmmssss] *Col (1)*	gal l [deg] *Col (2)*	gal b [deg] *Col (3)*	Ncyc no. *Col (4)*	rms [m Jy] *Col (5)*
07332576-2543462	240.44	-2.97	30	2.02
07343132-2444126	239.69	-2.28	48	1.32
07351136-2633207	241.35	-3.03	46	1.51
07361741-2522246	240.44	-2.24	18	2.41
07374792-1643482	233.07	2.29	15	2.57
07374848-1310042	229.95	4.03	17	2.57
07375734-2839078	243.49	-3.51	41	1.93
07380245-2710388	242.21	-2.77	62	1.61
07385787-2455377	240.34	-1.49	15	2.70
07411855-1642051	233.45	3.04	36	1.81
07413450-1611117	233.04	3.35	14	2.67
07414443-1608057	233.01	3.41	19	2.39
07431751-3333172	248.33	-4.91	26	2.47
07431853-2006196	236.65	1.77	15	2.58
07442784-1820196	235.25	2.88	13	2.96
07451725-3413310	249.12	-4.89	31	2.43
07452996-2715311	243.10	-1.37	27	2.10
07465855-2915253	244.99	-2.09	22	2.42
07471479-3049352	246.38	-2.83	15	3.32
07473672-2101573	237.96	2.17	12	3.02
07474347-2520380	241.69	0.02	29	1.98
07483527-2250005	239.63	1.46	13	2.89
07484838-2449451	241.37	0.49	18	2.65
07485088-2503171	241.57	0.39	25	2.14
07485977-2650561	243.14	-0.49	24	2.46
07490339-2458491	241.53	0.47	41	1.69
07494054-3341019	249.11	-3.83	26	2.82
07495208-2729568	243.79	-0.66	17	2.77
07500081-3142080	247.43	-2.76	41	2.09
07505059-3053204	246.82	-2.20	24	2.46
07515109-2523545	242.21	0.80	13	2.80
07521098-2100174	238.47	3.11	13	2.79
07523883-3224563	248.33	-2.65	39	2.58
07524324-2431356	241.57	1.41	34	2.34
075257-215608	239.37	2.79	17	2.78
07531836-3611492	251.66	-4.46	49	2.22
07541134-2423269	241.62	1.77	5	2.74
07541170-2423209	241.62	1.77	30	2.04
07543034-3524203	251.10	-3.85	26	2.81
07554671-2716477	244.28	0.58	29	2.09
07563338-2150060	239.71	3.55	16	2.50
07565545-3127593	247.99	-1.38	28	2.44
07575928-2157182	239.99	3.78	34	1.72
07582363-2159463	240.07	3.84	32	1.89
07585016-2214423	240.34	3.79	31	2.45
07585434-2219534	240.42	3.76	24	2.32
07585614-2220434	240.43	3.76	15	2.78
07591260-2050166	239.18	4.60	16	2.60
08000105-2415483	242.20	2.97	13	2.99
08005067-3155465	248.82	-0.91	16	3.16
08023477-3746569	253.98	-3.70	47	3.11
08032461-2727357	245.32	1.93	13	3.01
08074237-3544499	252.81	-1.74	29	2.77
08080066-3558243	253.03	-1.81	72	2.32
08090254-2427021	243.46	4.61	13	2.74

Table A.1 – Continued

2MASX identifier [hhmmssss ± ddmmssss] *Col (1)*	gal l [deg] *Col (2)*	gal b [deg] *Col (3)*	Ncyc no. *Col (4)*	rms [m Jy] *Col (5)*
08105503-3051287	249.07	1.48	24	2.54
08115216-2854143	247.55	2.72	13	3.23
08124035-3323491	251.40	0.40	30	2.31
08131734-3118595	249.73	1.65	16	2.66
08142478-3225000	250.78	1.24	39	2.80
08143768-3305480	251.37	0.90	36	2.66
08145230-3311297	251.48	0.89	29	2.32
08145956-3309457	251.47	0.93	24	2.54
08164477-3846546	256.33	-1.91	39	3.65
08170147-3410277	252.55	0.72	26	2.87
08172741-2759259	247.46	4.25	26	2.03
08182775-3547298	254.05	0.05	46	2.72
08224226-3240398	251.98	2.54	27	2.77
08242635-3642433	255.49	0.52	32	2.72
08293905-3526048	255.06	2.12	26	2.97
08305941-3249032	253.11	3.88	31	2.58
08441291-3612532	257.47	4.01	25	3.30
08480354-3555256	257.72	4.80	22	3.42
08522527-3926038	261.00	3.25	57	4.86
16160007-3730193	341.71	9.52	13	5.30
16163174-3826308	341.12	8.78	16	5.30
16171926-3740403	341.78	9.21	49	2.83
16173004-3649262	342.42	9.79	62	2.43
16180021-3657068	342.40	9.63	47	2.35
16183236-3723459	342.15	9.24	11	5.73
16193769-3757523	341.90	8.69	49	2.80
16220379-3811082	342.08	8.19	21	4.81
16221431-3809491	342.12	8.18	8	7.42
16230766-3739356	342.61	8.41	29	4.22
16342826-3857439	343.19	5.89	51	3.15
16414252-3619588	346.12	6.57	8	5.19
16465670-3721166	346.03	5.11	24	2.87
16470867-3616459	346.88	5.77	31	3.16
16481772-3810061	345.57	4.38	23	4.20
16512573-3307205	349.89	7.10	31	2.88
16515849-3545456	347.90	5.34	47	2.54
16522835-3303135	350.09	6.97	25	3.03
16530380-3548500	348.00	5.14	25	3.30
16553517-3532460	348.54	4.91	31	2.83
16574847-3438179	349.53	5.12	41	2.58
17000638-3152265	352.02	6.44	16	2.84
17024654-3405128	350.60	4.64	32	2.58
17073820-2814301	355.93	7.32	33	2.17
17123572-2548136	358.58	7.84	11	3.37
17144212-2550472	358.82	7.43	25	2.71
17160689-2438342	360.00	7.86	29	2.43
17165337-2647470	358.32	6.49	30	2.33
17172859-2417256	0.47	7.80	14	2.91
17172860-2409406	0.58	7.88	30	2.03
17173605-2413026	0.55	7.82	13	2.73
17183985-2454314	0.11	7.23	11	3.13
17194814-2528040	359.79	6.70	42	1.80
17423620-3854340	351.16	-4.68	29	4.70
17521905-1517459	12.52	5.67	27	1.99
17575504-1138276	16.39	6.30	17	2.57

Table A.1 – Continued

2MASX identifier [hhmmssss ± ddmmssss] *Col (1)*	gal l [deg] *Col (2)*	gal b [deg] *Col (3)*	Ncyc no. *Col (4)*	rms [m Jy] *Col (5)*
17581377-1241453	15.51	5.71	15	2.46
17582147-1137141	16.47	6.22	17	2.31
17585489-0836334	19.18	7.57	15	2.69
17590767-1333006	14.87	5.10	17	2.74
17591740-0833394	19.27	7.51	10	2.75
17592016-0831286	19.31	7.52	14	2.69
17594870-1328559	15.01	4.99	15	2.65
18010993-0822352	19.66	7.19	13	2.69
18035726-0813268	20.13	6.66	17	2.65
18100236-0043306	27.52	8.87	14	2.75
18103194-0652259	22.10	5.87	13	2.94
18140441-0822089	21.20	4.39	15	2.72
18141853-0607349	23.21	5.40	15	3.16
18151860-0834552	21.16	4.02	13	2.92
18160148-0826232	21.37	3.93	18	2.12
18172445-0424551	25.09	5.52	13	4.91
18192432-3107470	1.68	-7.45	34	2.28
18202335-0117447	28.22	6.31	9	3.07
18203316-0121387	28.18	6.24	18	2.24
18221913-0449343	25.30	4.25	15	2.55
18275944+0031420	30.72	5.46	16	2.62
18310342-2347198	9.45	-6.41	18	2.93
18333199-0001072	30.87	3.97	13	3.12
18360903-0036239	30.65	3.12	14	2.96
18384124+0141147	32.98	3.61	11	2.71
18432770+0553498	37.28	4.45	14	2.77
18452225+0533245	37.20	3.88	14	3.24
18504202+0715029	39.31	3.46	30	2.00
18524710+0939480	41.70	4.09	17	2.63
18531497-0623155	27.45	-3.31	13	4.43
18565611-0613346	28.01	-4.05	17	2.41
18573128-0436546	29.51	-3.45	16	2.51
18583627+1137375	44.10	3.71	13	2.92
19004514+1741359	49.77	5.98	9	3.85
19041528+1256371	45.91	3.08	12	2.77
19120105+2043284	53.70	4.98	15	2.51
19123993+1728258	50.87	3.35	13	2.99
19124699+0256056	37.99	-3.40	16	3.41
19203180+0836246	43.91	-2.47	13	2.92
19205612+1841331	52.87	2.17	14	2.80
19223320+2054242	55.00	2.88	13	2.99
19225733+0833551	44.16	-3.02	14	3.02
19241113+2208141	56.27	3.12	14	2.44
19285189+1307064	48.86	-2.15	16	2.28
19312354+2632370	60.93	3.77	18	2.69
19315025+2543597	60.27	3.29	17	2.35
19365060+3039283	65.13	4.69	37	1.96
19382863+2810502	63.13	3.18	15	2.51
19390019+1631210	53.03	-2.64	17	2.25
19390547+2856372	63.86	3.43	11	3.17
19410154+2638147	62.06	1.93	32	1.80
19530266+1953218	57.62	-3.85	11	2.84
19564949+2141345	59.62	-3.68	14	2.96
19573332+3211022	68.67	1.64	16	4.99
20000942+4321590	78.52	7.01	15	3.56

Table A.1 – Continued

2MASX identifier [hhmmssss ± ddmmssss] *Col (1)*	gal l [deg] *Col (2)*	gal b [deg] *Col (3)*	Ncyc no. *Col (4)*	rms [m Jy] *Col (5)*
20010969+2655338	64.60	-1.79	8	3.35
20092153+2718462	65.91	-3.12	15	2.71
20092934+2818579	66.77	-2.60	16	2.73
20100506+2557368	64.86	-3.99	12	3.32
20101324+2850488	67.30	-2.45	17	2.49
20114417+2743549	66.55	-3.34	16	2.17
20114644+3649348	74.16	1.64	16	3.01
20125530+4310184	79.60	4.94	16	3.56
20135618+4443093	81.00	5.63	10	4.47
20141998+3732490	75.04	1.62	25	2.55
20171300+4341267	80.47	4.57	37	3.57
20201507+4148266	79.22	3.05	34	2.83
20202170+3954306	77.66	1.96	22	3.20
20212592+4438079	81.68	4.48	27	2.33
20231262+3925015	77.57	1.23	38	2.73
20252529+4103192	79.15	1.83	34	3.57
20321160+4937105	86.82	5.85	17	3.35
20321954+4951445	87.03	5.98	2	8.18
20334726+4511401	83.40	3.02	34	2.81
20341242+4658296	84.88	4.02	44	3.39
20351333+3947557	79.23	-0.42	29	3.31
20351918+4542555	83.98	3.11	34	2.48
20362143+3634452	76.79	-2.53	24	2.54
20394281+3211363	73.70	-5.73	13	3.85
20400769+3853421	79.09	-1.72	16	3.49
20401346+5059165	88.70	5.64	16	3.60
20403052+5054257	88.66	5.55	10	4.43
20412222+5054235	88.74	5.45	12	4.23
20415515+4532386	84.55	2.09	16	3.49
20420550+4636124	85.40	2.72	24	2.93
20440027+4143156	81.77	-0.56	24	2.81
20453717+4046002	81.21	-1.40	26	2.51
20470471+4046165	81.39	-1.61	28	2.01
20491597+5119089	89.84	4.73	19	3.27
20494713+5206261	90.50	5.16	14	4.19
20494797+5041271	89.40	4.27	34	3.05
20514892+5132328	90.26	4.56	11	3.67
20525943+5311105	91.65	5.47	12	4.28
20535370+5012580	89.45	3.46	25	2.66
20550635+4603460	86.40	0.63	14	2.58
20564755+5441095	93.17	6.00	16	3.72
20573213+4548173	86.47	0.15	26	2.90
20584833+4535334	86.46	-0.16	17	3.10
20590227+4251273	84.42	-1.98	16	3.29
21042220+4742415	88.68	0.52	16	3.17
21053995+4958040	90.50	1.87	17	3.11
21054461+4958350	90.51	1.87	28	2.68
21055031+4956260	90.50	1.84	29	3.15
21060867+4532092	87.27	-1.16	10	3.80
21081300+4403398	86.43	-2.43	16	3.00
21084767+4354039	86.38	-2.61	30	2.74
21085630+4451164	87.10	-1.98	23	2.87
21121597+4531167	87.99	-1.96	13	3.92
21140974+4835425	90.44	-0.08	30	2.89
21155845+4655229	89.44	-1.45	47	2.41

Table A.1 – Continued

2MASX identifier [hhmmssss ± ddmmssss] *Col (1)*	gal l [deg] *Col (2)*	gal b [deg] *Col (3)*	Ncyc no. *Col (4)*	rms [m Jy] *Col (5)*
21162340+4547366	88.68	-2.29	18	2.98
21164349+5200341	93.18	2.00	13	4.57
21164758+5508395	95.44	4.17	23	3.26
21174271+4815503	90.61	-0.73	32	1.98
21181305+4526187	88.65	-2.77	14	3.04
21184034+5218497	93.61	2.00	15	3.88
21195943+5519423	95.89	3.98	42	2.85
21202103+4519063	88.83	-3.12	15	3.50
21214731+4414419	88.25	-4.06	11	3.30
21215894+5219203	93.97	1.65	15	3.43
21231420+4850254	91.66	-0.97	15	3.10
21240760+4943370	92.39	-0.44	21	3.94
21242503+4933591	92.31	-0.59	58	2.06
21253828+4809267	91.47	-1.74	22	2.72
21255239+4423193	88.87	-4.47	26	3.13
21263514+4541569	89.87	-3.61	30	3.39
21274031+4741107	91.39	-2.31	16	3.33
21292943+5030411	93.55	-0.47	23	2.93
21311568+4752142	91.95	-2.59	31	2.54
21324206+4816460	92.41	-2.46	26	2.66
21333640+4747326	92.19	-2.92	15	2.97
21350281+5309074	95.98	0.88	32	2.69
21355259+4734217	92.32	-3.34	29	2.48
21355399+4728217	92.26	-3.41	33	1.80
21362763+5936230	100.47	5.53	11	4.73
21411938+5103170	95.30	-1.32	16	3.10
21413756+5245302	96.45	-0.07	43	2.28
21464183+5427064	98.13	0.73	31	2.81
21511714+5439331	98.77	0.47	48	1.84
21523166+5245290	97.72	-1.13	45	2.16
21565664+5539243	100.02	0.75	61	1.60
22051447+6048418	104.01	4.20	42	3.82
22051749+5935350	103.29	3.22	49	2.35
22103166+5535087	101.52	-0.45	23	3.35
22131198+6153077	105.41	4.52	32	3.56
22200608+5846345	104.39	1.47	21	3.99
22201001+6345395	107.13	5.63	21	4.10
22220225+5837501	104.52	1.21	42	3.03
22234144+5140563	100.98	-4.78	47	2.03
22262597+6135161	106.56	3.42	46	2.66
22342113+5759454	105.57	-0.18	38	3.32
22491636+6053023	108.61	1.46	65	3.38
22505236+5930185	108.17	0.13	47	2.60
22540054+6728086	112.02	7.12	19	4.05
22541372+5702353	107.48	-2.27	48	2.28
22545382+5756391	107.95	-1.50	43	3.05
23013861+5711360	108.46	-2.56	43	2.64
23145710+5928024	110.95	-1.14	73	2.73
23160977+6136280	111.86	0.80	34	3.15
23170993+6131091	111.94	0.68	21	3.81
23230542+6135541	112.63	0.51	55	2.38
23360810+6223466	114.33	0.79	67	2.57
23530292+6727217	117.36	5.22	64	3.11
23541834+5959178	115.84	-2.09	32	2.69
23552751+6701119	117.50	4.74	62	2.76

Table A.1 – Continued

2MASX identifier [hhmmssss ± ddmmssss] *Col (1)*	gal l [deg] *Col (2)*	gal b [deg] *Col (3)*	Ncyc no. *Col (4)*	rms [m Jy] *Col (5)*
23570980+6437388	117.16	2.37	57	2.34

Appendix B

The 2MASX catalogue of the extinction-corrected ZoA galaxies

This appendix lists in Table. B.1 NIR parameters available from the 2MASS Extended Sources Catalogue. It is for all 928 bright ($K_s^o \leq 11\overset{\text{m}}{.}25$) galaxy candidates observed. Columns are sorted by right ascension and are as follows:

Column 1: 2MASX identifier [2MASXJhhmmss.sss ± ddmmss.ss].

Column 2 & 3: Galactic coordinates [deg].

Column 4: Galactic reddening, $E(B-V)$ (Schlegel et al. 1998) [mag].

Column 5: Log of the stellar density for stars brighter than $14\overset{\text{m}}{.}00$ in K_s (SD).

Column 6: $K_{s_{20}}$ isophotal major axis, $a_{K_{20}}$ [arcsec].

Column 7: $K_{s_{20}}$ isophotal minor axis, $b_{K_{20}}$ [arcsec].

Column 8: K_s-band $K_{s_{20}}$ isophotal magnitude [mag].

Column 9: The difference between the H-band and K_s-band magnitude $(H-K)$ [mag].

Column 10: The difference between the J-band and K_s-band magnitude$(J-K)$ [mag].

Column 11: Dust extinction in the K_s-band, A_{K_s} [mag].

Column 12: Extinction-corrected K_s-band K_s^o isophotal magnitude [mag].

Column 13: Extinction-corrected difference between the H-band and K_s-band magnitude $(H-K)_o$ [mag].

Column 14: Extinction-corrected difference between the J-band and K_s-band magnitude $(J-K)_o$ [mag]

Table B.1: The 2MASX NIR parameters of observed galaxies.

2MASXJ identifier [hhmmssss ± ddmmssss] (1)	gal l [deg] (2)	gal b [deg] (3)	$E(B-V)$ [mag] (4)	SD (5)	$a_{K_{20}}$ [arcsec] (6)	$b_{K_{20}}$ [arcsec] (7)	$K_{s_{20}}$ [mag] (8)	$H-K$ [mag] (9)	$J-K$ [mag] (10)	A_{K_s} [mag] (11)	K_s^o [mag] (12)	$(H-K)_o$ [mag] (13)	$(J-K)_o$ [mag] (14)
00102576+6520598	118.67	2.82	4.55	3.8	11.6	7.0	12.28	0.83	2.42	1.70	10.58	0.07	0.16
00141253+7036448	119.82	7.97	1.01	3.6	26.7	13.4	10.91	0.39	1.37	0.38	10.54	0.22	0.86
00161976+7025219	119.97	7.75	1.05	3.5	12.1	8.5	11.32	0.32	0.99	0.39	10.94	0.15	0.47
00223972+6139447	119.52	-1.02	1.73	3.9	41.6	28.3	11.49	0.48	1.64	0.70	10.85	0.19	0.78
00253292+6821442	120.54	5.61	1.04	3.6	33.9	17.0	10.04	0.40	1.37	0.39	9.66	0.23	0.85
00265869+6054037	119.96	-1.83	0.83	3.9	9.1	7.3	12.53	0.41	1.49	0.30	12.22	0.27	1.07
00265906+6049388	119.95	-1.90	0.93	3.8	31.2	22.5	11.53	0.45	1.47	0.30	11.18	0.30	1.01
00281959+6447011	120.47	2.02	3.25	3.8	13.3	5.3	11.84	0.64	1.91	1.21	10.63	0.10	0.29
00295328+6350552	120.56	1.08	2.80	3.9	14.9	6.0	11.48	1.13	2.99	1.04	10.44	0.66	1.60
00303425+6444585	120.71	1.97	1.76	3.8	28.8	19.0	11.82	0.50	1.81	0.70	11.17	0.21	0.94
00314802+6227440	120.66	-0.32	1.96	3.9	12.1	10.9	11.88	–	–	0.73	11.14	–	–
00321813+6029565	120.58	-2.29	0.81	3.8	28.8	21.9	11.38	0.35	1.27	0.30	11.08	0.22	0.87
00343086+6257451	121.01	0.15	1.45	3.9	38.2	16.8	11.23	0.34	1.28	0.60	10.69	0.09	0.56
00343656+6310260	121.03	0.36	1.53	3.9	25.0	18.5	11.53	0.41	1.57	0.60	10.96	0.17	0.81
00360888+6319171	121.22	0.50	1.37	3.9	37.0	15.5	11.37	0.69	1.95	0.50	10.86	0.46	1.27
00384223+6017130	121.35	-2.55	0.72	3.8	50.8	31.5	10.94	0.31	1.20	0.30	10.67	0.19	0.84
00402126+6732350	121.87	4.69	1.46	3.8	36.0	28.8	11.51	0.49	1.51	0.50	10.97	0.26	0.79
00402382+6428443	121.74	1.63	1.83	3.9	32.0	15.4	11.54	0.79	2.06	0.70	10.86	0.49	1.15
00450852+6549280	122.29	2.96	1.60	3.8	27.8	16.7	11.82	0.53	1.80	0.60	11.22	0.26	1.01
00475430+6807433	122.60	5.26	1.14	3.6	37.0	14.8	10.86	0.50	1.42	0.43	10.43	0.31	0.85
00501956+6702517	122.82	4.18	1.41	3.8	44.6	32.1	10.64	0.47	1.62	0.50	10.12	0.24	0.92
00532380+6128104	123.17	-1.40	1.02	3.8	28.0	17.9	11.61	0.49	1.46	0.40	11.23	0.32	0.96
00553400+6551452	123.36	2.99	4.39	3.8	22.0	15.0	12.52	0.55	1.60	1.50	10.88	0.18	-0.58
01010569+5804266	124.21	-4.77	0.48	3.6	19.5	3.9	10.34	0.17	0.81	0.18	10.16	0.09	0.57
01010771+6254430	124.03	0.06	3.02	3.9	75.2	43.6	10.82	0.92	1.99	1.00	9.70	0.43	0.49
01013460+6715038	123.92	4.40	1.28	3.8	34.8	24.4	11.26	0.43	1.52	0.50	10.78	0.22	0.89
01021854+6708091	123.99	4.29	1.29	3.8	21.6	10.8	11.32	–	1.51	0.48	10.85	–	0.87
01135448+6440014	125.33	1.90	1.56	3.9	40.8	30.2	10.47	0.52	1.60	0.60	9.89	0.26	0.82
01191829+6219297	126.16	-0.37	1.24	3.8	62.2	19.9	10.67	0.52	1.68	0.50	10.21	0.32	1.06
01203021+6525055	125.95	2.72	1.28	3.8	80.2	46.5	9.96	0.45	1.43	0.50	9.48	0.24	0.80
01230734+6049177	126.79	-1.81	0.55	3.9	51.2	19.5	10.85	0.31	1.19	0.20	10.65	0.21	0.91
01261932+6046064	127.18	-1.81	0.67	3.8	63.8	42.1	10.15	0.48	1.43	0.20	9.90	0.37	1.10
01273787+6308155	127.01	0.55	1.71	3.8	35.8	30.1	10.93	0.62	1.83	0.60	10.29	0.33	0.97

Table B.1 – Continued

2MASXJ identifier [hhmmssss ± ddmmssss] (1)	gal l [deg] (2)	gal b [deg] (3)	$E(B-V)$ [mag] (4)	SD (5)	$a_{K_{20}}$ [arcsec] (6)	$b_{K_{20}}$ [arcsec] (7)	$K_{s_{20}}$ [mag] (8)	$H-K$ [mag] (9)	$J-K$ [mag] (10)	A_{K_s} [mag] (11)	K_s^o [mag] (12)	$(H-K)_o$ [mag] (13)	$(J-K)_o$ [mag] (14)
01281012+6313517	127.05	0.65	1.66	4.0	77.8	24.9	10.30	0.49	1.62	0.60	9.68	0.23	0.80
01311294+6735115	126.72	5.01	1.02	3.7	16.0	14.4	11.52	0.44	1.47	0.38	11.13	0.27	0.96
01312331+6019128	127.86	-2.17	0.55	3.8	31.8	10.8	11.36	0.29	1.11	0.20	11.15	0.20	0.84
01312488+6450068	127.17	2.29	1.29	3.8	36.6	24.9	11.51	0.52	1.74	0.50	11.03	0.31	1.09
01330236+6404589	127.46	1.58	1.60	3.8	24.8	13.9	11.63	0.72	2.06	0.60	11.03	0.46	1.26
01343229+6641235	127.19	4.17	1.15	3.7	24.3	9.7	10.69	0.46	1.34	0.43	10.26	0.27	0.77
01345732+6628216	127.26	3.97	1.19	3.8	36.8	29.4	11.03	0.52	1.52	0.40	10.59	0.32	0.93
01472075+6207593	129.41	-0.03	1.79	3.7	36.2	26.8	11.22	0.51	1.83	0.70	10.55	0.20	0.94
01475111+6305278	129.26	0.91	1.31	3.8	54.2	40.1	9.81	0.52	1.61	0.50	9.32	0.30	0.96
01485859+6045514	129.90	-1.33	1.13	3.9	45.8	16.5	11.04	0.40	1.37	0.40	10.62	0.21	0.80
01572719+6601408	129.58	4.01	1.33	3.8	42.4	24.6	10.57	0.72	2.23	0.50	10.07	0.50	1.57
01575636+5726026	131.82	-4.29	0.42	3.7	71.6	27.2	9.87	0.29	1.08	0.20	9.71	0.22	0.88
01582742+6744421	129.23	5.70	1.30	3.6	13.0	10.4	11.62	0.44	1.49	0.49	11.13	0.23	0.84
02002296+6531178	130.00	3.60	0.85	3.8	35.0	30.8	11.18	0.40	1.33	0.30	10.86	0.26	0.91
02013241+6824219	129.34	6.41	1.12	3.6	44.4	26.6	9.59	0.41	1.37	0.42	9.17	0.23	0.81
02021798+6721240	129.69	5.42	1.64	3.7	27.1	10.8	10.82	0.48	1.61	0.61	10.21	0.21	0.80
02023124+6008000	131.68	-1.53	1.32	3.8	52.8	28.5	11.31	0.55	1.51	0.50	10.82	0.34	0.87
02034595+6650152	129.97	4.96	1.54	3.7	35.4	16.3	11.53	0.56	1.78	0.60	10.96	0.30	1.02
02034762+6843532	129.44	6.78	1.02	3.6	19.9	8.0	11.27	0.35	1.39	0.38	10.89	0.18	0.88
02035883+6737172	129.77	5.72	1.18	3.6	14.5	10.1	11.59	0.38	1.33	0.44	11.16	0.19	0.74
02055021+6749477	129.88	5.97	1.12	3.7	44.3	22.1	9.66	0.31	1.33	0.42	9.25	0.13	0.77
02061555+6823324	129.76	6.52	1.11	3.6	20.4	12.2	11.18	0.44	1.42	0.41	10.77	0.25	0.87
02063421+5855125	132.51	-2.55	0.79	3.9	44.4	21.3	10.40	0.39	1.23	0.30	10.11	0.26	0.83
02072277+5931285	132.43	-1.94	0.98	3.8	50.4	24.2	11.54	0.44	1.33	0.40	11.17	0.28	0.84
02082184+6640353	130.45	4.93	1.19	3.7	13.9	11.1	11.50	–	–	0.44	11.06	–	–
02084861+6228485	131.74	0.94	1.15	3.8	26.8	15.5	11.60	0.41	1.49	0.40	11.17	0.21	0.92
02085980+7114029	129.15	9.30	0.72	3.5	31.8	12.7	11.16	–	–	0.27	10.89	–	–
02085980+7114029	129.15	9.30	0.72	3.5	31.8	12.7	11.16	–	8.83	0.27	10.89	–	–
02101852+6300516	131.74	1.50	1.41	3.8	41.6	18.3	11.36	0.52	1.58	0.50	10.83	0.29	0.88
02103987+6304565	131.76	1.58	1.25	3.8	33.4	16.0	11.12	0.59	1.82	0.50	10.66	0.38	1.20
02121002+6144326	132.33	0.35	1.53	3.8	27.0	19.4	11.50	0.55	1.69	0.60	10.93	0.30	0.93
02132797+6316450	132.00	1.86	1.06	3.8	50.2	33.1	10.64	0.40	1.61	0.40	10.25	0.22	1.07
02153787+6139179	132.75	0.40	1.35	3.8	37.0	22.2	11.60	0.44	1.81	0.50	11.10	0.22	1.13

Table B.1 – Continued

2MASXJ identifier [hhmmssss ± ddmmssss] (1)	gal l [deg] (2)	gal b [deg] (3)	$E(B-V)$ [mag] (4)	SD (5)	$a_{K_{20}}$ [arcsec] (6)	$b_{K_{20}}$ [arcsec] (7)	$K_{s_{20}}$ [mag] (8)	$H-K$ [mag] (9)	$J-K$ [mag] (10)	A_{K_s} [mag] (11)	K_s^o [mag] (12)	$(H-K)_o$ [mag] (13)	$(J-K)_o$ [mag] (14)
02163334+5039016	136.44	-9.97	0.15	3.5	17.8	14.2	11.09	–	1.10	0.06	11.03	–	1.02
02173999+6701444	131.22	5.55	1.26	3.7	10.5	8.4	11.65	0.43	1.50	0.47	11.18	0.22	0.87
02174785+6911364	130.51	7.60	0.85	3.5	17.0	10.2	11.55	–	1.31	0.32	11.23	–	0.89
02220408+6500169	132.32	3.80	1.15	3.7	36.6	22.0	11.40	0.54	1.53	0.40	10.97	0.35	0.96
02235399+6337032	132.99	2.57	0.89	3.8	38.0	25.8	10.97	0.46	1.59	0.30	10.64	0.31	1.15
02240808+6458272	132.54	3.85	1.15	3.7	31.2	21.2	11.12	0.42	1.45	0.40	10.69	0.23	0.88
02243924+5926126	134.54	-1.32	1.08	3.8	35.0	18.2	11.35	0.46	1.51	0.40	10.95	0.27	0.97
02245812+6214020	133.59	1.31	6.65	3.9	20.0	14.0	12.77	0.80	2.33	3.10	10.29	-0.30	-0.98
02293092+6148180	134.24	1.11	1.46	3.9	29.2	12.3	11.47	0.52	1.76	0.60	10.93	0.29	1.05
02294695+6523350	132.94	4.45	1.02	3.7	54.4	17.4	10.72	0.36	1.21	0.40	10.34	0.20	0.70
02322165+6454104	133.38	4.10	1.15	3.7	42.0	17.6	11.37	0.47	1.49	0.40	10.94	0.28	0.92
02324853+6418145	133.65	3.56	0.97	3.8	49.2	26.6	10.90	0.43	1.41	0.40	10.54	0.27	0.94
02332153+6009100	135.29	-0.25	1.24	3.8	46.8	30.0	11.22	0.56	1.84	0.50	10.76	0.35	1.22
02341102+6700106	132.74	6.11	1.30	3.6	21.6	19.4	10.63	0.41	1.52	0.48	10.14	0.19	0.87
02343179+6755266	132.41	6.97	1.08	3.6	21.7	17.4	10.26	0.38	1.43	0.40	9.85	0.20	0.89
02353356+6656497	132.88	6.11	1.11	3.5	24.4	12.2	11.39	0.45	1.50	0.42	10.97	0.27	0.94
02361585+6845014	132.23	7.79	1.13	3.5	15.6	10.9	11.31	0.43	1.44	0.42	10.89	0.24	0.88
02370546+5936210	135.94	-0.57	1.04	3.8	24.0	18.2	11.12	0.47	1.58	0.40	10.73	0.31	1.06
02403604+5854138	136.63	-1.03	1.05	3.8	24.8	22.8	11.32	0.49	1.47	0.40	10.93	0.32	0.95
02421337+6723309	133.30	6.78	1.17	3.6	36.3	7.3	10.37	0.38	1.37	0.44	9.93	0.19	0.78
02422242+6213323	135.47	2.08	0.53	3.8	11.8	10.6	11.45	0.49	1.38	0.20	11.25	0.40	1.12
02440181+7005273	132.30	9.29	1.78	3.4	22.2	11.1	11.22	0.48	1.54	0.67	10.55	0.19	0.65
02442271+5507524	138.67	-4.25	0.61	3.7	35.8	12.2	11.21	0.40	1.37	0.20	10.98	0.30	1.06
02455702+5522336	138.77	-3.94	0.76	3.7	52.4	13.6	11.40	0.49	1.42	0.30	11.12	0.36	1.04
02471213+5528163	138.89	-3.77	0.79	3.7	27.4	17.0	11.43	0.46	1.39	0.30	11.14	0.32	1.00
02472414+6239425	135.81	2.73	0.84	3.7	81.8	22.9	10.18	0.42	1.35	0.30	9.87	0.27	0.93
02473993+5804489	137.82	-1.39	1.19	3.8	26.0	24.4	11.34	0.52	1.58	0.40	10.90	0.32	0.99
02475005+5832219	137.64	-0.97	1.23	3.8	44.2	32.7	11.13	0.43	1.50	0.50	10.67	0.23	0.89
02483731+6300467	135.78	3.10	1.04	3.8	37.8	18.1	11.07	0.49	1.43	0.40	10.68	0.32	0.91
02484584+6020478	136.96	0.71	3.52	3.8	18.2	15.3	12.45	0.86	2.11	1.20	11.14	0.28	0.36
02491146+6628401	134.31	6.24	1.09	3.6	37.1	22.3	9.89	0.39	1.29	0.41	9.48	0.21	0.75
02495036+6304092	135.88	3.21	0.88	3.7	35.6	31.3	11.00	0.46	1.44	0.30	10.67	0.31	1.00
02504965+5616424	138.99	-2.83	1.27	3.7	41.0	27.9	11.46	0.71	1.75	0.50	10.99	0.49	1.12

Table B.1 – Continued

2MASXJ identifier [hhmmssss ± ddmmssss] (1)	gal l [deg] (2)	gal b [deg] (3)	$E(B-V)$ [mag] (4)	SD (5)	$a_{K_{20}}$ [arcsec] (6)	$b_{K_{20}}$ [arcsec] (7)	$K_{s_{20}}$ [mag] (8)	$H-K$ [mag] (9)	$J-K$ [mag] (10)	A_{K_s} [mag] (11)	K_s^o [mag] (12)	$(H-K)_o$ [mag] (13)	$(J-K)_o$ [mag] (14)
02531484+5732583	138.72	-1.54	1.33	3.6	41.6	32.4	10.89	0.56	1.59	0.50	10.39	0.34	0.92
02531969+5529140	139.66	-3.38	1.31	3.6	33.2	27.2	10.77	0.49	1.48	0.50	10.28	0.28	0.83
02531969+5529140	139.66	-3.38	1.31	3.6	33.2	27.2	10.77	0.49	1.48	0.50	10.28	0.28	0.83
02545129+5625144	139.43	-2.45	1.30	3.7	27.2	21.8	11.67	0.50	1.50	0.50	11.19	0.29	0.86
02545182+5720004	139.01	-1.63	1.36	3.7	37.0	17.8	11.46	0.50	1.53	0.50	10.95	0.27	0.85
02545198+5812134	138.61	-0.86	1.82	3.8	30.6	15.9	11.54	0.47	1.64	0.70	10.86	0.17	0.73
02550583+6624065	134.88	6.44	1.03	3.6	35.4	17.7	9.73	0.42	1.37	0.38	9.34	0.25	0.86
02570346+5658488	139.44	-1.81	1.45	3.7	33.6	26.9	11.44	0.43	1.52	0.50	10.90	0.20	0.80
02573053+5825188	138.82	-0.51	1.52	3.8	11.9	8.3	11.79	0.76	2.06	0.57	11.23	0.50	1.31
02585431+5950161	138.32	0.83	0.87	3.8	35.8	26.5	10.97	0.35	1.31	0.30	10.65	0.21	0.88
02590152+5318199	141.41	-4.93	0.76	3.6	38.0	15.2	11.49	0.38	1.35	0.30	11.21	0.24	0.97
02592153+5736175	139.42	-1.11	1.64	3.7	38.8	21.7	10.85	0.51	1.74	0.60	10.24	0.24	0.93
03022154+6855070	134.29	8.98	1.19	3.4	22.3	11.1	11.23	0.46	1.44	0.44	10.79	0.26	0.85
03040456+6716077	135.24	7.62	1.39	3.5	13.7	11.0	11.35	0.48	1.48	0.52	10.83	0.25	0.78
03070158+5315165	142.48	-4.39	0.83	3.6	37.6	18.8	11.10	0.43	1.42	0.30	10.79	0.29	1.01
03071054+5517545	141.48	-2.61	1.48	3.6	71.0	46.9	9.32	0.48	1.61	0.60	8.77	0.24	0.88
03073914+5645235	140.81	-1.31	3.78	3.7	23.6	20.3	12.33	0.81	2.38	1.40	10.92	0.18	0.50
03082803+5745174	140.41	-0.39	1.39	3.8	58.4	19.9	10.70	0.53	1.74	0.50	10.18	0.29	1.05
03095915+5707553	140.90	-0.82	4.16	3.7	18.8	14.7	12.25	0.82	2.34	1.50	10.70	0.13	0.27
03101644+5656203	141.03	-0.97	4.88	3.7	22.6	11.3	12.42	0.63	2.25	1.90	10.60	-0.19	-0.18
03104409+6106477	138.96	2.65	1.26	3.7	132.6	76.9	8.08	0.48	1.51	0.50	7.61	0.27	0.88
03111176+6105047	139.03	2.66	1.23	3.7	40.8	27.7	11.46	0.48	1.49	0.50	11.00	0.28	0.88
03113572+6241207	138.25	4.06	1.22	3.6	28.2	20.9	11.45	0.54	1.55	0.50	11.00	0.35	0.95
03121951+6758295	135.57	8.63	1.01	3.5	15.8	11.1	11.34	0.43	1.33	0.38	10.96	0.26	0.83
03124522+5213583	143.75	-4.83	0.72	3.6	53.4	20.3	11.22	0.46	1.36	0.30	10.95	0.34	1.00
03124721+6231391	138.45	3.99	1.32	3.6	33.2	29.2	11.69	0.55	1.52	0.50	11.20	0.33	0.85
03130062+6752475	135.67	8.58	1.00	3.5	29.2	5.8	11.31	0.57	1.58	0.37	10.94	0.41	1.08
03132009+6224130	138.56	3.92	1.50	3.6	42.6	22.2	10.97	0.45	1.51	0.50	10.41	0.19	0.77
03135317+6232589	138.54	4.08	1.22	3.7	79.8	35.1	10.08	0.44	1.39	0.50	9.62	0.24	0.78
03161119+6242593	138.68	4.36	1.04	3.7	34.0	28.6	11.55	0.34	1.34	0.40	11.16	0.17	0.82
03162208+5215460	144.21	-4.52	0.91	3.5	29.0	27.3	11.39	0.47	1.41	0.30	11.05	0.32	0.96
03181353+6649422	136.67	7.96	1.04	3.5	32.0	28.8	9.38	0.37	1.33	0.39	8.99	0.20	0.82
03185163+5754376	141.51	0.46	2.52	3.6	26.6	23.4	12.05	0.73	2.10	0.90	11.11	0.31	0.85

Table B.1 – Continued

2MASXJ identifier [hhmmssss ± ddmmssss] (1)	gal l [deg] (2)	gal b [deg] (3)	$E(B-V)$ [mag] (4)	SD (5)	$a_{K_{20}}$ [arcsec] (6)	$b_{K_{20}}$ [arcsec] (7)	$K_{s_{20}}$ [mag] (8)	$H-K$ [mag] (9)	$J-K$ [mag] (10)	A_{K_s} [mag] (11)	K_s^o [mag] (12)	$(H-K)_o$ [mag] (13)	$(J-K)_o$ [mag] (14)
03202205+6645055	136.89	8.01	1.04	3.4	24.3	9.7	10.45	0.34	1.28	0.39	10.06	0.17	0.77
03210915+6655186	136.86	8.19	1.09	3.5	42.6	34.1	8.67	0.35	1.32	0.41	8.27	0.17	0.78
03212339+6654460	136.88	8.20	1.09	3.4	22.7	13.6	10.85	0.42	1.33	0.41	10.45	0.24	0.79
03214230+6649371	136.96	8.14	1.08	3.4	25.1	20.1	10.10	0.37	1.31	0.40	9.69	0.19	0.78
03221550+5752157	141.91	0.67	2.73	3.7	24.6	21.6	12.01	0.85	2.33	1.00	10.99	0.40	0.97
03231132+6548189	137.65	7.37	1.20	3.5	25.2	15.1	10.24	0.46	1.51	0.45	9.79	0.26	0.91
03235035+6102426	140.34	3.44	1.52	3.6	35.0	16.8	11.32	0.60	1.90	0.60	10.75	0.36	1.15
03244319+5811161	142.01	1.11	2.67	3.6	13.7	6.8	12.24	0.88	2.61	1.00	11.25	0.44	1.28
03245871+5310146	144.82	-3.05	1.22	3.6	38.4	26.1	11.63	0.62	1.73	0.50	11.18	0.42	1.12
03251590+5624122	143.06	-0.33	2.50	3.7	32.6	19.6	11.94	0.66	2.21	0.90	11.01	0.25	0.97
03264399+5419084	144.39	-1.95	1.56	3.6	39.0	14.0	11.80	0.54	1.58	0.60	11.22	0.28	0.81
03273938+5221060	145.61	-3.50	1.05	3.6	33.8	21.0	10.78	0.36	1.26	0.40	10.39	0.19	0.74
03285780+6656000	137.49	8.63	1.02	3.5	17.6	12.3	11.12	0.41	1.37	0.38	10.74	0.24	0.87
03290640+6458319	138.63	7.03	1.08	3.5	35.5	21.3	9.44	0.38	1.34	0.40	9.04	0.20	0.80
03292042+6601389	138.05	7.91	1.18	3.5	56.1	16.8	9.61	0.40	1.47	0.44	9.17	0.21	0.88
03292877+5429573	144.62	-1.58	2.09	3.7	42.0	19.3	11.48	0.61	1.90	0.80	10.70	0.25	0.86
03302327+6110135	140.93	3.98	0.98	3.6	85.8	48.0	9.39	0.43	1.49	0.40	9.02	0.27	1.00
03302327+6110135	140.93	3.98	0.98	3.6	85.8	48.0	9.39	0.43	1.49	0.40	9.02	0.27	1.00
03312960+6541405	138.42	7.76	1.08	3.4	36.2	14.5	11.61	0.51	1.57	0.40	11.21	0.33	1.04
03313677+5148312	146.42	-3.60	1.02	3.6	11.5	9.2	11.62	0.46	1.47	0.38	11.24	0.29	0.96
03331908+6609092	138.31	8.24	1.30	3.4	26.0	15.6	10.93	0.48	1.44	0.48	10.45	0.26	0.80
03334905+5201071	146.58	-3.24	1.15	3.6	30.2	28.4	11.28	0.44	1.47	0.40	10.85	0.25	0.90
03345483+5349073	145.66	-1.68	1.74	3.6	28.2	20.3	11.85	0.61	1.88	0.60	11.20	0.32	1.02
03360608+5416062	145.54	-1.21	1.95	3.7	34.8	23.0	11.40	0.63	1.65	0.70	10.68	0.31	0.68
03362290+5048356	147.61	-3.98	1.04	3.6	46.0	16.6	11.07	0.50	1.52	0.40	10.68	0.33	1.00
03362571+5132236	147.19	-3.39	1.48	3.6	40.2	29.7	10.84	0.45	1.57	0.50	10.29	0.21	0.84
03363315+6240256	140.65	5.63	1.36	3.6	13.3	10.6	11.75	0.36	1.40	0.51	11.25	0.14	0.72
03363871+6306096	140.40	5.98	1.27	3.5	19.2	13.4	10.66	0.33	1.35	0.47	10.18	0.12	0.72
03364414+5248386	146.48	-2.33	1.57	3.6	47.0	34.8	10.68	0.52	1.59	0.60	10.10	0.26	0.81
03373489+5412366	145.75	-1.13	2.02	3.6	39.4	11.8	11.88	0.53	1.79	0.80	11.13	0.19	0.79
03373616+5052062	147.73	-3.82	1.33	3.6	36.8	25.8	11.09	0.52	1.57	0.50	10.59	0.30	0.92
03373823+5106002	147.60	-3.63	1.26	3.6	28.0	20.2	11.46	0.50	1.51	0.50	10.99	0.29	0.89
03374463+5502466	145.28	-0.44	2.14	3.6	28.0	18.5	11.35	0.59	1.82	0.80	10.55	0.24	0.76

Table B.1 – Continued

2MASXJ identifier [hhmmssss ± ddmmssss] (1)	gal l [deg] (2)	gal b [deg] (3)	$E(B-V)$ [mag] (4)	SD (5)	$a_{K_{20}}$ [arcsec] (6)	$b_{K_{20}}$ [arcsec] (7)	$K_{s_{20}}$ [mag] (8)	$H-K$ [mag] (9)	$J-K$ [mag] (10)	A_{K_s} [mag] (11)	K_s^o [mag] (12)	$(H-K)_o$ [mag] (13)	$(J-K)_o$ [mag] (14)
03374624+5357452	145.92	-1.31	1.89	3.7	23.6	19.8	11.67	0.61	1.88	0.70	10.97	0.30	0.94
03374715+6542199	138.95	8.15	1.08	3.4	14.0	8.4	11.29	0.42	1.47	0.40	10.89	0.24	0.93
03380124+6642455	138.36	8.97	1.19	3.5	33.2	29.9	9.47	0.41	1.38	0.44	9.02	0.21	0.79
03381210+6642567	138.37	8.98	1.18	3.5	33.8	30.4	9.47	0.41	1.48	0.44	9.03	0.21	0.89
03384742+5421089	145.81	-0.91	2.06	3.7	28.4	22.2	11.77	0.65	1.89	0.80	11.00	0.31	0.86
03385418+6617499	138.68	8.69	1.22	3.5	28.4	14.2	10.79	0.49	1.49	0.45	10.34	0.29	0.89
03393055+5421369	145.89	-0.84	2.26	3.7	30.0	21.6	11.71	0.64	2.02	0.80	10.87	0.27	0.90
03393065+5449231	145.62	-0.47	2.36	3.7	23.2	15.8	12.05	0.61	2.09	0.90	11.17	0.22	0.92
03393937+6527116	139.25	8.06	1.02	3.5	24.6	14.8	11.03	0.36	1.32	0.38	10.65	0.19	0.82
03394709+6528486	139.25	8.09	1.04	3.4	37.7	18.9	10.15	0.40	1.43	0.39	9.76	0.23	0.91
03395792+4940197	148.75	-4.56	0.77	3.6	40.4	29.1	11.20	0.38	1.36	0.30	10.91	0.25	0.98
03403139+6649043	138.49	9.20	1.01	3.4	16.3	9.8	11.02	0.43	1.35	0.38	10.64	0.26	0.85
03433015+5825154	143.89	2.73	1.13	3.7	51.6	21.7	11.23	0.49	1.39	0.40	10.81	0.30	0.83
03441609+4919572	149.51	-4.41	0.86	3.6	24.8	20.8	11.38	0.44	1.37	0.30	11.06	0.30	0.94
03441729+5102202	148.47	-3.06	1.24	3.6	39.4	26.8	11.23	0.47	1.53	0.50	10.77	0.27	0.93
03450943+4921435	149.61	-4.30	0.92	3.6	30.6	25.7	10.96	0.35	1.26	0.30	10.62	0.19	0.80
03454256+5638563	145.21	1.51	1.43	3.7	28.4	17.0	11.72	0.53	1.66	0.50	11.19	0.29	0.95
03460488+5432382	146.54	-0.12	2.30	3.6	20.6	18.5	11.63	0.62	1.97	0.90	10.77	0.24	0.83
03462398+5430563	146.59	-0.11	2.18	3.7	49.8	40.8	10.41	0.55	1.79	0.80	9.60	0.19	0.71
03475375+5601049	145.83	1.20	1.61	3.7	28.6	24.6	11.43	0.49	1.54	0.60	10.83	0.22	0.75
03480684+4955450	149.64	-3.56	1.27	3.6	31.0	26.0	11.11	0.64	1.67	0.50	10.63	0.43	1.03
03480963+4955140	149.65	-3.56	1.26	3.6	32.2	20.0	11.24	0.63	1.63	0.50	10.77	0.42	1.01
03481049+5409119	147.02	-0.24	2.20	3.7	36.8	11.0	11.93	0.79	2.08	0.80	11.11	0.42	0.99
03481767+5413029	147.00	-0.18	2.19	3.7	38.2	19.9	11.62	0.54	1.80	0.80	10.80	0.17	0.70
03482002+4955207	149.67	-3.54	1.25	3.6	19.1	9.6	11.71	0.50	1.67	0.50	11.25	0.29	1.05
03492038+5029171	149.44	-3.00	1.43	3.6	28.6	17.7	11.47	0.41	1.52	0.50	10.94	0.18	0.81
03492373+4924181	150.13	-3.83	1.27	3.5	30.2	16.3	11.60	0.52	1.57	0.50	11.13	0.31	0.94
03514420+5105033	149.36	-2.29	1.98	3.6	59.8	25.1	10.54	0.61	1.96	0.70	9.80	0.28	0.98
03522801+5748301	145.20	2.99	1.44	3.8	10.0	9.0	11.52	1.12	2.58	0.54	10.99	0.88	1.87
03541837+5249110	148.57	-0.70	2.01	3.6	45.2	15.4	11.55	0.79	1.97	0.80	10.80	0.46	0.97
03543651+4910571	150.93	-3.47	1.33	3.6	38.0	19.0	11.33	0.39	1.50	0.50	10.83	0.17	0.84
03551424+5231391	148.86	-0.83	1.68	3.7	26.6	22.3	11.73	0.61	1.66	0.60	11.10	0.33	0.83
03573082+4956387	150.80	-2.58	1.12	3.7	18.9	11.3	11.67	0.50	1.57	0.42	11.25	0.31	1.01

Table B.1 – Continued

2MASXJ identifier [hhmmssss ± ddmmssss] (1)	gal l [deg] (2)	gal b [deg] (3)	$E(B-V)$ [mag] (4)	SD (5)	$a_{K_{20}}$ [arcsec] (6)	$b_{K_{20}}$ [arcsec] (7)	$K_{s_{20}}$ [mag] (8)	$H-K$ [mag] (9)	$J-K$ [mag] (10)	A_{K_s} [mag] (11)	K_s^o [mag] (12)	$(H-K)_o$ [mag] (13)	$(J-K)_o$ [mag] (14)
03585689+4911167	151.47	-3.01	1.14	3.7	28.8	12.1	11.63	0.51	1.57	0.40	11.21	0.32	1.00
04012641+5343171	148.80	0.68	1.76	3.7	23.2	19.5	11.59	1.15	2.70	0.60	10.93	0.86	1.83
04014132+5315002	149.14	0.35	2.28	3.7	23.6	21.2	11.41	0.48	1.71	0.80	10.56	0.10	0.58
04015541+4924171	151.69	-2.53	1.23	3.6	43.0	21.5	11.23	0.47	1.53	0.50	10.77	0.27	0.92
04020732+5241528	149.55	-0.03	1.68	3.8	26.6	22.9	11.68	0.49	1.84	0.60	11.05	0.20	1.01
04024870+5244088	149.60	0.07	1.68	3.7	29.0	22.0	11.36	0.61	1.90	0.60	10.74	0.32	1.07
04050668+4028583	158.08	-8.81	1.08	3.4	14.3	8.6	11.58	0.43	1.43	0.40	11.18	0.26	0.89
04055619+5023102	151.53	-1.36	1.54	3.7	22.8	22.3	11.67	0.64	1.77	0.60	11.10	0.39	1.01
04060596+4020487	158.32	-8.79	1.07	3.4	17.4	15.7	11.18	0.52	1.52	0.40	10.78	0.34	0.99
04062549+5321492	149.59	0.90	1.80	3.7	54.2	28.2	10.69	0.66	1.52	0.60	10.02	0.35	0.62
04075531+4549400	154.84	-4.52	0.81	3.5	53.2	25.5	11.22	0.34	1.26	0.30	10.92	0.20	0.85
04093213+4922208	152.64	-1.73	1.71	3.8	60.8	24.3	10.26	0.47	1.61	0.60	9.62	0.19	0.76
04104442+3957368	159.24	-8.47	1.12	3.4	15.2	9.1	11.57	0.45	1.48	0.42	11.15	0.26	0.92
04110830+3837269	160.23	-9.38	1.25	3.4	23.1	9.2	10.90	0.45	1.45	0.47	10.43	0.24	0.83
04111032+4710144	154.34	-3.15	1.09	3.6	51.0	22.4	11.29	0.50	1.44	0.40	10.88	0.32	0.90
04112872+5518091	148.82	2.83	1.51	3.7	13.4	6.7	11.81	0.60	1.52	0.56	11.25	0.35	0.77
04113162+3914215	159.85	-8.88	1.04	3.4	18.5	7.4	11.46	0.45	1.52	0.39	11.07	0.28	1.00
04114143+3841285	160.26	-9.26	1.42	3.4	26.9	16.1	10.22	0.44	1.52	0.53	9.69	0.20	0.82
04115755+3838463	160.33	-9.25	1.50	3.5	30.7	9.2	10.68	0.47	1.56	0.56	10.12	0.22	0.81
04115864+3842213	160.29	-9.21	1.58	3.5	15.4	9.2	11.33	0.47	1.57	0.59	10.74	0.21	0.79
04120068+3846073	160.25	-9.16	1.68	3.5	59.0	33.0	10.31	0.55	1.71	0.60	9.69	0.27	0.88
04121283+3842023	160.33	-9.18	1.68	3.5	45.2	28.0	11.02	0.50	1.79	0.60	10.40	0.22	0.97
04122913+3838553	160.40	-9.18	1.62	3.5	13.9	8.3	11.45	0.53	1.74	0.60	10.84	0.26	0.94
04124119+3843433	160.38	-9.10	1.63	3.3	69.8	15.4	10.53	0.59	1.89	0.60	9.92	0.32	1.08
04124692+3835153	160.49	-9.19	1.55	3.3	66.8	24.0	10.70	0.55	1.60	0.60	10.12	0.29	0.83
04131853+3819491	160.74	-9.30	1.65	3.3	17.9	16.1	11.32	0.52	1.73	0.61	10.70	0.25	0.91
04133389+5041476	152.21	-0.32	1.62	3.7	32.6	21.5	11.26	0.64	1.94	0.60	10.66	0.36	1.12
04151246+3840071	160.78	-8.80	1.46	3.4	18.4	12.9	11.34	0.62	1.54	0.54	10.80	0.38	0.82
04161779+5034094	152.61	-0.11	1.75	3.6	22.6	22.1	11.55	0.60	1.85	0.60	10.90	0.31	0.99
04164549+3925359	160.46	-8.04	1.02	3.4	12.2	12.2	11.39	0.37	1.39	0.38	11.01	0.20	0.89
04170636+4910038	153.68	-1.03	1.46	3.6	58.4	37.4	10.38	0.48	1.66	0.50	9.84	0.24	0.94
04173955+3745411	161.77	-9.10	1.64	3.3	23.4	14.0	11.09	0.57	1.58	0.61	10.48	0.30	0.77
04175296+4911337	153.75	-0.92	1.54	3.7	27.6	19.9	11.35	0.62	1.77	0.60	10.78	0.36	1.00

Table B.1 – Continued

2MASXJ identifier [hhmmssss ± ddmmssss] (1)	gal l [deg] (2)	gal b [deg] (3)	$E(B-V)$ [mag] (4)	SD (5)	$a_{K_{20}}$ [arcsec] (6)	$b_{K_{20}}$ [arcsec] (7)	$K_{s_{20}}$ [mag] (8)	$H-K$ [mag] (9)	$J-K$ [mag] (10)	A_{K_s} [mag] (11)	K_s^o [mag] (12)	$(H-K)_o$ [mag] (13)	$(J-K)_o$ [mag] (14)
04191179+5552439	149.22	4.00	1.12	3.6	85.0	28.9	10.46	0.43	1.36	0.40	10.04	0.24	0.80
04202281+4535327	156.58	-3.19	1.08	3.6	34.8	15.3	11.37	0.49	1.46	0.40	10.97	0.31	0.92
04204654+5237183	151.67	1.84	1.49	3.7	35.8	11.5	11.69	0.42	1.58	0.60	11.13	0.18	0.84
04210584+4830168	154.61	-1.04	1.69	3.6	41.8	31.8	10.71	0.63	1.89	0.60	10.08	0.34	1.04
04211472+3710123	162.70	-9.02	1.26	3.4	19.9	8.0	11.14	0.46	1.48	0.47	10.67	0.25	0.85
04220023+4302560	158.59	-4.78	0.72	3.5	38.6	20.1	11.46	0.56	1.51	0.30	11.19	0.45	1.15
04225185+4402328	157.99	-3.97	0.81	3.6	61.0	37.8	10.61	0.54	1.28	0.30	10.31	0.41	0.88
04230274+3722007	162.81	-8.62	1.60	3.4	62.0	27.3	11.31	0.41	1.56	0.60	10.71	0.15	0.77
04230985+4410103	157.94	-3.85	0.84	3.7	21.6	17.7	11.49	0.38	1.24	0.30	11.18	0.24	0.82
04233241+3748200	162.56	-8.25	1.31	3.4	22.8	6.8	11.37	0.47	1.44	0.49	10.88	0.25	0.79
04233266+5010274	153.71	0.42	1.40	3.7	35.8	14.3	11.26	0.47	1.55	0.50	10.74	0.24	0.85
04241490+3725180	162.94	-8.41	1.42	3.4	31.0	16.7	11.70	0.50	1.52	0.50	11.17	0.26	0.81
04242347+3724490	162.96	-8.40	1.44	3.4	25.5	23.0	10.28	0.44	1.49	0.54	9.74	0.20	0.78
04244617+4244494	159.16	-4.63	0.60	3.6	86.4	17.3	10.41	0.35	1.16	0.20	10.19	0.25	0.87
04250287+4726453	155.83	-1.31	1.49	3.7	49.8	28.9	10.48	0.54	1.67	0.50	9.93	0.30	0.93
04251272+4453366	157.67	-3.08	1.12	3.6	30.2	23.0	11.23	0.49	1.54	0.40	10.81	0.30	0.98
04253229+3739096	162.95	-8.07	1.22	3.3	21.2	10.6	10.99	0.38	1.41	0.46	10.53	0.18	0.81
04254161+4222276	159.54	-4.77	0.61	3.6	39.0	25.7	11.32	0.53	1.31	0.20	11.09	0.43	1.00
04254171+4631366	156.56	-1.88	1.27	3.6	34.4	26.8	11.24	0.54	1.59	0.50	10.77	0.33	0.95
04254723+4408199	158.29	-3.53	0.72	3.6	38.0	19.8	11.40	0.44	1.31	0.30	11.13	0.32	0.95
04263635+3813072	162.68	-7.52	1.26	3.5	15.6	7.8	11.52	0.46	1.50	0.47	11.04	0.25	0.88
04263959+4700055	156.34	-1.43	1.56	3.7	47.0	20.7	11.61	0.40	1.56	0.50	11.03	0.14	0.78
04264042+3810182	162.72	-7.55	1.34	3.5	39.2	27.4	10.94	0.66	2.10	0.50	10.44	0.44	1.44
04264449+3810182	162.73	-7.54	1.33	3.5	60.8	17.0	10.87	0.65	2.07	0.50	10.37	0.43	1.41
04271586+5049248	153.66	1.30	1.92	3.6	59.0	30.7	10.97	0.45	1.67	0.70	10.25	0.13	0.71
04273027+3750036	163.09	-7.66	1.27	3.4	24.7	7.4	10.76	0.47	1.45	0.47	10.28	0.26	0.82
04273554+4647302	156.60	-1.46	1.63	3.7	56.2	46.1	9.97	0.53	1.65	0.60	9.36	0.25	0.84
04283316+3625579	164.26	-8.47	1.93	3.4	47.4	17.1	11.40	0.69	1.87	0.70	10.68	0.37	0.91
04292626+4855120	155.27	0.24	1.63	3.7	44.6	21.4	10.87	0.54	1.62	0.60	10.26	0.26	0.81
04292839+3849211	162.63	-6.70	0.90	3.4	18.2	18.2	10.40	–	1.31	0.33	10.06	–	0.86
04293884+5125188	153.48	1.98	1.53	3.6	36.2	30.4	10.92	0.43	1.46	0.60	10.35	0.19	0.70
04295264+3521545	165.24	-9.00	10.05	3.7	21.4	11.1	12.67	0.69	1.84	4.30	8.92	-0.98	-3.15
04295532+4353088	158.99	-3.17	0.82	3.6	26.6	22.3	11.30	0.42	1.36	0.30	10.99	0.28	0.95

Table B.1 – Continued

2MASXJ identifier [hhmmssss ± ddmmssss] (1)	gal l [deg] (2)	gal b [deg] (3)	$E(B-V)$ [mag] (4)	SD (5)	$a_{K_{20}}$ [arcsec] (6)	$b_{K_{20}}$ [arcsec] (7)	$K_{s_{20}}$ [mag] (8)	$H-K$ [mag] (9)	$J-K$ [mag] (10)	A_{K_s} [mag] (11)	K_s^o [mag] (12)	$(H-K)_o$ [mag] (13)	$(J-K)_o$ [mag] (14)
04300586+3522252	165.26	-8.96	11.63	3.7	8.6	6.9	12.86	0.72	1.98	4.33	8.53	-1.21	-3.80
04301103+4729248	156.40	-0.66	1.59	3.6	36.6	13.9	11.61	0.49	1.71	0.60	11.02	0.23	0.92
04302392+5020090	154.35	1.32	1.43	3.7	28.4	19.3	11.57	0.47	1.44	0.50	11.04	0.24	0.74
04303090+5312130	152.28	3.30	1.31	3.7	29.8	19.7	11.29	0.49	1.55	0.50	10.80	0.27	0.90
04304765+4131316	160.82	-4.67	0.61	3.6	32.6	17.6	11.36	0.32	1.16	0.20	11.13	0.23	0.87
04312427+4748209	156.31	-0.29	1.66	3.7	25.2	10.6	11.76	0.46	1.45	0.60	11.14	0.18	0.63
04312715+4752279	156.26	-0.24	1.64	3.7	23.0	18.9	11.77	0.54	1.75	0.60	11.16	0.27	0.94
04313523+4714048	156.75	-0.66	1.51	3.6	37.8	11.3	11.79	0.61	1.80	0.60	11.23	0.36	1.04
04333811+4530061	158.25	-1.58	1.32	3.6	105.8	38.1	9.66	0.48	1.54	0.50	9.17	0.27	0.89
04340516+4101321	161.61	-4.55	0.63	3.6	34.0	29.2	11.30	0.32	1.24	0.20	11.07	0.23	0.93
04360363+4030314	162.24	-4.63	0.69	3.5	26.8	25.7	11.43	0.44	1.33	0.30	11.17	0.33	0.99
04361434+4500084	158.93	-1.58	1.36	3.7	24.8	17.9	11.64	0.55	1.61	0.50	11.13	0.32	0.93
04363002+4426469	159.38	-1.92	1.30	3.7	37.4	13.5	11.47	0.68	1.79	0.50	10.98	0.46	1.14
04382270+4746546	157.12	0.55	1.55	3.6	18.2	12.7	11.80	0.49	1.68	0.58	11.23	0.23	0.91
04383916+5154076	154.08	3.34	1.33	3.6	44.0	36.1	10.52	0.40	1.42	0.50	10.02	0.18	0.76
04390214+4608079	158.42	-0.46	1.66	3.7	111.4	35.6	9.04	0.51	1.62	0.60	8.42	0.23	0.79
04390278+3532568	166.36	-7.49	1.07	3.5	17.0	8.5	11.08	0.52	1.55	0.40	10.68	0.35	1.02
04393567+4436440	159.62	-1.40	1.25	3.6	28.6	26.9	11.51	0.46	1.42	0.50	11.05	0.25	0.80
04400189+4540140	158.88	-0.64	1.66	3.6	45.2	29.8	10.72	0.51	1.73	0.60	10.10	0.25	0.92
04412856+4622171	158.52	0.01	1.73	3.6	33.8	18.3	11.52	0.48	1.73	0.60	10.88	0.18	0.87
04413675+4203562	161.77	-2.81	0.94	3.7	38.0	23.6	11.13	0.38	1.44	0.30	10.78	0.22	0.97
04414382+4433342	159.91	-1.15	1.25	3.6	28.8	18.4	11.34	0.47	1.37	0.50	10.87	0.26	0.75
04415187+5045599	155.26	2.96	1.11	3.6	37.2	28.3	10.74	0.45	1.56	0.40	10.33	0.28	1.02
04421071+5120222	154.86	3.37	1.29	3.6	28.8	15.0	11.65	0.55	1.66	0.50	11.17	0.34	1.02
04422924+5108582	155.04	3.29	1.05	3.6	27.6	17.7	11.59	0.41	1.45	0.40	11.20	0.24	0.93
04424005+3541451	166.74	-6.83	1.00	3.5	24.1	21.7	10.18	0.42	1.39	0.37	9.80	0.25	0.89
04424586+3848466	164.38	-4.79	0.69	3.5	62.0	13.6	10.93	0.44	1.31	0.30	10.67	0.33	0.97
04424681+4052046	162.82	-3.44	0.59	3.6	60.2	51.8	9.92	0.37	1.21	0.20	9.70	0.27	0.92
04425181+5101358	155.17	3.25	0.94	3.7	74.6	11.9	11.05	0.47	1.48	0.40	10.70	0.31	1.02
04425353+5114549	155.00	3.40	1.16	3.6	42.4	14.4	11.33	0.46	1.57	0.40	10.90	0.28	1.00
04430935+4425043	160.19	-1.05	1.24	3.7	31.8	22.3	11.30	0.48	1.55	0.50	10.84	0.28	0.95
04431593+3850025	164.42	-4.70	0.69	3.6	48.8	42.9	10.20	0.37	1.24	0.30	9.94	0.26	0.90
04431899+4032175	163.14	-3.58	0.56	3.6	41.2	12.4	11.43	0.56	1.46	0.20	11.22	0.47	1.18

Table B.1 – Continued

2MASXJ identifier [hhmmssss ± ddmmssss] (1)	gal l [deg] (2)	gal b [deg] (3)	$E(B-V)$ [mag] (4)	SD (5)	a_{K20} [arcsec] (6)	b_{K20} [arcsec] (7)	K_{s20} [mag] (8)	$H-K$ [mag] (9)	$J-K$ [mag] (10)	A_{K_s} [mag] (11)	K_s^o [mag] (12)	$(H-K)_o$ [mag] (13)	$(J-K)_o$ [mag] (14)
04433407+4536452	159.33	-0.21	1.52	3.6	48.0	9.6	11.53	0.44	1.56	0.60	10.97	0.19	0.82
04440032+3900361	164.38	-4.47	0.69	3.6	16.9	6.8	12.05	0.37	1.32	0.30	11.80	0.25	0.98
04440562+3853161	164.49	-4.54	0.70	3.6	52.4	25.2	11.09	0.42	1.31	0.30	10.83	0.30	0.96
04441374+3911350	164.27	-4.32	0.72	3.6	12.2	12.2	13.78	–	1.65	0.30	13.51	–	1.29
04442990+4429146	160.29	-0.83	1.14	3.7	46.2	15.7	11.00	0.49	1.59	0.40	10.58	0.30	1.03
04445716+3231058	169.49	-8.53	1.16	3.4	21.8	15.3	11.07	0.43	1.35	0.43	10.64	0.24	0.77
04445949+4533441	159.53	-0.06	1.57	3.6	35.0	25.9	10.94	0.54	1.66	0.60	10.36	0.28	0.88
04450255+3758177	165.31	-4.99	0.91	3.5	46.0	23.0	10.98	0.41	1.31	0.30	10.64	0.26	0.85
04453613+5059042	155.48	3.55	1.12	3.6	37.0	21.5	11.07	0.48	1.55	0.40	10.65	0.29	1.00
04461266+3725188	165.88	-5.17	1.06	3.5	20.5	16.4	10.62	0.49	1.53	0.40	10.23	0.31	1.01
04463939+4540516	159.63	0.24	1.45	3.7	33.0	21.8	11.29	0.51	1.55	0.50	10.75	0.27	0.83
04464159+4943063	156.56	2.86	0.91	3.7	69.0	40.0	11.00	0.41	1.29	0.30	10.66	0.26	0.84
04464394+3435108	168.13	-6.92	1.35	3.5	22.6	13.6	11.20	0.37	1.39	0.50	10.69	0.14	0.72
04465712+4729304	158.29	1.45	1.09	3.7	30.2	21.7	11.52	0.46	1.51	0.40	11.11	0.28	0.97
04471937+4417021	160.77	-0.58	0.81	3.7	36.0	24.5	10.91	0.49	1.41	0.30	10.61	0.35	1.01
04472295+4013271	163.88	-3.19	0.58	3.6	34.2	19.8	11.36	0.38	1.28	0.20	11.14	0.28	0.99
04472421+4459281	160.24	-0.11	0.98	3.7	63.0	13.9	11.25	0.42	1.39	0.40	10.88	0.26	0.90
04473473+4529122	159.88	0.24	1.41	3.6	25.6	16.4	11.32	0.44	1.41	0.50	10.80	0.21	0.71
04475352+4432511	160.64	-0.33	0.97	3.7	26.2	22.5	11.52	0.35	1.36	0.40	11.16	0.19	0.88
04475541+3428204	168.38	-6.80	1.40	3.4	20.0	16.0	10.89	0.45	1.45	0.52	10.36	0.22	0.75
04481997+3436502	168.32	-6.65	1.56	3.5	21.6	13.0	10.70	0.54	1.68	0.58	10.12	0.28	0.90
04482813+4952069	156.63	3.18	0.90	3.7	46.0	13.8	11.51	0.43	1.45	0.30	11.18	0.28	1.00
04484325+4452164	160.49	-0.01	0.97	3.8	32.6	24.1	10.91	0.43	1.42	0.40	10.55	0.27	0.94
04484660+4334294	161.48	-0.83	0.65	3.7	26.0	12.0	11.32	0.34	1.15	0.20	11.08	0.23	0.83
04491793+4453124	160.54	0.08	1.04	3.7	40.2	16.9	11.25	0.33	1.07	0.40	10.86	0.15	0.55
04492256+3730389	166.22	-4.64	0.98	3.6	45.4	14.5	11.34	0.44	1.42	0.40	10.97	0.28	0.93
04493984+4409215	161.14	-0.34	0.76	3.7	55.4	46.5	10.07	0.40	1.27	0.30	9.79	0.27	0.89
04494005+4511185	160.35	0.33	1.15	3.7	30.4	14.6	11.52	0.47	1.49	0.40	11.09	0.28	0.92
04494400+4911411	157.28	2.90	0.84	3.6	31.6	24.6	11.48	0.47	1.49	0.30	11.17	0.33	1.06
04501168+4506057	160.48	0.34	1.18	3.7	36.2	16.7	11.24	0.47	1.55	0.40	10.80	0.27	0.96
04501843+4541517	160.03	0.74	1.36	3.6	33.2	18.6	11.28	0.49	1.56	0.50	10.77	0.26	0.88
04502798+4434077	160.92	0.04	0.93	3.7	34.8	13.2	11.21	0.46	1.43	0.30	10.86	0.31	0.97
04503277+4454116	160.67	0.26	1.08	3.7	26.6	23.4	11.57	0.44	1.54	0.40	11.17	0.26	1.00

Table B.1 – Continued

2MASXJ identifier [hhmmssss ± ddmmssss] (1)	gal l [deg] (2)	gal b [deg] (3)	$E(B-V)$ [mag] (4)	SD (5)	$a_{K_{20}}$ [arcsec] (6)	$b_{K_{20}}$ [arcsec] (7)	$K_{s_{20}}$ [mag] (8)	$H-K$ [mag] (9)	$J-K$ [mag] (10)	A_{K_s} [mag] (11)	K_s^o [mag] (12)	$(H-K)_o$ [mag] (13)	$(J-K)_o$ [mag] (14)
04504074+4503124	160.57	0.38	1.12	3.7	26.0	22.4	11.42	0.50	1.64	0.40	11.00	0.31	1.08
04504592+4506595	160.53	0.43	1.15	3.7	30.4	20.7	10.99	0.46	1.55	0.40	10.56	0.27	0.99
04504934+4457425	160.66	0.34	1.06	3.7	29.6	18.9	11.61	0.51	1.49	0.40	11.22	0.33	0.96
04505300+4508055	160.53	0.46	1.15	3.7	25.2	23.2	11.32	0.43	1.55	0.40	10.89	0.23	0.98
04510938+5128076	155.67	4.53	1.41	3.6	11.8	8.3	11.77	0.63	1.66	0.52	11.24	0.40	0.96
04511770+4512083	160.52	0.56	1.18	3.6	27.2	25.0	11.51	0.50	1.54	0.40	11.07	0.30	0.95
04512165+4517254	160.46	0.62	1.21	3.6	37.0	17.0	11.00	0.54	1.67	0.40	10.55	0.34	1.06
04512932+4518524	160.46	0.65	1.21	3.6	36.2	16.7	11.28	0.45	1.58	0.40	10.83	0.25	0.98
04514426+3856227	165.41	-3.37	0.98	3.6	76.6	21.4	10.56	0.42	1.43	0.40	10.20	0.26	0.94
04515659+4458144	160.77	0.50	1.10	3.7	38.4	19.2	11.29	0.47	1.44	0.40	10.88	0.29	0.89
04521994+4515456	160.59	0.73	1.06	3.7	51.8	24.9	10.83	0.43	1.40	0.40	10.44	0.25	0.87
04522577+4934396	157.26	3.48	0.72	3.7	34.6	25.6	11.37	0.38	1.20	0.30	11.10	0.27	0.84
04523133+4927346	157.37	3.42	0.73	3.7	50.4	19.2	11.41	0.45	1.35	0.30	11.14	0.32	0.98
04523985+5203046	155.37	5.08	1.29	3.7	13.3	10.6	11.70	0.47	1.41	0.48	11.21	0.26	0.77
04524568+4501058	160.83	0.64	1.09	3.7	46.6	28.9	10.56	0.46	1.52	0.40	10.15	0.28	0.99
04524698+5135515	155.73	4.80	1.44	3.5	45.8	22.9	11.36	0.56	1.71	0.50	10.82	0.33	1.00
04525192+4441218	161.09	0.44	0.97	3.6	36.8	16.9	11.32	0.47	1.49	0.40	10.96	0.30	1.01
04525281+5204476	155.36	5.12	1.37	3.5	21.3	19.2	10.57	0.48	1.53	0.51	10.06	0.26	0.85
04525545+5156396	155.47	5.04	1.33	3.5	17.2	6.9	11.65	0.50	1.53	0.49	11.15	0.28	0.87
04525591+3438448	168.90	-5.90	1.02	3.4	19.0	11.4	11.22	0.39	1.37	0.38	10.84	0.22	0.87
04532441+4511276	160.77	0.83	1.14	3.7	34.0	22.4	11.22	0.51	1.44	0.40	10.80	0.32	0.87
04532674+4419006	161.45	0.29	0.81	3.6	35.6	32.0	10.77	0.40	1.31	0.30	10.47	0.28	0.91
04532922+4152201	163.35	-1.25	0.72	3.7	38.6	12.4	11.48	0.39	1.28	0.30	11.21	0.27	0.92
04533259+4532326	160.51	1.08	1.15	3.7	26.4	21.6	11.45	0.49	1.50	0.40	11.02	0.30	0.93
04534624+4507475	160.85	0.85	1.11	3.7	39.4	28.4	11.35	0.48	1.49	0.40	10.94	0.30	0.94
04534877+4218445	163.04	-0.93	0.67	3.7	62.2	19.9	10.76	0.49	1.46	0.20	10.51	0.38	1.12
04541186+4127583	163.75	-1.41	0.77	3.7	34.0	19.7	11.17	0.44	1.44	0.30	10.88	0.31	1.06
04541490+4503149	160.97	0.86	1.08	3.7	51.4	42.1	10.87	0.56	1.43	0.40	10.47	0.38	0.89
04542558+5203496	155.53	5.29	1.62	3.5	14.3	12.9	10.96	–	1.50	0.60	10.36	–	0.69
04544599+4620599	160.02	1.75	1.01	3.7	48.2	27.0	10.81	0.50	1.70	0.40	10.43	0.34	1.20
04550178+5159483	155.64	5.32	1.67	3.5	38.0	19.8	11.67	0.54	1.79	0.60	11.05	0.26	0.96
04550702+4559478	160.33	1.57	1.02	3.7	42.8	20.5	10.91	0.39	1.40	0.40	10.53	0.22	0.90
04552286+4546214	160.53	1.47	0.99	3.6	45.4	26.3	10.93	0.56	1.66	0.40	10.56	0.40	1.17

Table B.1 – Continued

2MASXJ identifier [hhmmssss ± ddmmssss] (1)	gal l [deg] (2)	gal b [deg] (3)	$E(B-V)$ [mag] (4)	SD (5)	a_{K20} [arcsec] (6)	b_{K20} [arcsec] (7)	K_{s20} [mag] (8)	$H-K$ [mag] (9)	$J-K$ [mag] (10)	A_{K_s} [mag] (11)	K_s^o [mag] (12)	$(H-K)_o$ [mag] (13)	$(J-K)_o$ [mag] (14)
04554245+4402134	161.92	0.43	0.82	3.7	69.4	26.4	10.07	0.41	1.35	0.30	9.77	0.26	0.94
04554990+4533540	160.75	1.40	1.03	3.7	61.2	26.9	10.01	0.38	1.35	0.40	9.63	0.21	0.84
04562691+4555425	160.53	1.71	1.03	3.7	73.0	29.2	10.21	0.45	1.51	0.40	9.82	0.27	1.00
04563241+4534186	160.82	1.50	1.10	3.6	45.0	36.9	10.41	0.43	1.47	0.40	10.00	0.25	0.92
04563494+3723521	167.21	-3.60	0.85	3.5	38.8	14.0	11.55	0.51	1.45	0.30	11.23	0.37	1.03
04564373+4424037	161.75	0.80	0.90	3.7	31.8	26.1	11.52	0.50	1.43	0.30	11.19	0.34	0.98
04565773+4426507	161.74	0.86	0.91	3.7	34.2	30.1	11.04	0.46	1.45	0.30	10.70	0.31	1.01
04570846+4942147	157.65	4.16	0.89	3.6	36.2	13.0	11.11	0.37	1.06	0.30	10.78	0.22	0.63
04571144+4420115	161.85	0.82	0.88	3.6	33.2	13.9	11.45	0.37	1.38	0.30	11.12	0.21	0.93
04574655+4126307	164.19	-0.90	0.83	3.7	32.2	18.0	11.39	0.49	1.39	0.30	11.08	0.35	0.98
04574727+4146237	163.93	-0.69	0.75	3.7	27.2	19.0	11.20	0.48	1.53	0.30	10.92	0.36	1.16
04574731+4607167	160.52	2.02	0.95	3.7	19.8	9.9	11.60	0.37	1.35	0.35	11.25	0.21	0.88
04580654+4552108	160.75	1.90	0.93	3.6	28.8	24.8	11.49	0.56	1.38	0.30	11.15	0.41	0.91
04580915+4208498	163.68	-0.41	0.66	3.7	73.4	26.4	10.09	0.48	1.40	0.20	9.84	0.36	1.06
04580946+5134192	156.27	5.44	1.35	3.5	29.8	19.7	11.57	0.44	1.49	0.50	11.07	0.22	0.82
04584955+5133076	156.35	5.51	1.08	3.6	19.8	15.8	11.01	0.40	1.43	0.40	10.61	0.22	0.90
04595512+4312240	163.05	0.51	0.69	3.7	39.0	21.1	11.41	0.46	1.36	0.30	11.15	0.35	1.03
05003753+4231251	163.66	0.19	0.60	3.7	44.4	36.4	10.36	0.38	1.30	0.20	10.14	0.27	1.00
05004115+4238061	163.58	0.27	0.55	3.7	28.0	19.0	11.37	0.47	1.35	0.20	11.17	0.37	1.08
05012183+3409111	170.37	-4.84	0.84	3.5	28.4	22.2	11.28	0.34	1.24	0.30	10.97	0.20	0.81
05014040+4338109	162.90	1.02	0.77	3.7	75.4	16.6	10.71	0.40	1.44	0.30	10.42	0.27	1.06
05015592+4419410	162.38	1.48	1.82	3.8	29.2	23.4	11.24	0.49	1.67	0.60	10.56	0.19	0.77
05021216+4734599	159.84	3.51	0.72	3.6	43.2	28.5	10.75	0.43	1.34	0.30	10.48	0.31	0.98
05024020+3520357	169.59	-3.90	0.98	3.6	33.0	18.5	11.38	0.48	1.66	0.40	11.01	0.32	1.17
05031826+4357546	162.82	1.46	1.51	3.6	31.4	23.2	11.42	0.43	1.54	0.60	10.86	0.18	0.79
05032503+4749366	159.77	3.82	0.67	3.7	30.6	17.7	11.36	0.34	1.27	0.20	11.11	0.23	0.93
05043136+3731335	168.08	-2.28	0.95	3.6	56.6	27.2	10.66	0.47	1.38	0.40	10.31	0.31	0.91
05055384+4121469	165.18	0.26	0.55	3.7	49.0	15.7	11.40	0.38	1.34	0.20	11.19	0.29	1.07
05062450+3535105	169.85	-3.14	0.71	3.6	32.8	23.0	11.40	0.42	1.35	0.30	11.14	0.30	0.99
05063010+4512499	162.17	2.67	1.05	3.6	29.4	17.1	11.55	0.43	1.46	0.40	11.16	0.26	0.95
05063335+4417469	162.91	2.12	0.82	3.6	40.0	20.0	11.26	0.45	1.41	0.30	10.95	0.31	1.00
05072947+4723396	160.53	4.11	0.61	3.6	34.8	27.1	11.44	0.51	1.53	0.20	11.21	0.41	1.23
05095533+4436308	163.02	2.79	0.68	3.7	53.6	25.7	10.88	0.43	1.27	0.30	10.63	0.32	0.93

Table B.1 – Continued

2MASXJ identifier [hhmmssss ± ddmmssss] (1)	gal l [deg] (2)	gal b [deg] (3)	$E(B-V)$ [mag] (4)	SD (5)	$a_{K_{20}}$ [arcsec] (6)	$b_{K_{20}}$ [arcsec] (7)	$K_{s_{20}}$ [mag] (8)	$H-K$ [mag] (9)	$J-K$ [mag] (10)	A_{K_s} [mag] (11)	K_s^o [mag] (12)	$(H-K)_o$ [mag] (13)	$(J-K)_o$ [mag] (14)
05115105+3131317	173.80	-4.64	0.67	3.5	37.0	17.8	10.86	0.37	1.22	0.20	10.61	0.25	0.89
05115386+4537142	162.41	3.67	0.56	3.6	51.4	24.7	10.63	0.42	1.32	0.20	10.42	0.33	1.04
05122582+4519525	162.70	3.57	0.61	3.7	46.6	28.0	10.78	0.33	1.27	0.20	10.55	0.23	0.96
05123258+4426135	163.44	3.06	0.72	3.7	29.2	16.4	11.26	0.42	1.32	0.30	10.99	0.30	0.97
05141860+4622066	162.05	4.45	0.69	3.6	61.4	30.7	10.73	0.31	1.25	0.30	10.47	0.19	0.90
05142584+3423225	171.80	-2.53	1.07	3.5	13.0	4.9	14.82	0.33	0.85	0.40	14.42	0.15	0.32
05154589+3413462	172.08	-2.40	1.09	3.6	36.8	36.1	10.57	0.52	1.57	0.40	10.16	0.34	1.03
05165475+3421093	172.12	-2.13	2.04	3.7	33.2	18.6	11.43	0.39	1.26	0.70	10.67	0.05	0.25
05165843+3403392	172.37	-2.29	0.80	3.6	40.2	20.1	10.79	0.47	1.48	0.30	10.49	0.34	1.09
05170274+3352532	172.52	-2.38	0.71	3.6	38.8	31.8	11.24	0.43	1.54	0.30	10.98	0.31	1.18
05171201+3921481	168.07	0.81	2.37	3.7	39.6	23.0	11.31	0.71	1.65	0.70	10.43	0.32	0.47
05174322+3442322	171.93	-1.79	0.80	3.6	31.2	23.7	11.47	0.60	1.63	0.30	11.17	0.47	1.23
05192943+3408562	172.59	-1.81	0.68	3.6	28.6	22.9	11.34	0.51	1.49	0.30	11.09	0.39	1.14
05200866+4314313	165.21	3.49	0.61	3.6	34.8	33.4	10.67	0.29	1.11	0.20	10.44	0.19	0.81
05215822+4058480	167.26	2.48	0.91	3.6	37.4	20.2	11.28	0.44	1.43	0.30	10.94	0.29	0.99
05221454+3826469	169.38	1.09	0.79	3.7	56.4	11.3	10.98	0.54	1.61	0.30	10.69	0.41	1.21
05221961+2150424	183.15	-8.25	1.01	3.4	12.2	11.0	11.34	0.47	1.41	0.38	10.96	0.30	0.91
05250816+3221028	174.75	-1.86	0.81	3.6	41.6	34.1	10.65	0.39	1.41	0.30	10.35	0.27	1.01
05252560+2443418	181.12	-6.06	1.27	3.4	30.4	28.6	11.61	0.44	1.63	0.50	11.14	0.23	1.00
05253779+3419073	173.17	-0.67	0.58	3.6	33.0	29.0	10.93	0.47	1.51	0.20	10.71	0.38	1.23
05254062+4141530	167.06	3.46	0.68	3.5	52.0	35.4	9.89	0.79	1.89	0.30	9.64	0.69	1.55
05281320+3116566	176.00	-1.91	1.11	3.6	29.2	25.1	11.59	0.44	1.46	0.40	11.18	0.26	0.91
05295184+3835341	170.09	2.41	1.28	3.7	24.8	21.3	11.32	0.55	1.60	0.50	10.84	0.33	0.96
05295184+3835341	170.09	2.41	1.28	3.7	24.8	21.3	11.32	0.55	1.60	0.50	10.84	0.33	0.96
05313269+3529135	172.87	0.98	0.90	3.7	20.8	17.1	11.20	0.93	2.12	0.30	10.87	0.78	1.67
05332905+3110137	176.71	-1.03	1.53	3.6	34.6	18.7	11.48	0.56	1.63	0.60	10.91	0.31	0.87
05372363+3604312	173.02	2.30	1.44	3.6	14.1	9.9	11.64	0.69	2.39	0.54	11.10	0.45	1.67
05382465+3241509	175.99	0.67	0.72	3.6	39.2	33.7	11.46	0.42	1.31	0.30	11.19	0.30	0.95
05385507+3337492	175.26	1.26	0.89	3.7	27.8	12.8	11.56	0.52	1.62	0.30	11.23	0.37	1.18
05393522+2841388	179.51	-1.25	1.54	3.6	40.8	13.1	11.24	0.57	1.72	0.60	10.67	0.31	0.95
05395434+2656147	181.04	-2.12	1.22	3.6	34.4	17.9	11.56	0.51	1.57	0.50	11.10	0.31	0.96
05402435+3311311	175.79	1.29	0.80	3.7	45.2	33.4	10.93	0.47	1.46	0.30	10.63	0.34	1.07
05402818+3313361	175.77	1.32	0.81	3.7	30.8	24.6	11.22	0.49	1.49	0.30	10.92	0.37	1.09

Table B.1 – Continued

2MASXJ identifier [hhmmssss ± ddmmssss] (1)	gal l [deg] (2)	gal b [deg] (3)	$E(B-V)$ [mag] (4)	SD (5)	$a_{K_{20}}$ [arcsec] (6)	$b_{K_{20}}$ [arcsec] (7)	$K_{s_{20}}$ [mag] (8)	$H-K$ [mag] (9)	$J-K$ [mag] (10)	A_{K_s} [mag] (11)	K_s^o [mag] (12)	$(H-K)_o$ [mag] (13)	$(J-K)_o$ [mag] (14)
05405882+3159438	176.87	0.76	1.08	3.7	28.0	21.8	11.51	0.58	1.37	0.40	11.11	0.40	0.83
05411745+3440059	174.64	2.23	1.34	3.6	29.8	17.9	11.72	0.52	1.61	0.50	11.22	0.30	0.95
05411834+2249028	184.71	-4.03	1.52	3.5	35.6	32.8	11.04	0.66	1.93	0.60	10.47	0.42	1.17
05413586+2357039	183.78	-3.38	1.18	3.6	44.4	34.6	10.73	0.45	1.43	0.40	10.29	0.26	0.85
05413712+2930454	179.05	-0.44	1.61	3.7	40.8	30.2	10.70	0.54	1.73	0.60	10.10	0.27	0.93
05414547+2937244	178.97	-0.36	1.40	3.7	24.2	20.3	11.73	0.50	1.69	0.50	11.21	0.28	0.99
05425805+3049039	178.10	0.49	1.37	3.7	18.8	17.3	11.48	0.65	1.55	0.50	10.97	0.42	0.87
05431777+3138489	177.43	0.99	1.17	3.6	39.6	21.4	11.41	0.47	1.54	0.40	10.97	0.28	0.97
05434263+3516031	174.39	2.96	0.98	3.6	38.2	28.3	11.13	0.59	1.63	0.40	10.77	0.42	1.15
05434892+3056391	178.08	0.72	2.04	3.6	29.8	20.3	11.62	0.58	1.58	0.70	10.86	0.24	0.58
05452013+3649316	173.22	4.05	0.66	3.6	37.2	28.3	11.20	0.40	1.27	0.20	10.95	0.29	0.94
05452124+2321174	184.74	-2.96	1.33	3.6	36.4	10.9	11.63	0.48	1.66	0.50	11.14	0.26	1.00
05454087+2813165	180.62	-0.36	1.29	3.6	35.2	33.8	10.99	0.54	1.57	0.50	10.51	0.33	0.93
05471940+2444422	183.78	-1.85	1.03	3.7	37.8	12.9	11.30	0.49	1.55	0.40	10.92	0.32	1.03
05480756+2141579	186.49	-3.27	0.58	3.7	61.4	17.2	10.45	0.47	1.38	0.20	10.23	0.36	1.08
05491821+1947083	188.28	-4.01	0.82	3.6	44.4	38.2	10.55	0.44	1.44	0.30	10.24	0.30	1.02
05501167+3258153	177.05	2.92	0.63	3.7	38.0	25.8	10.73	0.40	1.34	0.20	10.50	0.30	1.04
05502254+2334244	185.14	-1.86	1.25	3.6	33.0	19.8	11.58	0.46	1.60	0.50	11.11	0.25	0.98
05504707+2701149	182.23	-0.01	1.35	3.6	34.0	24.5	11.39	0.47	1.63	0.50	10.89	0.25	0.97
05511944+1855027	189.27	-4.04	0.82	3.6	38.4	20.0	11.26	0.50	1.48	0.30	10.96	0.37	1.07
05515128+1818051	189.86	-4.25	0.68	3.6	29.6	19.5	11.37	0.40	1.38	0.20	11.12	0.29	1.04
05515780+1807051	190.03	-4.32	0.62	3.6	35.4	16.3	11.28	0.47	1.41	0.20	11.05	0.37	1.10
05521278+3344455	176.60	3.68	0.71	3.6	70.0	40.6	10.19	0.38	1.22	0.30	9.92	0.26	0.87
05524113+3056577	179.06	2.35	0.48	3.6	47.4	16.1	11.18	0.49	1.44	0.20	11.00	0.42	1.20
05531219+2144149	187.06	-2.23	0.85	3.7	35.2	25.3	11.37	0.38	1.07	0.30	11.05	0.24	0.65
05540495+3127485	178.77	2.87	0.49	3.7	25.0	22.0	11.42	0.44	1.31	0.20	11.24	0.37	1.08
05540715+1759352	190.40	-3.94	0.72	3.6	40.6	39.0	10.50	0.38	1.31	0.30	10.23	0.26	0.95
05575173+2233406	186.89	-0.88	1.22	3.7	31.0	24.2	11.48	0.57	1.58	0.50	11.03	0.37	0.97
05583187+2244210	186.81	-0.66	1.33	3.7	41.6	28.3	10.96	0.59	1.67	0.50	10.46	0.38	1.01
05583483+1754200	191.01	-3.06	1.19	3.6	51.0	33.7	10.98	0.42	1.36	0.40	10.54	0.22	0.77
05585447+1759445	190.97	-2.95	1.34	3.6	27.2	23.9	11.37	0.49	1.70	0.50	10.87	0.27	1.03
05590035+1806455	190.88	-2.87	1.41	3.6	36.4	24.0	11.31	0.44	1.58	0.50	10.78	0.21	0.89
05590393+1804285	190.92	-2.88	1.43	3.6	32.0	22.4	10.90	0.62	1.71	0.50	10.37	0.39	1.00

Table B.1 – Continued

2MASXJ identifier [hhmmssss ± ddmmssss] (1)	gal l [deg] (2)	gal b [deg] (3)	$E(B-V)$ [mag] (4)	SD (5)	$a_{K_{20}}$ [arcsec] (6)	$b_{K_{20}}$ [arcsec] (7)	$K_{s_{20}}$ [mag] (8)	$H-K$ [mag] (9)	$J-K$ [mag] (10)	A_{K_s} [mag] (11)	K_s^o [mag] (12)	$(H-K)_o$ [mag] (13)	$(J-K)_o$ [mag] (14)
06020437+2311047	186.83	0.27	1.22	3.7	33.0	31.0	11.63	0.59	1.57	0.50	11.17	0.40	0.97
06021688+1901026	190.48	-1.75	1.57	3.6	25.8	18.1	11.79	0.50	1.57	0.60	11.21	0.24	0.79
06022068+2844085	182.03	3.06	0.43	3.6	41.4	30.6	11.38	0.48	1.22	0.20	11.22	0.41	1.01
06023546+2201525	187.89	-0.20	1.13	3.7	56.2	20.2	10.82	0.53	1.60	0.40	10.40	0.35	1.04
06031802+1847563	190.79	-1.65	1.54	3.5	23.4	12.2	11.70	0.47	1.54	0.60	11.13	0.22	0.78
06034588+1812362	191.35	-1.84	2.23	3.6	31.6	12.0	11.85	0.66	2.02	0.80	11.02	0.29	0.91
06060282+3003307	181.26	4.41	0.87	3.5	46.4	33.4	10.82	0.64	1.93	0.30	10.49	0.49	1.50
06074379+1608036	193.63	-2.03	1.50	3.6	29.4	17.6	11.76	0.39	1.75	0.60	11.20	0.14	1.02
06080358+3122592	180.31	5.42	0.95	3.6	26.9	13.4	10.67	0.97	2.23	0.35	10.32	0.81	1.76
06080417+2802003	183.26	3.81	0.47	3.6	37.4	34.4	10.58	0.37	1.20	0.20	10.40	0.29	0.96
06092756+1338133	196.02	-2.87	2.94	3.6	19.4	15.5	12.29	0.57	1.72	1.10	11.20	0.08	0.26
06095101+1839501	191.66	-0.36	1.82	3.6	24.8	14.9	11.69	0.75	2.23	0.70	11.01	0.46	1.33
06095948+1910113	191.23	-0.08	1.57	3.6	38.4	23.0	10.92	0.61	1.89	0.60	10.33	0.35	1.11
06110644+1551489	194.26	-1.45	1.33	3.7	73.8	17.7	10.66	0.54	1.76	0.50	10.16	0.32	1.10
06130977+1427300	195.73	-1.69	0.76	3.6	41.2	23.1	10.99	0.40	1.44	0.30	10.71	0.27	1.06
06133075+1604359	194.35	-0.84	1.78	3.7	11.3	10.2	10.52	0.76	2.08	0.66	9.85	0.46	1.19
06141832+1658308	193.65	-0.24	1.73	3.6	29.8	19.7	11.81	0.58	1.70	0.60	11.17	0.30	0.84
06160639+1659496	193.84	0.15	1.48	3.6	37.4	30.7	10.74	0.50	1.69	0.60	10.19	0.25	0.96
06162063+0717492	202.41	-4.40	0.50	3.6	96.0	42.2	9.02	0.36	1.24	0.20	8.83	0.28	0.99
06162583+1654326	193.95	0.18	1.53	3.7	37.6	21.1	11.59	0.53	1.60	0.60	11.02	0.28	0.83
06163615+1058407	199.19	-2.60	0.70	3.6	72.4	49.2	9.36	0.48	1.42	0.30	9.10	0.36	1.06
06171616+1655575	194.03	0.36	1.39	3.6	33.4	26.7	10.95	0.43	1.49	0.50	10.43	0.20	0.80
06193159+1601422	195.08	0.41	1.28	3.6	26.4	20.6	11.64	0.43	1.44	0.50	11.16	0.21	0.79
06200969+1650483	194.43	0.93	0.84	3.7	40.4	26.7	11.45	0.34	1.12	0.30	11.14	0.21	0.70
06201192+2332563	188.51	4.09	0.92	3.6	34.6	20.8	11.49	0.49	1.53	0.40	11.15	0.34	1.07
06222944+1027158	200.34	-1.58	0.80	3.7	34.4	33.0	11.18	0.50	1.59	0.30	10.88	0.37	1.20
06225815+1108312	199.78	-1.15	1.06	3.7	52.8	20.1	11.14	0.57	1.57	0.40	10.75	0.40	1.04
06245794+1458369	196.62	1.07	0.88	3.6	41.8	37.6	10.80	0.39	1.30	0.30	10.47	0.24	0.86
06255436+0632286	204.19	-2.66	0.78	3.6	23.6	15.1	11.52	0.50	1.52	0.30	11.23	0.37	1.13
06262702+0727287	203.44	-2.11	0.66	3.6	50.6	26.3	11.06	0.52	1.43	0.20	10.81	0.41	1.10
06263895+1601067	195.89	1.92	0.55	3.6	30.2	18.1	11.16	0.34	1.18	0.20	10.95	0.26	0.92
06283437+0623064	204.64	-2.14	1.11	3.6	39.8	19.1	11.35	0.59	1.64	0.40	10.93	0.41	1.09
06284616+0149197	208.72	-4.21	0.95	3.6	44.0	40.5	10.59	0.42	1.39	0.40	10.24	0.26	0.91

Table B.1 – Continued

2MASXJ identifier [hhmmssss ± ddmmssss] (1)	gal l [deg] (2)	gal b [deg] (3)	$E(B-V)$ [mag] (4)	SD (5)	$a_{K_{20}}$ [arcsec] (6)	$b_{K_{20}}$ [arcsec] (7)	$K_{s_{20}}$ [mag] (8)	$H-K$ [mag] (9)	$J-K$ [mag] (10)	A_{K_s} [mag] (11)	K_s^o [mag] (12)	$(H-K)_o$ [mag] (13)	$(J-K)_o$ [mag] (14)
06294669+1032181	201.10	0.05	1.07	3.7	30.4	17.0	11.57	0.59	1.65	0.40	11.17	0.41	1.12
06315346-0930076	219.24	-8.63	1.11	3.5	13.2	9.2	11.55	0.43	1.32	0.41	11.14	0.25	0.77
06341652+0758280	203.88	-0.15	0.97	3.7	59.8	16.7	11.29	0.46	1.52	0.40	10.93	0.30	1.04
06343138+0904375	202.93	0.41	0.75	3.7	84.8	67.8	8.93	0.28	1.06	0.30	8.65	0.16	0.69
06343673+0238144	208.66	-2.54	2.96	3.6	23.2	19.5	11.86	0.61	1.73	1.10	10.76	0.12	0.27
06344020+0139344	209.54	-2.97	1.30	3.7	39.6	16.6	11.36	0.41	1.52	0.50	10.87	0.19	0.87
06344281+0445594	206.78	-1.53	2.81	3.6	61.6	16.0	11.07	0.76	2.10	1.10	10.02	0.29	0.70
06344281+0445594	206.78	-1.53	2.81	3.6	61.6	16.0	11.07	0.76	2.10	1.10	10.02	0.29	0.70
06352675+0230578	208.87	-2.41	1.96	3.7	34.6	23.5	11.11	0.55	1.87	0.80	10.38	0.23	0.91
06353794+0022498	210.79	-3.34	1.58	3.6	30.4	15.8	10.86	0.51	1.60	0.60	10.27	0.25	0.80
06354230+0226468	208.96	-2.38	1.81	3.7	60.4	16.9	10.78	0.61	1.90	0.70	10.10	0.31	1.00
06355362+0438272	207.03	-1.33	1.36	3.6	44.2	26.5	10.75	0.48	1.72	0.50	10.24	0.25	1.04
06383251+1035536	202.04	1.99	1.05	3.7	39.4	26.8	11.00	0.42	1.21	0.40	10.61	0.25	0.69
06393966+0846004	203.79	1.39	1.32	3.7	35.4	14.2	11.72	0.51	1.57	0.50	11.23	0.29	0.91
06414770+1102252	202.01	2.90	0.82	3.6	30.2	17.5	11.29	0.52	1.42	0.30	10.99	0.38	1.00
06455492-1812493	228.68	-9.38	0.38	3.5	41.4	41.4	10.12	-0.03	0.69	0.14	9.98	0.10	0.50
06473930-0000098	212.50	-0.84	0.98	3.7	41.2	14.0	11.08	0.50	1.67	0.40	10.71	0.34	1.18
06474744-0048518	213.24	-1.18	0.89	3.7	43.6	27.0	11.18	0.42	1.34	0.30	10.85	0.27	0.90
06483359+0145387	211.04	0.16	0.68	3.8	33.0	23.8	11.42	0.40	1.27	0.20	11.17	0.29	0.93
06503049-0248387	215.33	-1.49	1.16	3.8	50.8	24.4	10.31	0.44	1.46	0.40	9.88	0.25	0.89
06503679-0352597	216.29	-1.95	1.45	3.7	42.8	12.0	11.69	0.46	1.74	0.50	11.15	0.22	1.02
06504824-0336287	216.07	-1.78	1.19	3.7	28.8	19.0	11.63	0.54	1.60	0.40	11.19	0.35	1.02
06513438-0350052	216.36	-1.72	1.65	3.7	27.6	17.7	11.34	0.48	1.57	0.60	10.73	0.21	0.75
06532549-1122118	223.30	-4.72	1.16	3.6	11.4	9.1	11.68	0.62	1.59	0.43	11.25	0.43	1.01
06535387-0337410	216.44	-1.11	0.92	3.7	63.2	15.2	10.80	0.57	1.61	0.40	10.46	0.42	1.15
06541984-1208232	224.09	-4.87	0.77	3.7	33.8	19.6	11.13	0.33	1.17	0.30	10.84	0.20	0.79
06552670-0411095	217.11	-1.02	1.29	3.7	40.8	27.7	11.46	0.52	1.55	0.50	10.98	0.31	0.91
06562541-0300515	216.18	-0.27	1.68	3.7	27.0	23.8	11.69	0.58	1.78	0.60	11.06	0.30	0.95
06570322-0501137	218.04	-1.04	1.10		54.3	11.9	11.54	0.74	1.10	0.40	11.13	0.18	0.55
06572149-0508597	218.19	-1.03	1.14	3.7	83.6	18.4	11.00	0.42	1.48	0.40	10.57	0.23	0.91
0658452+063640	207.87	4.63	0.25	–	–	–	–	–	–	–	–	–	–
06590153+0634579	207.92	4.68	0.26	3.4	59.8	22.7	11.09	0.30	1.04	0.10	10.99	0.25	0.90
06590970-0249301	216.33	0.43	1.27	3.8	42.8	31.7	11.39	0.64	1.78	0.50	10.92	0.43	1.15

Table B.1 – Continued

2MASXJ identifier [hhmmssss ± ddmmssss] (1)	gal l [deg] (2)	gal b [deg] (3)	$E(B-V)$ [mag] (4)	SD (5)	$a_{K_{20}}$ [arcsec] (6)	$b_{K_{20}}$ [arcsec] (7)	$K_{s_{20}}$ [mag] (8)	$H-K$ [mag] (9)	$J-K$ [mag] (10)	A_{K_s} [mag] (11)	K_s^o [mag] (12)	$(H-K)_o$ [mag] (13)	$(J-K)_o$ [mag] (14)
07003437-1020151	223.17	-2.69	0.76	3.8	14.5	11.6	11.53	0.40	1.37	0.28	11.25	0.28	0.99
07005613-1147344	224.51	-3.27	0.65	3.6	89.2	32.1	9.69	0.51	1.61	0.20	9.45	0.40	1.29
07011704-0711332	220.45	-1.10	1.20	3.8	28.4	17.6	11.41	0.44	1.40	0.40	10.96	0.24	0.80
07021533-0313467	217.04	0.93	2.02	3.7	44.0	21.1	11.63	0.40	1.37	0.70	10.88	0.07	0.38
07030812-1109581	224.20	-2.51	2.03	3.6	25.6	20.5	11.16	0.54	1.79	0.70	10.40	0.20	0.78
07031926-1246259	225.65	-3.20	0.61	3.7	28.4	18.2	11.33	0.33	1.38	0.20	11.10	0.23	1.08
07044419-1106510	224.33	-2.13	2.83	3.7	22.5	20.2	10.53	1.02	2.83	1.05	9.47	0.56	1.42
07052068-1711008	229.81	-4.77	0.48	3.7	34.0	21.8	11.37	0.28	1.17	0.20	11.19	0.20	0.93
07054925-1611251	228.97	-4.22	0.49	3.7	35.8	17.2	11.25	0.51	1.39	0.20	11.07	0.43	1.15
07093459-0525404	219.83	1.54	0.46	3.7	78.8	50.4	10.10	0.33	1.14	0.20	9.93	0.25	0.91
07143657-1857385	232.41	-3.62	1.68	3.7	29.4	23.5	10.98	0.66	1.76	0.60	10.35	0.38	0.92
07143807-1003285	224.52	0.51	0.74	3.7	34.8	21.6	11.50	0.33	1.25	0.30	11.23	0.20	0.87
07160927-1950273	233.36	-3.71	1.09	3.7	41.2	23.9	11.00	0.48	1.44	0.40	10.59	0.30	0.91
07165094-1852251	232.57	-3.11	1.78		95.6	13.4	11.20	1.28	1.88	0.70	10.54	0.31	1.00
07165193-1852341	232.58	-3.11	1.78	3.7	30.2	9.1	11.50	0.69	2.01	0.67	10.83	0.39	1.12
07231967-1618397	231.03	-0.55	1.35	3.7	49.4	15.8	10.94	0.46	1.64	0.50	10.44	0.24	0.97
07235168-1053287	226.31	2.12	0.47	3.7	39.4	23.6	11.03	0.31	1.15	0.20	10.85	0.22	0.91
07245535-2430057	238.44	-4.08	1.56	3.8	32.8	27.6	11.13	0.43	1.55	0.60	10.55	0.17	0.77
07245535-2430057	238.44	-4.08	1.56	3.8	32.8	27.6	11.13	0.43	1.55	0.60	10.55	0.17	0.77
07264631-2351096	238.06	-3.40	1.19	3.8	44.6	32.1	10.64	0.50	1.55	0.40	10.20	0.30	0.97
07273064-1308046	228.72	1.85	0.51	3.7	35.0	25.2	11.20	0.37	1.25	0.20	11.01	0.28	1.00
07273273-2319396	237.68	-3.00	1.57	3.7	23.6	17.9	11.09	0.56	1.72	0.60	10.51	0.30	0.94
07273400-1308106	228.72	1.86	0.51	3.7	51.0	30.6	10.68	0.48	1.30	0.20	10.49	0.40	1.05
07291623-2048113	235.65	-1.45	1.22	3.8	25.6	25.1	11.66	0.69	1.79	0.50	11.21	0.49	1.17
07294973-2534569	239.92	-3.62	0.92	3.8	37.0	31.8	10.98	0.51	1.43	0.30	10.64	0.36	0.98
07304535-2823585	242.50	-4.77	0.53	3.8	74.2	65.3	10.80	0.25	0.80	0.20	10.60	0.16	0.54
07323290-1923246	234.78	-0.09	2.64	3.8	31.4	22.6	11.51	0.85	2.13	1.00	10.53	0.41	0.82
07324220-1354035	229.99	2.59	0.43	3.7	68.6	15.1	10.00	0.49	1.40	0.20	9.84	0.41	1.19
07332576-2543462	240.44	-2.97	0.78	3.8	28.0	26.3	11.24	0.42	1.49	0.30	10.95	0.29	1.10
07343132-2444126	239.69	-2.28	0.80	3.8	35.4	16.3	11.47	0.51	1.45	0.30	11.17	0.38	1.06
07344923-2404306	239.14	-1.90	1.37	3.8	55.6	16.7	11.49	0.54	1.75	0.50	10.98	0.31	1.07
07351136-2633207	241.35	-3.03	0.79	3.8	18.5	5.6	11.54	0.41	1.26	0.29	11.25	0.28	0.87
07360443-2748552	242.55	-3.46	0.82	3.8	36.0	15.1	11.43	0.40	1.44	0.30	11.12	0.26	1.03

Table B.1 – Continued

2MASXJ identifier [hhmmssss ± ddmmssss] (1)	gal l [deg] (2)	gal b [deg] (3)	$E(B-V)$ [mag] (4)	SD (5)	$a_{K_{20}}$ [arcsec] (6)	$b_{K_{20}}$ [arcsec] (7)	$K_{s_{20}}$ [mag] (8)	$H-K$ [mag] (9)	$J-K$ [mag] (10)	A_{K_s} [mag] (11)	K_s^o [mag] (12)	$(H-K)_o$ [mag] (13)	$(J-K)_o$ [mag] (14)
07361741-2522246	240.44	-2.24	1.46	3.8	33.2	17.3	11.39	0.40	1.46	0.60	10.85	0.17	0.74
07374792-1643482	233.06	2.29	0.62	3.7	36.6	32.2	10.88	0.42	1.28	0.20	10.65	0.32	0.97
07374848-1310042	229.95	4.03	0.28	3.6	29.8	25.6	11.20	0.37	1.18	0.10	11.09	0.32	1.04
07375734-2839078	243.49	-3.51	0.77	3.9	62.8	21.4	11.07	0.43	1.41	0.30	10.78	0.30	1.02
07380245-2710388	242.21	-2.77	1.08	3.8	54.8	43.8	10.02	0.42	1.50	0.40	9.62	0.24	0.96
07385787-2455377	240.34	-1.49	1.05	3.8	36.6	21.2	11.22	0.52	1.56	0.40	10.83	0.35	1.04
07385822-2855357	243.84	-3.45	0.70	3.8	55.6	12.2	11.19	0.53	1.57	0.30	10.93	0.41	1.22
07403156-2618279	241.72	-1.86	0.82	3.8	41.0	15.6	11.21	0.45	1.29	0.30	10.90	0.32	0.89
07411855-1642051	233.45	3.04	0.43	3.7	40.2	22.5	11.14	0.31	1.14	0.20	10.98	0.24	0.92
07413450-1611117	233.04	3.35	0.35	3.6	46.2	29.6	10.77	0.34	1.15	0.10	10.64	0.28	0.98
07413554-2544190	241.34	-1.37	0.79	3.8	32.4	31.1	11.10	0.44	1.35	0.30	10.80	0.31	0.96
07414115-2231134	238.56	0.24	0.66	3.8	108.4	23.8	9.49	0.56	1.60	0.20	9.24	0.45	1.27
07414443-1608057	233.01	3.41	0.34	3.6	47.8	11.5	11.26	0.44	1.37	0.10	11.13	0.38	1.20
07414792-3028212	245.49	-3.67	0.55	3.8	57.2	13.7	11.16	0.51	1.40	0.20	10.95	0.42	1.13
07431472-2545501	241.55	-1.06	0.72	3.8	43.0	25.8	10.89	0.62	1.49	0.30	10.62	0.49	1.13
07431751-3333172	248.33	-4.91	1.44	3.7	41.8	25.1	10.61	0.53	1.69	0.50	10.07	0.28	0.97
07431853-2006196	236.65	1.76	0.79	3.8	36.6	23.4	11.44	0.46	1.39	0.30	11.15	0.33	1.00
07440237-2721456	243.03	-1.71	0.75	3.8	41.6	26.6	11.25	0.47	1.33	0.30	10.97	0.34	0.96
07442784-1820196	235.25	2.88	0.57	3.7	30.6	16.5	11.45	0.38	1.29	0.20	11.24	0.29	1.00
07451725-3413310	249.12	-4.88	1.49	3.8	30.4	18.2	11.76	0.60	1.65	0.60	11.20	0.35	0.91
07452996-2715311	243.10	-1.37	0.84	3.8	62.6	12.5	11.28	0.49	1.36	0.30	10.97	0.34	0.94
07465855-2915253	244.99	-2.09	0.94	3.8	35.0	28.7	11.25	0.62	1.53	0.40	10.90	0.46	1.06
07471479-3049352	246.38	-2.83	0.82	3.8	44.0	27.3	10.59	0.39	1.23	0.30	10.28	0.25	0.82
07473672-2101573	237.96	2.17	0.53	3.8	29.2	21.0	11.41	0.36	1.17	0.20	11.21	0.27	0.90
07474347-2520380	241.69	0.02	0.53	3.9	34.6	21.5	11.44	0.38	1.29	0.20	11.24	0.29	1.03
07475295-3041265	246.33	-2.65	0.78	3.8	31.8	28.0	10.50	0.34	1.21	0.30	10.21	0.20	0.81
07483070-2532370	241.95	0.07	0.63	3.9	90.6	27.2	10.53	0.44	1.30	0.20	10.30	0.34	0.99
07483252-2516431	241.73	0.21	0.54	3.9	49.2	11.8	10.80	0.32	1.21	0.20	10.60	0.23	0.94
07483527-2250005	239.63	1.46	0.80	3.8	32.6	17.0	11.44	0.38	1.34	0.30	11.14	0.24	0.94
07484838-2449451	241.37	0.49	0.60	3.9	42.6	26.4	11.02	0.40	1.31	0.20	10.80	0.31	1.02
07485088-2503171	241.57	0.39	0.54	3.8	35.0	28.7	11.35	0.46	1.35	0.20	11.15	0.36	1.08
07485977-2650561	243.14	-0.49	0.53	3.8	25.0	18.0	11.20	0.44	1.36	0.20	11.00	0.34	1.10
07490339-2458491	241.53	0.47	0.55	3.9	26.4	19.0	11.36	0.38	1.29	0.20	11.16	0.29	1.02

Table B.1 – Continued

2MASXJ identifier [hhmmssss ± ddmmssss] (1)	gal l [deg] (2)	gal b [deg] (3)	$E(B-V)$ [mag] (4)	SD (5)	$a_{K_{20}}$ [arcsec] (6)	$b_{K_{20}}$ [arcsec] (7)	$K_{s_{20}}$ [mag] (8)	$H-K$ [mag] (9)	$J-K$ [mag] (10)	A_{K_s} [mag] (11)	K_s^o [mag] (12)	$(H-K)_o$ [mag] (13)	$(J-K)_o$ [mag] (14)
07492337-3542214	250.83	-4.89	1.32	3.7	76.4	52.0	10.69	0.46	1.64	0.50	10.20	0.24	0.98
07494054-3341019	249.11	-3.83	2.22	3.8	16.2	6.5	11.63	–	1.61	0.83	10.80	–	0.50
07495208-2729568	243.79	-0.66	1.16	3.9	21.6	18.6	11.54	0.55	1.71	0.40	11.11	0.36	1.13
07500081-3142080	247.43	-2.76	1.11	3.9	26.2	22.5	11.62	0.48	1.67	0.40	11.21	0.31	1.12
07505059-3053204	246.82	-2.20	1.08	3.8	42.4	19.5	10.85	0.38	1.24	0.40	10.45	0.19	0.70
07515109-2523545	242.21	0.80	0.42	3.8	30.8	17.2	11.19	0.36	1.16	0.20	11.03	0.29	0.94
07521098-2100174	238.47	3.11	0.34	3.7	35.6	29.2	11.04	0.35	1.19	0.10	10.92	0.28	1.01
07523883-3224563	248.33	-2.65	1.51	3.8	40.0	21.6	11.52	0.51	1.66	0.60	10.96	0.26	0.91
07524324-2431356	241.56	1.41	0.46	3.8	54.8	14.2	11.28	0.38	1.28	0.20	11.11	0.29	1.05
075257-215608	239.37	2.79	–	0.6	–	–	–	–	–	–	–	–	–
07530159-2158341	239.41	2.78	0.54	3.7	37.2	35.7	10.47	0.40	1.28	0.20	10.27	0.32	1.02
07531836-3611492	251.66	-4.46	1.75	3.8	40.0	24.0	11.25	0.52	1.77	0.60	10.60	0.22	0.90
07533288-2129485	239.06	3.13	0.42	3.7	53.6	24.7	10.74	0.38	1.17	0.20	10.58	0.31	0.96
07541134-2423269	241.62	1.77	0.39	...	39.6	16.6	12.05	0.91	1.30	0.10	11.90	0.33	1.11
07541170-2423209	241.62	1.77	0.39	3.8	23.7	14.2	10.72	0.36	1.21	0.15	10.57	0.30	1.01
07543034-3524203	251.10	-3.85	1.46	3.8	42.0	16.8	11.63	0.48	1.50	0.60	11.08	0.24	0.77
07545229-2756453	244.75	0.07	0.77	3.8	26.8	24.1	11.19	0.41	1.32	0.30	10.90	0.27	0.93
07545280-3318173	249.34	-2.70	1.28	3.8	44.6	23.2	11.07	0.44	1.50	0.50	10.59	0.24	0.86
07554671-2716477	244.28	0.58	0.80	3.8	30.2	25.4	11.24	0.42	1.42	0.30	10.94	0.28	1.02
07561560-3656270	252.60	-4.33	1.43	3.8	33.6	32.3	10.80	0.46	1.59	0.50	10.27	0.22	0.88
07563338-2150060	239.71	3.55	0.29	3.8	39.8	18.3	11.27	0.30	1.09	0.10	11.16	0.25	0.95
07565545-3127593	247.99	-1.38	0.90	3.8	34.4	22.0	11.41	0.46	1.29	0.30	11.08	0.31	0.84
07573774-2540197	243.12	1.77	0.25	3.8	29.8	26.8	11.20	0.37	1.15	0.10	11.11	0.33	1.02
07573774-2540197	243.12	1.77	0.25	3.8	29.8	26.8	11.20	0.37	1.15	0.10	11.11	0.33	1.02
07575928-2157182	239.99	3.78	0.34	3.8	58.8	37.6	10.48	0.43	1.25	0.10	10.35	0.37	1.07
07582363-2159463	240.07	3.83	0.32	3.8	34.0	21.8	11.20	0.50	1.33	0.10	11.08	0.44	1.16
07585016-2214423	240.34	3.79	0.29	3.8	11.0	5.5	12.96	0.56	1.42	0.10	12.85	0.51	1.27
07585434-2219534	240.42	3.76	0.28	3.8	50.8	39.6	10.57	0.37	1.10	0.10	10.46	0.32	0.96
07585614-2220434	240.43	3.76	0.28	3.8	6.2	5.0	12.43	0.37	1.05	0.10	12.32	0.32	0.91
07591260-2050166	239.18	4.60	0.26	3.8	45.0	29.7	10.74	0.34	1.10	0.10	10.64	0.30	0.96
08000105-2415483	242.20	2.97	0.23	3.8	34.0	24.5	10.80	0.28	1.07	0.10	10.71	0.24	0.96
08005067-3155465	248.82	-0.91	0.85	3.8	27.0	11.3	11.24	0.54	1.64	0.30	10.92	0.39	1.21
08015503-3810213	254.25	-4.01	1.02	3.8	31.4	22.6	11.57	0.52	1.50	0.40	11.19	0.35	0.99

Table B.1 – Continued

2MASXJ identifier [hhmmssss ± ddmmssss] (1)	gal l [deg] (2)	gal b [deg] (3)	$E(B-V)$ [mag] (4)	SD (5)	$a_{K_{20}}$ [arcsec] (6)	$b_{K_{20}}$ [arcsec] (7)	$K_{s_{20}}$ [mag] (8)	$H-K$ [mag] (9)	$J-K$ [mag] (10)	A_{K_s} [mag] (11)	K_s^o [mag] (12)	$(H-K)_o$ [mag] (13)	$(J-K)_o$ [mag] (14)
08023477-3746569	253.98	-3.70	1.10	3.8	51.2	19.5	10.47	0.41	1.41	0.40	10.06	0.23	0.87
08032461-2727357	245.32	1.93	0.34	3.8	27.8	16.1	11.13	0.33	1.11	0.10	11.00	0.27	0.94
08074237-3544499	252.81	-1.74	1.55	3.8	47.2	34.9	10.33	0.49	1.62	0.60	9.75	0.23	0.85
08080066-3558243	253.03	-1.81	1.80	3.8	41.0	18.9	10.41	0.29	0.78	0.70	9.74	-0.01	-0.13
08090254-2427021	243.46	4.61	0.20	3.8	31.8	28.0	11.11	0.38	1.24	0.10	11.03	0.34	1.14
08105503-3051287	249.07	1.48	0.63	3.8	43.0	15.5	11.34	0.48	1.38	0.20	11.11	0.39	1.07
08111394-3854530	255.85	-2.88	1.78	3.8	27.6	24.8	11.23	0.47	1.61	0.70	10.57	0.19	0.74
08115216-2854143	247.55	2.72	0.43	3.8	32.0	26.9	11.24	0.35	1.14	0.20	11.08	0.28	0.92
08124035-3323491	251.40	0.40	0.71	3.8	29.0	20.9	11.44	0.42	1.34	0.30	11.17	0.30	0.98
08131734-3118595	249.73	1.65	0.54	3.8	32.6	30.0	10.91	0.49	1.29	0.20	10.71	0.40	1.02
08142154-3819354	255.69	-2.04	1.67	3.8	82.4	41.2	9.68	0.53	1.66	0.60	9.06	0.25	0.83
08142478-3225000	250.78	1.24	0.55	3.8	27.8	25.0	11.26	0.44	1.35	0.20	11.06	0.35	1.08
08143768-3305480	251.37	0.90	0.59	3.8	43.4	38.2	10.43	0.41	1.26	0.20	10.21	0.32	0.97
08145230-3311297	251.48	0.89	0.56	3.8	29.0	19.1	11.44	0.38	1.26	0.20	11.23	0.29	0.98
08145956-3309457	251.47	0.93	0.58	3.8	48.8	35.1	10.65	0.41	1.30	0.20	10.43	0.31	1.01
08164477-3846546	256.33	-1.91	2.02	3.8	29.6	23.1	11.89	0.77	2.05	0.70	11.14	0.43	1.04
08170147-3410277	252.54	0.72	0.48	3.8	78.4	12.5	10.73	0.50	1.46	0.20	10.55	0.42	1.22
08172741-2759259	247.46	4.25	0.29	3.8	21.4	17.5	11.04	0.44	1.25	0.10	10.93	0.39	1.12
08182775-3547298	254.05	0.05	2.10	3.8	34.8	34.1	9.95	0.75	1.86	0.80	9.17	0.39	0.81
08191136-3833104	256.41	-1.38	1.55	3.8	24.6	23.6	10.88	0.55	1.68	0.60	10.30	0.30	0.92
08213966-3903268	257.10	-1.27	2.13	3.8	22.4	17.0	11.93	0.57	1.81	0.80	11.14	0.22	0.75
08224226-3240398	251.98	2.54	0.36	3.8	32.2	30.9	11.03	0.33	1.15	0.10	10.90	0.27	0.97
08242635-3642433	255.49	0.52	0.92	3.8	49.0	11.8	11.32	0.43	1.39	0.30	10.98	0.28	0.94
08243293-3637484	255.44	0.58	0.94	3.8	46.0	15.6	11.15	0.47	1.38	0.40	10.80	0.31	0.90
08255863-3639240	255.62	0.80	0.85	3.8	38.8	19.4	11.31	0.45	1.42	0.30	10.99	0.30	0.99
08293905-3526048	255.06	2.12	0.76	3.8	45.2	38.9	10.45	0.44	1.35	0.30	10.17	0.30	0.96
08305941-3249032	253.10	3.88	0.37	3.8	38.0	19.8	11.17	0.33	1.16	0.10	11.03	0.26	0.97
08441291-3612532	257.47	4.00	0.51		45.0	20.7	11.15	0.86	1.25	0.20	10.96	0.31	1.00
08480354-3555256	257.72	4.79	0.44	3.7	32.8	20.3	11.36	0.41	1.28	0.20	11.20	0.34	1.06
08522527-3926038	261.00	3.25	0.97	3.8	42.6	30.7	10.98	0.53	1.54	0.40	10.62	0.37	1.06
16160007-3730193	341.71	9.52	1.21	3.9	15.5	9.3	11.36	0.41	1.43	0.45	10.91	0.21	0.83
16163174-3826308	341.12	8.78	1.03	3.9	14.6	11.7	11.10	0.48	1.40	0.38	10.72	0.31	0.88
16171926-3740403	341.78	9.21	1.21	3.9	47.8	30.6	11.21	0.42	1.36	0.40	10.76	0.21	0.75

Table B.1 – Continued

2MASXJ identifier [hhmmssss ± ddmmssss] (1)	gal l [deg] (2)	gal b [deg] (3)	$E(B-V)$ [mag] (4)	SD (5)	$a_{K_{20}}$ [arcsec] (6)	$b_{K_{20}}$ [arcsec] (7)	$K_{s_{20}}$ [mag] (8)	$H-K$ [mag] (9)	$J-K$ [mag] (10)	A_{K_s} [mag] (11)	K_s^o [mag] (12)	$(H-K)_o$ [mag] (13)	$(J-K)_o$ [mag] (14)
16173004-3649262	342.42	9.79	1.15	3.8	31.0	26.7	11.44	0.58	1.54	0.40	11.01	0.38	0.97
16180021-3657068	342.40	9.63	1.24	3.9	54.8	23.0	10.62	0.51	1.70	0.50	10.16	0.29	1.07
1618262-373604	341.99	9.11	1.38	–	–	–	–	–	–	–	–	–	–
16182851-3739379	341.95	9.06	1.38	3.9	36.2	26.8	10.65	0.48	1.57	0.50	10.14	0.26	0.89
16183236-3723459	342.15	9.24	1.28	3.9	39.4	27.6	9.82	0.43	1.34	0.48	9.34	0.22	0.71
16193769-3757523	341.90	8.69	1.14	3.9	27.8	22.2	11.48	0.50	1.54	0.40	11.06	0.31	0.98
16220379-3811082	342.08	8.19	1.03	4.0	38.6	36.3	10.76	0.40	1.40	0.40	10.38	0.23	0.89
16221431-3809491	342.12	8.18	1.05	4.0	9.6	7.7	11.64	0.40	1.34	0.39	11.25	0.23	0.82
16230766-3739356	342.61	8.41	1.42	3.9	38.4	22.3	11.52	0.47	1.63	0.50	10.99	0.24	0.93
16254669-3707583	343.36	8.39	0.98	4.0	37.6	16.5	11.11	0.48	1.62	0.40	10.74	0.32	1.13
16342826-3857439	343.19	5.89	0.85	4.2	27.0	24.8	11.34	0.28	1.15	0.30	11.02	0.13	0.72
16414252-3619588	346.12	6.57	1.05	4.2	26.8	10.7	10.46	0.36	1.29	0.39	10.06	0.19	0.77
16434955-3705384	345.82	5.75	1.03	4.2	34.4	24.1	9.52	0.37	1.37	0.38	9.13	0.20	0.86
16463421-3903086	344.68	4.07	1.00	4.5	34.8	32.7	10.84	0.38	1.40	0.40	10.47	0.21	0.90
16465670-3721166	346.02	5.11	0.94		45.0	26.1	10.40	0.76	1.21	0.40	10.05	0.29	0.74
16470867-3616459	346.88	5.77	1.05	4.3	29.1	17.5	10.17	0.48	1.40	0.39	9.78	0.30	0.87
16481772-3810061	345.57	4.38	0.95	4.4	27.0	20.0	11.24	0.37	1.32	0.40	10.89	0.21	0.85
16490239-3642570	346.79	5.20	0.84	4.4	64.6	12.9	10.90	0.44	1.50	0.30	10.59	0.30	1.09
16490503-3619500	347.09	5.43	1.18	4.3	36.2	20.3	11.55	0.39	–	0.40	11.11	0.19	–
16500224-3712073	346.54	4.73	0.71	4.5	42.6	23.0	10.59	0.46	1.27	0.30	10.33	0.33	0.92
16512573-3307205	349.89	7.10	0.61	4.3	32.4	22.7	11.13	0.34	1.23	0.20	10.90	0.24	0.93
16515849-3545456	347.90	5.34	1.01	4.3	27.8	14.5	11.33	0.35	1.29	0.40	10.95	0.17	0.79
16520999-3550026	347.87	5.27	1.05	4.3	43.6	26.2	10.66	0.45	1.34	0.40	10.27	0.28	0.82
16522835-3303135	350.08	6.97	0.56	4.3	35.8	25.8	10.90	0.31	1.14	0.20	10.69	0.23	0.87
16530380-3548500	348.00	5.14	0.98	4.4	55.4	15.5	10.63	0.46	1.44	0.40	10.27	0.30	0.95
16532065-3532311	348.25	5.27	0.96	4.4	60.2	19.3	10.79	0.50	1.56	0.40	10.43	0.34	1.08
16540803-3534375	348.32	5.12	0.87	4.4	40.6	34.1	10.15	0.37	1.27	0.30	9.82	0.23	0.84
16553517-3532460	348.54	4.91	0.81	4.5	27.8	15.0	11.30	0.39	1.29	0.30	11.00	0.26	0.89
16574847-3438179	349.53	5.12	0.93	4.5	29.8	28.0	11.13	0.34	1.26	0.30	10.78	0.18	0.80
17000638-3152265	352.02	6.44	0.51	4.5	53.0	35.0	10.35	0.32	1.11	0.20	10.16	0.23	0.84
17024654-3405128	350.60	4.64	0.62	4.6	13.6	12.2	10.99	–	–	0.23	10.76	–	–
17054244-3329451	351.44	4.52	0.75	4.7	50.8	27.4	10.36	0.43	1.26	0.30	10.08	0.31	0.89
17073820-2814301	355.93	7.32	0.40	4.5	25.0	7.5	11.31	–	–	0.15	11.16	–	–

Table B.1 – Continued

2MASXJ identifier [hhmmssss ± ddmmssss] (1)	gal l [deg] (2)	gal b [deg] (3)	$E(B-V)$ [mag] (4)	SD (5)	a_{K20} [arcsec] (6)	b_{K20} [arcsec] (7)	K_{s20} [mag] (8)	$H-K$ [mag] (9)	$J-K$ [mag] (10)	A_{K_s} [mag] (11)	K_s^o [mag] (12)	$(H-K)_o$ [mag] (13)	$(J-K)_o$ [mag] (14)
17123572-2548136	358.58	7.84	0.57	4.4	34.8	16.0	10.96	0.34	1.17	0.20	10.75	0.25	0.89
17144212-2550472	358.82	7.43	0.88	4.4	30.6	27.5	11.02	0.33	1.34	0.30	10.69	0.18	0.90
17160689-2438342	360.00	7.86	0.89	4.4	14.3	12.9	11.56	–	–	0.33	11.23	–	–
17165337-2647470	358.32	6.49	1.11	4.6	57.6	46.1	9.99	0.31	1.26	0.40	9.58	0.13	0.71
17172214-2650068	358.35	6.38	1.16	4.6	28.8	19.6	10.88	0.41	–	0.40	10.45	0.22	–
17172859-2417256	0.47	7.80	1.01	4.4	45.6	13.7	11.22	0.41	1.40	0.40	10.84	0.24	0.90
17172860-2409406	0.58	7.88	0.95	4.4	13.4	10.7	11.42	0.41	1.24	0.36	11.06	0.26	0.76
17173605-2413026	0.55	7.82	1.02	4.4	14.2	8.5	11.51	0.34	1.41	0.38	11.13	0.17	0.90
17183985-2454314	0.11	7.23	0.96	4.5	35.0	17.5	11.56	0.40	–	0.40	11.20	0.24	–
17184154-2750144	357.69	5.56	1.21	4.8	20.9	14.6	10.39	–	–	0.45	9.94	–	–
17194814-2528040	359.79	6.70	0.96	4.6	28.6	17.2	11.14	0.31	–	0.40	10.78	0.15	–
17423620-3854340	351.16	-4.67	0.84	4.7	126.0	58.0	9.34	0.26	1.20	0.30	9.03	0.12	0.78
17521905-1517459	12.52	5.67	0.71	4.5	19.9	13.9	11.02	0.25	–	0.27	10.75	0.14	–
17575504-1138276	16.39	6.30	1.09	4.3	44.2	28.3	10.84	0.45	1.45	0.40	10.43	0.27	0.91
17581377-1241453	15.51	5.71	1.23	4.3	9.7	8.7	11.54	0.51	1.52	0.46	11.08	0.31	0.91
17582147-1137141	16.46	6.21	1.04	4.3	32.2	12.2	11.59	0.50	1.43	0.40	11.20	0.33	0.92
17585489-0836334	19.18	7.57	1.18	4.1	17.7	15.9	10.82	0.47	1.45	0.44	10.38	0.28	0.87
17590767-1333006	14.87	5.10	1.03	4.5	30.2	26.6	11.38	0.35	–	0.40	11.00	0.18	–
17591740-0833394	19.27	7.51	1.17	4.1	22.2	16.9	11.66	0.42	1.44	0.40	11.22	0.23	0.86
17592016-0831286	19.31	7.51	1.16	4.1	34.0	27.9	11.32	0.46	1.36	0.40	10.89	0.27	0.78
17594870-1328559	15.01	4.99	1.15	4.5	40.8	26.9	10.86	0.79	–	0.40	10.43	0.60	–
18010993-0822352	19.66	7.19	1.23	4.1	27.4	21.9	11.56	0.63	1.65	0.50	11.10	0.43	1.04
18035726-0813268	20.13	6.66	1.37	4.1	21.2	18.2	11.63	0.56	1.64	0.50	11.12	0.34	0.97
18100236-0043306	27.52	8.87	1.04	3.9	22.5	11.2	10.93	0.50	1.36	0.39	10.54	0.33	0.84
18103194-0652259	22.10	5.87	1.23	4.2	21.4	18.8	11.64	0.59	1.88	0.50	11.18	0.39	1.28
18140441-0822089	21.20	4.39	1.68		61.4	44.2	11.06	1.21	1.69	0.60	10.43	0.20	0.85
18141853-0607349	23.21	5.40	1.19	4.3	36.6	18.3	11.61	0.39	1.37	0.40	11.17	0.19	0.79
18151860-0834552	21.16	4.02	1.50	4.4	69.2	13.8	10.87	0.60	1.67	0.60	10.31	0.35	0.92
18160148-0826232	21.36	3.93	1.70	4.4	32.2	22.5	11.12	0.54	1.63	0.60	10.49	0.26	0.79
18172445-0424551	25.09	5.52	1.45	4.2	24.8	14.4	11.75	0.43	1.38	0.50	11.21	0.19	0.66
18192432-3107470	1.68	-7.45	0.29	4.5	21.7	6.5	11.15	–	–	0.11	11.04	–	–
18202335-0117447	28.22	6.31	1.59	4.0	52.6	15.8	11.47	0.51	1.69	0.60	10.88	0.25	0.90
18203316-0121387	28.18	6.24	1.63	4.0	47.0	44.2	10.15	0.48	1.62	0.60	9.54	0.21	0.81

Table B.1 – Continued

2MASXJ identifier [hhmmssss ± ddmmssss] (1)	gal l [deg] (2)	gal b [deg] (3)	$E(B-V)$ [mag] (4)	SD (5)	$a_{K_{20}}$ [arcsec] (6)	$b_{K_{20}}$ [arcsec] (7)	$K_{s_{20}}$ [mag] (8)	$H-K$ [mag] (9)	$J-K$ [mag] (10)	A_{K_s} [mag] (11)	K_s^o [mag] (12)	$(H-K)_o$ [mag] (13)	$(J-K)_o$ [mag] (14)
18221913-0449343	25.30	4.25	1.63	4.4	31.2	22.5	11.49	0.59	1.76	0.60	10.88	0.33	0.95
18275944+0031420	30.72	5.46	2.01	4.1	38.8	15.5	11.58	0.68	1.89	0.80	10.83	0.34	0.89
18310342-2347198	9.45	-6.41	0.56	4.6	27.8	19.5	10.72	–	–	0.21	10.51	–	–
18333199-0001072	30.87	3.97	2.17	4.3	54.6	18.6	11.52	0.66	–	0.80	10.71	0.30	–
18360903-0036239	30.65	3.12	2.17	4.4	25.2	19.2	11.50	0.70	–	0.80	10.69	0.34	–
18384124+0141147	32.98	3.61	1.84	4.3	14.6	11.7	11.32	0.52	1.75	0.69	10.64	0.21	0.83
18432770+0553498	37.28	4.45	0.92	4.3	29.4	18.2	11.50	0.32	1.22	0.40	11.16	0.16	0.76
18452225+0533245	37.20	3.88	1.37	4.3	21.4	16.3	11.74	0.42	1.45	0.50	11.23	0.18	0.77
18504202+0715029	39.31	3.46	2.08	4.4	11.8	8.3	12.00	0.65	–	0.77	11.23	0.31	–
18513759-0859297	24.94	-4.13	0.39	4.5	39.8	29.5	10.79	0.32	1.12	0.10	10.64	0.26	0.93
18524710+0939480	41.70	4.09	0.93	4.3	37.8	28.0	11.34	0.48	1.29	0.30	10.99	0.34	0.83
18531497-0623155	27.45	-3.31	0.64	4.6	30.4	15.8	11.05	0.27	0.89	0.20	10.81	0.16	0.57
18565611-0613346	28.01	-4.05	0.45	4.4	42.2	38.8	10.21	0.35	1.18	0.20	10.04	0.26	0.94
18573128-0436546	29.51	-3.45	0.72	4.5	27.8	19.5	11.27	0.49	–	0.30	11.00	0.37	–
18583627+1137375	44.10	3.71	0.90	4.3	36.6	31.5	10.77	0.40	1.33	0.30	10.44	0.25	0.88
19004514+1741359	49.77	5.98	0.62	4.0	56.8	10.2	11.47	0.47	1.57	0.20	11.24	0.37	1.26
19041528+1256371	45.91	3.08	1.47	4.3	32.2	12.2	11.53	0.53	1.79	0.50	10.98	0.28	1.05
19120105+2043284	53.70	4.97	1.09	4.1	36.6	15.4	11.47	0.45	1.40	0.40	11.06	0.26	0.86
19123993+1728258	50.87	3.35	1.52	4.3	23.6	17.9	11.32	0.38	1.34	0.60	10.75	0.12	0.58
19124699+0256056	37.98	-3.40	0.92	4.4	52.0	34.3	10.79	0.36	–	0.30	10.45	0.21	–
19194212+0721408	42.71	-2.88	1.53	4.4	39.4	27.6	11.10	0.54	1.68	0.60	10.53	0.29	0.92
19203180+0836246	43.91	-2.47	1.37	4.5	38.0	9.9	11.44	0.36	–	0.50	10.93	0.13	–
19205612+1841331	52.87	2.17	2.70	4.4	35.6	16.4	11.03	0.64	–	1.00	10.03	0.20	–
19223320+2054242	55.00	2.88	2.05	4.4	22.4	18.4	11.87	0.56	–	0.80	11.11	0.22	–
19225733+0833551	44.16	-3.02	1.01	4.4	9.5	9.5	11.36	0.41	1.21	0.38	10.98	0.24	0.71
19241113+2208141	56.27	3.12	1.40	4.3	12.0	8.4	11.66	0.48	1.35	0.52	11.14	0.25	0.65
19255928+2100385	55.47	2.22	2.01	4.5	10.0	7.0	11.55	0.45	–	0.75	10.80	0.12	–
19285189+1307064	48.86	-2.15	1.50	4.4	33.6	23.5	11.05	0.61	–	0.60	10.49	0.36	–
19312354+2632370	60.93	3.77	0.86	4.2	29.6	23.7	11.37	0.32	1.25	0.30	11.05	0.17	0.82
19315025+2543597	60.27	3.29	1.08	4.3	41.8	29.3	10.84	0.42	1.51	0.40	10.44	0.23	0.97
19365060+3039283	65.13	4.69	0.45	4.0	30.2	21.7	11.31	0.34	1.10	0.20	11.14	0.26	0.88
19382863+2810502	63.13	3.18	0.84	4.3	38.2	13.8	11.26	0.36	1.28	0.30	10.95	0.22	0.86
19390019+1631210	53.02	-2.64	1.30	4.3	44.2	31.8	10.64	0.44	1.52	0.50	10.16	0.22	0.87

Table B.1 – Continued

2MASXJ identifier [hhmmssss ± ddmmssss] (1)	gal l [deg] (2)	gal b [deg] (3)	$E(B-V)$ [mag] (4)	SD (5)	a_{K20} [arcsec] (6)	b_{K20} [arcsec] (7)	K_{s20} [mag] (8)	$H-K$ [mag] (9)	$J-K$ [mag] (10)	A_{Ks} [mag] (11)	K_s^o [mag] (12)	$(H-K)_o$ [mag] (13)	$(J-K)_o$ [mag] (14)
19390547+2856372	63.86	3.43	0.79	4.3	29.6	21.9	11.51	0.38	1.35	0.30	11.21	0.25	0.95
19410154+2638147	62.06	1.93	2.11	4.4	25.7	20.6	10.16	0.36	1.34	0.79	9.37	0.01	0.29
19505731+1822281	56.06	-4.20	0.49	4.1	72.4	24.6	10.40	0.34	1.11	0.20	10.22	0.26	0.87
19521116+3229039	68.34	2.76	1.35	4.3	39.2	21.2	10.94	0.58	1.55	0.50	10.44	0.36	0.88
19530266+1953218	57.62	-3.85	0.65	4.2	27.6	15.5	11.42	0.32	1.24	0.20	11.18	0.21	0.92
19564949+2141345	59.62	-3.68	0.88	4.2	15.2	12.2	11.39	–	0.94	0.33	11.06	–	0.50
19573332+3211022	68.67	1.64	1.99	4.4	29.2	22.8	11.33	0.56	–	0.70	10.59	0.24	–
20000942+4321590	78.52	7.01	0.43	3.9	17.9	14.3	11.16	–	1.33	0.16	11.00	–	1.11
20010969+2655338	64.60	-1.79	2.31	4.3	32.6	16.3	11.59	0.50	1.62	0.80	10.73	0.12	0.47
20084824+4339589	79.61	5.83	1.26	3.9	23.6	9.4	11.20	0.41	1.41	0.47	10.73	0.20	0.79
20092153+2718462	65.91	-3.12	2.28	4.1	72.0	44.6	10.27	1.47	–	0.80	9.42	1.09	–
20092934+2818579	66.77	-2.60	2.62	4.1	18.4	13.6	12.07	0.56	2.20	1.00	11.09	0.13	0.90
20100506+2557368	64.86	-3.99	1.70	4.0	9.5	8.6	11.87	0.53	1.71	0.63	11.23	0.25	0.87
20101324+2850488	67.30	-2.45	2.08	4.1	23.4	19.2	11.98	0.50	1.69	0.80	11.20	0.15	0.66
20114417+2743549	66.55	-3.34	2.63	4.0	30.4	20.7	11.76	0.74	1.94	1.00	10.78	0.30	0.63
20114644+3649348	74.16	1.64	3.99	4.3	25.6	23.0	10.09	0.80	1.90	1.49	8.61	0.14	-0.08
20125530+4310184	79.60	4.94	1.62	4.0	48.8	21.5	11.45	0.39	1.42	0.60	10.85	0.12	0.60
20135618+4443093	81.00	5.63	1.30	3.9	22.4	9.0	11.29	0.50	1.52	0.49	10.80	0.29	0.87
20135690+2902036	67.91	-3.03	1.61	4.1	53.8	29.1	10.91	0.53	1.61	0.60	10.31	0.27	0.82
20141998+3732490	75.04	1.61	2.28	4.3	61.6	12.3	10.89	0.78	–	0.90	10.04	0.40	–
20170253+3150065	70.61	-2.03	2.59	4.2	74.8	25.4	10.25	0.65	1.99	1.00	9.28	0.22	0.70
20171300+4341267	80.47	4.57	1.18	4.0	33.8	25.7	11.39	0.61	1.79	0.40	10.95	0.40	1.20
20183871+4041003	78.11	2.67	3.40	4.2	37.2	30.5	10.71	0.78	2.29	1.30	9.44	0.22	0.60
20194861+4046363	78.32	2.54	4.31	4.3	66.2	41.0	10.10	0.72	2.36	1.70	8.49	0.01	0.23
20201209+4039396	78.26	2.41	2.98	4.2	46.0	31.3	10.29	0.81	2.34	1.10	9.18	0.33	0.86
20201507+4148266	79.22	3.05	0.97	4.0	29.6	26.6	11.48	0.95	2.85	0.40	11.12	0.79	2.37
20202170+3954306	77.66	1.96	4.30	4.3	11.2	5.6	12.60	–	–	1.60	11.00	–	–
20212592+4438079	81.67	4.48	2.72	4.0	18.1	16.3	10.84	0.59	2.05	1.01	9.83	0.14	0.70
20214907+4400399	81.20	4.07	1.32	4.1	36.6	22.0	11.20	0.55	1.67	0.50	10.71	0.33	1.01
20231262+3925015	77.57	1.23	2.45	4.3	37.6	18.8	10.06	1.42	3.35	0.90	9.15	1.01	2.13
20252529+4103192	79.15	1.83	2.95	4.2	23.4	15.4	12.21	1.17	–	1.10	11.11	0.68	–
20321160+4937105	86.82	5.85	1.54	3.9	26.5	8.0	11.06	0.60	1.77	0.57	10.49	0.35	1.00
20321211+3255568	73.35	-4.02	0.92	4.0	69.2	18.0	11.21	0.29	1.13	0.30	10.87	0.14	0.69

Table B.1 – Continued

2MASXJ identifier [hhmmssss ± ddmmssss] (1)	gal l [deg] (2)	gal b [deg] (3)	$E(B-V)$ [mag] (4)	SD (5)	$a_{K_{20}}$ [arcsec] (6)	$b_{K_{20}}$ [arcsec] (7)	$K_{s_{20}}$ [mag] (8)	$H-K$ [mag] (9)	$J-K$ [mag] (10)	A_{K_s} [mag] (11)	K_s^o [mag] (12)	$(H-K)_o$ [mag] (13)	$(J-K)_o$ [mag] (14)
20321954+4951445	87.03	5.98	1.60	3.9	21.2	8.5	11.29	0.41	1.48	0.60	10.69	0.15	0.68
20334726+4511401	83.40	3.02	1.98	4.2	58.0	27.8	10.60	0.45	1.48	0.70	9.86	0.11	0.50
20341242+4658296	84.88	4.02	5.61	4.1	41.0	18.9	11.29	0.77	2.45	2.00	9.20	-0.16	-0.34
20351333+3947557	79.23	-0.42	6.85	4.0	14.2	9.9	11.75	1.27	–	2.55	9.20	0.13	–
20351918+4542555	83.98	3.11	2.18	4.1	64.8	25.9	10.27	0.68	2.03	0.80	9.46	0.32	0.95
20362143+3634452	76.79	-2.53	1.93	4.1	26.4	12.1	11.80	0.50	1.73	0.70	11.08	0.18	0.77
20363702+4647294	84.98	3.58	2.99	4.1	49.2	13.8	11.55	0.99	–	1.10	10.44	0.50	–
20363825+4546254	84.17	2.96	2.18	4.2	41.8	23.4	10.99	0.68	2.15	0.80	10.18	0.31	1.06
20394281+3211363	73.70	-5.73	1.33	3.9	20.6	16.5	10.92	0.52	1.70	0.50	10.43	0.30	1.04
20400769+3853421	79.09	-1.72	3.16	4.0	15.0	4.5	12.42	0.90	–	1.18	11.24	0.38	–
20401346+5059165	88.69	5.64	1.51	3.9	36.8	25.8	9.11	0.48	1.55	0.56	8.55	0.22	0.80
20403052+5054257	88.66	5.55	1.36	3.9	26.3	21.0	10.41	0.41	1.43	0.51	9.90	0.19	0.76
20412222+5054235	88.74	5.45	1.39	3.9	21.0	16.8	10.50	0.53	1.53	0.52	9.98	0.30	0.85
20415515+4532386	84.55	2.09	3.67	4.2	13.1	11.8	11.36	1.17	–	1.37	9.99	0.56	–
20420550+4636124	85.40	2.72	3.04	4.1	35.4	26.2	10.83	0.88	2.74	1.10	9.70	0.37	1.22
20435702+5032583	88.71	4.91	1.41	3.9	63.6	28.0	10.57	0.44	1.43	0.50	10.05	0.21	0.73
20440027+4143156	81.77	-0.56	2.02	4.0	53.0	37.1	10.66	0.94	2.89	0.80	9.91	0.62	1.89
20440241+5043362	88.86	5.00	1.43	3.9	32.7	13.1	10.64	0.45	1.56	0.53	10.11	0.21	0.85
20441259+4940566	88.05	4.34	1.76	4.0	24.2	18.4	11.83	0.48	1.77	0.70	11.17	0.19	0.89
20453717+4046002	81.21	-1.40	2.12	4.2	18.2	16.7	11.96	0.60	1.77	0.80	11.17	0.24	0.71
20470471+4046165	81.39	-1.61	1.96	4.1	33.6	14.1	11.95	0.45	1.68	0.70	11.22	0.13	0.71
20470471+4046165	81.39	-1.61	1.96	4.1	33.6	14.1	11.95	0.45	1.68	0.70	11.22	0.13	0.71
20491597+5119089	89.84	4.73	1.42	3.9	78.2	10.9	7.39	4.65	1.03	0.50	6.86	4.42	0.33
20494713+5206261	90.50	5.16	1.44	3.9	20.6	16.5	10.20	0.42	1.46	0.54	9.66	0.19	0.74
20494797+5041271	89.40	4.27	2.02	4.0	44.4	13.3	11.47	0.58	2.05	0.80	10.72	0.25	1.05
20501144+4516514	85.25	0.79	2.20	4.2	33.6	32.3	11.34	0.92	–	0.80	10.52	0.56	–
20514892+5132328	90.26	4.56	2.01	3.9	26.6	17.6	11.94	0.51	1.69	0.80	11.19	0.18	0.68
20525943+5311105	91.65	5.47	1.66	3.9	17.0	10.2	11.62	0.53	1.69	0.62	11.00	0.25	0.87
20535370+5012580	89.45	3.46	3.06	4.1	15.5	10.8	12.34	1.09	–	1.14	11.20	0.58	–
20540993+4608346	86.35	0.81	2.64	4.3	53.6	28.9	10.40	0.69	2.21	1.00	9.41	0.25	0.90
20550635+4603460	86.40	0.63	2.75	4.3	31.8	22.9	11.51	0.77	–	1.00	10.49	0.32	–
20564755+5441095	93.17	6.00	1.21	3.8	24.2	16.9	10.21	0.45	1.43	0.45	9.76	0.25	0.83
20571736+4738373	87.84	1.38	2.29	4.2	56.2	36.0	9.95	0.44	1.31	0.90	9.09	0.06	0.18

Table B.1 – Continued

2MASXJ identifier [hhmmssss ± ddmmssss] (1)	gal l [deg] (2)	gal b [deg] (3)	$E(B-V)$ [mag] (4)	SD (5)	$a_{K_{20}}$ [arcsec] (6)	$b_{K_{20}}$ [arcsec] (7)	$K_{s_{20}}$ [mag] (8)	$H-K$ [mag] (9)	$J-K$ [mag] (10)	A_{K_s} [mag] (11)	K_s^o [mag] (12)	$(H-K)_o$ [mag] (13)	$(J-K)_o$ [mag] (14)
20572285+4808542	88.24	1.69	2.48	4.2	82.0	21.3	10.42	0.59	1.86	0.90	9.50	0.17	0.63
20573213+4548173	86.47	0.14	2.45	4.2	46.8	11.2	11.66	1.16	–	0.90	10.75	0.75	–
20581676+4615252	86.90	0.34	3.29	4.3	36.4	18.9	11.87	0.55	–	1.20	10.64	0.01	–
20584833+4535334	86.46	-0.16	2.27	4.2	15.3	10.7	10.91	0.52	1.75	0.84	10.06	0.14	0.62
20590227+4251273	84.42	-1.98	1.76	4.1	53.2	22.3	11.07	0.57	1.99	0.70	10.41	0.29	1.12
21012083+4624515	87.37	0.05	1.78	4.2	29.0	15.1	11.73	0.51	1.87	0.70	11.07	0.21	0.98
21042220+4742415	88.68	0.52	2.48	4.2	29.0	15.7	11.86	0.58	2.05	0.90	10.94	0.17	0.82
21053995+4958040	90.50	1.87	3.90	4.1	15.6	9.4	10.98	0.76	2.10	1.45	9.53	0.12	0.17
21054461+4958350	90.51	1.87	3.98	4.1	22.4	11.2	12.16	0.80	2.36	1.50	10.68	0.13	0.38
21055031+4956260	90.50	1.83	4.13	4.1	31.6	20.2	11.33	0.76	2.57	1.60	9.79	0.08	0.51
21055135+4957389	90.52	1.85	4.14	4.1	9.4	7.5	12.41	–	–	1.54	10.87	–	–
21060821+4500472	86.88	-1.51	1.17	4.2	48.2	29.9	10.53	0.45	1.52	0.40	10.09	0.25	0.94
21060867+4532092	87.27	-1.16	1.15	4.1	51.8	23.8	10.86	0.38	1.40	0.40	10.43	0.19	0.83
21061631+4503203	86.93	-1.50	1.18	4.1	50.4	34.3	10.26	0.36	1.26	0.40	9.82	0.16	0.67
21064188+4525375	87.25	-1.30	1.09	4.2	31.2	20.0	11.57	0.52	1.61	0.40	11.16	0.34	1.07
21064324+4741525	88.94	0.22	2.42	4.3	29.6	23.1	10.89	0.59	1.81	0.90	9.99	0.19	0.61
21071353+4456529	86.96	-1.70	1.31	4.1	50.4	44.4	10.34	0.45	1.58	0.50	9.85	0.23	0.92
21081300+4403398	86.43	-2.43	0.86	4.1	34.6	31.1	11.01	0.39	1.23	0.30	10.69	0.26	0.81
21084767+4354039	86.38	-2.61	0.86	4.0	52.4	25.2	10.84	0.45	1.34	0.30	10.52	0.30	0.91
21085630+4451164	87.10	-1.98	1.30	4.1	59.8	19.1	10.44	0.44	1.51	0.50	9.96	0.23	0.87
21095816+5437431	94.39	4.53	1.97	3.9	32.8	19.0	11.75	0.66	1.73	0.70	11.02	0.33	0.75
21104814+4341173	86.47	-3.02	0.85	4.0	41.2	35.4	10.82	0.38	1.29	0.30	10.50	0.24	0.87
21121597+4531167	87.98	-1.96	0.81	4.1	50.0	29.0	10.37	0.35	1.26	0.30	10.07	0.22	0.86
21123923+4556037	88.33	-1.72	1.13	4.1	72.0	14.4	11.22	0.61	1.71	0.40	10.80	0.42	1.15
21132159+4945237	91.19	0.82	2.51	4.2	37.2	18.6	11.65	0.65	2.10	0.90	10.71	0.23	0.85
21132528+4956168	91.33	0.94	2.42	4.2	31.2	30.0	11.95	0.84	–	0.90	11.05	0.44	–
21140974+4835425	90.44	-0.07	2.30	4.2	28.4	20.4	11.55	0.52	1.81	0.80	10.69	0.14	0.67
21154360+4725180	89.77	-1.08	1.85	4.2	38.8	22.5	10.81	0.42	1.25	0.70	10.12	0.11	0.33
21155335+4726430	89.81	-1.08	1.98	4.2	32.2	21.3	11.63	0.62	1.66	0.70	10.89	0.29	0.68
21155845+4655229	89.44	-1.45	1.34	4.1	34.2	30.8	10.66	0.40	1.30	0.50	10.16	0.18	0.63
21162340+4547366	88.68	-2.29	1.16	4.0	23.6	18.9	11.60	0.47	1.50	0.40	11.17	0.28	0.92
21164349+5200341	93.18	2.00	3.79	4.1	17.9	7.2	12.11	1.02	–	1.41	10.69	0.39	–
21164758+5508395	95.44	4.17	1.54	4.0	35.6	17.8	11.04	0.42	1.37	0.60	10.46	0.16	0.60

Table B.1 – Continued

2MASXJ identifier [hhmmssss ± ddmmssss] (1)	gal l [deg] (2)	gal b [deg] (3)	$E(B-V)$ [mag] (4)	SD (5)	$a_{K_{20}}$ [arcsec] (6)	$b_{K_{20}}$ [arcsec] (7)	$K_{s_{20}}$ [mag] (8)	$H-K$ [mag] (9)	$J-K$ [mag] (10)	A_{K_s} [mag] (11)	K_s^o [mag] (12)	$(H-K)_o$ [mag] (13)	$(J-K)_o$ [mag] (14)
21172770+4646547	89.52	-1.73	1.86	4.1	8.9	8.0	11.77	0.45	1.51	0.69	11.08	0.14	0.59
21173015+4915194	91.29	-0.01	3.02	4.1	37.4	24.7	11.78	0.70	–	1.20	10.65	0.20	–
21174271+4815503	90.61	-0.73	2.87	4.1	35.4	14.2	11.91	0.79	2.27	1.10	10.84	0.32	0.85
21181305+4526187	88.65	-2.77	0.94	4.0	28.8	21.9	11.41	0.40	1.32	0.40	11.06	0.24	0.85
21183139+5431287	95.17	3.56	1.93	4.0	59.4	17.8	10.49	0.66	1.90	0.70	9.77	0.34	0.94
21184034+5218497	93.61	2.00	4.00	4.1	22.0	18.5	12.18	1.14	–	1.50	10.69	0.48	–
21185980+4401180	87.73	-3.86	1.02	4.0	44.0	29.9	11.56	0.41	1.25	0.40	11.18	0.24	0.74
21195943+5519423	95.89	3.98	3.15	4.0	52.2	36.5	10.94	0.85	1.59	1.00	9.76	0.33	0.02
21202103+4519063	88.83	-3.12	1.00	4.0	29.0	13.9	11.60	0.40	1.25	0.40	11.23	0.23	0.75
21214731+4414419	88.25	-4.06	0.88	3.9	55.8	33.5	10.33	0.36	1.26	0.30	10.00	0.21	0.81
21215894+5219203	93.97	1.65	5.12	4.1	16.2	13.3	12.68	0.88	–	2.00	10.77	0.02	–
21231420+4850254	91.66	-0.97	1.80	4.1	21.6	15.6	11.87	0.61	1.85	0.70	11.20	0.31	0.96
21240760+4943370	92.39	-0.44	2.58	4.2	15.9	7.9	11.81	0.73	–	0.96	10.85	0.30	–
21242503+4933591	92.31	-0.59	2.48	4.2	24.8	15.9	11.65	0.58	1.74	0.90	10.73	0.17	0.51
21253828+4809267	91.47	-1.74	1.42	4.0	32.0	20.5	11.08	0.54	1.69	0.50	10.55	0.30	0.98
21255239+4423193	88.87	-4.47	0.80	3.9	87.8	33.4	11.16	0.35	1.18	0.30	10.86	0.22	0.78
21263514+4541569	89.87	-3.61	0.77	4.0	31.8	29.3	11.27	0.43	1.14	0.30	10.98	0.30	0.76
21273041+4525157	89.80	-3.93	0.69	3.9	55.6	32.2	11.02	0.28	1.18	0.30	10.76	0.16	0.84
21274031+4741107	91.39	-2.31	1.03	4.0	23.4	15.4	11.38	0.31	1.23	0.40	11.00	0.15	0.73
21292943+5030411	93.55	-0.47	2.81	4.1	23.8	21.9	11.82	0.70	2.32	1.00	10.77	0.23	0.92
21305323+4813559	92.15	-2.29	1.03	4.0	63.6	26.7	9.92	0.39	1.32	0.40	9.54	0.22	0.81
21310014+4814279	92.17	-2.29	1.04	4.0	84.6	49.1	9.74	0.45	1.40	0.40	9.35	0.27	0.88
21311568+4752142	91.95	-2.59	1.01	4.0	57.4	21.8	10.77	0.37	1.34	0.40	10.39	0.20	0.84
21324206+4816460	92.41	-2.46	0.93	4.0	34.4	27.5	11.26	0.50	1.40	0.40	10.91	0.34	0.93
21333640+4747326	92.19	-2.92	1.00	4.0	29.8	28.0	11.04	0.50	1.45	0.40	10.67	0.33	0.95
21350281+5309074	95.97	0.88	2.27	4.1	22.2	16.9	11.68	0.49	1.80	0.80	10.83	0.11	0.66
21355259+4734217	92.32	-3.34	0.64	4.0	63.6	38.2	10.48	0.32	1.01	0.20	10.24	0.21	0.69
21355399+4728217	92.26	-3.41	0.64	4.0	26.2	12.6	11.46	0.53	1.41	0.20	11.22	0.42	1.09
21362763+5936230	100.47	5.53	1.06	3.9	17.6	7.0	11.62	0.57	1.55	0.40	11.22	0.39	1.02
21375000+5929172	100.52	5.33	1.05	3.8	24.0	14.4	10.94	0.57	1.65	0.39	10.55	0.39	1.13
21411938+5103170	95.30	-1.32	1.92	4.1	14.7	11.8	11.49	–	1.60	0.72	10.77	–	0.65
21413756+5245302	96.45	-0.07	3.16	4.1	22.8	12.8	12.23	0.63	2.16	1.10	11.05	0.11	0.59
21464183+5427064	98.13	0.73	1.48	4.2	16.0	8.0	11.78	0.56	1.61	0.55	11.23	0.32	0.88

Table B.1 – Continued

2MASXJ identifier [hhmmssss ± ddmmssss] (1)	gal l [deg] (2)	gal b [deg] (3)	$E(B-V)$ [mag] (4)	SD (5)	$a_{K_{20}}$ [arcsec] (6)	$b_{K_{20}}$ [arcsec] (7)	$K_{s_{20}}$ [mag] (8)	$H-K$ [mag] (9)	$J-K$ [mag] (10)	A_{K_s} [mag] (11)	K_s^o [mag] (12)	$(H-K)_o$ [mag] (13)	$(J-K)_o$ [mag] (14)
21511714+5439331	98.77	0.47	2.72	4.0	40.6	29.2	11.25	0.70	2.00	1.00	10.24	0.26	0.66
21512814+5316383	97.92	-0.62	1.41	4.1	35.2	19.0	11.06	0.51	1.58	0.50	10.54	0.28	0.88
21523166+5245290	97.72	-1.13	1.33	4.1	30.4	21.3	11.25	0.39	1.51	0.50	10.76	0.17	0.85
21554534+5228186	97.92	-1.66	1.14	4.0	44.0	33.4	11.47	0.45	1.28	0.40	11.04	0.26	0.72
21565664+5539243	100.02	0.75	1.87	4.1	18.8	16.9	11.77	0.62	1.85	0.70	11.07	0.30	0.91
21584706+5408535	99.31	-0.61	1.73	4.1	28.0	17.9	11.72	0.52	1.74	0.60	11.08	0.23	0.88
22051447+6048418	104.01	4.20	1.08	4.0	38.6	20.8	11.39	0.73	1.82	0.40	10.99	0.55	1.28
22051749+5935350	103.29	3.21	1.22	4.0	20.6	15.2	11.66	0.41	1.38	0.50	11.21	0.21	0.78
22103166+5535087	101.52	-0.45	2.49	4.1	29.2	14.6	11.85	0.78	1.83	0.80	10.92	0.37	0.60
22131198+6153077	105.41	4.52	1.12	3.9	39.4	33.9	11.08	0.63	1.68	0.40	10.66	0.44	1.12
22134060+6026059	104.63	3.29	1.95	4.0	31.8	14.0	11.83	0.70	2.06	0.70	11.10	0.39	1.10
22143934+5902441	103.95	2.08	2.19	4.0	27.8	20.6	11.77	0.63	2.07	0.90	10.95	0.27	0.98
22200608+5846345	104.39	1.47	2.75	4.0	14.7	10.3	11.85	0.62	2.15	1.02	10.82	0.17	0.78
22201001+6345395	107.12	5.63	2.57	3.7	11.6	5.8	12.18	0.76	2.30	0.96	11.22	0.33	1.02
22202196+5447486	102.25	-1.89	0.66	4.0	61.6	20.9	11.00	0.40	1.42	0.20	10.75	0.29	1.09
22220225+5837501	104.52	1.21	3.78	4.0	24.4	17.1	11.93	0.73	2.08	1.50	10.52	0.10	0.19
22234144+5140563	100.98	-4.78	0.33	3.9	36.8	29.4	11.30	0.49	1.17	0.10	11.18	0.44	1.01
22262597+6135161	106.56	3.42	1.59	3.9	27.2	21.2	11.37	0.55	1.70	0.60	10.78	0.28	0.90
22342113+5759454	105.57	-0.18	1.12	4.0	73.0	48.2	9.45	0.45	1.53	0.40	9.03	0.26	0.97
22352646+6048150	107.09	2.19	1.75	4.0	36.0	23.8	10.84	0.59	1.72	0.70	10.19	0.30	0.85
22491636+6053023	108.61	1.46	2.75	3.9	23.2	19.5	11.78	0.78	2.21	1.00	10.75	0.32	0.84
22505236+5930185	108.17	0.13	2.78	4.0	39.2	25.1	9.62	1.11	2.57	1.00	8.58	0.65	1.19
22540054+6728086	112.02	7.12	1.26	3.7	32.2	9.7	10.62	0.53	1.62	0.47	10.15	0.32	0.99
22541372+5702353	107.48	-2.27	0.67	3.9	27.4	24.7	11.38	0.45	1.41	0.30	11.13	0.34	1.08
22545382+5756391	107.95	-1.50	1.07	4.0	29.0	26.7	11.25	0.47	1.53	0.40	10.85	0.29	1.00
22555131+5622305	107.39	-2.97	0.95	3.9	59.4	30.9	11.01	0.34	1.34	0.40	10.65	0.18	0.87
23013861+5711360	108.45	-2.56	1.00	3.9	27.0	25.4	11.51	0.52	1.40	0.40	11.14	0.35	0.90
23145710+5928024	110.95	-1.14	2.73	4.0	28.0	19.0	12.16	0.49	1.67	1.00	11.14	0.05	0.32
23160977+6136280	111.86	0.80	6.67	3.9	14.5	11.6	11.30	2.17	–	2.49	8.81	1.07	–
23170993+6131091	111.94	0.68	3.85	3.9	22.8	18.2	10.71	1.14	2.71	1.43	9.27	0.50	0.80
23230542+6135541	112.63	0.51	1.11	4.0	34.2	26.0	11.15	0.62	1.76	0.40	10.74	0.44	1.21
23360810+6223466	114.33	0.79	1.72	3.9	23.4	18.7	11.40	0.94	2.18	0.60	10.76	0.66	1.33
23530292+6727217	117.36	5.22	1.57	3.7	32.8	28.2	11.44	0.62	2.18	0.60	10.85	0.36	1.40

Table B.1 – Continued

2MASXJ identifier [hhmmssss ± ddmmssss] (1)	gal l [deg] (2)	gal b [deg] (3)	$E(B-V)$ [mag] (4)	SD (5)	$a_{K_{20}}$ [arcsec] (6)	$b_{K_{20}}$ [arcsec] (7)	$K_{s_{20}}$ [mag] (8)	$H-K$ [mag] (9)	$J-K$ [mag] (10)	A_{K_s} [mag] (11)	K_s^o [mag] (12)	$(H-K)_o$ [mag] (13)	$(J-K)_o$ [mag] (14)
23541834+5959178	115.84	-2.09	1.13	3.8	24.2	18.4	11.64	0.35	1.40	0.40	11.22	0.16	0.84
23552751+6701119	117.50	4.74	2.02	3.7	32.0	19.8	11.74	0.56	1.77	0.70	10.99	0.23	0.77
23553308+6014324	116.05	-1.88	1.63	3.9	35.2	26.0	11.71	0.48	1.20	0.60	11.10	0.21	0.39
23570980+6437388	117.16	2.37	1.55	3.9	31.0	27.3	11.31	0.52	1.77	0.60	10.73	0.26	1.00

Bibliography

Allen, R. J. 1969, A&A, 3, 316

Bertschinger, E. & Dekel, A. 1989, ApJL , 336, L5

Bird, C. M. 1994, AJ , 107, 1637

Böhringer, H., Schuecker, P., Guzzo, L., Collins, C. A., Voges, W., Schindler, S., Neumann, D. M., Cruddace, R. G., De Grandi, S., Chincarini, G., Edge, A. C., MacGillivray, H. T., & Shaver, P. 2001, A&A, 369, 826

Bond, J. R., Kofman, L., & Pogosyan, D. 1996, Nature , 380, 603

Broeils, A. H. & Rhee, M.-H. 1997, A&A, 324, 877

Cardelli, J. A., Clayton, G. C., & Mathis, J. S. 1989, ApJ , 345, 245

Chamaraux, P., Cayatte, V., Balkowski, C., & Fontanelli, P. 1990, A&A, 229, 340

Chamaraux, P. & Masnou, J.-L. 2004, MNRAS , 347, 541

Christiansen, W. N. & Hindman, J. V. 1951, Nature , 167, 635

Crook, A. C., Huchra, J. P., Martimbeau, N., Masters, K. L., Jarrett, T., & Macri, L. M. 2007, ApJ , 655, 790

Cutri, R. M., Skrutskie, M. F., van Dyk, S., Beichman, C. A., Carpenter, J. M., Chester, T., Cambresy, L., Evans, T., Fowler, J., Gizis, J., Howard, E., Huchra, J., Jarrett, T., Kopan, E. L., Kirkpatrick, J. D., Light, R. M., Marsh, K. A., McCallon, H., Schneider, S., Stiening, R., Sykes, M., Weinberg, M., Wheaton, W. A., Wheelock, S., & Zacarias, N. 2003, 2MASS All Sky Catalog of point sources., ed. Cutri, R. M., Skrutskie, M. F., van Dyk, S., Beichman, C. A., Carpenter, J. M., Chester, T., Cambresy, L., Evans, T., Fowler, J., Gizis, J., Howard, E., Huchra, J., Jarrett, T., Kopan, E. L., Kirkpatrick, J. D., Light, R. M., Marsh, K. A., McCallon, H., Schneider, S., Stiening, R., Sykes, M., Weinberg, M., Wheaton, W. A., Wheelock, S., & Zacarias, N.

Davis, M., Huchra, J., Latham, D. W., & Tonry, J. 1982, ApJ , 253, 423

Davis, M. & Peebles, P. J. E. 1983, ARA&A , 21, 109

de Lapparent, V., Geller, M. J., & Huchra, J. P. 1986, ApJL , 302, L1

Dekel, A. 1994, ARA&A , 32, 371

Dekel, A., Bertschinger, E., & Faber, S. M. 1990, ApJ , 364, 349

Djorgovski, S. & Davis, M. 1987, ApJ , 313, 59

Donley, J. L., Staveley-Smith, L., Kraan-Korteweg, R. C., Islas-Islas, J. M., Schröder, A., Henning, P. A., Koribalski, B., Mader, S., & Stewart, I. 2005, AJ , 129, 220

Ebeling, H., Edge, A. C., Bohringer, H., Allen, S. W., Crawford, C. S., Fabian, A. C., Voges, W., & Huchra, J. P. 1998, MNRAS , 301, 881

Ebeling, H., Kocevski, D., Tully, R. B., & Mullis, C. R. 2005, in Astronomical Society of the Pacific Conference Series, Vol. 329, Nearby Large-Scale Structures and the Zone of Avoidance, ed. A. P. Fairall & P. A. Woudt, 83

Emerson, J. P. 2001, in Astronomical Society of the Pacific Conference Series, Vol. 232, The New Era of Wide Field Astronomy, ed. R. Clowes, A. Adamson, & G. Bromage, 339

Epchtein, N., de Batz, B., Capoani, L., Chevallier, L., Copet, E., Fouqué, P., Lacombe, P., Le Bertre, T., Pau, S., Rouan, D., Ruphy, S., Simon, G., Tiphène, D., Burton, W. B., Bertin, E., Deul, E., Habing, H., Borsenberger, J., Dennefeld, M., Guglielmo, F., Loup, C., Mamon, G., Ng, Y., Omont, A., Provost, L., Renault, J.-C., Tanguy, F., Kimeswenger, S., Kienel, C., Garzon, F., Persi, P., Ferrari-Toniolo, M., Robin, A., Paturel, G., Vauglin, I., Forveille, T., Delfosse, X., Hron, J., Schultheis, M., Appenzeller, I., Wagner, S., Balazs, L., Holl, A., Lépine, J., Boscolo, P., Picazzio, E., Duc, P.-A., & Mennessier, M.-O. 1997, The Messenger, 87, 27

Ewen, H. I. & Purcell, E. M. 1951, Nature , 168, 356

Fairall, A. P., ed. 1998, Large-scale structures in the universe

Fisher, K. B., Lahav, O., Hoffman, Y., Lynden-Bell, D., & Zaroubi, S. 1995, MNRAS , 272, 885

Fisher, K. B., Scharf, C. A., & Lahav, O. 1994, MNRAS , 266, 219

Focardi, P., Marano, B., & Vettolani, G. 1984, A&A, 136, 178

—. 1986, A&A, 161, 217

Giovanelli, R., Havnes, M. P., & Chincarini, G. L. 1985, in Bulletin of the American Astronomical Society, Vol. 17, Bulletin of the American Astronomical Society, 581

Gordon, K. D., Clayton, G. C., Misselt, K. A., Landolt, A. U., & Wolff, M. J. 2003, ApJ , 594, 279

Granet, C., James, G. L., & Pezzani, J. 1997, IEEE Transactions on Antennas and Propagation, 45, 1366

Griffiths, D. J. 1982, American Journal of Physics, 50, 698

Guth, A. H. & Pi, S.-Y. 1982, Physical Review Letters, 49, 1110

Hauschildt, M. 1987, A&A, 184, 43

Hauser, M. G. 1988, in Bulletin of the American Astronomical Society, Vol. 20, Bulletin of the American Astronomical Society, 1071

Hawking, S. W. 1982, Physics Letters B, 115, 295

Haynes, M. P. & Giovanelli, R. 1986, ApJL , 306, L55

Helou, G., Madore, B. F., Schmitz, M., Bicay, M. D., Wu, X., & Bennett, J. 1991, in Astrophysics and Space Science Library, Vol. 171, Databases and On-line Data in Astronomy, ed. M. A. Albrecht & D. Egret, 89–106

Henning, P. A., Kraan-Korteweg, R. C., Rivers, A. J., Loan, A. J., Lahav, O., & Burton, W. B. 1998, AJ , 115, 584

Henning, P. A., Springob, C. M., Day, F., Minchin, R., Momjian, E., Catinella, B., Muller, E., Koribalski, B., Masters, K., Pantoja, C., Putman, M., Rosenberg, J. L., Schneider, S., & Staveley-Smith, L. 2008, in American Institute of Physics Conference Series, Vol. 1035, The Evolution of Galaxies Through the Neutral Hydrogen Window, ed. R. Minchin & E. Momjian, 246–248

Henning, P. A., Springob, C. M., Minchin, R. F., Momjian, E., Catinella, B., McIntyre, T., Day, F., Muller, E., Koribalski, B., Rosenberg, J. L., Schneider, S., Staveley-Smith, L., & van Driel, W. 2010, AJ , 139, 2130

Herschel, J. F. W. 1864, Royal Society of London Philosophical Transactions Series I, 154, 1

Hewett, P. C., Warren, S. J., Leggett, S. K., & Hodgkin, S. T. 2006, MNRAS , 367, 454

Hey, J. S. 1971, The radio universe, ed. Hey, J. S.

Hoffman, Y., Scharf, C., & Lahav, O. 1991, Annals of the New York Academy of Sciences, 647, 687

Holtzman, J. A. 1989, ApJS , 71, 1

Hubble, E. 1929, Proceedings of the National Academy of Science, 15, 168

Hubble, E. P. 1925, The Observatory, 48, 139

Huchra, J., Jarrett, T., Skrutskie, M., Cutri, R., Schneider, S., Macri, L., Steining, R., Mader, J., Martimbeau, N., & George, T. 2005, in Astronomical Society of the Pacific Conference Series, Vol. 329, Nearby Large-Scale Structures and the Zone of Avoidance, ed. A. P. Fairall & P. A. Woudt, 135

Huchra, J. P., Macri, L. M., Masters, K. L., Jarrett, T. H., Berlind, P., Calkins, M., Crook, A. C., Cutri, R., Erdoğdu, P., Falco, E., George, T., Hutcheson, C. M., Lahav, O., Mader, J., Mink, J. D., Martimbeau, N., Schneider, S., Skrutskie, M., Tokarz, S., & Westover, M. 2012, ApJS , 199, 26

Jarrett, T. 2004, PASA , 21, 396

Jarrett, T. H., Chester, T., Cutri, R., Schneider, S., Skrutskie, M., & Huchra, J. P. 2000, AJ , 119, 2498

Jarrett, T. H., Chester, T., Cutri, R., Schneider, S. E., & Huchra, J. P. 2003, AJ , 125, 525

Kerp, J., Winkel, B., Ben Bekhti, N., Flöer, L., & Kalberla, P. M. W. 2011, Astronomische Nachrichten, 332, 637

Kerr, F. J. & Henning, P. A. 1987, ApJL , 320, L99

Kerr, F. J. & Hindman, J. V. 1953, AJ , 58, 218

Kogut, A., Lineweaver, C., Smoot, G. F., Bennett, C. L., Banday, A., Boggess, N. W., Cheng, E. S., de Amici, G., Fixsen, D. J., Hinshaw, G., Jackson, P. D., Janssen, M., Keegstra, P., Loewenstein, K., Lubin, P., Mather, J. C., Tenorio, L., Weiss, R., Wilkinson, D. T., & Wright, E. L. 1993, ApJ , 419, 1

Kolatt, T., Dekel, A., & Lahav, O. 1995, MNRAS , 275, 797

Kraan-Korteweg, R. C. 2005, in Reviews in Modern Astronomy, Vol. 18, Reviews in Modern Astronomy, ed. S. Röser, 48–75

Kraan-Korteweg, R. C. & Huchtmeier, W. K. 1992, A&A, 266, 150

Kraan-Korteweg, R. C. & Lahav, O. 2000, A&A Rev., 10, 211

Kraan-Korteweg, R. C., Loan, A. J., Burton, W. B., Lahav, O., Ferguson, H. C., Henning, P. A., & Lynden-Bell, D. 1994, Nature , 372, 77

Kraan-Korteweg, R. C., Woudt, P. A., Cayatte, V., Fairall, A. P., Balkowski, C., & Henning, P. A. 1996, Nature , 379, 519

Lahav, O. 1994, in Astronomical Society of the Pacific Conference Series, Vol. 67, Unveiling Large-Scale Structures Behind the Milky Way, ed. C. Balkowski & R. C. Kraan-Korteweg, 171

Lahav, O., Lilje, P. B., Primack, J. R., & Rees, M. J. 1991, MNRAS , 251, 128

Lavaux, G. & Hudson, M. J. 2011, MNRAS , 416, 2840

Lawrence, A., Warren, S. J., Almaini, O., Edge, A. C., Hambly, N. C., Jameson, R. F., Lucas, P., Casali, M., Adamson, A., Dye, S., Emerson, J. P., Foucaud, S., Hewett, P., Hirst, P., Hodgkin, S. T., Irwin, M. J., Lodieu, N., McMahon, R. G., Simpson, C., Smail, I., Mortlock, D., & Folger, M. 2007, MNRAS , 379, 1599

Lineweaver, C. H. 1997, in Microwave Background Anisotropies, ed. F. R. Bouchet, R. Gispert, B. Guiderdoni, & J. Trân Thanh Vân , 69–75

Loeb, A. & Narayan, R. 2008, MNRAS , 386, 2221

Lu, N. Y. & Freudling, W. 1995, ApJ , 449, 527

Lynden-Bell, D., Lahav, O., & Burstein, D. 1989, MNRAS , 241, 325

Masters, K. L., Springob, C. M., & Huchra, J. P. 2008, AJ , 135, 1738

Mather, J. C., Fixsen, D. J., Shafer, R. A., Mosier, C., & Wilkinson, D. T. 1999, ApJ , 512, 511

Matthews, L. D. & van Driel, W. 2000, A&AS, 143, 421

Meyer, M. J., Zwaan, M. A., Webster, R. L., Staveley-Smith, L., Ryan-Weber, E., Drinkwater, M. J., Barnes, D. G., Howlett, M., Kilborn, V. A., Stevens, J., Waugh, M., Pierce, M. J., Bhathal, R., de Blok, W. J. G., Disney, M. J., Ekers, R. D., Freeman, K. C., Garcia, D. A., Gibson, B. K., Harnett, J., Henning, P. A., Jerjen, H., Kesteven, M. J., Knezek, P. M., Koribalski, B. S., Mader, S., Marquarding, M., Minchin, R. F., O'Brien, J., Oosterloo, T., Price, R. M., Putman, M. E., Ryder, S. D., Sadler, E. M., Stewart, I. M., Stootman, F., & Wright, A. E. 2004, MNRAS , 350, 1195

Monnier Ragaigne, D., van Driel, W., Schneider, S. E., Balkowski, C., & Jarrett, T. H. 2003, A&A, 408, 465

Mould, J., Kennicutt, Jr., R. C., & Freedman, W. 2000, Reports on Progress in Physics, 63, 763

Muller, C. A. & Oort, J. H. 1951, Nature , 168, 357

Navarro, J. F., Frenk, C. S., & White, S. D. M. 1997, ApJ , 490, 493

Neugebauer, G., Habing, H. J., van Duinen, R., Aumann, H. H., Baud, B., Beichman, C. A., Beintema, D. A., Boggess, N., Clegg, P. E., de Jong, T., Emerson, J. P., Gautier, T. N., Gillett, F. C., Harris, S., Hauser, M. G., Houck, J. R., Jennings, R. E., Low, F. J., Marsden, P. L., Miley, G., Olnon, F. M., Pottasch, S. R., Raimond, E., Rowan-Robinson, M., Soifer, B. T., Walker, R. G., Wesselius, P. R., & Young, E. 1984, ApJL , 278, L1

Nilson, P. 1973, Uppsala general catalogue of galaxies

O'Neil, K. 2004, AJ , 128, 2080

Pantoja, C. A., Altschuler, D. R., Giovanardi, C., & Giovanelli, R. 1997, AJ , 113, 905

Paturel, G., Theureau, G., Bottinelli, L., Gouguenheim, L., Coudreau-Durand, N., Hallet, N., & Petit, C. 2003, A&A, 412, 57

Proctor, R. 1878, The Universe of Stars, ed. Proctor, R.

Saintongé, A. 2007, AJ , 133, 2087

Sandage, A., Tammann, G. A., & Hardy, E. 1972, ApJ , 172, 253

Saunders, W., Frenk, C., Rowan-Robinson, M., Lawrence, A., & Efstathiou, G. 1991, Nature , 349, 32

Scharf, C., Hoffman, Y., Lahav, O., & Lynden-Bell, D. 1992, MNRAS , 256, 229

Schlegel, D. J., Finkbeiner, D. P., & Davis, M. 1998, ApJ , 500, 525

Schneider, S. E., Thuan, T. X., Magri, C., & Wadiak, J. E. 1990, ApJS , 72, 245

Schröder, A., Kraan-Korteweg, R. C., Mamon, G. A., & Ruphy, S. 1997, in Extragalactic Astronomy in the Infrared, ed. G. A. Mamon, T. X. Thuan, & J. Tran Thanh Van, 381

Schröder, A. C., Mamon, G. A., Kraan-Korteweg, R. C., & Woudt, P. A. 2007, A&A, 466, 481

Seeberger, R., Huchtmeier, W. K., & Weinberger, R. 1994, A&A, 286, 17

Shapley, H. 1961, JRASC, 55, 273

Skrutskie, M. F., Cutri, R. M., Stiening, R., Weinberg, M. D., Schneider, S., Carpenter, J. M., Beichman, C., Capps, R., Chester, T., Elias, J., Huchra, J., Liebert, J., Lonsdale, C., Monet, D. G., Price, S., Seitzer, P., Jarrett, T., Kirkpatrick, J. D., Gizis, J. E., Howard, E., Evans, T., Fowler, J., Fullmer, L., Hurt, R., Light, R., Kopan, E. L., Marsh, K. A., McCallon, H. L., Tam, R., Van Dyk, S., & Wheelock, S. 2006, AJ , 131, 1163

Spinrad, H. 1975, ApJL , 199, L1

Springel, V., Frenk, C. S., & White, S. D. M. 2006, Nature , 440, 1137

Springob, C. M., Haynes, M. P., Giovanelli, R., & Kent, B. R. 2005, ApJS , 160, 149

Staveley-Smith, L., Wilson, W. E., Bird, T. S., Disney, M. J., Ekers, R. D., Freeman, K. C., Haynes, R. F., Sinclair, M. W., Vaile, R. A., Webster, R. L., & Wright, A. E. 1996, PASA , 13, 243

Strauss, M. A., Davis, M., Yahil, A., & Huchra, J. P. 1992, ApJ , 385, 421

Strauss, M. A. & Willick, J. A. 1995, Phys. Rep., 261, 271

Takata, T., Yamada, T., Saito, M., Chamaraux, P., & Kazes, I. 1994, A&AS, 104, 529

Theureau, G., Coudreau, N., Hallet, N., Hanski, M., Alsac, L., Bottinelli, L., Gouguenheim, L., Martin, J.-M., & Paturel, G. 2005, A&A, 430, 373

Trumpler, R. J. 1930, PASP , 42, 214

Tully, R. B. & Fisher, J. R. 1977, A&A, 54, 661

van Driel, W. 2008, in 2nd MCCT-SKADS Training School. Radio Astronomy: Fundamentals and the New Instruments

van Driel, W., Schneider, S. E., Kraan-Korteweg, R. C., & Monnier Ragaigne, D. 2009, A&A, 505, 29

Westpfahl, D. J. 1999, in Astronomical Society of the Pacific Conference Series, Vol. 180, Synthesis Imaging in Radio Astronomy II, ed. G. B. Taylor, C. L. Carilli, & R. A. Perley, 201

Wheelock, S. L., Gautier, T. N., Chillemi, J., Kester, D., McCallon, H., Oken, C., White, J., Gregorich, D., Boulanger, F., & Good, J. 1994, NASA STI/Recon Technical Report N, 95, 22539

Wiener, N. 1949, Extrapolation and Smoothing of Stationary Time Series, ed. Wiener, N.

Wright, E. L., Eisenhardt, P. R. M., Mainzer, A. K., Ressler, M. E., Cutri, R. M., Jarrett, T., Kirkpatrick, J. D., Padgett, D., McMillan, R. S., Skrutskie, M., Stanford, S. A., Cohen, M., Walker, R. G., Mather, J. C., Leisawitz, D., Gautier, III, T. N., McLean, I., Benford, D., Lonsdale, C. J., Blain, A., Mendez, B., Irace, W. R., Duval, V., Liu, F., Royer, D., Heinrichsen, I., Howard, J., Shannon, M., Kendall, M., Walsh, A. L., Larsen, M., Cardon, J. G., Schick, S., Schwalm, M., Abid, M., Fabinsky, B., Naes, L., & Tsai, C.-W. 2010, AJ , 140, 1868

Yahil, A., Strauss, M. A., Davis, M., & Huchra, J. P. 1991, ApJ , 372, 380

Zwaan, M. A., Meyer, M. J., Staveley-Smith, L., & Webster, R. L. 2005, MNRAS , 359, L30